



HAL
open science

Implementation of 3-D printing and laser machining manufacturing technologies for the conception of high-frequency ceramic devices and their integration in modern communication systems

Andrés Fontana

► **To cite this version:**

Andrés Fontana. Implementation of 3-D printing and laser machining manufacturing technologies for the conception of high-frequency ceramic devices and their integration in modern communication systems. Electronics. Université de Limoges, 2022. English. NNT : 2022LIMO0057 . tel-03763672

HAL Id: tel-03763672

<https://theses.hal.science/tel-03763672v1>

Submitted on 29 Aug 2022

HAL is a multi-disciplinary open access archive for the deposit and dissemination of scientific research documents, whether they are published or not. The documents may come from teaching and research institutions in France or abroad, or from public or private research centers.

L'archive ouverte pluridisciplinaire **HAL**, est destinée au dépôt et à la diffusion de documents scientifiques de niveau recherche, publiés ou non, émanant des établissements d'enseignement et de recherche français ou étrangers, des laboratoires publics ou privés.

University of Limoges

ED 610 – Sciences et Ingénierie des Systèmes, Mathématiques, Informatique (SISMI)
Faculty of Sciences and Techniques – XLIM Research Institute

Thesis to obtain the degree of
Doctor of the University of Limoges
High-frequency electronics, photonics and systems

Presented and defended by

Andrés FONTANA

On 13 July 2022

IMPLEMENTATION OF 3-D PRINTING AND LASER MACHINING MANUFACTURING TECHNOLOGIES FOR THE CONCEPTION OF HIGH-FREQUENCY CERAMIC DEVICES AND THEIR INTEGRATION IN MODERN COMMUNICATION SYSTEMS

Thesis directed by Nicolas DELHOTE and Stéphane BILA

JURY :

Rapporteurs

Mr. Erwan FOURN, Associate Professor - HDR – INSA Rennes

Mr. Roberto GÓMEZ GARCÍA, Professor – University of Alcalá

Examinators

Mr. Cyrille MENUDIER, Professor – XLIM – University of Limoges

Mr. Stéphane BILA, Research Director – CNRS – University of Limoges

Mr. Nicolas DELHOTE, Associate Professor – XLIM – University of Limoges

Mr. David CARSENAT, Engineer – Thales SIX GTS – Brive

Guests

Ms. Dimitra PSYCHOGIOU, Professor – Tyndall National Institute – University College Cork

Mr. Aurélien PERIGAUD, Engineer – XLIM – University of Limoges



To my family and friends

We can judge our progress by the courage of our questions and the depth of our answers, our willingness to embrace what is true rather than what feels good.

Carl Sagan

Acknowledgements

I would like to acknowledge all the people who have accompanied me during this journey and that helped me to reach the end of the road.

First of all I want to thank to my parents and my sisters for their unconditional love and support. For always being present in every moment of my life and for encourage me to follow my dreams.

To my supervisors, Dr. Stéphane Bila and Dr. Nicolas Delhote, for opening the doors of their research group and giving me the chance to work in France with them. I have nothing but words of gratitude for this enriching experience. Thanks for all the trust and valuable time guiding me through the beautiful adventure that is pursuing a doctorate.

To all the researchers that make up the team I worked, especially, to Dr. Aurelien Perigaud and Dr. Olivier Tantot, for the interesting scientific exchanges, their priceless advise, and particularly for their quality not only as professionals but also as the kind persons they are.

To the technical and administrative staff of the Laboratory, Mr. Damien Passerieux, Mr. Clément Hallepee, Mr. Cyril Guines and Mrs. Marie Claude Lerouge, for their tireless support, their always good predisposition, and their help to make my stay in Limoges an unforgettable memory.

To my research team colleagues for their great human kindness and for making me feel at home in France. Thank you for integrating me into your lives and families as a brother, to help me to discover this beautiful country and its culture, and for all the patience you had in teaching me a new language.

I would also not like to forget the people who accompanied me from afar. To my former colleagues in the Laboratory of Nanoelectronics in UTN.BA, Argentina, Dr. Félix Palumbo, Dr. Sebastián Pazos and Dr. Fernando Aguirre, for their continuous support, for motivating me to seek new horizons, and their advise and friendship.

Finally, I would like to acknowledge to Thales SIX GTS and their staff, Dr. David Carsenat,

Mr. Guillaume Acikalin, Mr. Richard Patrice, and Mr. Rachid El Mostadi, without whose support I would not have been able to develop this work. Thank you for your interest in this Thesis and for the numerous meetings that finally shaped its content.

Droits d'auteurs

Cette création est mise à disposition selon le Contrat :

« Attribution-Pas d'Utilisation Commerciale-Pas de modification 3.0 France »

disponible en ligne : <http://creativecommons.org/licenses/by-nc-nd/3.0/fr/>

This work is licensed under the Creative Commons License:

Attribution–NonCommercial–NoDerivs 3.0 France

To view a copy of this license, visit: <http://creativecommons.org/licenses/by-nc-nd/3.0/fr/>



Contents

1	General Introduction	20
2	Massive communication networks and novel manufacturing technologies applied to modern wireless systems	25
2.1	Evolution of mobile networks and wireless communications	28
2.1.1	The First Generation (1G)	28
2.1.2	The Second Generation (2G)	28
2.1.3	The Third Generation (3G)	29
2.1.4	The Fourth Generation (4G)	30
2.1.5	The Fifth Generation (5G)	30
2.1.6	5G and beyond: the arrival of the Sixth Generation (6G)	33
2.2	Modern transceivers for wireless communications	36
2.2.1	Massive Multiple-Input Multiple-Output beamforming communication systems	38
2.2.2	Microwave and millimeter-wave passive filters	41
2.3	Additive manufacturing technologies	55
2.3.1	3-D printing techniques	56
2.3.2	3-D printed electronics: technological trends and challenges	61
2.4	Conclusions and motivations	63
3	3-D printed tunable microwave resonators and filters	65
3.1	Current tuning methods	67
3.1.1	Planar technologies	68
3.1.2	Acoustic-wave-resonators (AWR)	68
3.1.3	Substrate Integrated Waveguide (SIW) devices	69
3.1.4	Tunable dielectric resonator filters	71
3.2	N-bit hybrid tunable filter bank	72
3.2.1	Monolithic ceramic cavity resonators study	73
3.3	1-bit tunable resonators	78

3.3.1	Tuning effect	79
3.3.2	Frequency shift effect control	81
3.4	Modelling and characterization setup	89
3.4.1	P-i-n diode RF switch	90
3.5	3-D printed tunable resonators: cases of study	92
3.5.1	Ceramic tunable resonators: general structure	93
3.5.2	Resonator prototypes	97
3.6	Manufacturing process	101
3.6.1	Monolithic ceramic resonators fabrication	103
3.6.2	Metal plating and gold coating	104
3.6.3	Printed shapes characterization	106
3.7	Experimental validation of manufactured devices	108
3.7.1	Measurement campaign at room temperature	109
3.7.2	Thermal characterization	112
3.8	Envisioning a monolithic 2-state tunable filter	113
3.9	Conclusions and perspectives	117
4	Bulky 3-D printed ceramic microwave devices	121
4.1	SLA ceramic devices: previous work	124
4.1.1	Laser engraving tuning methodology	125
4.1.2	Laser tuning patterns	127
4.1.3	Demonstration of laser tuned 4-pole ceramic cavity filter	129
4.2	Fully 3-D printed SMD ceramic filters	130
4.2.1	I/O terminal structure analysis	130
4.2.2	Band-pass filter design	133
4.2.3	3-D printed filters manufacturing characterization	136
4.2.4	Laser tuning strategy implemented in complex-shape 3-D printed filters	141
4.3	Temperature drift characterization	145
4.4	Application example: Filtenna	149
4.5	Conclusions and perspectives	152
5	Passive ceramic devices development for mm-Wave band applications	156
5.1	Laser Micro-machined Substrate Technology	158
5.1.1	Fabrication flow	158
5.1.2	LMST First Generation (G1)	160
5.1.3	LMST Second Generation (G2)	161

5.1.4	LMST Third Generation (G3)	162
5.1.5	Manufactured millimeter-wave devices	169
5.2	Temperature stability and surface-mount devices	177
5.2.1	Thermal study of LMST G3	179
5.3	Thermally-stable devices (G4)	180
5.3.1	Surface-mount transitions	184
5.4	Technology comparison	190
5.5	Supports as tuning structures	193
5.6	Frequency shift effect	194
5.6.1	Device tuning	195
5.6.2	2-pole filter tuning	201
5.7	Conclusion	202
6	Conclusions	205
6.0.1	Surface-mount transitions	206
6.0.2	Low-loss ceramics and metallization tests	206
6.0.3	3-D printed designs and technology integration	207
6.0.4	LMST millimeter-wave devices for 5G applications	209
6.0.5	Temperature stability and weight	209
A	Annexes	211
A.1	Wirebonds interconnections model	212
A.1.1	Estimation of bond wire S-parameters with de-embedding technique	214
A.1.2	Generic π -circuit Y-parameters (left) and bond wire model (right).	217
A.2	3-D printed filters extracted coupling matrices	221
A.2.1	Untuned devices	221
A.2.2	Tuned devices	222
A.3	LMST G4	223
B	Bibliography	224
Bibliography		225

List of Figures

2.1	ITU standard frequency bands and applications [5].	26
2.2	Evolution of mobile communications from the First Generation (1G) to the current Sixth Generation (6G).	29
2.3	(a) 5G ITU IMT-2020 use cases [21] and (b) massive MIMO (mMIMO) wireless mobile network [23].	31
2.4	5G frequency bands in several regions [26].	32
2.5	Estimated Fifth Generation (5G) and upcoming sixth generation (6G) worldwide communication networks [26].	33
2.6	Non-terrestrial networks: possible aerial/space stations (left) and use cases (right) [29].	34
2.7	GEO HTS multibeam satellite network scheme (a) and software-defined payload architecture (b) [34].	35
2.8	Some examples of digital multibeam antenna (DMBA) architectures: full DMBA (a), fixed subarray DMBA (b) and phased subarray DMBA (c) [36].	37
2.9	Massive digital MIMO beamforming transceiver block diagram with 64 antenna elements array [44].	38
2.10	Massive MIMO beamforming millimeter-wave front-end [44]: circuit schematic (a) and printed circuit board implementation (b).	39
2.11	Typical filter templates (purple) and frequency response of Chebyshev low-pass filter (a), band-stop filter (b), band-pass filter (c) and high-pass filter (d).	43
2.12	Equivalent schematic circuit model of a coupled resonator.	45
2.13	Influence of the variation of the external quality factor Q_e (a) and the unloaded quality factor Q_0 (b) in a coupled resonator frequency response.	46
2.14	Band-pass prototype of a coupled resonators loseless network.	47
2.15	Low-pass prototype of a coupled resonators loseless network.	48
2.16	Standalone network used to analyze the coupling matrix.	49
2.17	Relative insertion loss, size and cost of various RF resonators [55].	52
2.18	Different additive manufacturing processes [76].	57

2.19	Several 3-D printed microwave devices and systems. SLM : Feed Horn Antenna [91] (a), Butler matrices [88] (b), and monolithic feed chains [123] (c); Material jetting : origami antenna [82] (d), passive components [85] (e), and manifold-coupled triplexer [84] (f); SLA (polymers) : coaxial BPF [74] (g), and DR BPF [98] (h); SLA (ceramics) : monolithic Zirconia BPF [106] (i), 2-pole TM BPF [110] (j), and Multi-permittivity dual-band circularly polarized antenna [121] (k).	60
3.1	Block diagram of classic filter bank (a) and hybrid filter bank with tunable (2-state) filters (b).	72
3.2	Subdivision in N channels of a fixed portion of the frequency spectrum in the C-band.	73
3.3	Fundamental mode and spurious mode evolution with the resonator thickness (a). Minimum quality factor (Q_{0min}) needed to fulfill the specifications in terms of losses and estimated area in N channel filter bank with a fixed operating band (b).	76
3.4	Hybrid filter bank configuration block diagram.	77
3.5	SIW tunable resonator developed in [161] (left) and tuning effect generated with the disconnection (a) and connection (b) of a metallic via [159]. The surface current through the tuning post is represented on top and the vector magnetic field of the dominant mode on bottom.	80
3.6	Via post design parameters study performed in a rectangular ceramic-filled cavity resonator 3-D model.	81
3.7	Magnitude of the E-field distribution of two states (ON/OFF) for three tuning post positions: corner (P1), center edge (P2) and center (P3).	84
3.8	Normalized frequency shift Δf_0 (a), unloaded quality factor ΔQ_0 (b), and simulated S-parameters (S_{21}) (c and d) of a ceramic-filled rectangular cavity resonator for different via post positions and number of connections.	85
3.9	Alumina-filled rectangular cavity resonators study of quality factor (a) and frequency tuning range (b). Several substrate thickness (t) and post positions ($D_{post} = 1\text{ mm}$) were used to adjust the design to the specifications.	86
3.10	Alumina-filled rectangular cavity resonators study of quality factor (a) and frequency tuning range (b). Several substrate thickness (t) and post positions ($W_{post} = 1\text{ mm}$) were used to adjust the design to the channel specifications. The area of each resonator is specified in black.	87

3.11 Tuning effect simulations and measurements S-parameters (S_{21}) comparison of a 2-state rectangular cavity resonator developed in a 0.4 mm thick RO4003C substrate.	89
3.12 P-i-n diode forward and reverse small signal electrical model.	92
3.13 Pin-diode and bias network circuit model (left). The component values are $C_1 = C_2 = 10 \text{ pF}$, $C = 39 \text{ pF}$, $L = 8.2 \text{ nH}$. Simulated frequency response of every part of the network (right). f_c stands for the cutoff frequency and f_i and f_s the inferior and superior frequencies of the operating band $BW_{op. \text{ band}}$	93
3.14 3-D printed flip-chip tunable resonator design.	94
3.15 Circuit model of the cavity resonator loaded with the tuning via post.	95
3.16 Termination line effect on the quality factor and frequency shift for each via post state.	96
3.17 Suggested 3-D printed tunable resonator prototypes.	98
3.18 Normalized frequency spectrum in the tunable filter operating band.	101
3.19 Manufactured 3-D printed ceramic resonators and PCB carrier boards without metallization (a) and metallized with all the components surface-mounted before the final assembly (b).	102
3.20 Tunable resonator (Prototype 3) solder paste deposition (a) and device assembly with a pick and place machine (b).	102
3.21 Ceramic 3-D printed stereolithography manufacturing process flow.	103
3.22 Metal stack layers deposited with gold coating processes.	105
3.23 3-D scanned profiles of ramps and bumps manufactured with ceramic SLA. The ideal design profiles are highlighted in red to facilitate the comparison.	107
3.24 Tunable resonator functioning tests performed (a) before and (b) after the assembly onto the carrier board.	108
3.25 Measured Q-factor and frequency shift for the six prototypes (1 to 6) tested before and after the device assembly onto the carrier board.	110
3.26 Measured and simulated S-parameters (S_{21}) and Q-factor of Prototype 3.	112
3.27 2-state tunable filter design. The tuning method is based on prototype 1.	114
3.28 Tunable filter simulated S-parameters.	115
3.29 All the manufacturing steps of a SMT monolithic ceramic tunable filter.	116

4.1	5G MIMO beamforming transceiver board and mm-Wave front-end schematic circuit [44]. Auxiliary metal structures are utilized to electromagnetically isolate the different regions of the system.	122
4.2	Examples of surface-mounted 3-D printed ceramic devices adapted to different scenarios.	123
4.3	Post-fabrication tuning method process flow [193].	126
4.4	Electromagnetic field on the different tuning patterns for the case of resonance frequency shift (left) and inter-resonator coupling factor (right) [193].	128
4.5	Manufactured cavity filters (a). Simulation and measurements of ceramic filters (b): manufactured (A) and tuned (B) device [193].	129
4.6	SMT I/O terminal port transitions: Y-shaped terminal [50] (a), vertical posts excitation [205] and SIW to SMW transition [211].	130
4.7	Coplanar to TE_{101} cavity resonator transition: magnetic field and surface-mount assembly.	131
4.8	I/O terminal external quality factor analysis: (a) dependency with geometrical dimensions ($H_{acc} = 0.2 \text{ mm}$) and (b) variability due to misalignment.	132
4.9	Reference In-line filter design and frequency response.	133
4.10	3-D Alumina-based designs: Bridge, C-shaped, U-shaped and Box filters. Support anchor points are highlighted in red.	134
4.11	3-D printed filters footprint (a) and relative area ($W_T \times L_T$) comparison (b).	134
4.12	3-D printed waveguide design derived from the Bridge filter.	135
4.13	Manufactured ceramic filters placed in the printed orientation (a) and surface-mounted devices into the carrier board (b).	137
4.14	Measured manufactured filters dispersion (Δx , Δy and Δz) of every sample dimension (d_i) in the x-, y- and z- direction (a). The terms Suspended and Vertical structure refer to a resonator or iris in contact to the board (e.g. resonator 1 or iris 1 in Cs filter) or hanging as in resonators 2 and 3 of the Bridge filter. The mean filter manufacturing tolerance and dispersion is shown in (b), discriminated by the printing direction and the part of the device.	138
4.15	3-D printed filters back-simulations and simulated tuning: C-shaped (a), Bridge (b), Box (c) and U-shaped (d).	139
4.16	Laser scanned 3-D reconstruction of the Box filter (a). Scanned structure and reference CAD design comparisons (b). Deformations characterization of the manufactured device in millimeters (c, d).	141

4.17	Surface-mounted and laser-tuned devices (a). Patterns Ⓐ and Ⓑ are the typical tuning square and rectangular patterns used for the frequency tuning.	142
4.18	Equivalent quality factor extracted after laser tuning (a) and resonance frequency error correction (b).	143
4.19	Pre-tuning and post-tuning measured S-parameters of 3-D printed filters: C-shaped (a), Bridge (b), Box (c) and U-shaped (d).	144
4.20	3-D printed filters temperature characterization setup (a) and probe tips and sensing elements (b).	146
4.21	C-shaped filter pre-tuning (a) and post-tuning (b) measured S-parameters.	147
4.22	Additively manufactured ceramic filters response evolution with temperature in one cycle: relative frequency shift (a), relative bandwidth variation (b) and relative increment of losses (c).	148
4.23	Normalized coupling matrix factors dependency with temperature extracted from DUTs measurements: main diagonal factors m_{ii} (a) and inter-resonator coupling factors m_{ij} for the C-shaped (b), Bridge (c), Box (d) and U-shaped (e) filters.	148
4.24	CAD model of filtenna design. The in-line BPF is placed on a side to be used as the reflector of a Yagi-Uda antenna element.	150
4.25	Simulated radiation patterns comparison of the single Yagi-Uda antenna element (blue) and the integrated filtenna (red): H plane (left) and E plane (right).	151
4.26	Simulated gain and reflection coefficient of the filtenna design.	152
5.1	Laser micro-machined fabrication flow.	159
5.2	LMST filters: (a) 4-pole dual-mode Chebyshev (G1 and G2), (b) 6-pole quasi-elliptic (G1).	161
5.3	LMST evolution: (a) passive microwave filters and (b) quality factor dependency with the substrate loss ($\tan \delta$), electrical conductivity (ρ) and thickness (T) for a TE_{102} rectangular resonator.	162
5.4	Rectangular resonator profile (a) and 3-D reconstruction of the side wall (b) measured with a digital microscope.	164
5.5	SEM images of LMST structures fabricated in G3. Cross section of silver coated Alumina substrate (a). Metal layer after support trimming (b). . .	164

5.6	Coplanar access engraving on silver layer: (a) SEM and (b) profilometer measurements. A total ceramic substrate over-etching (t_{oe}) of $3.586 \mu m$ is measured.	164
5.7	LMST collective fabrication (G3) of microwave passive devices: 4-pole band-pass filters, waveguides and cavity resonators.	166
5.8	Electromagnetic field attenuation in function of normalized (N) values for the guided wave frequency ($f < f_c$ or $f_N < 1$), support length and width.	168
5.9	Simulated EM fields of a ceramic rectangular cavity resonator at 42 GHz (TE_{102} absolute values) (a). S-parameters comparison of three ceramic-filled rectangular cavity resonator samples: TE_{101} mode resonance frequency measured on-frame (b), and measured TE_{102} modes before ($L_{sup} = 350 \mu m$) and after the device separation from the substrate, testing different lengths for L_{sup} (330, 175 and 33 μm) (c).	170
5.10	Attenuation of E_y at $f_0 = 42 GHz$ for a given L_{SUP} and W_{SUP} . The markers indicates the supports size used in LMST G3.	171
5.11	Manufactured ceramic rectangular waveguide: engraved coplanar access (a), and simulated and measured S-parameters of two samples (b).	173
5.12	Inter-resonator coupling variation with: iris position ($L_{IRIS_N} = \frac{L_{IRIS}}{L_{RES}} = 53\%$) (a) and length (sided) (b).	174
5.13	LMST filters: 4-pole single-mode Chebyshev G3 without (a) and with transmission zeros (b). The area colored in gray illustrates the simulated geometrical parameters sensitivity analysis.	176
5.14	LMST devices temperature characterization setup (a). Defects in aerosol-deposited silver layer after exposure to temperatures greater than 200 °C. (b)	179
5.15	Alumina band-pass filters exposed to several temperatures: (a) single-mode filter and (b) single-mode filter with transmission zeros. Temperatures up to 123 °C were obtained heating the device in a furnace.	180
5.16	Laser micro-machined fabrication of BMT substrates ($\epsilon_r = 24.1$): (a) collective manufacturing (STEP 1) and (b) exposed structural weaknesses using straight corners (left) and rounded corners (right).	181
5.17	Measured S-parameters on-frame of 5G mm-Wave band thermally-stable filters: (a) frequency response comparison between four samples of the same run and (b) on-frame/SMD simulations and measurements (23 °C, 30 °C, 60 °C and 90 °C).	182
5.18	Coplanar access transition on: ceramic substrate (a) and carrier PCB (b).	185

5.19 Laser Micro-Machined Substrate Technology fourth generation (G4) filters and transitions optimization flow.	186
5.20 Photography taken with a digital microscope of a LMST ceramic device surface-mount transition (a). Excessive separation from the substrate and electrical disconnections can be observed. Surface-mounted components on a PCB carrier board (b).	187
5.21 BMT substrate-based manufactured filters in G4 scattering parameters. On-frame, surface-mounted and back-simulations (a). Optimized coplanar access simulations for $60 \mu m$ separation gap (b).	188
5.22 Photography taken with a digital microscope of a LMST ceramic device surface-mount transition. Excessive separation from the substrate and electrical disconnections can be observed.	190
5.23 Relative features comparison between LMST G3 filters [242] and 40 GHz mm-Wave band fabrication technologies (LTCC [257], air-filled SIW [261], and crystalline quartz [254]) [236]. The device thickness is represented in millimeters.	192
5.24 LMST filters relative frequency shift (a) and fractional bandwidth mismatch (b) statistics and Gaussian distribution.	192
5.25 Rectangular cavity resonator TE_{101} electric field distribution evaluated at different support lengths ($W_{SUP_N} = 50\%$) for a support located at $P_{OS} = 0$. $L_{SUP_1} = 25\%$, $L_{SUP_2} = 19.5\%$, $L_{SUP_3} = 10\%$, $L_{SUP_4} = 2.5\%$	195
5.26 LMST resonator examples manufactured in organic PCB substrates: quad-support with no EM influence (Prototype 1), double-support with high-frequency tuning range (Prototype 2), and quad-support with medium frequency shift tuning range (Prototype 3).	196
5.27 Frequency tuning range (a) and unloaded quality factor degradation (b) observed on prototype 2.	199
5.28 Simulated double-support resonator radiation pattern in decibel.	199
5.29 Frequency tuning range (a) and unloaded quality factor degradation (b) observed on prototype 3.	199
5.30 Iris trimming coupling factor (a) and LMST 2-pole filter (b) manufactured in organic PCB substrates: inter-resonator coupling tuning example (left) and 2-poles tunable filter example at 8 GHz (right).	200
5.31 2-pole filter S-parameter comparison: simulated design (black), manufactured prototype without corrections (blue), and post-tuned device (red).	201

A.1	Typical lumped element bond wire circuit model.	212
A.2	Manufactured coplanar line S-parameter measurement, and circuit and electromagnetic simulations comparison.	213
A.3	MA4AGSW1 bias network assembly on a Rogers RO4003C board. . . .	214
A.4	P-i-n diode switch control network comparison of circuit/electromagnetic model (without bond wires) and measurements.	215
A.5	Scheme of the bias network circuit blocks to be de-embedded.	216
A.6	Reference In-line filter design and frequency response.	216
A.7	Cross-check between bond wire inductance theoretical calculation and experimental data (a), and de-embedded bond wire model inductance (b), resistance (c), and capacitance (d).	218
A.8	P-i-n diode switch bias network electromagnetic and circuit simulation implementing the bond wire lumped-element model (a) and Touchstone files (b).	218
A.9	P-i-n diode switch control network (with bond wires) comparison of hybrid simulation complete model and measurements.	219

List of Tables

2.1	Additive manufacturing features comparison between polymer, ceramic and metal 3-D objects printed with different processes.	62
3.1	Alumina and Zirconium Dioxide rectangular cavity resonators features comparison.	74
3.2	Filter bank (fixed channels) estimated losses and area implemented with SPNT p-i-n diode switches and ceramic technology. (*) stands for the only case with more than one kind of switch (SPDT and SP5T). (**) stands for the minimum area cases.	75
3.3	Mixed technology filter bank estimated losses and area implemented with SPNT p-i-n diode switches and ceramic technology. In each case the used filter is a 1-bit (2-states) tunable filter. (*) stands for the minimum area cases.	78
3.4	Tunable resonator prototypes features comparison.	99
3.5	Simulated surface-mounted resonators resonance frequency, quality factor, and frequency shift between two states (Δf_0) with and without bond wire parasitics for channel 0 and 1.	100
3.6	Tunable filter samples tolerance comparison. The printed devices were exposed to a milling process to enhance the structure tolerance and definition.	116
4.1	Different coplanar tuning patterns case of study [193].	127
4.2	Filter design dimensional parameters.	136
4.3	Filter design dimensional parameters.	145
5.1	Measured dispersion in two manufactured resonator samples.	171
5.2	LMST G3 measured filters performances.	177
5.3	Temperature-stable band-pass filters technology comparison.	183
5.4	Millimeter-wave filters manufacturing technologies.	191
5.5	Measured dispersion in manufactured dummy resonators.	197

A.1 LMST G4 filter footprint dimensions (in millimeters). 223

1

General Introduction

DURING the last decades, the fast growth of communication applications have demanded a continuous effort from part of the scientific and industrial community to re-think and build the required infrastructure for modern communication services. With the implementation of the fifth generation of mobile communications (5G), the global vision of a highly interconnected world set as objective for the 2020s is finally taking place in many countries around the world. The continuous emergence of new services utilized in every aspect of our daily lives bring a fast increase of mobile data traffic and a great increase of interconnected devices. In the recent years, many applications targeted for early 2020s such as augmented reality, ultra-high-definition video and mobile cloud are making their first appearance in the international scene, being rapidly integrated in our society and changing the way we interact and experience the world. The first terrestrial 5G antennas and satellite constellations such as Starlink have been deployed in order to provide Internet access to every part of the planet. Last generation cellphones have successfully integrated the very first 5G receptors in their RF front-ends, providing access to high data rate transmission services to the users.

According to Omdia, the global acceleration of wireless 5G communications have exceed a half-billion connections by the end of 2021 and is expected to reach 1.3 billion

by the end of 2022. In 2021, 216 5G commercial networks have been deployed around the world that can be expanded up to 342 by the end of 2024. The economic impact of the 5G market forecast foreseen by IDTechEx for mobile services is expected to reach \$ 800 billion by 2032. In the case of France, an inform released by Omdia in 2021 estimates a positive impact of 5G technologies in the employment and the economy of the country, as well as a reduction of 10.1MtCO₂e of GHG emissions generated by 2030. The initiatives taken since 2018 could lead to the creation of 422 thousand jobs related to this sector and an increment of the incomes around € 190 billion in 5G-enabled sales. The implementation of real-time communications, flexibility, and low latency are seen as attractive features to strengthen and automatize the manufacturing sector, specially in the aerospace, defence, automotive and energy industry.

A great amount of work will still be required in the next 8 to 10 years to achieve the goals set for 5G technologies and beyond. For example, millimeter-wave point-to-point links have not been deployed yet for short-distance terrestrial-coverage services. The devices integrating these systems are expected to exhibit multiple features: good electromagnetic performances, compact size, affordable cost, reconfigurability, integration of several functionalities, light weight, and good reliability under harsh conditions. An impressive amount of manufacturing processes and communication techniques were explored to fulfill the specifications of a wide range of systems, from mobile phones to base-band stations and satellite links. In the frame of this thesis, we will study the development of ceramic-based microwave and millimeter-wave passive devices for modern 5G front-ends. The characteristics of ceramic materials in terms of high electric permittivity, low electromagnetic losses, resistance to high temperatures, temperature stability, light weight, among others, motivated their utilization throughout this thesis as components for 5G transceivers.

The manufacturing technologies utilized in our investigations for the conception of ceramic passive devices can be subdivided in two main categories: additive manufacturing processes, focused on the 3D printing of ceramic components; and classical subtractive technologies carried out by means of laser machining processes.

The devices explored were designed to cover the frequency bands established by the United Nations International Telecommunication Union (ITU) in the last World Radiocommunication Conference (WRC-19) for 5G communications (sub-6 GHz and European millimeter-wave bands).

In principle, the flexibility of additive manufacturing processes was exploited to integrate useful functionalities at subsystem level while reducing fabrication waste. However,

state-of-the-art ceramic printing process tolerances impose a limitation to the maximum operating frequency as a consequence of the current fabrication mismatch. This effect hinders the accurate frequency response of devices as the frequency augments. The aforementioned situation is addressed in this thesis. The fabrication of passive microwave devices, especially band-pass filters is pushed towards the X-band, where the tolerance of state-of-the-art ceramic stereolithography (SLA) processes highly impacts on the final device operation. Two tuning approaches compatible with the designed devices presented along this work are introduced to the lecturer and discussed to overcome the observed difficulties. However, in the case 5G millimeter-wave devices additive manufacturing is replaced by subtractive fabrication to be compliant with the stringent tolerances needed at these frequencies. A collective manufacturing strategy was investigated to amortise the expensive costs of ceramics devices and develop miniaturized cost-effective devices with good electromagnetic performances and light weight features.

All the ceramic components studied were designed to be surface-mounted in a main system board, compliant with the industrial standard of surface-mount assembly process handled by pick and place machines. Many transitions are shown and applied depending on the particular scenario to fulfill the component requirements. The main goals pursued in this thesis are:

1. Identify and characterize the main milestones throughout the whole fabrication flow implemented in every case to be used as a necessary information during the design stage.
2. Explore the benefits of 2.5-D and 3-D printed ceramic technologies that could lead to innovative solutions for RF devices at different microwave and millimeter-wave operating bands.
3. Investigate the integration 3-D printed ceramic devices with other technologies such as planar circuits or CMOS ICs, to provide compact and high-performance components appropriated for different circuits and subsystems scenarios.
4. Design the integrated devices with an assembly transition compatible to surface-mount technologies available in the industry.

Even though the developed devices in this work do not fully implements a packaging technology, the 3-D printed devices introduced in chapters 2 and 3 were devised as a System-on-Package components. This approach could be further explored in future research activities.

For the sake of clarity, the manuscript was subdivided in three lines of work depending on the operating frequency band and the main device functionality. The results and the experience obtained in every line of work resulted in useful feedback information for the rest, generating a synergy between the different projects.

Chapter 2 summarizes the evolution of modern wireless communications and the trend of the new technologies used in 5G and beyond. Furthermore, a review of 3D printing technologies implemented in the domain of microwave devices is introduced in this chapter.

In **Chapter 3**, additive manufacturing SLA is implemented for the conception of ceramic-filled 3-D printed tunable SMD resonators and filters operating in the C-band. The chapter starts with a review of the tuning and reconfigurable strategies reported in several filter technologies. A theoretical study of N-bit filter banks and tunable filter scenarios is carried out with Alumina and Zirconium Dioxide substrates. A hybrid solution between both cases is proposed. Furthermore, the tuning effect chosen for the implementation of compact resonators is studied at simulation level. The main design parameters are identified and their impact on the resonance frequency shift and quality factor is analyzed. The contribution of the external circuits and connections necessary for the tuning effect control is modelled and included in mixed electromagnetic/circuit simulations. Several resonator prototypes are designed, fabricated, measured and compared. A temperature characterization analysis is performed to estimate the effect of temperature drift on the device operation. Finally, a 2-channels band-pass filter is designed based on the experimental results.

Chapter 4 explores the utilization of 3-D printing technologies for the conception of non-conventional ceramic-filled cavity structures operating in the X-band. The investigated devices were targeted to be integrated in several representative scenarios commonly found in RF front-end boards and leverage the flexibility of 3-D printing processes to provide more functionalities in a reduced space. The manufacturing constraints observed during the prototypes development are addressed in this chapter and used to characterize the limitations imposed in the designs working around 10 GHz. A laser tuning strategy is applied in a post-fabrication step to overcome the measured frequency response mismatch. The devices are also characterized in temperature and compared between them to identify the less sensitive case. In the end, a filtenna application

example is suggested using the proposed approaches studied.

Millimeter-wave devices are designed in **Chapter 5** using a laser micro-machining process developed in the laboratory XLIM. The fundamentals of the manufacturing process flow, the explanation of the process characterization and its evolution throughout four generations is introduced to the lecturer. A collective manufacturing process inspired in CMOS fabrication was developed in ceramic substrates to enhance the device manipulation during the metallization and reduce the production time and cost. Furthermore, a testing functionality is included thanks to this approach in order to detect failed devices before their extraction. A SMD transition is proposed for the device assembly onto a carrier board by leveraging the device extraction method without adding extra steps. Commercially available temperature stable substrates were also used in this process to conceive millimeter-wave filters working in harsh conditions. Finally, an electromagnetic study of the supports that links the devices to the substrate was carried out. A tuning functionality was given to these elements to be able to correct the filter response during the fabrication at the same time that the components are removed from the main substrate. The devices are compared to state-of-the-art manufacturing technologies at 26 and 42 GHz.

The manuscript is concluded by a general conclusion of the overall work, the perspectives and the potential research lines. This work has been financed by Thales SIX GTS in addition to the region of Nouvelle Aquitaine.

2

Massive communication networks and novel manufacturing technologies applied to modern wireless systems

SINCE the first successful demonstration of radio signal transmission across the Atlantic ocean performed by Guglielmo Marconi in 1901 [1], wireless communications have revolutionized every single aspect of our daily lives. The development in communication theory and multiplexing methods contributed to the evolution of mobile communications during the 20th century [2]. However, it took around eighty years to implement wireless communications into commercial applications. Since early 1980s, these technologies have seen an impressive progress from simple voice to mobile multimedia systems [3] thanks to the advancement of microwave engineering, solid state devices, integrated circuits (ICs) and the implementation of satellite networks. Furthermore, the implementation of new approaches such as Internet of Things (IoT) and multimedia consumption is expected to increase the demand and exceed the hundred of millions high-data rate connections in the next decade [4]. As a result, the frequency spectrum is becoming more crowded, pushing wireless communications to move into higher frequencies to attend the near-future challenges.

With the popularization of mobile communications and wireless applications the electromagnetic wave spectrum (30 Hz to 300 GHz) was standardized by the International Communication Union (ITU) and regulated by national laws. The classification of the spectrum into several bands helped to avoid interference between users, enhance the efficient use of the resources and implement several services at different transmission frequencies. In 1947, the International Radio Conference decided to establish as a convention the division of the spectrum into 12 bands, defined by the wavelength range and designated by progressive whole numbers (fig. 2.1) [6]. Unlike lower bands, the transmission of electromagnetic waves in band 12 (300 to 3000 GHz), also known as Terahertz or Tremendously high frequency band present high attenuation by Earth's atmosphere [7] making it unsuitable for satellite to terrestrial communication links. In the case of the microwave spectrum (300 MHz to 30 GHz), radar technologies were widely implemented during World War II (WW2) at these frequencies. Their utilization in military communications led to a different convention where the bands were identified with letters for military uses. Since the frequency bands were not unified, in 1976, the IEEE standardized the radar bands to avoid confusion between different definitions and later on millimeter-wave bands (wavelength between 1 cm and 1 mm) were included in IEEE convention [8]. Other standards originated during WW2 for military radar applications were introduced by the North Atlantic Treaty Organization (NATO). In 1982, NATO's member states signed the first NATO Joint Civil/Military Frequency Agreement (NJFA) treaty to regulate the military access to the radio frequency spectrum. A comparison between the different frequency band standards can be consulted in Appendix I. For the sake of clarity, the definition of the operating frequencies treated along this work will

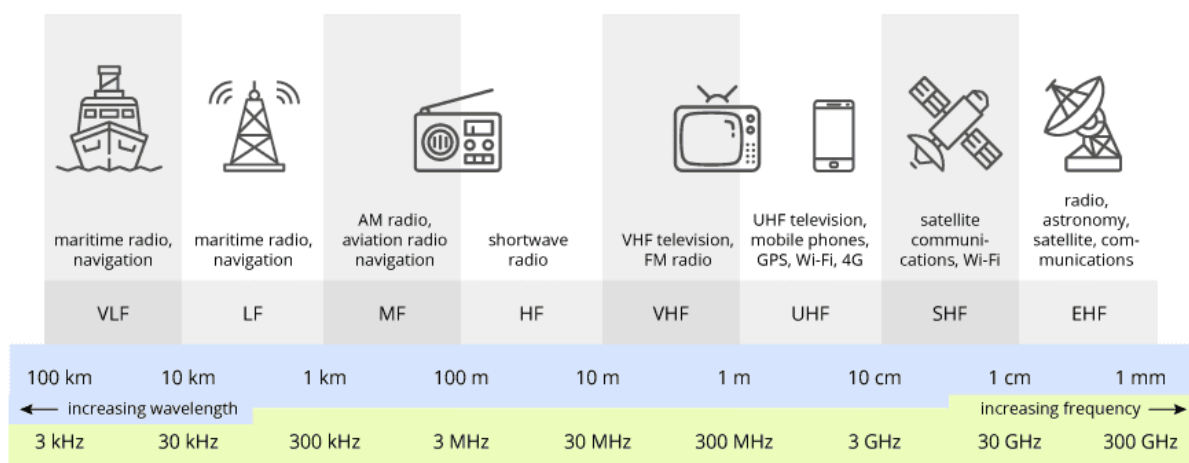


Figure 2.1: ITU standard frequency bands and applications [5].

follow the standard established by IEEE. Some application examples implemented at the different bands are shown below:

- **VHF (30 - 300 MHz):** FM, television broadcasts, line-of-sight ground-to-aircraft and aircraft-to-aircraft communications, land mobile and maritime mobile communications, amateur radio, weather radio.
- **UHF (300 - 3000 MHz):** Television broadcasts, microwave oven, microwave devices/communications, radio astronomy, mobile phones, wireless LAN, Bluetooth, ZigBee, GPS and two-way radios such as land mobile, FRS and GMRS radios, amateur radio, satellite radio, Remote control Systems, ADSB.
- **L (1 - 2 GHz):** mobile services, navigation (1550, 1650 MHz), weather-sat.
- **S (2 - 4 GHz):** TM/TC (2.2 - 2.3 GHz), inter-satellite links.
- **C (4 - 8 GHz):** civil communications (e.g INTELSAT systems), Earth observation (2.4 - 5 GHz).
- **X (8 - 12 GHz):** military communication (7 - 8 GHz), data transmission.
- **Ku (12 - 18 GHz):** satellite communications for television broadcasting, NASA's Tracking Data Relay applications.
- **K (18 - 27 GHz):** satellite communications, astronomical observations.
- **Ka (26 - 40 GHz):** broadband satellite communications (27.5 - 30 GHz).
- **V (40 - 75 GHz):** satellite constellations crosslink communication, very short range Wi-Fi.
- **W (75 - 110 GHz):** satellite communications, millimeter-wave radar research, military radar targeting and tracking applications.
- **G (110 - 300 GHz):** Earth observation and science, medical treatments.

In this chapter, an overview of the evolution of mobile communications, as well as the implementation of new broadband transmission approaches will be presented to the reader. Massive MIMO transceivers used for new mobile generations will be evaluated from the hardware point of view. Additionally, a review of current additive manufacturing technologies and their benefit in the implementation of microwave components will be exposed. Finally, conclusions and the motivation for this research work can be found at the end of the chapter.

2.1 Evolution of mobile networks and wireless communications

Since the beginning of the 1980s, commercial wireless communications have seen an impressive evolution from voice to advanced mobile multimedia broadband systems [9]. A new mobile generation emerged almost every decade thanks to the continuous development of new technologies. The convergence of Internet and wireless mobile communications services lead to a massive growth of cellular users, significantly changing our daily lives and the way we interact with the society. The amount of connections and data traffic demanded nowadays continues motivating the network operators to ensure fast reliable systems to satisfy the current and future necessities. An overview of mobile communication networks evolution (fig. 2.2) is firstly required in order to understand the actual trends in this sector.

2.1.1 The First Generation (1G)

The First Generation (1G) mobile network was deployed in Tokyo during 1979 to deliver voice services using the Nippon Telephone and Telegraph (NTT) system in Japan. It was then popularized in early 1980s and implemented in the United States, Australia, South America and China with the Advance Mobile Phone System (AMPS); parts of Europe with the European Total and Total Access Communication System (ETACS / TACS); and other parts of Northern Europe with the Nordic Mobile Phone System (NMPS). The First Generation used analog signals, frequency modulation (FM) and Frequency Division Multiple Access (FDMA) for broadcasting between 800 and 900 MHz bands [10]. Nevertheless, the voice quality was rather poor due to interferences, the calls were not secure (easily decoded with a FM demodulator) and the number of users and area coverage was very limited. Moreover, the mobile phones used in this generation were large in size and weight, and their self-autonomy was very limited.

2.1.2 The Second Generation (2G)

The Second Generation (2G) was introduced in early 1990s as a substantial improvement to 1G. In this generation, digital technologies for wireless transmission were implemented bringing considerable progresses to communication systems. The established standard for this generation, known as Global System for Mobile communication (GSM) became the base standard for future wireless network development [11]. The

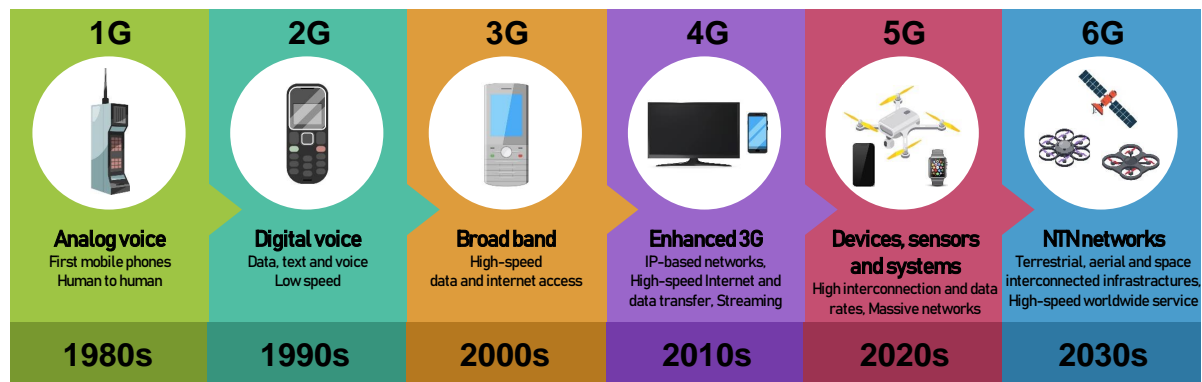


Figure 2.2: Evolution of mobile communications from the First Generation (1G) to the current Sixth Generation (6G).

digital multiple access technologies implemented such as Time Division Multiple Access (TDMA) and Code Division Multiple Access (CDMA) introduced by Qualcomm improved the spectral efficiency, data rate and number of users. GSM supported data rates up to 64 kbps, sufficient for SMS and e-mail services. The frequency bands for typical GSM networks were deployed between 900 and 1800 MHz. Besides, 2G had an enhanced security with encrypted voice transmission and it was the first generation to provide Internet services. However, the service still supported a limited number of users in a restricted coverage area and the Internet data rate was low. Enhanced GSM networks (2.5G and 2.75G) were developed to support higher data rates. For example, General Packet Radio Service (GPRS) supported data rate up to 171 kbps; Enhanced Data FMS Evolution (EDGE) up to 473.6 kbps; and CDMA2000 supported higher data rate for CDMA networks (384 kbps).

2.1.3 The Third Generation (3G)

The Third Generation was conceived with the perspective to provide subscribers with high-speed IP-based data and voice services, enhance the network security and reliability, integrate Internet applications and multimedia, and handle the mobility amongst different network providers. The standardization for this generation started in late 1990s and was implemented in early 2000s with the introduction of Universal Mobile Terrestrial/Telecommunication Systems (UMTS) [12]. 3G cellular networks reached data rates of 144 kbps for users in high-speed vehicles on vast areas, 384 kbps for pedestrians and 2048 kbps for stationary users. With the introduction of 3G networks, smartphones became popular and mobile video calling, e-commerce, e-mail, multimedia chat, social media, games and healthcare applications were seen for the first time. In contrast, the

major drawbacks of this generation were the high costs for operators and users due to the expensive spectrum licenses, infrastructure and mobile devices.

2.1.4 The Fourth Generation (4G)

Fourth Generation systems are an All Internet Protocol Based Packet Switched Network providing seamless communication/mobility anywhere and anytime. 4G is an enhanced version of 3G networks with higher data rate (up to 100 Mbps for high mobility and 1 Gbps for low mobility), worldwide roaming, and enhanced security and mobility. Third Generation Partnership Project (3GPP) Long Term Evolution (LTE) standards were upgraded in this generation [13]. Hence, the integration and simultaneous transmission of voice (VoIP) and data (video streaming, web navigation, FTP, online gaming, etc.) was possible in 4G, facilitating the implementation of MIMO technologies. Connectivity is also improved in this generation and latency reduced for mission critical applications. More complex modulations were used to enhance the uplink (OFDMA) and downlink (SC-FDMA) capacity.

2.1.5 The Fifth Generation (5G)

With the arise of new technologies as Big Data, Internet of Things [14], Machine to Machine (M2M) communications [15] and Smart Factories [16], experts have foreseen an unprecedented growth of data traffic for future communications systems [17]. Even though the Fourth Generation was conceived to support higher connectivity than ever before, advanced 4G networks were not fully prepared to handle such dense amount of connections [18]. The Fourth Generation was mainly focused on high data rates and worldwide smartphones deployment [9]. As a consequence, a new era of reliable massive network architectures is required to provide service to emerging technologies and deliver ultra-low latency data rates. The Fifth Generation (5G) moved from smartphone communications towards a different approach where everything and everyone will interact every time in the network [19]. During the last years, many efforts were done by the community to create the technological bricks needed to lunch the first 5G networks in early 2020s. The capabilities planned for 5G exceeded those implemented until the moment in previous generations, with peak data rates up to 10 Gbps and 1000 times larger network capacity than 4G [20]. 5G services can be globally classified into three main categories: massive IoT applications, enhanced mobile broadband (eMBB) and mission-critical applications [21], [22] (see fig. 2.3).

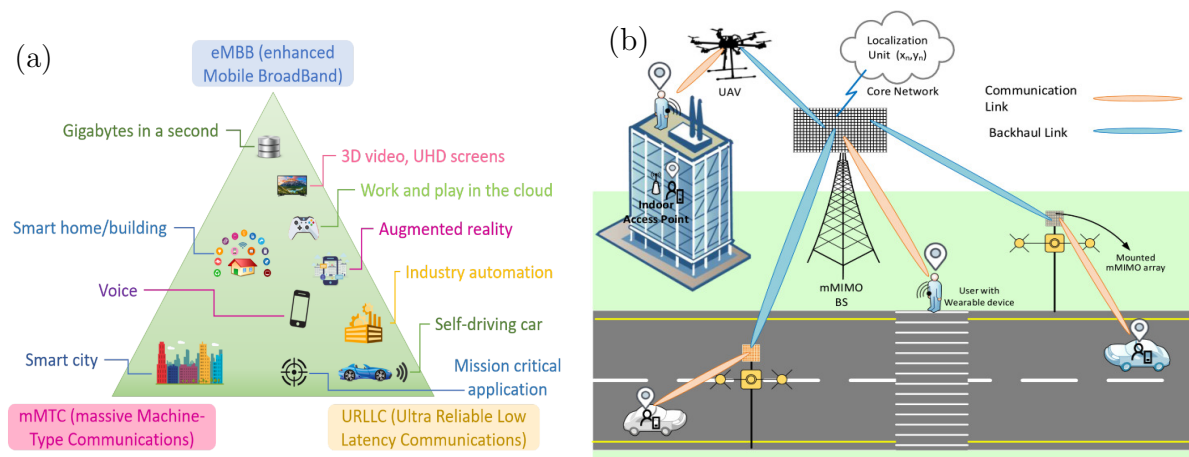


Figure 2.3: (a) 5G ITU IMT-2020 use cases [21] and (b) massive MIMO (mMIMO) wireless mobile network [23].

The **Internet of Things** is a network of sensors, software and other technologies interacting and exchanging information with other devices and systems connected to Internet. These electronic systems can be embedded in a great variety of objects to monitor physical parameters and collect information. Many useful applications such as smart grids, traffic management, smart cities, and environmental monitoring can benefit from this scenario. Besides, 5G has also the potential to provide new services and transform the industry making safer transportation, remote healthcare, digitized logistics, and precision agriculture. This evolution known as smart factories or Industry 4.0 is possible thanks to the integration of multiple interconnected objects (industrial IoT or IIoT) collaborating with each other and high-capacity ultra-reliable low-latency links for remote control, real-time monitoring and automation of critical infrastructure, robots/vehicles and medical procedures [18]. As a result, several research groups have focused their investigations in this topic during the last years to develop self-sufficient low-cost IoT devices that could satisfy the needs of the market [24]. Therefore, 5G networks must meet the requirements to ensure the massive device connectivity expected in the near future.

Enhanced mobile broadband is a technology intended to guarantee broadband access in densely populated areas with multiple users. On the one hand, 5G mobile networks are expected to provide service to moving users in vehicles (cars, buses, trains or planes) and also support augmented and virtual reality with uniform and faster data rates. On the other hand, Fixed Wireless Access (FWA) would supply high performance

broadband wireless access to home and offices at millimeter-wave (mm-Wave) frequencies.

Historically, the typical bands for mobile communications were located below 5 GHz. However, the emerging interest for higher speed communications motivated the exploration of the underutilized spectrum at higher frequencies, where a dramatic increase in bandwidth and data rate was possible [25]. Frequencies at mm-Wave bands (30 to 300 GHz) became notably interesting, specially for FWA applications. Nevertheless, microwave transmission at mm-Wave spectrum shows a higher signal attenuation that limits the coverage to a few hundred meters. Therefore, three main technological advances are considered in 5G to make the use of mm-Wave bands viable for massive communications: increase in the number of cells, large-scale Multiple-Input Multiple-Output (MIMO) systems and broader bandwidth.

Besides the millimeter-wave spectrum, 5G networks will also operate in the sub-6 GHz bands. For instance, the LTE band (1 to 6 GHz) could be used for eMBB services with bandwidths of 100 MHz. Applications that requires long range and lower data rates such as 4G IoT and massive Machine to Machine Type Communications (mMTC) could also be implemented in the UHF band.

Even though 5G mm-Wave frequencies are still in process of standardization, some common bands are starting to be implemented in different countries and regions (see fig. 2.4). The International Telecommunications Union (ITU) has treated this subject in the World Radiocommunication Seminar (WRC-19), identifying different mm-Wave

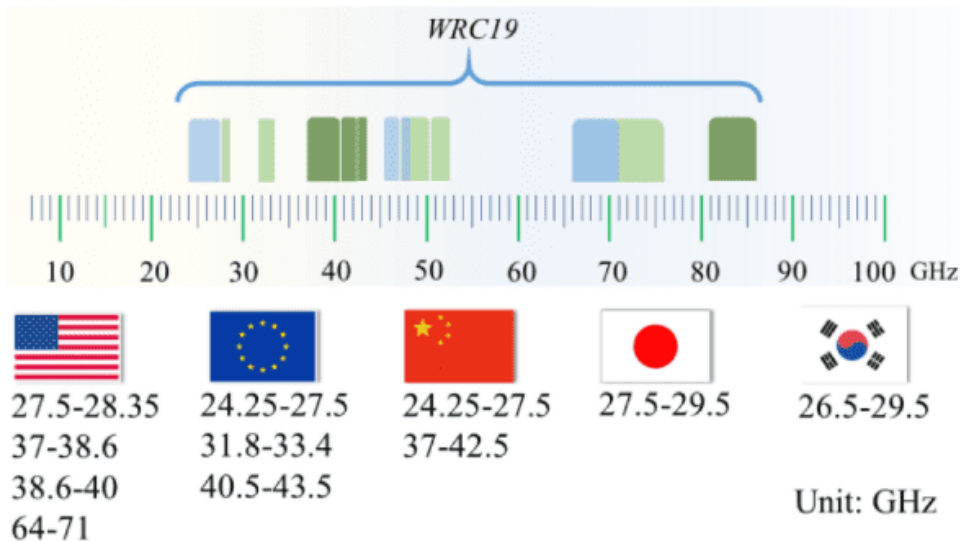


Figure 2.4: 5G frequency bands in several regions [26].

bands for 5G worldwide deployments [27]. In 2019, first 5G networks were deployed successfully in more than sixty countries.

2.1.6 5G and beyond: the arrival of the Sixth Generation (6G)

In order to provide global coverage for 5G services, both terrestrial and non-terrestrial wireless infrastructure must be deployed. The leverage of mm-Wave communications to meet 5G performances in terms of data rate and latency are being implemented in space by utilizing satellite installations (fig. 2.5). 3GPP Release 15 introduced for the first time the possibility to integrate satellite to ground connectivity while several conditions were defined afterwards in Release 16 and 17 for non-terrestrial networks (NTNs) deployment [28]. Nowadays, many efforts are being made to establish aerial/space architecture scenarios. For example, the European Union's Sat5G project identified four use cases for satellite integration in 5G: fixed backhaul for hard-to-reach areas, complementary service for underserved areas, complementary broadband connectivity at the edge, and moving platforms. Globally, these cases can be grouped into three

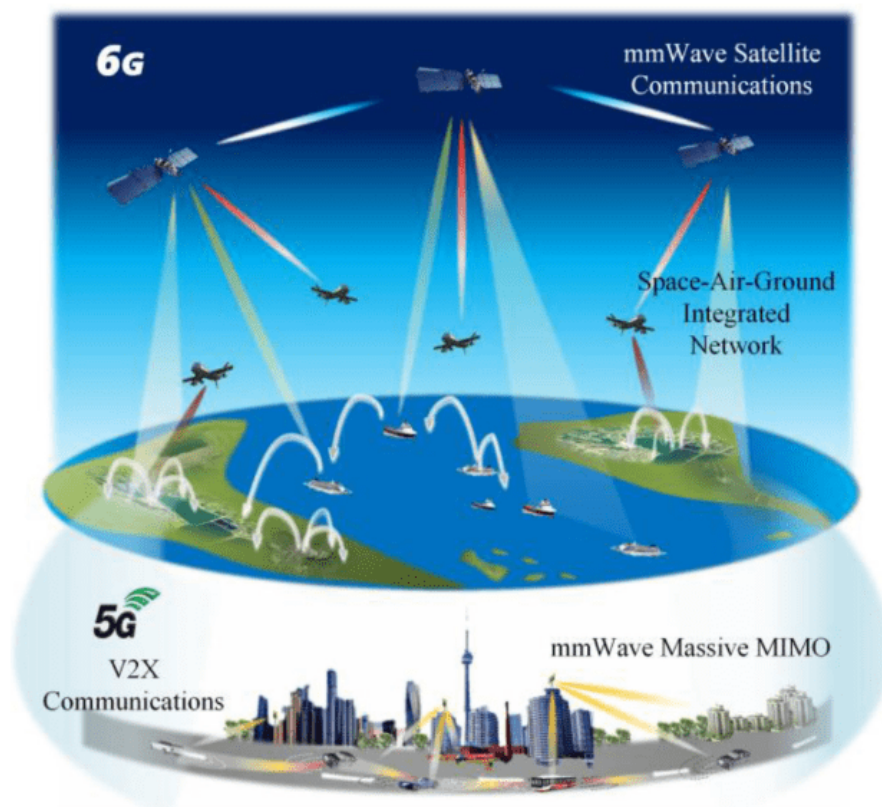


Figure 2.5: Estimated Fifth Generation (5G) and upcoming sixth generation (6G) worldwide communication networks [26].

main categories (3GPP Release 17):

1. Service scalability: utilizes the satellites' multicasting capability to transmit coded information to a group of users at the same time (e.g. TV broadcasting or video streaming services).
2. Service ubiquity: grants cellular service to regions with difficult reach access such as rural areas or remote factories, where the infrastructure could be affected by natural disasters or IoT applications covering large distances (e.g. smart agriculture).
3. Service continuity: provides continuous service to mobile user equipment (e.g. tracking applications) in ships, airplanes, trains and cars.

Research in 6G is intended to address these needs and promote NTN technology as a solution to complement terrestrial infrastructures with aerial/space stations (fig. 2.6). The overall architecture would be compounded of low altitude platforms using Unmanned Aerial Vehicles (UAVs) [30] to provide quick on-demand service during natural disasters; High Altitude Platforms (HAPs) located in the stratosphere for wide coverage and flexible deployment; and satellites [31] that could provide service to industrial and agricultural IoT for monitoring and tracking purposes in large areas. The satellite-communication industry (SATCOM) and research activities are currently developing the integration of 5G space platforms in various orbits. For instance, novel nanosatellite-5G integration network was reported in [32] for mm-Wave communication constellations.

Typically, satellite network architectures (fig. 2.7.a) are comprehended by a feeder uplink/downlink (satellite - ground Gateway connected to the terrestrial network) and a mobile uplink/downlink (satellite - end user). Satellites' features depend specifically on the operating orbit. Satellite stations located in Geostationary Earth Orbit (GEO) are used to cover large geographical regions but with higher latency (around 280 ms) and

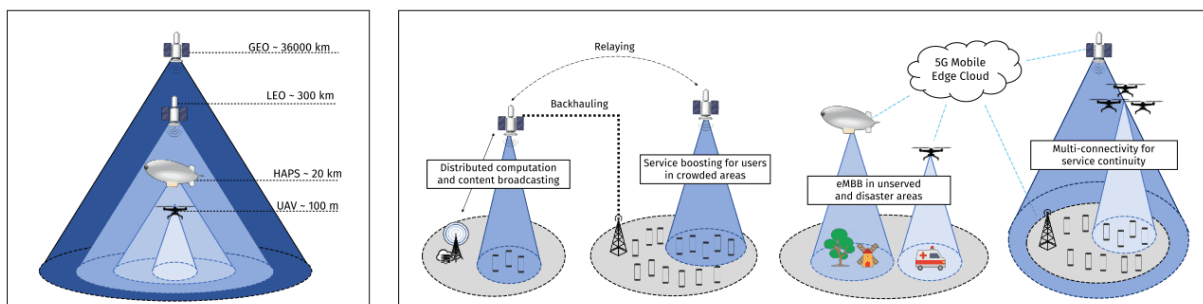


Figure 2.6: Non-terrestrial networks: possible aerial/space stations (left) and use cases (right) [29].

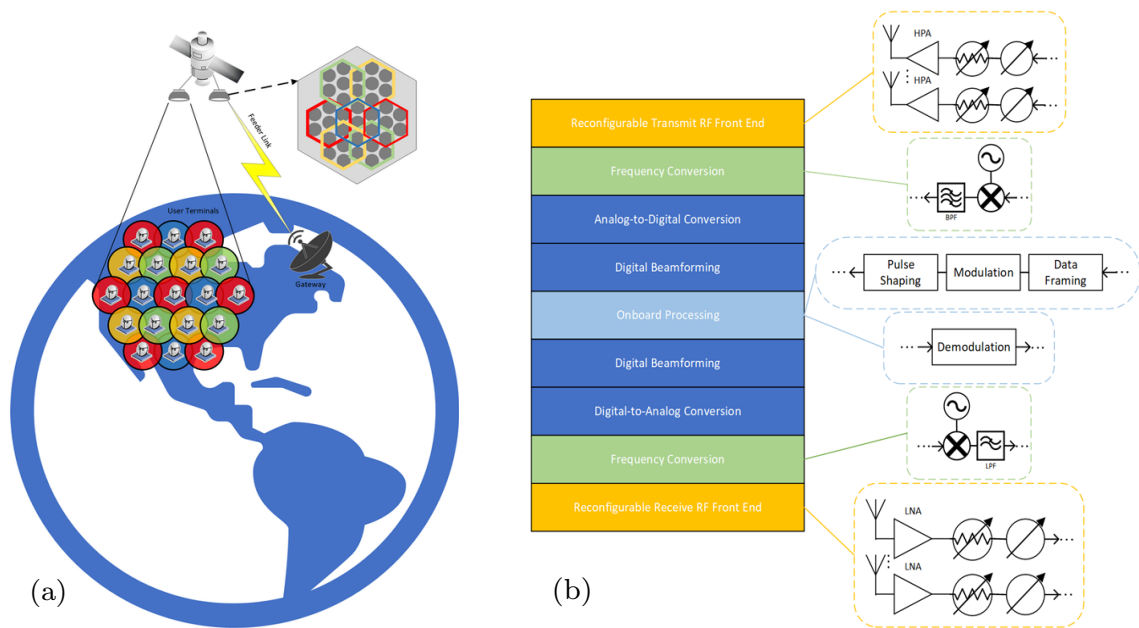


Figure 2.7: GEO HTS multibeam satellite network scheme (a) and software-defined payload architecture (b) [34].

signal attenuation [33] than lower orbits. High-throughput satellite (HTS) technology is currently implemented to combine frequency reuse and multiple spot beams to cover confined regions from GEO orbit. The utilization of mm-Wave communication bands such as Q or V could also increment the capacity up to terabit data rates for thousands of spot beams.

The deployment of small satellite constellations in Low Earth Orbit (LEO) provides lower latency than GEO satellites (6 to 30 ms) for satellite-to-ground/ground-to-satellite (S2G/G2S) and satellite-to-satellite (S2S) links. LEO constellations can be used to increase the coverage area with a mesh network compounded by regenerative satellite-based Radio Access Network (RAN) for inter-satellite links (ISLs); transparent satellite-based RAN to repeat the feeder signal to the service link; and multi-connectivity network between two transparent RANs (GEO, LEO or both) [35].

Regarding to satellites architecture, flexible software-defined payloads could be implemented to configure the multibeam transmission and frequency allocation at Ku-, Ka- and mm-Wave bands. A general satellite architecture scheme is represented in figure 2.7.b. More details about 5G transceivers for satellite and terrestrial applications will be introduced in Section 2.2.

2.2 Modern transceivers for wireless communications

The important growth in voice/multimedia data transfer and wireless communications during the last decade has driven to an increase on the demand of faster reliable communication services. According to the standards proposed for 5G mobile communication networks, data rates peaks should reach up to tens of Gbps, representing a substantial increase compared to 4G current capacity [36]. From the point of view of electromagnetic spectrum efficiency, the limited resources in the sub-6 GHz frequency bands no longer satisfies all the needs for next generation communication services [37]. According to the Shannon–Hartley theorem, the capacity of a wireless system is defined by equation 2.1 [38]. Consequently, the channel capacity C can be extended by increasing the channel bandwidth BW , the spatial multiplexing level K or the transmit power S_k . Other possibility is to decrease the in band interference on link k and the noise N_x , improve the receive sensitivity or implement a higher order modulation (e.g. 256QAM).

$$C = BW \sum_{k=1}^K \log_2 \left(1 + \frac{S_k}{N_x + I_k} \right) \quad (2.1)$$

Wider bandwidth channels necessary to achieve low-latency high data rate networks could be implemented in the rather underutilized spectrum between 6 and 300 GHz [29]. As a result, millimeter-wave bands have become of great interest for the next-generation of commercial wireless systems. Q-band, V-band and E-band are less crowded and allows wider channel bandwidth, thus, resulting a very effective choice to increase the peak data rate to the expected standards. Millimeter-wave broadcasting emerges as a promising solution to meet the needs for high density connections.

The integration of both sub-6 GHz bands (5G frequency range 1) and the mm-Wave spectrum (5G frequency range 2) as well as other radio technologies [39] such as WiFi (2.4GHz/5GHz), Bluetooth (2.4GHz), NFC (13.56KHz), GPS (1.17GHz, 1.5GHz) and UWB (6 - 8GHz) [40] allows the development of new use cases. Mission critical applications, augmented reality, industry automation or self-driving vehicles are some examples. In addition to wider bandwidth channels, innovative strategies for multiple-access include ultra dense networking, all-spectrum access, non-orthogonal multiple access (NOMA) system, massive multiple-input and multiple-output (MIMO) technology, control-plane user-plane separation (C/U- separation) and full/flexible duplex.

These requirements suppose new technical challenges to be addressed by antenna and microwave engineers in order to provide good-performance flexible network infrastructures [41]. It is known that the transmitted signals at high frequencies such as mm-Wave

bands are substantially attenuated since electromagnetic waves suffers from free-space loss [42]. Thus, the signal-to-interference-plus noise ratio (SINR) is highly degraded. As a result, the coverage area range is much smaller than lower frequency signals. Mobile network operators are considering mm-Wave 5G technology for fixed wireless access point-to-point, point-to-multipoint connections and inter-satellite links by implementing higher gain or directional antennas. In order to achieve this goal, 5G antennas are conceived with multi-element array antenna implementing massive phased-array based MIMO techniques supporting beamforming configurations (fig. 2.8) [36]. Some advance beamforming techniques implemented in 5G communications includes lens-based beam-switching antenna system, passive multibeam antenna and active phased array. Additionally, the system can broadcast multiple beams to support multi-user multi-gigabit data rate communications in different particular directions at a line-of-sight distance of a few kilometers, maintaining the spatial coverage and increasing the antenna gain. In the case of non-terrestrial networks such as aerial/space communications, beam-steering technology is also being implemented to obtain compact and light reconfigurable phased antennas with lower power consumption. Future advances in this domain includes custom flexible-membrane materials and fractal antennas for high directivity, intelligent structures and programmable metasurfaces for fine beamwidth control and low sidelobes [29]. Multibeam approach for multi-spot ground communication at mm-Wave operating frequencies allows the miniaturization of large antenna arrays in a small space while maximizing antenna gains through beamforming. The implementation of low-cost massive beamforming MIMO technology is fundamental for the development of 5G/6G broadcasting to fulfill the demand of an unprecedented

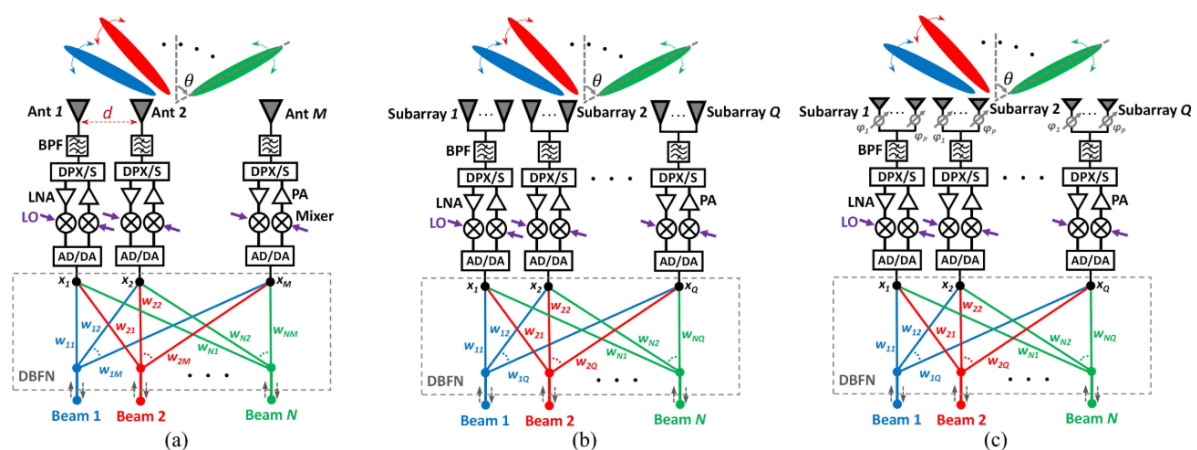


Figure 2.8: Some examples of digital multibeam antenna (DMBA) architectures: full DMBA (a), fixed subarray DMBA (b) and phased subarray DMBA (c) [36].

amount of reconfigurable RF/mm-Wave transceivers. The fundamentals of these systems will be exposed in the next section.

2.2.1 Massive Multiple-Input Multiple-Output beamforming communication systems

The design of communication systems compatible to 5G technology has been object of great interest in the research community. The utilization of transceivers (transmitter/receptor) in ground stations, user terminals and satellites links require the investigation of diverse scenarios with different constraints, specifications and technological solutions. Several obstacles had to be faced from the point of view of data processing techniques and hardware level. On one side, RF front ends must handle many carrier frequencies used in the different service's channels (e.g. 1.5 GHz, 2 GHz, 20 GHz, 30 GHz, and 40 to 50 GHz) [37]. On the other side, the use of mm-Wave frequencies to satisfy the communication data rates demands higher power levels in order to enhance the channel capacity and overcome the signal attenuation. Nevertheless, a direct increase of a single-antenna power would be unacceptable owing to the limited efficiency of the power amplifier (PA) drivers and the spatial coverage reduction as a result of a higher antenna gain. As previously explained, another possible option is to employ a reconfigurable array compound of directional antennas with lower transmission power to cover different distances and data rates. Phased-array configurations can be found in the literature implementing this approach up to 1024 antennas [43].

Figure 2.9 depicts the block diagram of a 28 GHz digital beamforming-based massive

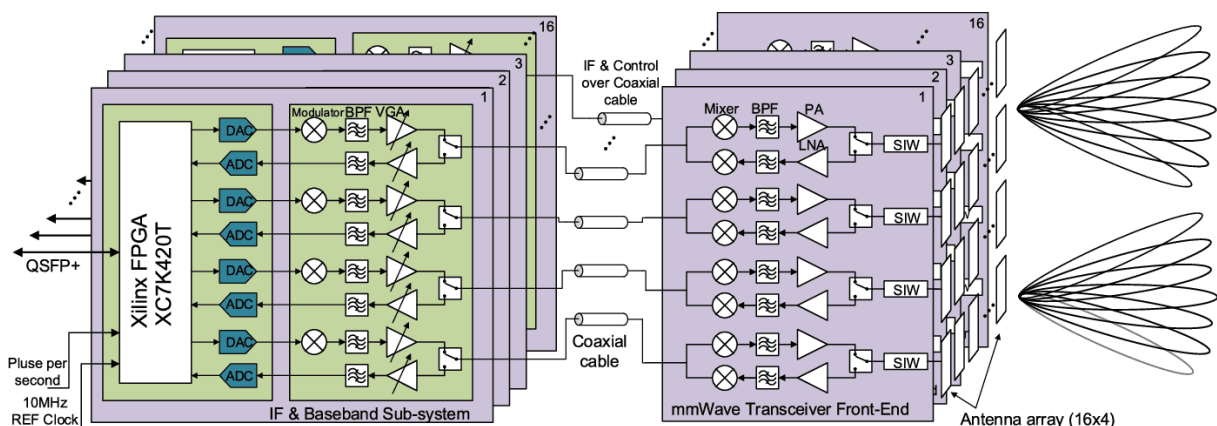


Figure 2.9: Massive digital MIMO beamforming transceiver block diagram with 64 antenna elements array [44].

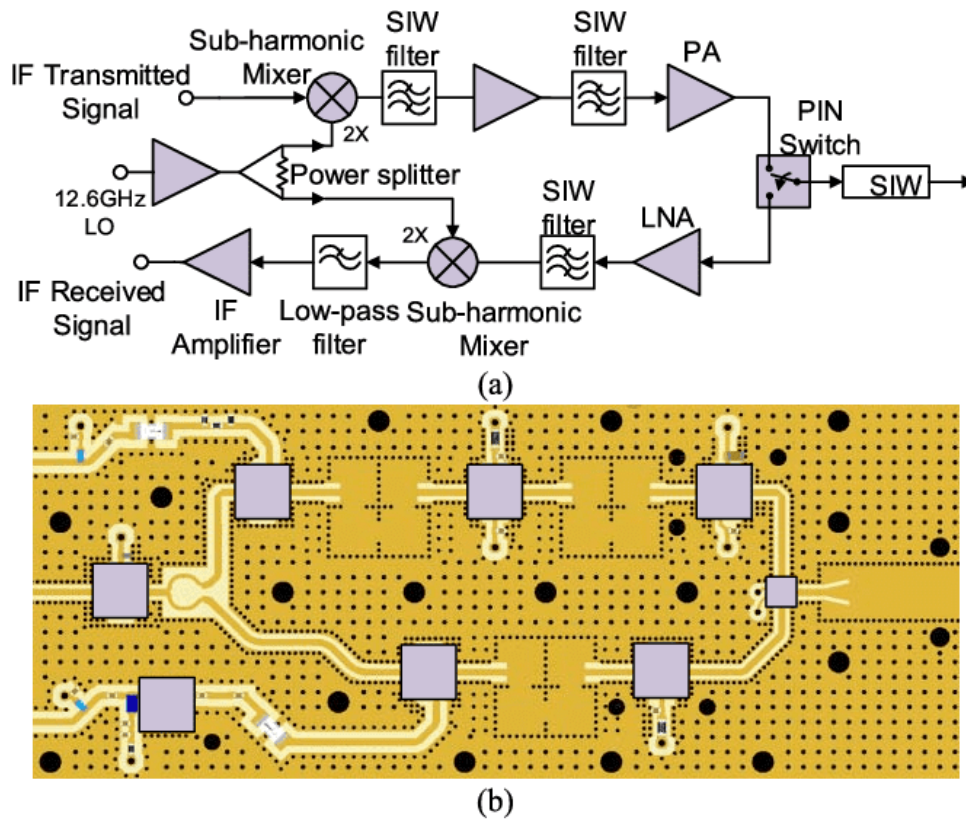


Figure 2.10: Massive MIMO beamforming millimeter-wave front-end [44]: circuit schematic (a) and printed circuit board implementation (b).

MIMO transceiver [44]. Superheterodyne architectures are usually preferred in modern transmitter/receptors due to its better performances compared to direct-conversion and low-immediate frequency (IF) architectures [45]. This approach has been widely used in television, mobile, satellite communications, and radar applications. It can be subdivided in three main stages: radio-frequency, intermediate-frequency and baseband. In the radio-frequency stage, the signal received/transmitted in the antenna is filtered by a RF filter to suppress spurious signals result of the non-linearity of the transmitter PAs and image frequencies that could propagate through the system in the receptor. The signal is also amplified by a low-noise amplifier (LNA) before a down-converting step (heterodyning process using a mixer) to an intermediate lower frequency (IF) [46]. These operations are performed in the RF front-end (RFFE). High-frequency components such as RF filters, circulators, oscillators, PAs, LNAs, power splitters/combiners, switches and mixers constitute the different front-end subsystems [47], [48] (see fig. 2.10). In the following stages, the signal down-conversion to intermediate frequencies facilitates the filtering task since filters with higher selectivity are easier to build. In

the IF module many down-conversion operations could be carry out to properly remove harmonics, interference signals or noise before the signal demodulation [45]. The use of intermediate frequency stages relieves the design of highly constraints broadband filters in the RF block with flat response and sharp stop-band attenuation. Finally, the signal is down-converted to baseband where the transmitted information is recovered by the demodulator.

The major inconvenient at hardware level of this approach is the amount of in-parallel transceivers, electronic components and interconnection techniques required to drive the antenna array. The overall cost, size and weight of the system greatly increases with the number of antenna elements. Hence, a challenging factor is how to integrate the circuit blocks and subsystems to achieve compact and cost-effective systems for 5G and beyond [49]. A promising solution is the development MIMO systems with heterogeneous-technology integration and packaging technology such as system on package (SoP) to achieve multiple functionalities, reconfigurability and compactness at the same time. RF filters are a widely utilized component in communication systems and play a critical role in the front-end. Additionally, they allow multiple bands to co-exist simultaneously by selecting the desired communication channel and rejecting the others. For example, the lack of proper RF filtering systems in Unmanned Aerial Vehicles (UAS) can affect their normal operation due to interferences caused by external environmental factors and other communication systems. Then, the reception of GPS signals could be compromised affecting the operation of the device.

Furthermore, electronic devices dedicated to non-terrestrial applications as satellite payloads or nano-satellites for space science, earth observation, navigation and telecommunications demand particular specifications depending on the orbit. These devices are required to accomplish with very strict specifications such as low loss, good selectivity, tunability, compact size, light weight, thermal stability and optimized transitions to be assembled to the rest of the system. Space is a hostile environment where very high vacuum, high energy electromagnetic radiation, atomic oxygen, debris or particle radiation conditions are present. For example, in circumnavigating orbits such as Low Earth Orbit (LEO: 200-2000 km) satellites are exposed to extreme temperature variations (in front of the sun or hidden in the earth shadow) and the inner radiation belt conditions (energetic protons and electrons). Besides, these conditions varies with the orbit; Geostationary Earth Orbit (GEO: 35786 km) and Medium Earth Orbit (MEO: 2000-35876km) are placed in the outer radiation belt, where satellites are exposed to high energy electrons in the magnetosphere, violent temperature changes and vacuum/zero gravity. On the other hand, space is a very clean environment and with zero effective gravity and no

water vapour/rain or wind.

To summarize, the application of new mm-Wave bands for broadband broadcasting terrestrial and non-terrestrial wireless communications, together with the implementation of massive MIMO beamforming technology for flexible system transceivers require the development of affordable and compact mm-Wave front ends. Microwave and mm-Wave filters are a fundamental basic block for the conception of reliable communication systems [50], and their implementation should fulfill the following specifications:

- Low cost.
- Compact size.
- Light weight.
- Frequency reconfigurability/tunability.
- Thermal stability in commercial/space temperature range.
- Optimized transitions and easy assembly.
- Easy to manufacture in large scale.
- Good process repeatability.

Due to the importance of this topic in this thesis, an introduction to passive microwave filters fundamentals and manufacturing technologies will be addressed in the following sections.

2.2.2 Microwave and millimeter-wave passive filters

The utilization of a specific filter topology or technology mainly depends on the particular solutions required by the system and its environment. Several aspects must be considered as specification inputs during the pre-design stage of a filter: frequency range, cost, selectivity, out-of-band rejection, roll-off, power handling, temperature stability, size and weight, among others. For instance, the filters employed in a superheterodyne transceiver will change depending on the stage (RF front-end, IF or baseband block) and the application use (terrestrial or non-terrestrial service provider, wearable devices or smartphones systems, UAVs, etc.). In satellite and radar communications, waveguide filters are commonly implemented to handle high transmit power in RF stages. On the other hand, ceramic-based filters are often found in IF applications due to their compact size and lower cost. Usually, it is not possible to simultaneously satisfy all the required electrical/physical filter specifications. Designers may find themselves in

the position to make a trade-off between the specifications to meet the most important requirements. In microwave passive filters, the unloaded quality factor is an important design parameter; as higher the quality factor the lower the insertion loss and noise figure achieved. This parameter is totally dependent on the technology implemented. For example, the quality factor of a device developed using cavity resonators technology is related to the material quality, the resonance mode and generally proportional to its physical dimensions. In order to improve the insertion loss and the noise figure the overall size and cost of the component will be affected. Other topological strategies such as dual-mode cavities could be taken into consideration by the designer to overcome those problems. The channel selectivity could be enhanced by adding more resonance structures, thus increasing the filter order. However, this solution will directly increase the size and insertion loss along the transmission path.

Some necessary concepts for the selection, design and construction of microwave filters will be presented as follows to the reader.

Electronic filters classification

The fundamentals of filter design theory were established in the mid-1930s. Since then, many filters topologies were developed and implemented in electronic systems. Electronic filters can be classified in different categories: analog or digital; active or passive; linear or non-linear; time-variant or time-invariant; and causal or non-causal. An ideal filter transmits the electrical signals from the input port to the output port without attenuation in the specified frequency band. Additionally, those signals outside the band would be totally eliminated, avoiding their propagation to the output. In reality, it is not possible to build a mathematically ideal filter. Real filters cannot totally remove unwanted signals outside the band, will degrade the transmitted signal in certain degree, and will radiate energy to the environment. Therefore, the correct definition of the filter specifications is of the utmost importance during the pre-design stage. Filter templates are a graphical representation of the required specifications that helps designers during the filter synthesis. This is an useful tool to define the appropriate topology, number of poles, or technology that could potentially satisfy the requirements. It also helps to visualize the design margins, an important aspect to be considered due to possible imperfections during the manufacturing process. The frequency range where the signals are allowed to be transmitted from input to output ports is called pass band. The frequency range determines the bandwidth (BW) of a filter. Additionally, reflection or attenuation effects due to mismatch in the ports or dissipation/radiation are known

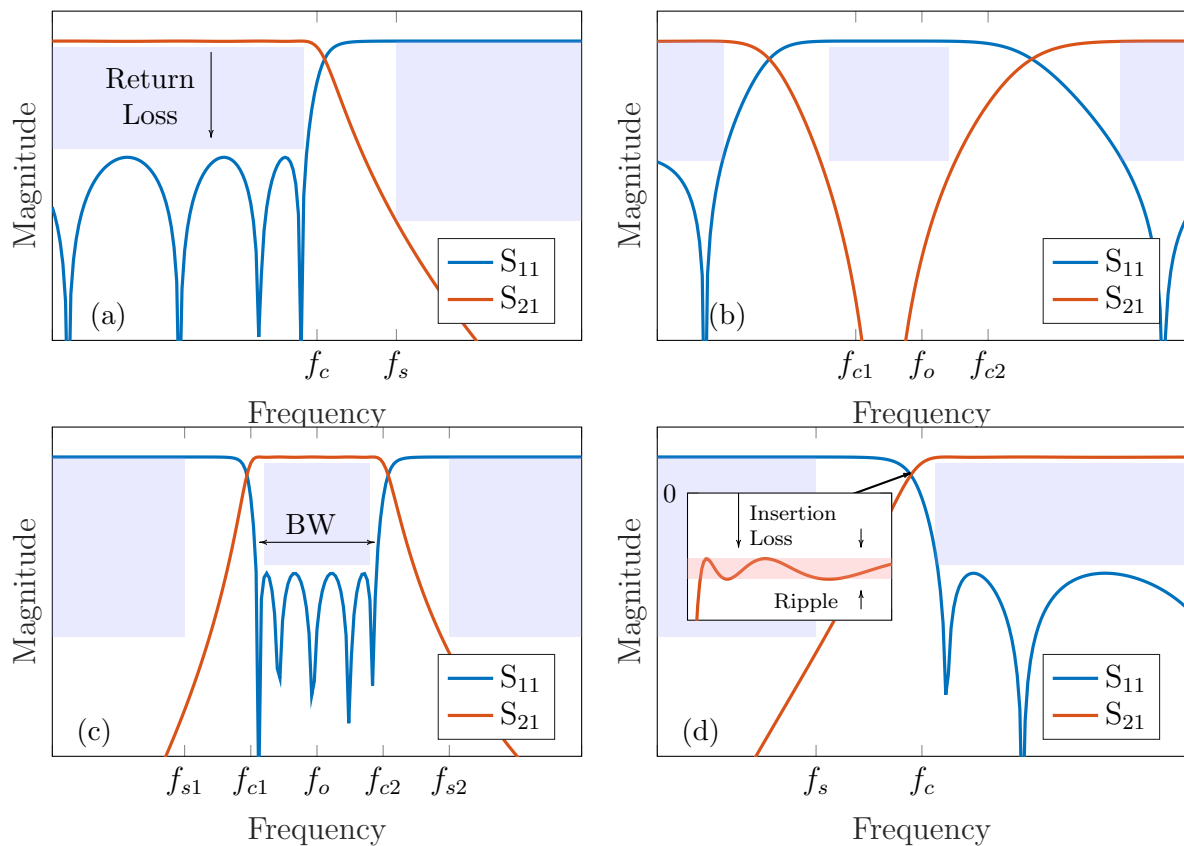


Figure 2.11: Typical filter templates (purple) and frequency response of Chebyshev low-pass filter (a), band-stop filter (b), band-pass filter (c) and high-pass filter (d).

as return loss (RL) and insertion loss (IL), respectively (fig. 2.11). Other common specifications are related to the ripple level in the pass band. Ideally, it is desired to achieve a flat response in S_{21} , nevertheless, it is not always possible and the ripple level will depend on the topology. Some topologies as Chebyshev or Quasi-elliptic filters provides a stepper attenuation in the rejection band (those frequencies between the pass band and the stop band) but incrementing the ripple.

Mathematically speaking there are essentially four different types of filters that provides different functionalities: low-pass filters (LPFs), high-pass filters (HPFs), bandpass filters (BPFs), and a band-stop or band-reject (notch) filters. Figure 2.11 depicts the some typical filter templates and frequency response.

Low-pass filters: this filter attenuates every signal over a determined frequency threshold known as cut-off frequency (f_c). As in every filter, the attenuation in the out-of-band region depends on the topology and electrical/electromagnetic quality of the components or materials. A specific attenuation could be requested from a certain frequency

known as stop-band (fs). One of their main applications is the the suppression of the RF amplifier's harmonics in transmitters and the rejection of spurious signals at base-band frequencies after the heterodyning operation in receptors.

High-pass filters: high-pass filters provides the opposed operation to low-pass filters; they attenuate those signals whose frequencies are below the cut-off frequency of the filter. For instance, waveguides operate as high-pass filters since signals will be propagated only when the input signal frequency is over the fundamental mode cut-off frequency. These kind of filters are complementary to LPF and can be even used to produce band-pass filters.

Band-pass filters: A band-pass filter is a circuit that only allows signals in a specific frequency range called bandwidth (BW) to pass through and attenuates the rest. They are implemented on the transmitter side to suppress out-of-band spurious signals and inter-modulation products, consequence of previous stages as nonlinear active circuits. In the receiver, they select the frequency band to be processed and prevent noise and unwanted interfering signals to propagate through the system [46].

Band-stop filters: Band-reject or band-stop filters are used when a specific frequency range is intended to be attenuated without affecting the rest of the spectrum. This function can be thought as the exactly opposite effect to the band-pass filter. Basically, it allows to signals between zero and the first cut-off frequency point to be transmitted, and above the second cut-off frequency point function to pass unaltered. Those signals between both cut-off frequencies will be rejected, thus eliminating that specific band.

Band-pass filters are widely required in communication applications. Their implementation in new mobile systems demands researchers and microwave engineers an effort to address the actual difficulties and provide flexible devices that accomplish multiple needs. Along this work we will focus our attention on analog passive filters developed with coupled resonators as a case of study.

Typical parameters of coupled resonators

The equivalent electrical model of a resonator externally coupled to an input and output port can be represented as depicted in figure 2.12, where a_i and b_i represents the incident and reflected waves in the ports; n_i is the transformers turn ratio that

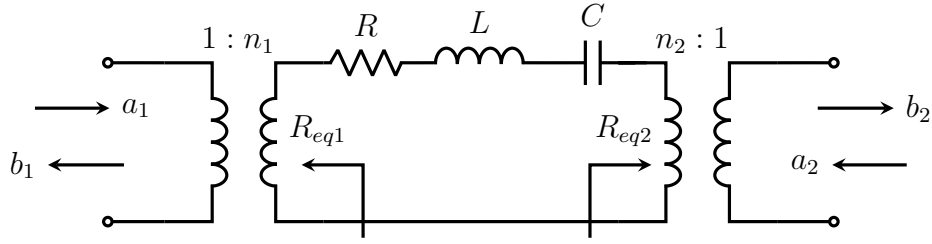


Figure 2.12: Equivalent schematic circuit model of a coupled resonator.

models the coupling between the ports and the resonator; and R , L , and C are the electrical parameters of a lossy LC tank. The resonance frequency of the resonator is given by $\omega_o = 1/\sqrt{LC}$ [rad/sec]. At this frequency the circuit is capable to transmit maximum energy from the input to the output. Then, the unloaded quality factor (Q_o) is defined as the ratio between the stored reactive energy on the resonator (Q) and the dissipated active energy (P) as a result of the losses (eq. 2.2) without taking into account external loads [51].

$$Q_o = \frac{Q}{P} = \omega_o \frac{\frac{1}{2}LI^2}{\frac{1}{2}RI^2} = \omega_o \frac{L}{R} \quad (2.2)$$

The external loads could be converted as equivalent resistors with the transformation ratio $R_{eq} = n^2 R_L$ and included into the previous analysis (eq. 2.3) to calculate the loaded quality factor. In equation 2.4, Q_e is known as the external quality factor, and defines the ratio between the stored and the dissipated energy due to the external losses.

$$Q_L = \frac{\omega_o L}{R + R_{eq1} + R_{eq2}} \quad (2.3)$$

$$\frac{1}{Q_L} = \frac{R}{\omega_o L} + \frac{R_{eq1}}{\omega_o L} + \frac{R_{eq2}}{\omega_o L} = \frac{1}{Q_o} + \frac{1}{Q_{e1}} + \frac{1}{Q_{e2}} \quad (2.4)$$

The loaded quality factor Q_L characterizes the total losses present in the circuit and is an important parameter to determine the quality of a material or component to build a filter. The loaded quality factor can be calculated by measuring the circuit frequency response at the resonance frequency and implementing the expression in equation 2.5, where f_o is the resonance frequency in Hz and $\Delta f_{-3dB} = f_{c2} - f_{c1}$ is the bandwidth at -3 dB from the S21 resonance peak (fig. 2.13).

$$Q_L = \frac{f_o}{\Delta f_{-3dB}} \quad (2.5)$$

A two-port network analysis of the quadripole depicted in figure 2.12 can be performed

to assess the frequency response. The quadripole's S-parameters (eq. 2.6 and 2.7) are obtained considering the same load conditions in both ports, then $Q_{e1} = Q_{e2} = Q_e$ and $S_{21} = S_{12}$ due to the reciprocal nature of passive networks.

$$S_{11} = \frac{1 + 2jQ_o \frac{\Delta f}{f_o}}{1 + 2\frac{Q_o}{Q_e} + 2jQ_o \frac{\Delta f}{f_o}} \quad (2.6)$$

$$S_{21} = \frac{2\frac{Q_o}{Q_e}}{1 + 2\frac{Q_o}{Q_e} + 2jQ_o \frac{\Delta f}{f_o}} \quad (2.7)$$

For the sake of this thesis, it is interesting to understand how the quality of a substrate material in terms of electromagnetic performances and the external coupling impacts on the frequency response of a basic block as it could be a coupled resonator structure. In equation 2.8 is shown the expression of the magnitude of the transmission response between ports.

$$|S_{21}|_{f_o} = \frac{2\frac{Q_o}{Q_e}}{1 + 2\frac{Q_o}{Q_e}} \quad (2.8)$$

On the one hand, if the external quality factor Q_e is increased then the value of Q_L increases and Δf decreases (see eq. 2.4 and 2.5) augmenting the selectivity. Nev-

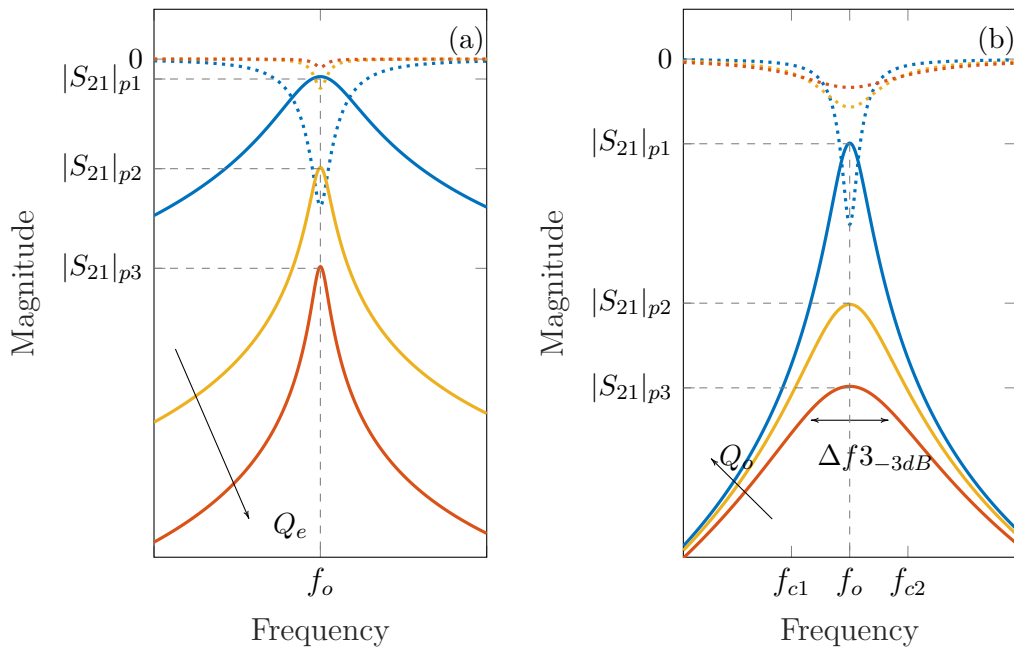


Figure 2.13: Influence of the variation of the external quality factor Q_e (a) and the unloaded quality factor Q_o (b) in a coupled resonator frequency response.

ertheless, as it can be seen in fig.2.13.a, as higher the selectivity higher the insertion losses ($IL = |S_{21}|^2$). On the other hand, if the unloaded quality factor is modified due to different material characteristics or conditions in the resonator, the selectivity improves as Q_o increases, thus reducing the insertion losses (fig. 2.13.b). The utilization of low quality factor resonator for the conception of microwave filters leads to higher insertion losses with rounded corner filters, which can be problematic for narrow band applications. Therefore, it is desired to enhance the unloaded quality factor as much as possible by improving the quality of the materials and the fabrication processes used to build these passive devices.

The coupling matrix

The design of band-pass and low-pass filters results of our particular interest due to their wide application in the high-frequency stages of the superheterodyne architectures utilized in modern RF front-ends (see fig. 2.10). Some of the key parameters evaluated by the designers during the design stage of band-pass filters are the quality factor (Q), which will determine the filter selectivity and the insertion loss (IL), that represents the dissipated power of the transmitted signal along the path between the input and output ports. Additionally, the filter bandwidth is affected by the inter-resonators coupling factors.

There are different approaches in the literature to synthesize and design the filter physical structure to accomplish with the desired specifications (e.g. classical network synthesis with ABCD matrix). In microwave engineering, one of the most common tools for the design of coupled resonator filters is the use of the coupling matrix theory. A brief introduction to coupling matrix will be presented to the reader, in order to better

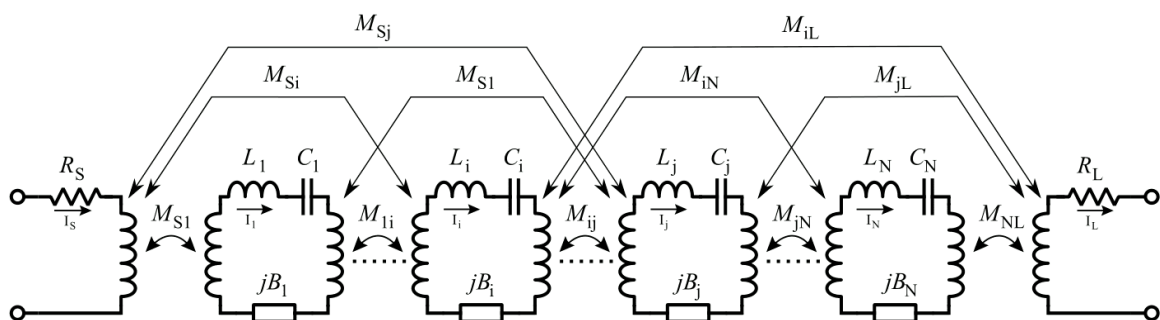


Figure 2.14: Band-pass prototype of a coupled resonators lossless network.

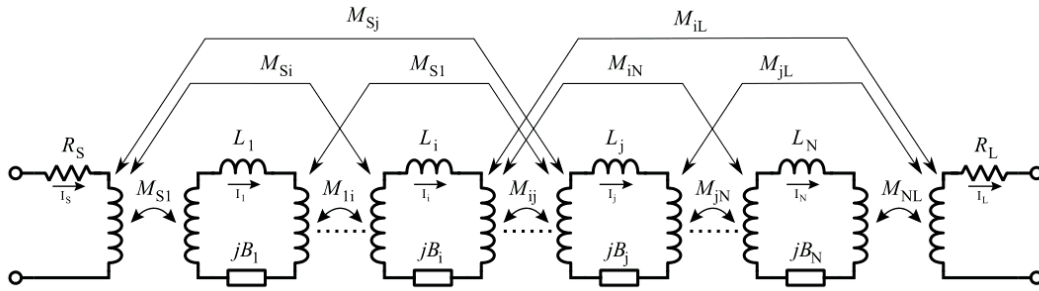


Figure 2.15: Low-pass prototype of a coupled resonators lossless network.

understand the concepts in the following chapters. A complete explanation of this topic together with mathematical demonstrations could be found in the bibliography [52]. The coupling matrix theory allows to convert the scattering parameters into a matrix format where each coefficient describes the physical behaviour of the structure. Additionally, this approach allows to perform matrix operations as inversion or partitioning that can simplify the synthesis, topology reconfiguration and simulation performance. A band-pass prototype network can be represented by lumped elements circuit model where each component corresponds to the coupling value between each resonator in the filter. The schematic representation is shown in figure 2.14, where a series of cascade-connected resonant tank structures conformed by an inductor L_i , a capacitor C_i and a frequency invariant reactance element (FIR) B_i are coupled by means of transformers ($i \in \mathbb{N}$). Therefore, each i -th resonator is coupled with any j -th (M_{ij}), modelling the coupling between adjacent and non-adjacent resonators. This generalization promotes not only the implementation of direct coupling filter such as Butterworth or Chebyshev topologies, but also Elliptic filter functions. The addition of FIR elements into the resonators gives more flexibility to designers in order to model resonant frequency shifting in asynchronous filters. Resistors R_s and R_L represent the external loads at the input and output ports of the quadripole. Although, losses are not taken into account for simplification of the analysis, resistors could be included in each resonator to reproduce the effect. The coupling coefficients and the network terminating impedances R_s and R_L are considered to be frequency invariant. The synthesis of the BPF prototype can be done with a low-pass network (fig. 2.15) mapped to the right frequency with the use of equation 2.9, where ω_o is the BPF center frequency, BW is the BPF bandwidth, Ω_{LP} is the normalized angular frequency associated to the low-pass filter, and ω_{BP} is the de-normalized angular frequency associated to the BPF [52].

$$\Omega_{LP} = \frac{\omega_o}{BW} \left[\frac{\omega_{BP}}{\omega_o} - \frac{\omega_o}{\omega_{BP}} \right] \quad (2.9)$$

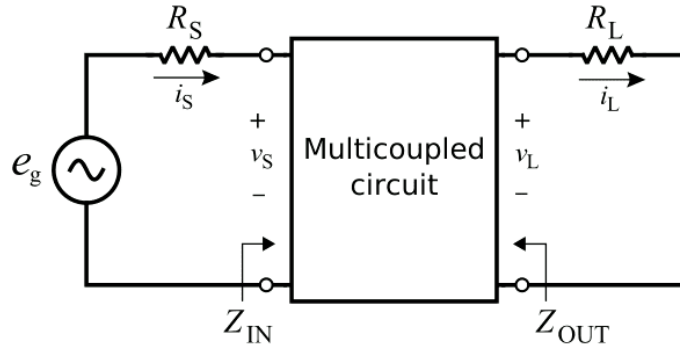


Figure 2.16: Standalone network used to analyze the coupling matrix.

The band-pass filter can be normalized to present a bandwidth equal to $BW = 1 \text{ rad/sec}$, a resonant frequency of $f_o = 1 \text{ rad/sec}$ ($L_i = 1 \text{ H}$ and $C_i = 1 \text{ F}$). The external source and load impedances may be also normalized to unity with the use of transformers turns ratio $1 : n_1$ and $n_2 : 1$, thus absorbing the impedances in the inner network (fig. 2.16). This approach facilitates the synthesis and provides a certain degree of generalization. The coupling matrix may be represented by a $N \times N$ matrix that contains the inner mutual couplings of the filter network or by a $N+2$ coupling matrix absorbing the external loads. The second representation brings some clear advantages with respect to the first matrix:

- Simplifies the synthesis process and no orthogonalization process is required.
- Multiple input/output ports can be considered.
- Fully canonical filtering functions can be synthesized (N poles and N finite transmission zeros).

The elements may be unnormalized to obtain the final values for each particular case. The inner network represented by the low-pass prototype can be analyzed by implementing Kirchhoff law analysis in every mesh of the circuit. Therefore, the following system of equations can be obtained:

$$\begin{cases} e_S = R_s \cdot i_S + jM_{S1} \cdot i_1 + jM_{S2} \cdot i_2 + \dots + jM_{Si} \cdot i_i + \dots + jM_{SL} \cdot i_L \\ \vdots \\ 0 = jM_{iS} \cdot i_S + jM_{i1} \cdot i_1 + jM_{i2} \cdot i_2 + \dots + (s \cdot L_i + jM_{ii}) \cdot i_i + \dots + jM_{iL} \cdot i_L \\ \vdots \\ 0 = jM_{LS} \cdot i_S + jM_{L1} \cdot i_1 + jM_{L2} \cdot i_2 + \dots + jM_{Li} \cdot i_i + \dots + R_L \cdot i_L \end{cases} \quad (2.10)$$

Then, expressing the system of equations in matrix form $[e_S] = [Z].[i]$:

$$\begin{bmatrix} e_S \\ 0 \\ \vdots \\ 0 \\ \vdots \\ 0 \\ 0 \end{bmatrix} = \begin{bmatrix} R_S & M_{S1} & \dots & M_{Si} & \dots & M_{SN} & M_{SL} \\ M_{1S} & s.L_1 + jM_{11} & \dots & M_{1i} & \dots & M_{1N} & M_{1L} \\ \vdots & \vdots & \ddots & \vdots & \ddots & \vdots & \vdots \\ M_{iS} & M_{i1} & \dots & s.L_i + jM_{ii} & \dots & M_{2N} & M_{2L} \\ \vdots & \vdots & \ddots & \vdots & \ddots & \vdots & \vdots \\ M_{NS} & M_{N1} & \dots & M_{Ni} & \dots & s.L_N + jM_{NN} & M_{NL} \\ M_{LS} & M_{L1} & \dots & M_{Li} & \dots & M_{LN} & R_L \end{bmatrix} \cdot \begin{bmatrix} i_S \\ i_1 \\ \vdots \\ i_i \\ \vdots \\ i_N \\ i_L \end{bmatrix} \quad (2.11)$$

As a result, the impedance matrix $[Z]$ for the system of equations:

$$[Z] = \begin{bmatrix} R_S & 0 & \dots & 0 & \dots & 0 & 0 \\ 0 & s.L_1 & \dots & 0 & \dots & 0 & 0 \\ \vdots & \vdots & \ddots & \vdots & \ddots & \vdots & \vdots \\ 0 & 0 & \dots & s.L_i & \dots & 0 & 0 \\ \vdots & \vdots & \ddots & \vdots & \ddots & \vdots & \vdots \\ 0 & 0 & \dots & 0 & \dots & s.L_N & 0 \\ 0 & 0 & \dots & 0 & \dots & 0 & R_L \end{bmatrix} + j \begin{bmatrix} 0 & M_{S1} & \dots & M_{Si} & \dots & M_{SN} & M_{SL} \\ M_{1S} & M_{11} & \dots & M_{1i} & \dots & M_{1N} & M_{1L} \\ \vdots & \vdots & \ddots & \vdots & \ddots & \vdots & \vdots \\ M_{iS} & M_{i1} & \dots & M_{ii} & \dots & M_{2N} & M_{2L} \\ \vdots & \vdots & \ddots & \vdots & \ddots & \vdots & \vdots \\ M_{NS} & M_{N1} & \dots & M_{Ni} & \dots & M_{NN} & M_{NL} \\ M_{LS} & M_{L1} & \dots & M_{Li} & \dots & M_{LN} & 0 \end{bmatrix} \quad (2.12)$$

Generalizing, the impedance matrix may be represented as in equation 2.13, where R is an NxN matrix, M is the NxN reciprocal coupling matrix ($M_{ij} = M_{ji}$) and I is the identity matrix.

$$[Z] = [jM + sI + R] \quad (2.13)$$

The generic coupling matrix form of a Nth-order filter network is depicted in equation 2.14. In this representation it can be clearly seen how the different elements are linked between them in the overall network:

$$M = \begin{bmatrix} M_{SS} & M_{S1} & M_{S2} & \dots & M_{Si} & \dots & M_{Sj} & \dots & M_{SN} & M_{SL} \\ M_{1S} & M_{11} & M_{12} & \dots & M_{1i} & \dots & M_{1j} & \dots & M_{1N} & M_{1L} \\ M_{2S} & M_{21} & M_{22} & \dots & M_{2i} & \dots & M_{2j} & \dots & M_{2N} & M_{2L} \\ \vdots & \vdots & \vdots & \ddots & \vdots & \ddots & \vdots & \ddots & \vdots & \vdots \\ M_{iS} & M_{i1} & M_{i2} & \dots & M_{ii} & \dots & M_{ij} & \dots & M_{iN} & M_{iL} \\ \vdots & \vdots & \vdots & \ddots & \vdots & \ddots & \vdots & \ddots & \vdots & \vdots \\ M_{jS} & M_{j1} & M_{j2} & \dots & M_{ji} & \dots & M_{jj} & \dots & M_{jN} & M_{jL} \\ \vdots & \vdots & \vdots & \ddots & \vdots & \ddots & \vdots & \ddots & \vdots & \vdots \\ M_{NS} & M_{N1} & M_{N2} & \dots & M_{Ni} & \dots & M_{Nj} & \dots & M_{NN} & M_{NL} \\ M_{LS} & M_{L1} & M_{L2} & \dots & M_{Li} & \dots & M_{Lj} & \dots & M_{LN} & M_{LL} \end{bmatrix} \quad (2.14)$$

- The coupling elements M_{Si} , M_{iS} and M_{Li} , M_{iL} highlighted in red indicate the existing coupling between the source/load port and each resonator, with $1 \leq i \leq N$. In waveguide or cavity filters technology these factors refer to the link between the input/output ports.
- The elements present in the main diagonal M_{ii} (highlighted in blue) do not represent a coupling value but the resonant frequency ω_o of each resonator. In the normalized format this elements are zero if every resonant frequency $\omega_{oi} = \frac{1}{\sqrt{L_i \cdot C_i}}$ equals the filter center frequency ω_{oN} (synchronous filter). In the contrary case these factors indicates the frequency shift in every resonant tank. In the case of the coupling factors M_{SS} and M_{LL} , their values are always zero since they represent the source and load which are non-resonating elements.
- The rest of the coefficients M_{ij} and M_{ji} (in green) are the actual inter-resonator couplings that links every resonator of the network to each other.

The specific arrangement of the coupling matrix will describe the particular network configuration (arrow, folded, triplets, quadruplets, etc.) and physical link between the resonators and the ports.

The synthesized polynomial mathematical transfer function (S_{11} , S_{21}) for the filter topology is linked to the coupling matrix by the short-circuit admittance parameters of the passive electrical network. A complete demonstration can be found in [53] for the synthesis of a single- and double-terminated cases.

Electronic filter technologies

In order to construct and integrate a specific filtering function into a system architecture, it is important to understand the actual technological limitations related to the manufacturing constraints. The success of a microwave filter design is closely related to the identification of the hardware characteristics to meet the required system specifications. With the arrival of new mobile networks as 5G and 6G and the increase of wireless communication appliances, an exponential increase of interconnected devices is expected in the years to come. A high demand of low-cost, high-density integration and compact radio-frequency, microwave and millimeter-wave filters are required to satisfy the need of massive communication system front-ends. In addition to these characteristics, good electromagnetic performances are expected on these devices to provide sufficient selectivity and out-of-band rejection for multi-band communication systems.

Many microwave filters were developed and integrated through the years with the use of

new manufacturing techniques in several materials. The most common technologies developed for the conception of passive filters can be classified in: lumped elements filters, planar filters, coaxial filters, cavity filters and waveguide filters [52]. These different technological approaches have demonstrated a particular trade-off between the electrical and physical features, thus directly affecting the frequency range, performance, cost, size, weight and power handling of the filter (fig. 2.17).

Lumped element filters are made up with discrete through hole or surface-mount technology (SMT) components as resistors, capacitors and inductors. Even though lumped element filters can also be used in millimeter-wave applications up to 40 GHz with planar thin film technology, the tolerances of the manufacturing processes hinders the fabrication of such components. Besides, planar filters are limited by a low quality factor and power handling and are typically utilized around the VHF band. As a result, microwave and millimeter-wave filters are typically developed with distributed elements techniques as coupled resonators in different technologies as transmission line or cavity filters depending on the frequency band [54].

Planar transmission lines have been widely implemented in mobile and wireless systems as power dividers, antennas, fixed and tunable filters, couplers or diplexers, thanks to its compact size and high integration for low-cost applications. Besides, microstrip or

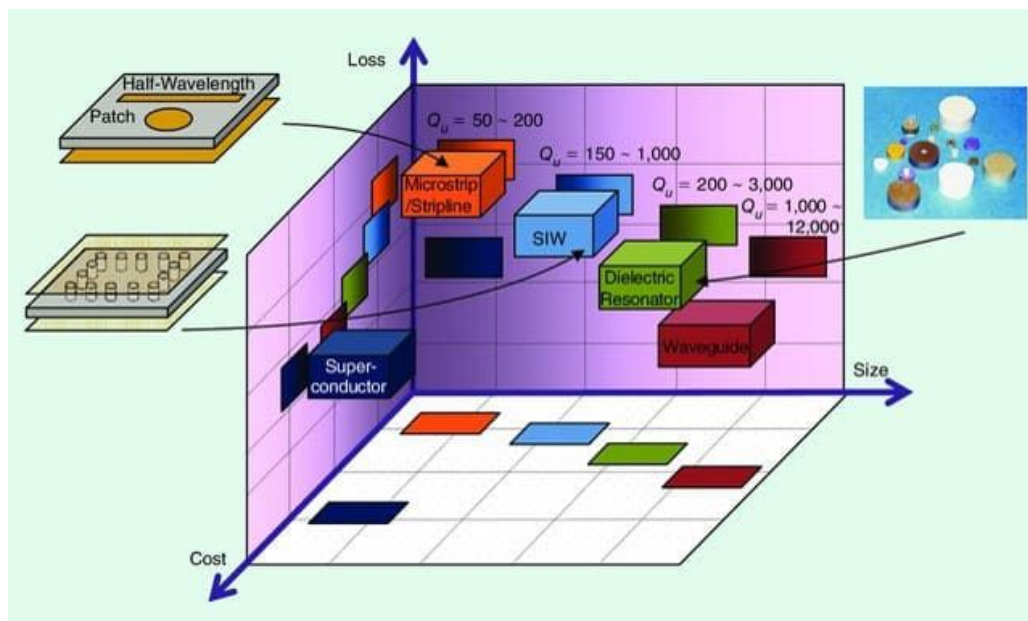


Figure 2.17: Relative insertion loss, size and cost of various RF resonators [55].

stripline devices can be directly printed or etched on the same substrate of the overall system. However, this technology is not recommended for high performance devices due to the high insertion loss and low quality factor.

When high selectivity components are needed, bulk technologies as **cavity resonators** or non-planar **waveguide filters** are a better option. Classically, **waveguides** are hollow rectangular or circular metal tubes with the ability to transmit electromagnetic waves inside. Since the devices developed with this technology are usually air-filled, good capabilities are achieved in terms of wide frequency response, low-insertion losses, high-power handling and quality factor. As drawback, this approach is rather expensive, greater in size and heavier in comparison with other technologies. Additionally, a final tuning step is often required, making them unsuitable for mobile devices applications. Waveguide filters, duplexers/multiplexers and power splitters are generally implemented in radars, satellite communications and microwave links applications.

Filters based on **cavity resonators** are widely used in the microwave and millimeter-wave range for wireless and satellite applications [56]. These filters consists of several resonance cavities as building blocks electromagnetically linked between them by irises to perform inter-resonator couplings [57]. Coupling loops, screws and inductive irises are some of the methods implemented to perform the couplings [58], while the resonators are usually build with waveguide, coaxial or dielectric cavities [59], [60]. In the case of waveguide or coaxial technology, the resonators can be obtained by short-circuiting both extremities of a transmission line section [61]. On the other side, even though dielectric resonators (DR) were introduced in 1960s, the wide frequency drift as consequence of the thermal instability inherent to the material hindered their practical use. Nowadays, the advances in the field of materials science lead to new thermally-stable dielectric resonators feasible to be implemented in real applications. Cavity filters have a significant improvement in quality factor, insertion loss, power handling capability and reduced size than lumped element and planar filters. However, spurious and parasitic resonances due to typical higher-order resonance modes represents an inconvenient for microwave engineers during the design stage. Several approaches (nonresonating nodes, cavity height boundaries, symmetric structures, etc.) were presented to minimize the contribution of these undesired effects and improve the out-of-band rejection [62]. As drawback, these techniques brings an increase of the insertion loss and the overall size of the component. Another technique related to high-frequency cavity-based components fabrication is the micromachined technology. The devices are manufactured in

a silicon wafer where the resonators are directly etched in the substrate and metallized. Finally, the cavities are closed with a second metallized silicon wafer and bonded to avoid extra losses [63].

Substrate integrated circuits (SICs) as **substrate integrated waveguide (SIW)** technology allows the integration of planar and non-planar structures in the same substrate to conceive low-cost high-density circuits in a single fabrication process. A SIW component is basically a non-planar waveguide structure made of metallized via arrays or trenches integrated in a planar dielectric substrate as printed circuit boards (PCB), ceramic substrates or low-temperature cofired ceramic (LTCC) technology. The metallized slots are arranged in an equidistant periodic separation and designed to confine the electromagnetic field inside the structure. Since longitudinal current flow is not allowed due to the side walls discontinuities, only quasi-transverse electric modes (TE) are propagated. These modes can be excited with planar transmission lines as microstrip or coplanar lines, thus mixing both technologies. As a result of the hybrid nature of this technology, SIW features are an intermediate case between planar and non-planar technologies. On one side, the pierce and metallization of vias/slots on the substrate increase the fabrication cost (higher than regular planar systems) that can vary depending on the substrate material and the drilling process. On the other side, the overall cost is lower than cavity/waveguide technologies and better quality factors and size reduction than microstrip/strip line devices are achieved. Thanks to the aforementioned advantages, SIW technology became very popular in the last years and successfully implemented in several RF and microwave systems as power dividers, couplers, filters, antennas and oscillators, among others.

Another kind of approach for the development of passive microwave filters is the utilization of **piezoelectric materials**. These materials transform physical acoustic vibrations into electrical signals. Logically, there is a great variety of piezoelectric materials (e.g. ceramics, quartz crystals, lithium niobate, lithium tantalite) and the choice of the substrate is critical for the final performances of the device. For example, quartz crystal are usually more accurate and temperature stable than ceramic materials but also more costly. One of the most widely used piezoelectric materials for these kind of implementations is aluminum nitride (AlN), due to their good trade-off between manufacturability and performance.

Acoustic resonators can be subdivided in two main categories: surface acoustic wave (SAW) and bulk acoustic wave (BAW) [64]. These components use interdigital trans-

ducers (IDTs) to convert electrical signals to acoustic waves and then to electrical signals. SAW filters operates at the S-band, are more compact and less lossy, while BAW filters usually works well into the Ku-Band (up to 15 GHz), are less sensitive to temperature variations but more expensive. These devices are commonly implemented in smartphones, automotive navigation and military radar systems.

2.3 Additive manufacturing technologies

As explained in previous sections, new massive terrestrial and satellite broadband communications networks are being deployed around the world. As part of this revolution, Internet of Things together with the leverage of millimeter-wave bands will demand billions of electronic devices in the next years. In order to fulfill those requirements, a new sustainable and ecological approach is required to enhance the technology, reduce the energy consumption, increase the flexibility in terms of reconfigurability and functionalities, reduce fabrication wastes and provide fast inexpensive production. Additive manufacturing (AM) emerges as a promising and innovative solution to be implemented in many fields of the industry: automotive, consumer products, aerospace, medical, dentistry, academic institutions, power and energy, government and military, architecture/construction and electronics [65]. In the case of aerospace and wireless applications some advantages that AM could bring are:

- Complete aircraft components such as fuel nozzles and brackets can be manufactured avoiding the assembly of several pieces, thus providing lighter and more robust parts.
- With the use of laser direct structuring (LDS), electronic circuits can be embedded on 3-D injection-molded thermoplastic objects [66] or directly printed with Inkjet [67] or Aerosol Jet printing technologies [68] for IoT applications.
- The implementation in microwave and millimeter-wave 3-D devices removes the geometrical constraints related to conventional manufacturing processes providing higher design flexibility. For example, complex-shape multifunction (electrical, thermal, or structural) passive devices are now possible driving more compact, efficient and easily adapted to space limitations components.
- In next-generation satellite communications (SatCom), multispot architectures implementing space-diversity schemes will be utilized to provide a system capacity in the order of terabits. Due to the great amount of antenna-feed systems required and assembled in the satellite payload, weight, size and cost arises as meaningful

constraints to be considered. AM could provides higher design flexibility for the embedding of compact multifunctionality antenna-feed chains and RF circuits onto the satellite walls and supporting structures, while reducing their mass, cost and dimensions [69].

Lately, the use of AM 3-D printed devices in the microwave domain has been extended to many materials (i.e. polymers, ceramics and metals) and printing technologies. Additive manufacturing offers new possibilities to microwave designers to create custom-manufactured non-conventional shape components in a reduced time between design and fabrication. The flexibility of this technology has encouraged researchers in the RF community to explore the conception of antennas, waveguide filters and duplexers, reconfigurable devices, packaging and microelectronic ICs with different results in terms of integration, fabrication accuracy, electromagnetic performances and embedding of functionalities [70]. For instance, new classes of filter such as slotted slant ridges [71], mushroom shaped resonators [72], cup shape resonators [73], and coaxial filters without dielectric holding the inner conductor [74], [75] can be implemented with the leverage of AM versatility. The maximum size and accuracy of the components depends exclusively in the the required material and printing technology, that could range from tens of centimeters to few millimeters thickness. In this section, the actual 3-D fabrication technologies will be presented, explaining the drawbacks and benefits of their use for microwave components design.

2.3.1 3-D printing techniques

With the popularization of 3-D printed technologies and their availability in the market, additive manufacturing processes were explored in both academia and industry sectors to implement next generation of microwave and millimeter-wave devices. Their applications ranges from LAN wireless communication systems to automotive and wearable sensors, high-resolution imaging systems and satellite communications.

Unlike subtractive processes (milling, electroerosion or laser cutting), the final shape of the produced device is very close to the design, reducing post-processing tooling and almost no process waste. AM consists of a layer-by-layer fabrication flow by selective adding material instead of machining raw material blocks [76].

Initially, AM was adopted as a powerful tool for rapid prototyping, fast testing and optimization before the final product fabrication, shortening the time between simulations and fabrication [24]. Thanks to these characteristics, the overall design flow

evolved to the point that AM begun to be implemented as the final fabrication process. Nowadays, additive manufacturing is an attractive technology to produce lightweight complex parts and hyper-frequency components for wireless communications and space applications and many other industrial sectors [65]. Furthermore, this workflow reduces the manufacturing costs and its capability for material waste reduction results in interesting environmental benefits.

Additionally, their geometrical flexibility, variety in terms of materials, relative low cost and manufacturing tolerance improvements promoted microwave designers to develop monolithic proof of concept components and systems. These features depend in the implemented AM process and can vary from one approach to the other. The different manufacturing processes share the same layer selectivity principle and are classified into seven categories: material extrusion, material jetting, powder bed fusion, vat photopolymerization, binder jetting, direct energy deposition, and sheet lamination [76]–[78]. Four these techniques are of our interest since they are implemented for the conception of microwave and millimeter-wave components and systems (fig. 2.18).

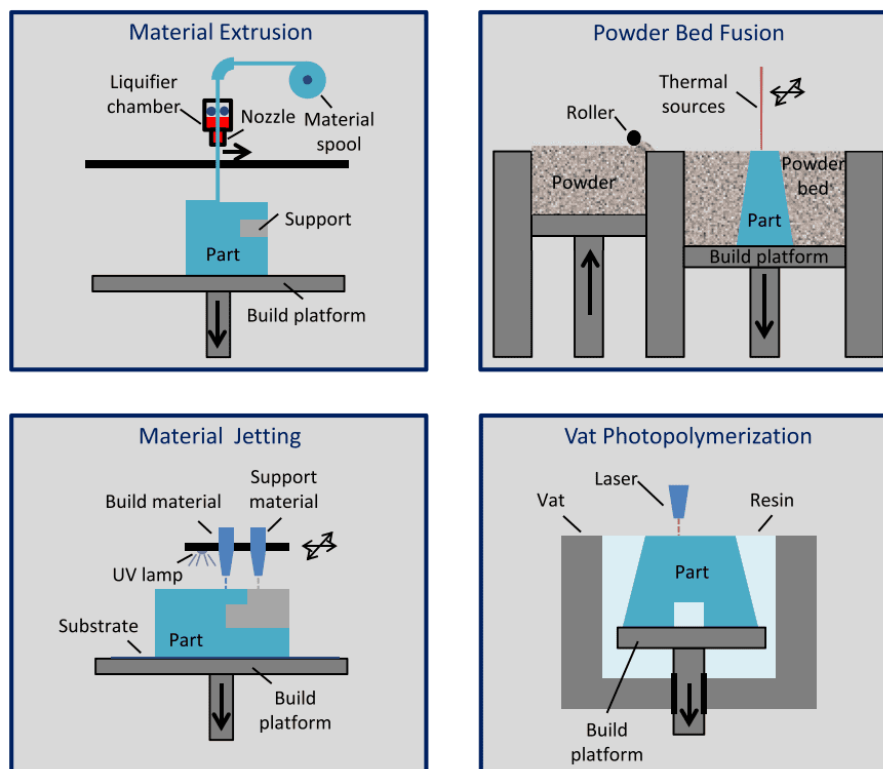


Figure 2.18: Different additive manufacturing processes [76].

Material extrusion

The principle of material extrusion process is the deposition of thermoplastic filament layers on a platform by means of a hot nozzle. The build platform moves in the vertical direction a distance equal to the layer thickness as the process progresses. One of the most extended technologies that implements this approach is known as fused deposition modelling (FDM). Printed layers features a typical resolution between 10 to 100 μm [79] and the fabrication accuracy is determined by the nozzle diameter. Complex multi-material objects can be built with FDM mixing polymers (PLA, ABS, PET, etc.), conductive inks or metals.

Material Jetting

Material jet printing is a 3-D jetting technology similar to inkjet printing process where ultra-violet (UV) curable materials are precisely deposited layer-by-layer in the form of droplets through a print head that are then cured by an UV lamp. Unlike inkjet printing, in this technology the printed layers are thicker (more than 1 μm) and cured at the same time. Typical printing resolutions are around 42 μm with minimum layer thickness of 16 μm , approximately [79]. Arbitrary shapes can be conceived with this methodology by mixing curable and uncured water-soluble polymers to create locally support structures. The mechanical supports can be removed afterwards by washing the part with high pressure water spray during a post-fabrication step. Additionally, multi-nozzle print heads are often utilized for multimaterial deposition and faster printing. Between the most utilized technologies we could mention PolyJet technology, compatible with many different low- and high-dielectric constant polymers materials, a typical accuracy between 20 to 80 μm and moderate losses [70]; and NanoParticle Jetting (NPJ), where conductive or dielectric inks compound of metal or ceramic nanoparticles can be implemented. Material jetting has been applied as a valuable solution to integrate waveguide filters [80], antennas [81], [82], manifold-coupled multiplexers [83], directional couplers [84] or passive discrete components as MIM capacitors [85]. One of the actual drawbacks of material jetting technology is the limited volume size. Current research is intended to remove the limitations to create bulky multilayered devices as SIW components, improve the layer thickness homogeneity, improve the metallic ink conductivity and overcome the formation of cracks after the sintering step.

Powder Bed Fusion

In the powder bed fusion technology, a laser or an electron beam is used as heating source to selective fuse the powder particles of a determined material spread on the build platform. As in the previous processes, the part is built by overlapping constant thickness layers and cleaned with compressed air in a post-fabrication stage. The durability of manufactured parts equates to them performed by traditional methods. Depending on the additive manufacturing process, powder bed fusion technologies can be classified as selective laser sintering (SLS), selective laser melting (SLM) direct metal laser sintering (DMLS) and electron beam melting (EBM). In SLS, plastic, glass or ceramic powders are implemented, while SLM mainly concern to metallic alloys. SLM has been widely explored for the conception of complex-shape all-metal components with good accuracy, mechanical properties, light weight and acceptable conductivity. Several waveguide devices as filters [86]–[89], beamforming networks, antennas [90], [91] and orthomode transducers [92] were successfully fabricated in this technology for high-power microwave applications. Currently, research efforts are being made to reduce the high surface roughness inherent of this method and optimize their quality with different treatments (polishing, shot peening, sand papering, among others).

Vat Photo-polymerization

Vat Photo-polymerization has been the first available AM technology. Its operation principle consists of a vat full of photosensitive liquid resin, a movable platform and a radiating source that selectively scans and solidifies the liquid by activating the polymerization process. The layout can be transferred to the material by means of a narrow laser beam or projecting the pattern with a mask and large beam source. The existing AM processes that implements vat photo-polymerization are stereolithography (SLA), digital light processing (DLP), daylight polymer printing (DPP) and continuous liquid interface production (CLIP) of which the first is the most commonly used. In stereolithography, an UV laser beam is controlled by a dual-axis (XY) mirror galvanometer to cure the photosensitive liquid resin (typical layer heights around 10 to 50 μm). Ceramic and polymer materials can be manufactured with this method. Typical fabrication speed is approximately 100 layers/hour [93]. The manufacturing resolution could range 25 to 150 μm for laser spot techniques and 30 μm for mask-based processes (DLP), while surface roughness as good as 1 μm and better for some polymers can be achieved [79]. After the photo-polymerization stage, the fabricated objects need to be cleaned with solvents to remove possible rests of resin. In the case of structures made of pure polymers

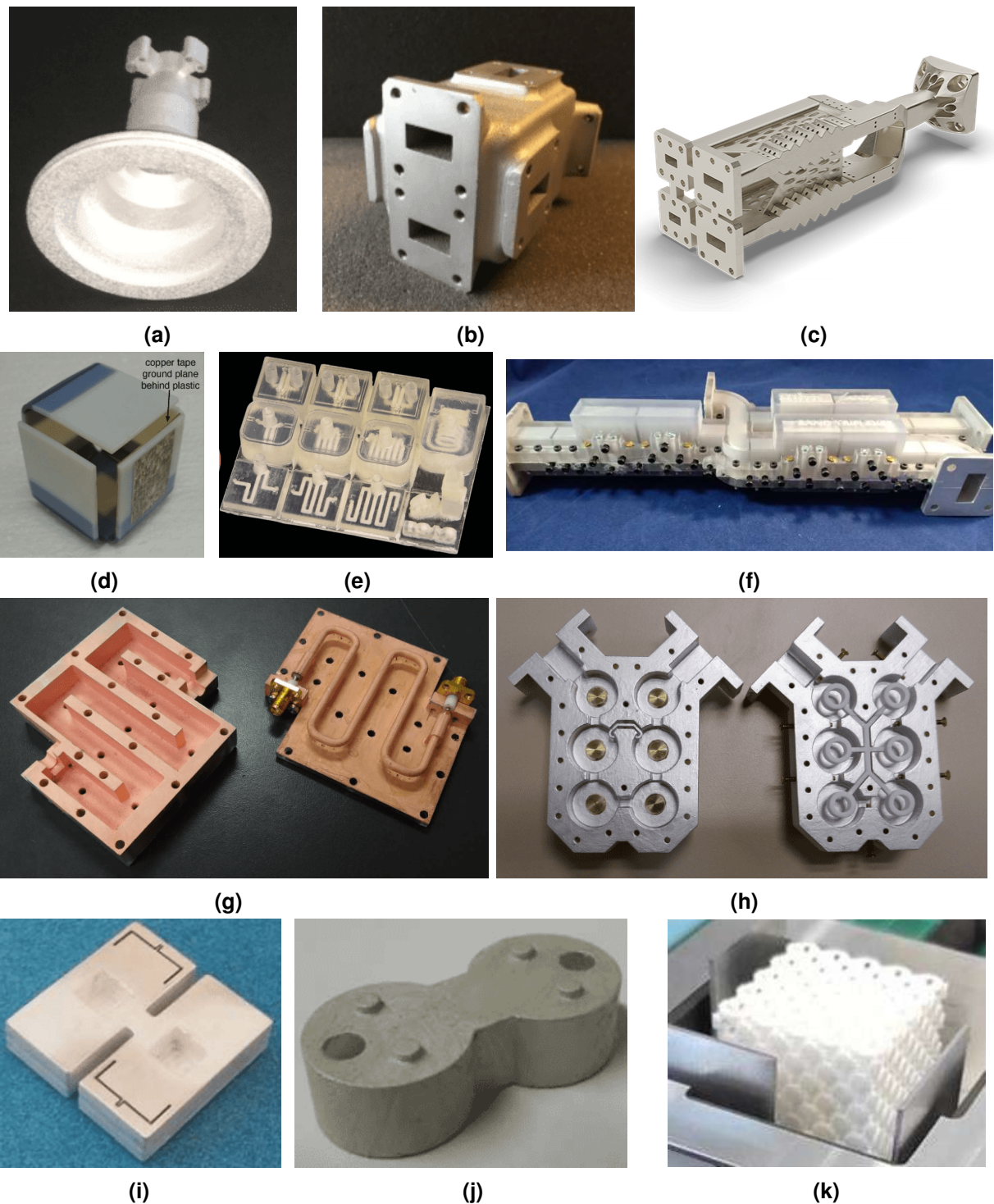


Figure 2.19: Several 3-D printed microwave devices and systems. **SLM:** Feed Horn Antenna [91] (a), Butler matrices [88] (b), and monolithic feed chains [123] (c); **Material jetting:** origami antenna [82] (d), passive components [85] (e), and manifold-coupled triplexer [84] (f); **SLA (polymers):** coaxial BPF [74] (g), and DR BPF [98] (h); **SLA (ceramics):** monolithic Zirconia BPF [106] (i), 2-pole TM BPF [110] (j), and Multi-permittivity dual-band circularly polarized antenna [121] (k).

or polymers with small amounts of inorganic materials, the structures are exposed to an extra curing stage with UV lamps to complete the polymerization and acquire the final mechanical resistance. Ceramic parts are subjected to a debinding and sintering process in a furnace to evaporate the solvents and harden the structure. In particular, it must be remarked that for ceramic SLA part of the accuracy may be lost due to the structure shrinkage. Special care must be taken during the last step to avoid critical deformations that could affect the part's dimensions and integrity [94]. Additionally, requirements in terms of durability, temperature range and mechanical properties must be considered before adopting SLA polymer parts [95]. In the case of ceramic-based devices, low-loss 3-D printable ceramics such as Alumina ($\epsilon_r = 9.2$, $\tan \delta < 10^{-4}$ at 10 GHz) and Zirconia ($\epsilon_r = 32.5$, $\tan \delta < 10^{-3}$ at 10 GHz) [70], [93], [96] could be implemented for hyper-frequency applications [97]. In the case of metal coating requirements, plating processes such as electroless (gold or copper), electroplating or chemical vapor deposition (CVD) are compatible solutions with these technologies. The exposed SLA features are very interesting for microwave and millimeter-wave applications. A large diversity of prototypes were reported based in this technology: cavity filters [98]–[101], tunable and reconfigurable filters [102]–[104], monolithic ceramic filters [105]–[110], waveguide filters [111]–[114], Magic-T [115], antennas [116]–[121] and transmission lines [122].

2.3.2 3-D printed electronics: technological trends and challenges

Additive manufacturing is a technology that is growing rapidly thanks to its rapid prototyping, customized reduced-cost production, and good product performance in industry. These interesting features have a lot of potential in sectors such as the aerospace industry where expensive production to achieve high reliability hardware could hinder the progress of space services and human space flight.

The implementation of this approach in a variety of materials for fully 3-D printed electronics allows the conception of complex devices and circuits before unthinkable. In microwave devices domain, the possibility to design exotic geometries, reduce the assembly complexity or print metallic lines on 3-D parts promotes the creation of a brand new generation of microwave and millimeter-wave systems. The research activities on additive manufacturing were mostly focused on polymers, followed by metal and ceramic materials. Table 2.1 shows a comparison between the different processes features. Different kind of devices were fabricated as proof of concept providing new insights, functionalities and higher integration than classical fabrication techniques. Even though

Characteristic	FDM	SLM	SLA (Polymers)	SLA (Ceramics)
Weight	Low	Moderate	Low	Moderate
Dielectric Losses	Moderate/High	Low	High	Low/Moderate
Accuracy	Low	Good	High	High
Resolution	Low	Good	High	High
Roughness	High	Moderate/High	Low	Low/Moderate
Stiffness	Low	High	Low	High
Thermal stability (TCF)	Low	High	Low	Low/Moderate

Table 2.1: Additive manufacturing features comparison between polymer, ceramic and metal 3-D objects printed with different processes.

waveguides, filters and horn antennas are the most popular passive components manufactured, other devices such as OMTs and polarizers, slotted waveguide antennas and integrated components have been also reported by the community. The implementation bands mainly ranges between 5 to 15 GHz and 15 to 30 GHz while some devices were reported at higher frequency bands.

The utilization of this manufacturing process as a final product process still requires some challenges to overcome. On the one hand, critical parameters for microwave components such as the fabrication accuracy, the surface finishing or the properties and quality of available materials have room for improvement. Hybrid processes using conventional CNC machining and multimaterial printing could provide valuable solution to enhance the tolerances and the surface roughness. On the other hand, a successful device printing requires to the RF designer a deep knowledge of the fabrication process, thus demanding solid interdisciplinary skills to understand the mechanical boundaries and limitations before the application of the electromagnetic architectures. In this aspect, research and academic institutions together with professional societies are indispensable to spread their knowledge and experience and promote educational activities oriented to industry.

2.4 Conclusions and motivations

In this chapter an overview of the actual status of mobile and wireless technologies has been presented. The interaction between machines and humans-to-machines and the vast diversity of applications, some of them critical, must be supported by flexible and reliable infrastructures with broadband, high data rates, low latency and extensive geographical coverage. In this way, exciting technological progresses are envisioned in the next decades in areas such as healthcare, where artificial intelligence (AI) driven systems, Intelligent Wearable Devices (IWD), telesurgery or Hospital-to-Home (H2H) services could be implemented to enhance our lifestyle [124]. An effort from community in different areas is required to address the needs and provide the proper infrastructure towards faster highly interconnected networks in the years to come. Several challenges are still needed to be faced in the fifth-generation and beyond. The implementation of millimeter-wave bands in order to increase the communication bandwidth of commercial mobile services as well as the implementation of massive MIMO beamforming transmissions lead to an increasing demand of versatile transceivers. These systems are intended to accomplish with the flexibility needed to synthesize several communication channels. Therefore, the utilized reconfigurable electronic systems should integrate more functionalities in a reduced space. Furthermore, MIMO beamforming transceivers are intended to be implemented at the different points of the network: from satellite systems and air vehicles to terrestrial antenna arrays and user terminals. Therefore, different particular requirements such as power handling, temperature stability, size, cost and weight must be satisfied depending on the application.

Ceramic devices show a balanced trade-off between compactness, performances and cost, which makes them an interesting option for the development of microwave components feasible to be utilized in 5G MIMO beamforming RF front-ends. This fact together with the strong collaborations between research institutions dedicated to science materials in Limoges and the XLIM laboratory motivated the implementation of state-of-the-art materials to develop high quality devices for telecommunication applications.

The research activities in advanced ceramic materials performed by the Research Institute of Ceramics (IRCER) during the last years lead to a deep understanding of the physical/chemical properties and the enhancement of fabrication techniques. High quality refined structures were created thanks to the vast experience and the know-how achieved during these activities. Additionally, the know-how transfer and the technological assistance of the Center of Ceramic Technology Transfer (CTTC of Limoges)

promoted the apparition of 3-D printing small and medium enterprises (SMEs). These companies are an valuable asset in the research ecosystem of the city to implement the technological innovations in the industry sector and help to research activities at the same time. The high degree of free-form fabrication of 3-D printing and the relative low fabrication tolerances achieved for ceramic SLA and other machined manufacturing processes permits to realize innovative non-conventional shape devices. Even though 3-D printing could lead to new design scenarios it also brings new challenges and investigations for the correct realization of microwave components.

In this work, commercial and under development ceramic materials were implemented for the conception of high quality microwave and millimeter-wave components for performance wireless systems. Prototypes of dual-mode and single-mode 4-pole Chebyshev monolithic filters are used as proof of concept to explore the technological boundaries at different frequencies. Additive and subtractive techniques are applied for the fabrication of ceramic components for 5G and other communication applications. A discussion about the difficulties found during the different manufacturing and metallization processes, as well as the strategies adopted to overcome those limitations are proposed along this manuscript. All the designed prototypes shown are intended to be surface mounted in commercial PCBs for compatibility and integration with other planar and SIW structures. Challenges associated to interconnections and a variety of transitions were taken into account and optimized with commercial finite element method solver for electromagnetic structures. Furthermore, the integration of heterogeneous planar, non-planar and active component technologies in a System-on-Package fashion were also explored. Flip-chip tunable resonators and filters were implemented with this approach and assembled on a printed-circuit board carrier. Finally, sensitivity due to environmental effects such as temperature drift were considered and temperature stable materials implemented to meet the standards of space and defense applications were also explored.

3

3-D printed tunable microwave resonators and filters

THE continuous growth of the communications market led to the need for service providers to satisfy the costumers' sustained demand for increasingly diverse services [125]. Until now, the majority of the commercial satellite payloads were designed to cover a predetermined service, with fixed channel bandwidth and power resource allocation. Consequently, the system architecture was restricted to a specific frequency band being unable to adapt its operation to different conditions. However, current technologies are turning to more flexible system architectures motivated by the new paradigm of 5G and 6G networks. In this framework, modern communication systems require more than ever highly reconfigurable capabilities to enhance the adaptability of satellite networks and other wireless front-ends to the upcoming market needs. On one side, this new approach offers a better management of the resources from the operators point of view. On the other side, from the manufacturer point of view formerly customized satellites projects could be changed to standard programmable architectures, enhancing the productivity in terms of fabrication costs and time, avoiding a rapid obsolescence, amortizing costs and making them operational during their whole lifetime. National projects such as FILIPIX [108], [125] were set in motion in order to evaluate the architecture

requirements of software-defined satellite payloads at system and device level, ranging from base-band processors to RF front-end components (oscillators, microwave filters, antennas, among others). Furthermore, flexible highly integrated architectures are also required in terrestrial communication systems such as, in smartphones, self-driving cars, UAVs or massive MIMO antennas [37], [39], [126] to support multi-band wireless services like LTE or 5G.

High-performance microwave tunable filters are key building blocks for new reconfigurable architectures. Their utilization in RF front-ends is often associated to the discrimination of a determined portion of the frequency spectrum for the detection of the transmitted data, the suppression of out-of-band interfering signals and the reduction of harmonics or intermodulation products generated by power amplifiers. In recent years, tunable filters attracted the attention of the microwave device community as candidates for the replacement of large switched filter banks in advanced communication systems. These devices are expected to provide the needed flexibility for multi-band services projected for the new communications paradigm in the near future [127]. Miniaturization is also a mandatory feature to fit microwave filters into the assigned area within the RF module. Many efforts are being conducted by the research community to fulfill desirable specifications such as, compact size, full adaptation to the operating conditions (frequency or bandwidth reconfiguration), integration of multiple functionalities, high quality factor, low ripple, and low insertion losses within the band. These specifications impose a great challenge from the technological point of view to meet all the requirements in a single device [57]. Novel wide band and narrow band filter configurations with high quality factor values and miniaturize size are required to accomplish the challenging task.

The use of ceramic technologies has been widely used in microwave filters for communication applications owing to their good electromagnetic characteristics in terms of low-loss and high Q-factor, as well as good mechanical features such as, high hardness, small size, light weight, high heat resistance, good corrosion and chemical resistance [128]. The implementation of ceramic devices could offer a balanced trade-off between size, weight and the performances desired for the new generation of tunable filter systems. The introduction of additive manufacturing in the field of microwave devices has proven to be an useful tool for the development of complex architectures and the integration of functionalities. However, the implementation of 3-D printed microwave ceramic components has not been exploited as much as with other materials such as, metals and polymers. In this chapter, we will explore the utilization

of ceramic additive manufacturing and its integration with heterogeneous technologies for the development of monolithic surface-mounted microwave components for modern multi-band communication systems.

3.1 Current tuning methods

A wide variety of tuning and reconfigurability techniques were investigated in the spectrum of filter technologies known so far. These techniques can be clearly separated into different categories depending on their capability to adapt their transfer function: switched filter banks, reconfigurable filters, and tunable filters.

Switched filter banks are systems of filters where each band is performed by a specific device. The channels are selected by switches that activate or deactivate the corresponding device. This approach permits to deliver a high-quality filtering function at expenses of large area requirements [129]–[132].

Tunable filters are the opposite to switched filter banks. This approach usually stands for the continuous sliding of the filter pass band and stop band in the frequency domain, handled by a control signal in order to cover multiple bands with one device. The major challenge of current tunable filters is the tuning range increasing while maintaining a constant bandwidth and low losses within the band.

Reconfigurable filters are an intermediate case where additional elements such as circuits or parts of filters are selectively added (e.g., electrically connected) to the main filter in order to modify the frequency response.

The aforementioned methods are generic techniques that are not associated to any particular technology. Each strategy implements an actuator to modify the electric or electromagnetic characteristics of the main resonators. The actuators can be discrete components or distributed elements such as controllable materials. In general, the most common actuators used in the domain are RF micro-electromechanical systems (MEMS) switches, semiconductor p-i-n diode switches and varactor diodes, tuning screws and mechanical movable parts, and ferroelectric and piezoelectric materials. The integration of these elements became more and more relevant owing to the important role of tunable microwave filters in future multi-band systems. Nonetheless, the utilization of one or the other will exclusively depend on the system requirements: tuning range, in-band insertion and return loss, bandwidth reconfigurability, isolation, power handling, tuning speed, linearity, size and cost.

Tuning methods implemented in bulk devices such waveguide and metal cavity technologies [57], [133]–[136] are outside the scope of this thesis. Otherwise, we will focus

on components designed to be integrated in the system carrier board.

3.1.1 Planar technologies

Electronically tunable/reconfigurable microwave devices were extensively explored in planar technologies. Microstrip and coplanar filters offer a simple way to perform the circuits integration in a reduced space [137]. Among the classification found in the literature we can discern between: single and multiple bands tunable planar devices such as combline filters, RF MEMS filters, reflectionless adaptive filters [138]–[140], piezoelectric transducer (PET) filters [141], [142], tunable high-temperature superconductor (HTS) filters [143]; and reconfigurable architectures such as UWB filters [144] and switched delay-line filters. The development of filters carried out digitally with RF MEMS switches can offer linear low-loss devices with large tuning range. The demonstrations reported in the majority of cases are implemented in the UHF, L and S band with tuning ratio up to (1.54:1) [145], and fixed or tunable bandwidth up to (6.55:1) [146]. Furthermore, co-integration of multiple functionalities such as reconfigurable Wilkinson-type power dividers with added single/multi-band filtering behavior were investigated in [147] in order to reduce the system size and losses.

Generally, the quality factor of planar devices is lower than other technologies. As a result, the Q-factor exhibited by tunable devices can be insufficient to accomplish the specifications demanded by modern low-loss narrowband filters. However, effective Q-factors up to 240-255 were reported in [146], [148].

3.1.2 Acoustic-wave-resonators (AWR)

Filters based on acoustic-wave-resonators (AWR) such as SAW and BAW technologies are suitable for the development of steep narrow-band filters owing to their high quality factor, low insertion losses and high linearity. They are usually utilized to fulfill the stringent size and wide bandwidth specifications required in mobile phones transceivers with several fixed filters. However, the majority of the deployed filters are designed to work in fixed bands. In order to turn AWR filters into tunable devices, the acoustic waves propagation time delay in the solid material should be modified by changing the mechanical stiffness or mass density. Nevertheless, these two material properties are inherent to the atomic structure and hard to change. Another possibility is to play with the mass loading or the thickness, however, good repeatability is usually difficult to achieve. Although fully AWR tunable filters have not been successfully demonstrated for the

moment, reconfigurable filters focused on switched ferroelectric resonators [149]–[151] and hybrid acoustic-wave-lumped-element resonator (AWLR) configurations [152]–[156] have been proposed. In the first case, the manufacturing process of devices based on ferroelectric substrates is complicated and exhibit high insertion loss. In the second case, the combination of AWR and lumped elements permits to reconfigure and increase the filter bandwidth. In [152], a RF-switched multi-band AWLR device was developed at 1, 1.1 and 1.4 GHz, showing a fractional bandwidth of $FBW = 0.08 - 0.1\%$ and $Q_{eff} = 3500 - 5300$. AWR filter bank prototypes have also been reported in the bibliography controlled by MEMS switches.

3.1.3 Substrate Integrated Waveguide (SIW) devices

A great diversity of tunable antennas and filters were developed with substrate integrated waveguide (SIW) technology in commercial printed circuit boards [157]. This technology combines the conventional advantages of metallic waveguide structures and the integration with other passive and active components. Their implementation in PCBs results in devices with quality factors in the range of a couple of hundred, suitable for low-cost and mass production. However, wide tuning range filters with high quality factor are still elusive in tunable filters developed with this technology. Methods like the side reactively loaded SIW tunable resonators (A), the via post-loaded SIW cavity (B), the floating patch diode-loaded SIW cavity (C), the ferrite disk-loaded SIW tunable resonator (D), the mechanically tunable SIW resonators (E), and the surface ring-gap varactor-loaded SIW cavity (F), are some of the approaches investigated in tunable SIW technology [157].

The use of electrically tuned capacitors as a variable load is a common practice to modify the resonator conditions. In the first method (A) a varactor can be coupled to the resonator as shown in [158], thus loading the cavity with a reactive impedance. In this approach, the Q-factor degradation can be reduced if the varactor is placed in a region of minimum E-field (286 - 299). No extra losses are added since the cavity metal layer is not engraved to perform the varactor coupling. However, the tuning range is limited (2%) owing to the locally weak influence within the resonator.

Method B is based on the connection/disconnection of a via post placed inside the resonator to the cavity wall in order to perturb the resonant mode [159]–[162]. Moreover, multiple via posts can be used to increase the tuning range at expense of a higher

Q-factor degradation [159]. P-i-n diode or RF MEMS switches can be utilized to perform the resonator tuning [160], [163]. Q-factors between 100 - 200 and tuning ratio up to (1.33:1) can be found in prototypes developed from UHF to X-band [159], [160], [163]. Furthermore, a 4-bit tunable with one via post was investigated in [160] by increasing the number of connections. In [164], an agile tunable SIW filter was developed on low-temperature co-fired ceramic (LTCC) technology implementing a via post connected to coplanar stubs selected with RF MEMS switches. The device exhibit a tuning frequency of up to 7.2 % (1077 MHz) and in-band losses between 4.7 - 5.7 dB for a filter bandwidth of 4.9 % (728 MHz).

In the third method (C), the E-field inside the cavity is disturbed with a via post connected to an isolated floating metal pad by mean of a varactor [165]–[168]. Then, a controlled capacitive effect is generated by adjusting the varactor bias voltage. The floating patch engraving introduces higher leakage than the former method. The patch size could also hinder the inclusion of multiple via posts for larger tuning range. Quality factors between 40 and 160 were demonstrated in [165] for a tuning range of 18 % (1.19:1). In [168], a surface-mounted monoblock device was developed in a 3.81 mm thick single layer of Rogers Thermoset Microwave Material (TMM) 10i substrate implementing this method with RF MEMS and GaAs varactors. Quality factors between 110 - 166 and 113 - 273, in addition with a tuning ratio of (1.08:1) and (1.19:1) were measured. Minimum insertion loss of 2 dB and 1.5 dB were also reported for the GaAs varactor and the RF MEMS switch, respectively.

The magnetic or electric and magnetic tuning can be carried out with ferrite materials (method D) embedded in the cavity resonator. The utilization of such materials imposes a more challenging manufacturing process. Nevertheless, a tuning range up to 20 % with unloaded Q-factor of 130 can be achieved by mixing this approach with capacitive load techniques [169]. Tunable filters with 10% tuning range, variable frequency bandwidth of 3–5% and maximum Q-factor of 160 were also reported in [170].

Mechanically controlled tuning elements (method E) can be also introduced to modify the E-field distribution into the resonator by adjusting their position. A SIW cavity comprised of a tuning screw and a flap was introduced in [171]. The screw was connected to a via post isolated from the cavity top metal layer while one of the flap extremities was resting on the cavity top wall. Therefore, the coupling capacitance can be controlled by turning the screw and adjusting the flap angle. A moderate tuning range of 8 % and

quality factor below 100 was reported in this work.

Finally, the last method (F) consists of the introduction of a capacitive effect in a cylindrical SIW resonator by implementing a via-post connecting both top and bottom resonator walls and isolated at one of the ends with a ring gap. Furthermore, a second annular slot is machined on the surface. The annular ring gaps are loaded with several varactors resulting in an improved tuning range. This method carried out in [172] at $f_0 = 0.9 \text{ GHz}$ exhibit a Q-factor of 84 - 206, whereas the tuning range is (2.2:1).

3.1.4 Tunable dielectric resonator filters

Dielectric resonator filters have been commonly utilized in communication systems owing to their compact size, light weight, high Q and temperature stability features [59], [173]. The electromagnetic wavelength in dielectrics is shortened by a factor of $1/\sqrt{\epsilon_r}$ with respect to the wavelength in vacuum as a result of their high electrical permittivity [174]. Several dielectric resonator prototypes were reported in the literature embedded in metal cavity enclosures and making use of mechanical [57], piezoelectric [175] or MEMS [176] actuators. Although these devices exhibit good tuning capabilities and performances, they are large in size and volume, heavier than other technologies and their integration is not suitable for SMT devices intended to be mounted on a carrier board. In general, miniature high-Q SMT tunable filters remain a challenge to overcome.

An example of a lumped-element tunable filter developed in an Alumina carrier substrate has been proposed in [125]. This 9-bit filter with reconfigurable bandwidth operating at 2 GHz shows tuning ratio of (1.53:1). Furthermore, 2.5-D and 3-D filters can achieve higher quality factors while providing the integration with tuning elements. SIW devices performed in ceramic substrates have been investigated in the FILIPIX project in order to overcome the quality factor limitations of planar technologies. The studied devices implement the capacitive via post principle introduced in 3.1.3 to carry out the tuning function. The utilization of ceramic materials in 3-D printing manufacturing processes can be also beneficial for the proliferation of integrated monolithic filters. A design of a compact continuously-tunable 3-D printed X-band filter was introduced in [177]. In this work, a capacitive effect similar to the method shown in 3.1.3 was carried out with varactor diodes and 3-D printed hollow vias. The authors claim that the device was designed to provide a compact footprint (14 mm x 3 mm x 1.65 mm), a frequency shift of 56 % with Q-factors between 60 - 200 and minimum insertion loss better than 2 dB.

3.2 N-bit hybrid tunable filter bank

As shown in the former section, several technologies and different approaches were investigated to accomplish the specifications of agile adaptive filters for multi-band communications. However, there is no specific technology that can fulfil all the requirements of modern communication systems. Many advantages and drawbacks can be seen in all the cases. The choice of a technology will depend exclusively on the main requirements of the system. We will focus the efforts towards the miniaturization and integration of heterogeneous technologies for the conception of digitally tunable filters. In order to achieve this goal, we explore an hybrid scenario where the best features of filter banks (fig. 3.1.a) and tunable filters are merged into a N-bit filter (3.1.b). The mix between both worlds is intended to: reduce the amount of switches (and losses), interconnections and high-Q filters required by half; and relief tunable filters of the stringent large band coverage specifications, preserving the balance between Q-factor and frequency shift. Furthermore, the implementation of ceramic materials and 3-D printing technologies can help to the miniaturization and the fabrication of complex geometrical structures that facilitate the integration in a self-packaged SMT component. Single mode monolithic ceramic resonators are considered for higher Q and power handling.

The device will be designed to operate in the sub-6 GHz frequency range, specifically in a fixed portion of the C-shape band. The frequency spectrum $BW_{op. band}$ comprised from f_i to f_s is subdivided by the number of channels N giving as a result the pass band of each particular channel BW_i (see fig. 3.2).

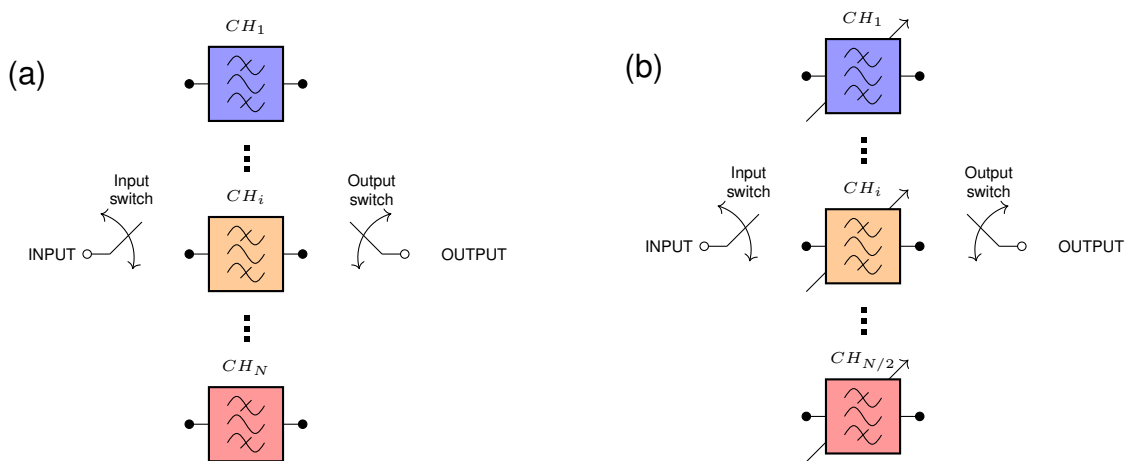


Figure 3.1: Block diagram of classic filter bank (a) and hybrid filter bank with tunable (2-state) filters (b).

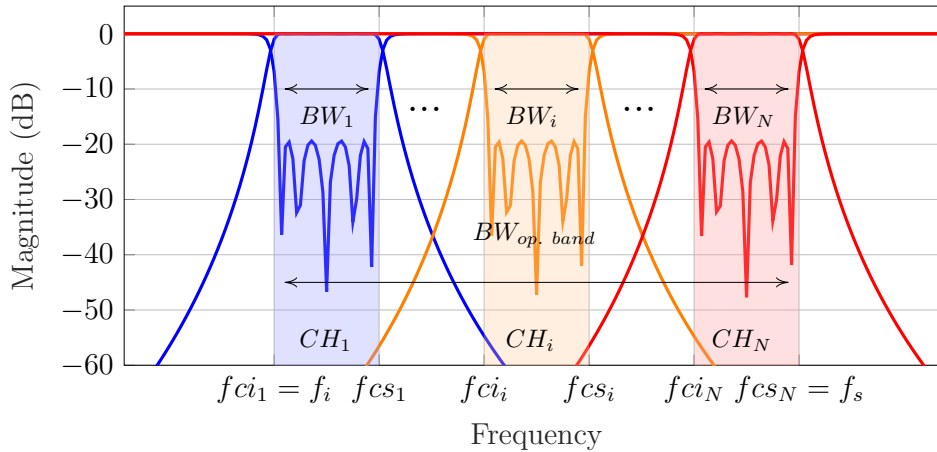


Figure 3.2: Subdivision in N channels of a fixed portion of the frequency spectrum in the C-band.

3.2.1 Monolithic ceramic cavity resonators study

Ceramic-filled cavity resonators are the fundamental block utilized in this chapter for the construction of hybrid tunable filter banks. Two ceramic materials are considered for the study of compact monolithic devices with different degrees of miniaturization thanks to the substrate EM properties. On the one hand, Alumina (Al_2O_3) is a very popular ceramic material with an electrical permittivity of $\epsilon_r \approx 10$. The dielectric losses could vary between $5 \cdot 10^{-5} \leq \tan \delta \leq 5 \cdot 10^{-3}$ depending on the quality of the material. On the other hand, Zirconium Dioxide (ZrO_2) has a higher electrical permittivity ($\epsilon_r \approx 32$) leading to very compact ceramic-filled cavity components. However, the loss tangent of Alumina substrates is 10 to 100 times better than current Zirconium Dioxide materials and much better than regular polymers.

Some design strategies could be utilized to improve the miniaturization of TE_{m0p} rectangular cavities such as inner posts that generates additional capacitive effects on the resonant mode. Therefore, the resonance frequency is shifted towards lower frequencies leading to the implementation of smaller resonators. Logically, the utilization of one or the other approach will depend on the application and its particular specifications. For instance, the utilization of low-loss Alumina substrates leads to higher Q_0 than Zirconium Dioxide materials but with larger area requirements. Smaller-size components developed with high permittivity Zirconium Dioxide substrates hinders the external coupling posing a challenge for interconnections. Additionally, thicker substrates are needed to achieve the same Q_0 values than with Alumina. The application of metal coated inner posts (blind holes, see examples I and III in Table 3.1) with a height less than the substrate thickness can contribute to the device miniaturization at the expense of higher sensitivity to manufacturing tolerances and lower quality factor.

In this scenario, the spurious modes are shifted towards higher frequencies. These posts should not be confused with the via post used later on in this chapter. Features comparison between different C-band rectangular cavity resonators implementing the aforementioned approaches could be found in Table 3.1.

The exhibited resonators were used as a first order estimation of possible monolithic filter bank scenarios developed with ceramic technologies. In the case of a complete switched filter bank where every channel is physically implemented by a filter, the number of switches increases with the number of channels. Off-the-shelf switches were chosen considering the best components combination that minimizes the costs, and reduces the size and loss along the transmission path. P-i-n diode switches seem to have a good trade-off between these characteristics that fit to compact filter bank applications. Lower losses and better linearity can be achieved by replacing the p-i-n diode technology with more costly RF MEMS switches. Therefore, better performances could be obtained, specially in scenarios with multiple cascaded switches.

Table 3.2 exhibit the area occupied by ceramic filter banks developed with the resonators evaluated in Table 3.1. Commercially-available p-i-n diode switches were utilized to estimate the extra area and losses introduced by the devices and their associated bias and control circuit networks. The total estimated control area is assumed to be ten times the switch area, as a worst case scenario. From 2 to 8 channels the utilization of a minimum amount of switches (one at the device input and one at the output as depicted in fig. 3.1) was prioritized to reduce the area and the accumulated loss. In the case of

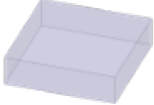
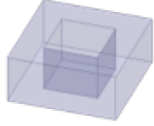

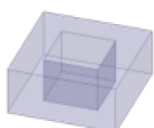
Example	Resonator	Material	Size (mm x mm x mm)	Qo	$f_0(T E_{102})$ ($X \cdot f_0(T E_{101})$)	Comments
I		Al_2O_3	15.00 x 15.90 x 1.00	527	$X = 1.56$	<ul style="list-style-type: none"> • Largest size. • Highest Q.
II		Al_2O_3	8.70 x 9.18 x 1.00	437	$X = 2.93$	<ul style="list-style-type: none"> • $f_0(T E_{102})$ shifted towards higher freq. • More compact. • Sensitive to fab dispersion.
III		ZrO_2	8.00 x 8.33 x 2.00	471	$X = 1.56$	<ul style="list-style-type: none"> • Smaller size than alumina. • Thicker substrate. • More difficult to couple.
IV		ZrO_2	4.80 x 5.10 x 2.00	345	$X = 2.63$	<ul style="list-style-type: none"> • Smallest size. • Lowest Q. • Sensitive to fab dispersion.

Table 3.1: Alumina and Zirconium Dioxide rectangular cavity resonators features comparison.

Losses		Channels				
		2	4	6	8	10
IL sources (dB)	Switches	2 x 0.3	2 x 0.4	2 x 1	2 x 1.5	2x(0.3+0.55)(*)
	Interconnections	0.92	2.88	1.95	4.8	6.24
	Filter	0.56 [IV]	1.076 [III]	0.95 [II]	0.96 [I]	1.035 [I]
Total losses (dB)		2.080	4.756	4.900	8.760	10.675
Area		2	4	6	8	10
Switch (mm^2)		1.378	3.976	21.274	6.130	6.454 (*)
Control and bias circuit (mm^2)		13.78	39.76	212.74	61.3	64.54
Filter technology (mm^2)	Al ₂ O ₃ [I]	2034	4068	6102	8136	10170
	Al ₂ O ₃ (w/post) [II]	712	1424	2136	x	x
	ZrO ₂ [III]	602	1204	x	x	x
	ZrO ₂ (w/post) [IV]	238	x	x	x	x
Total area (mm^2) (**)		252	1244	2349	8198	10235

Table 3.2: Filter bank (fixed channels) estimated losses and area implemented with SPNT p-i-n diode switches and ceramic technology. (*) stands for the only case with more than one kind of switch (SPDT and SP5T). (**) stands for the minimum area cases.

a 10 channels filter bank, a combination of SPDT and SP5T can be applied to carry out this scenario. The filters were designed to provide an adjacent channel rejection better than 20 dB and a return loss within the pass band better than 15 dB.

In order to perform the interconnections needed between the switches and filters, the losses introduced by coplanar lines on 1 mm thick Alumina ($G_{CPW} = 100 \mu m$ and $W_{CPW} = 95 \mu m$) and Zirconium Dioxide ($G_{CPW} = 100 \mu m$ and $W_{CPW} = 25 \mu m$) substrates were taken into account. The calculated interconnection losses were $IL_{|ZrO_2} = 0.09 dB/mm$ and $IL_{|Al_2O_3} = 0.032 dB/mm$. The cases marked with a red cross in Table 3.2 identify the scenarios where the quality factor needed to accomplish the filter specifications cannot be satisfied as the number of channels increases, and depending on the substrate material chosen. These constraints are better illustrated in fig. 3.3, where the quality factor of a synthesized 4-pole Chebyshev filter was calculated to estimate the minimum Qo necessary to maintain the channel requirements ($RL \geq 20 dB$ and $IL \leq 2 dB$). The increment of Qo in TE_{m0p} cavity resonators is linked to their thickness as shown in fig. 3.3.a. However, some spurious modes shift towards lower frequencies as thicker the resonator, thus hindering the stop band rejection [178]. Figure 3.3.a illustrates the fundamental mode and the first three spurious modes dependency with the substrate thickness (H_{RES}). We set as a practical limit a

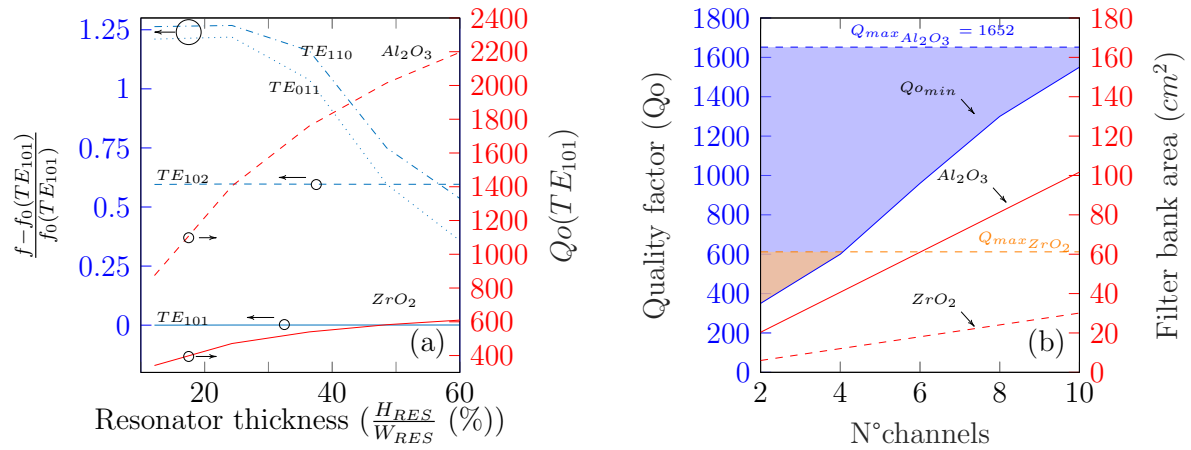


Figure 3.3: Fundamental mode and spurious mode evolution with the resonator thickness (a). Minimum quality factor ($Q_{o_{min}}$) needed to fulfill the specifications in terms of losses and estimated area in N channel filter bank with a fixed operating band (b).

maximum height of 5 mm to avoid thick devices and the excitation of spurious modes at frequencies closer to the operating band. The maximum Q_o reasonable to be obtained with the ceramic materials proposed are $Q_{max Al_2O_3} = 1652$ and $Q_{max ZrO_2} = 612$. As it can be seen, Zirconium Dioxide resonators could be theoretically used in filter banks up to 4 channels (region highlighted in orange) with this limitation. However, the quality factor is too close to the minimum necessary value to fulfill the filters specifications in terms of IL, making it a risky scenario. On the contrary, Alumina-filled cavity resonators could provide the Q-factor needed up to 10 channels (region highlighted in blue) in the expense of more area consumption.

The implementation of switched filter banks (fixed frequency) with a balance between loss and size is only feasible up to two bands. Otherwise, the losses would be too high for real applications, specially for eight or ten channels (more than 8 dB and 10 dB, respectively).

The area requirements and the losses added with the increment of the number of channels make switched filter banks an impracticable scenario. The utilization of tunable devices with movable parts that disturb the EM field or change the cavity dimensions are difficult to carry out in small monolithic components. Some demonstrations can be found in [175], where a piezoelectric transducer is used to control the conductive sheet position of a metallic enclosure filled with a dielectric resonator. Another viable way to modify the resonance frequency is to perform an electronic tuning that interacts with the electromagnetic field inside the structure. The use of varactors is a very common technique to vary the resonator inner electric field in a continuous way. Nevertheless,

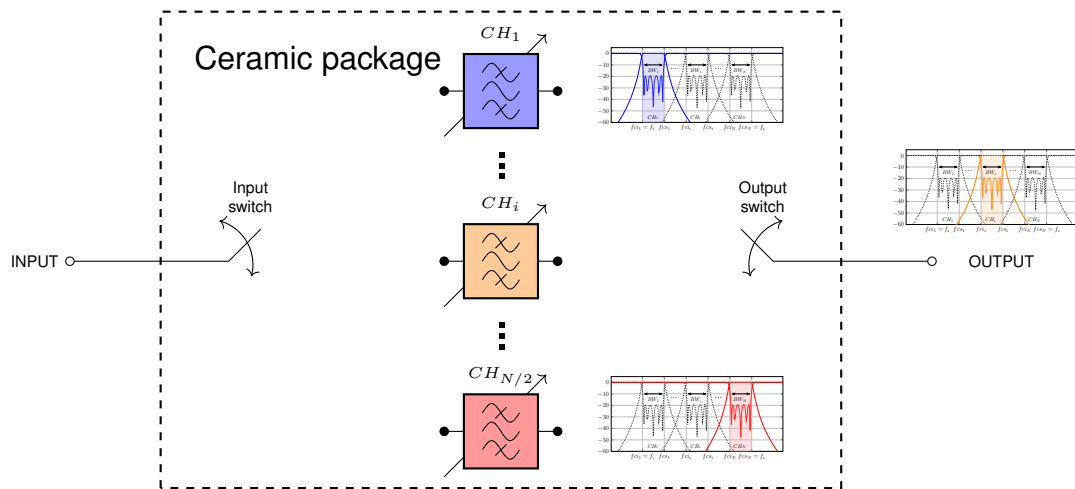


Figure 3.4: Hybrid filter bank configuration block diagram.

the added losses introduced by the parasitic resistance of these elements usually leads to poor quality factors [172], [179], mainly when wide tuning ranges are needed. MEMS technology is also utilized as tuning elements owing to their linearity and low insertion losses [176]. Nevertheless, these devices are usually more expensive than varactors. An intermediate configuration is explored in order to reduce the area of the device taking advantage of the permittivity of ceramics and save half of the filters by implementing 2 states tunable filters inside a switched filter bank. A discrete states tunable filter capable to move between contiguous channels only needs a small frequency shift and less IL compared to a wide tuning range single filter. Fig. 3.4 shows a generic block diagram of such device, as it was proposed in [160], implementing a tunable 4-pole filter controlled by RF MEMS switches.

A similar evaluation of different scenarios developed with this hybrid configuration shows, in principle, an improvement in terms of size and loss. Table 3.3 summarizes the main characteristics of potential monolithic filter banks. Since in this approach a 1-bit tunable band-pass filter is used as an elemental cell for the construction of different filter bank configurations, the 2-channels case can therefore be implemented with just one basic cell. Therefore, no switches or internal interconnections between filters are needed here. Very compact devices could be manufactured with the use of Zirconium Dioxide resonators. The overall size of each configuration is also reduced by half compared to two switched fixed-frequency filters. As a result, the amount of components and interconnections is diminished, thus drastically lowering the losses and leaving some room for the implementation of more channels. In regard to the filter quality factor, the tuning technique chosen will determine the electromagnetic performance of each

Losses		Channels				
		2	4	6	8	10
IL sources (dB)	Switches	-	2x0.3	2x0.5	2x0.4	2*0.55
	Interconnections	-	1.5	2.88	3.36	4.8
	Filter	0.56 [III]	1.076 [III]	0.95 [I]	0.96 [I]	1.035 [I]
Total losses (dB)		0.560	3.176	4.840	5.120	6.935
Area		2	4	6	8	10
Switch (mm^2)		-	1.378	3.976	21.274	6.130 (II)
Control and bias circuit (mm^2)		-	13.78	39.76	212.74	61.3
Filter technology (mm^2)	Al ₂ O ₃ [I]	1017	2034	3051	4068	5085
	ZrO ₂ [III]	301	x	x	x	x
Total area (mm^2) (*)		301	2048	3091	4281	5147

Table 3.3: Mixed technology filter bank estimated losses and area implemented with SPNT p-i-n diode switches and ceramic technology. In each case the used filter is a 1-bit (2-states) tunable filter. (*) stands for the minimum area cases.

tunable filter. Despite a larger size compared to Zirconium Dioxide filters, the utilization of Alumina substrates provides more margin for the fulfillment of the filter specifications that could be compromised as a consequence of the Qo degradation of these methods.

Having presented the arguments derived from the theoretical study, the rest of this chapter will be focused on the investigation of 1-bit tunable filter blocks in Alumina that could be potentially used in larger monolithic hybrid filter banks. The application of 3-D printing manufacturing techniques are also considered for the necessary interconnection and integration of the system control circuits. The goals pursued under the scope of this work are the integration of diverse technologies and the identification of the main constraints during the construction of 3-D printed flip-chip SMT hybrid filter banks for telecommunication applications in sub-6 GHz bands.

3.3 1-bit tunable resonators

The key element for the implementation of a monoblock SMD filter bank is, in principle, the construction of a compact 2-state tunable filter bank implemented in low-loss ceramic materials. As it has been already mentioned, the biggest challenge of current

tunable filters is to maintain a constant bandwidth and losses in all the channels of the operating band. Besides, the quality factor is a fundamental parameter in microwave filters design that can be rapidly reduced depending on the filter technology and tuning technique chosen. Monolithic ceramic cavity filters can offer a relatively high Q-factor as well as high hardness, light weight, corrosion and chemical resistance; desired characteristics in applications working under harsh environments such as in space, or at high altitude in the Earth atmosphere. Moreover, ceramics have a higher resistance to high temperatures than metals or polymers thanks to their fusion point. These characteristics makes ceramics an interesting candidate for our approach. Even more, the utilization of SLA fabrication processes could facilitate the integration with heterogeneous technologies towards the conception of ceramic System on Package (SoP).

3.3.1 Tuning effect

Electrically-controlled microelectronic devices such as, varactors, diodes, RF MEMS or transistor switches fit better the requirements of monolithic SMD devices assembled on RF front-ends printed circuit boards (PCBs) than mechanical or piezoelectrical tuning strategies. Tunable filters reported in the literature based on added capacitive effects performed with varactors usually exhibit low Q-factors. However, the utilization of metallic vias as tuning elements introduced in [180] is an attractive concept that exhibits better performances. This approach has been mainly implemented in SIW technologies where plated via holes are the fundamental element for the structures fabrication on carrier substrates. Nevertheless, regular PCBs often provide higher dielectric losses and lower permittivity values than ceramics. Therefore, in [160], [161] this approach was implemented in Alumina substrates with dielectric losses of $\tan \delta = 3.10^{-4}$.

The digital connection/disconnection of the via post to the cavity metallic layer changes the boundary conditions inside the resonator from one state to the other, thus disturbing the resonant mode frequency. Furthermore, the position of the post contributes to the modification of the frequency tuning range (see fig. 3.5). The discrete tuning states are a major difference to varactor-based tuning filters, where in the former method the modification of the resonance frequency is carried out analogically. A continuous tuning is mandatory in certain applications, however, in the case under study in this chapter this is not a requirement. If necessary, the number of tuning states could be extended by adding tuning posts at different locations within the cavity. Nonetheless, it has to be considered that the quality factor is reduced as the number of posts increases [159],

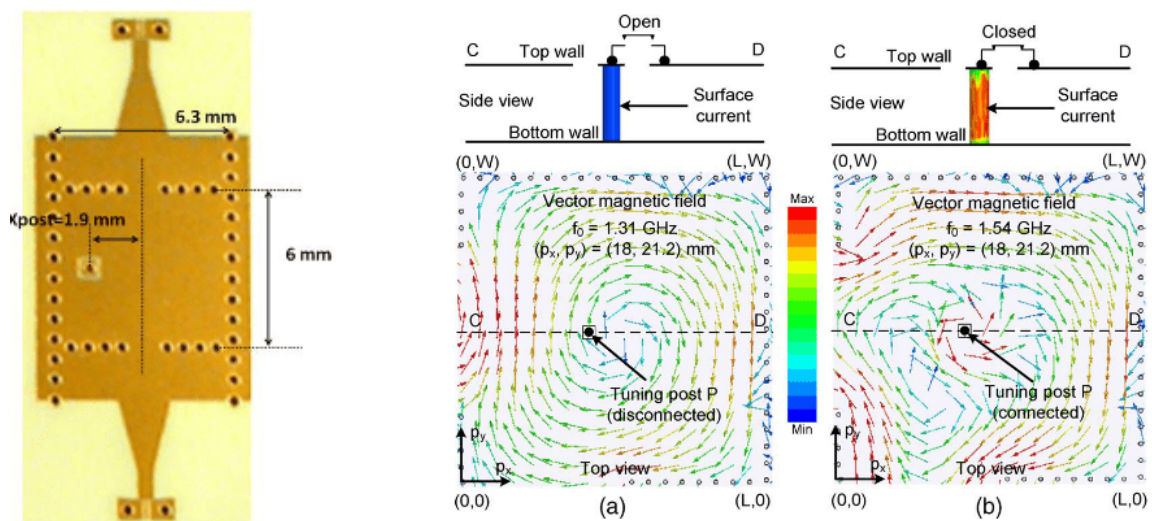


Figure 3.5: SIW tunable resonator developed in [161] (left) and tuning effect generated with the disconnection (a) and connection (b) of a metallic via [159]. The surface current through the tuning post is represented on top and the vector magnetic field of the dominant mode on bottom.

[180]. In [159], a 14-states SIW tunable filter is reported with multiple tuning posts controlled by RF MEMS switches. The filter exhibit a tuning range from 1.2 to 1.6 GHz with a Q-factor between 93 to 132. Packaged RF MEMS switches has the advantage to integrate the control circuit on the device and can be directly soldered onto the filter without bond wires. In summary, in addition to the high quality factor of RF MEMS the parasitic reduction of external elements improves the overall system performances. Nevertheless, these devices are usually larger in size than other switches and the small amount of RF MEMS manufacturers around the world elevates significantly the costs. The use of compact p-i-n diode switches represents an affordable option in expense of lower performances.

The tuning posts are connected in one extremity to the bottom wall and to a square opening in the cavity top wall in order to avoid a fixed short circuit. Special attention must be paid to maintain the openings small enough to avoid an excessive leakage of the resonators field and therefore, a degradation of its Q-factor. As shown in fig. 3.5.a, when the tuning post is disconnected and isolated from the top metallic plate, no surface current flows through the via. Therefore, no magnetic field is induced around the post and the mode H-field results unchanged driving to the dominant mode inside the cavity to remains almost unaffected.

By contrast, a current density flow is imposed trough the via if the post is short circuited using any of the aforementioned elements, thus inducing a concentrated magnetic field

in the surroundings (fig. 3.5.b). As a result, the cavity modes are significantly perturbed depending on their influence in the post location. This effect causes a variation in the resonance frequency owing to the boundary condition changes inside the resonator. The location of via posts near inductive irises or coplanar accesses imposes some constraints driven by the tuning effect itself. Basically, the external coupling to the resonator is affected by the influence of the induced magnetic field around the post. Therefore, the external quality factor may change to a greater or lesser extent depending on the post position.

It is mandatory to study and identify the role of via posts design parameters in order to understand how to enhance the control of the frequency shift effect on the device. This study will be addressed as follows.

3.3.2 Frequency shift effect control

Electrically-controlled vertical via posts are the main element for the construction of monolithic tunable resonators. The two possible states (isolated or short circuited post) induce variations in the cavity dominant mode leading to a change in the resonance frequency.

A complete analysis of the tuning post design elements should be carried out to provide a better control of the tuning range and the side effects on other parameters such as, the unloaded and external quality factor or the inter-resonator couplings. The structure was modelled and simulated in a full-wave simulator (ANSYS HFSS) to gather more information about the EM fields behaviour and the resonance frequency dependency

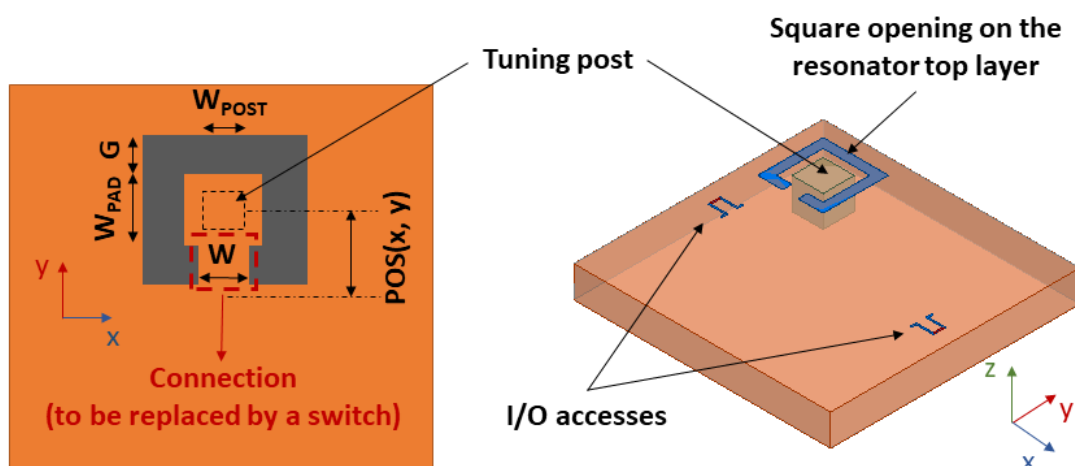


Figure 3.6: Via post design parameters study performed in a rectangular ceramic-filled cavity resonator 3-D model.

with the design parameters. Figure 3.6 illustrates the CAD view of a ceramic rectangular resonator with a perfect electric conductor (PEC) and a tuning post coating. The resonator is excited by two magnetic coupling slot accesses located on the top face. In rectangular cavity resonators, the fundamental TE mode half-wavelength resonance frequency is given by eq. 3.1. In this expression ϵ_0 and μ_0 are the vacuum permittivity and permeability; ϵ_r is the relative permittivity of the material; and m, n and p represent half-wavelength variation of the E-field lines along the resonator width (W_{RES}), height (H_{RES}) and the length (L_{RES}) of the resonator, respectively.

$$f_0 = (2\sqrt{\epsilon_r \cdot \epsilon_0 \cdot \mu_0})^{-1} \sqrt{\left(\frac{m}{W_{RES}}\right)^2 + \left(\frac{n}{H_{RES}}\right)^2 + \left(\frac{p}{L_{RES}}\right)^2} \quad (3.1)$$

In TE_{m0p} modes, the resonance frequency is only determined by W_{RES} and L_{RES} . Nevertheless, the resonator height H_{RES} determines the quality factor and contributes to control the frequency location of higher order modes. In Chapter 2 we shown that the quality factor depends on four main losses sources: the ohmic losses due to the finite conductivity of the metal layer Q_c ; the dielectric losses inherent of the substrate material Q_d ; the radiation losses through openings on the metal enclosure Q_r ; and the external losses Q_e . The first three sources are part of the unloaded quality factor Q_o and the overall loaded Q-factor Q_L can be calculated as shown in eq. 3.2.

$$\frac{1}{Q_L} = \frac{1}{Q_d} + \frac{1}{Q_c} + \frac{1}{Q_r} + \frac{1}{Q_e} = \frac{1}{Q_o} + \frac{1}{Q_e}; \quad \text{with} \quad \frac{1}{Q_e} = \frac{1}{Q_{acces1}} + \frac{1}{Q_{acces2}} \quad (3.2)$$

In PEC materials, the conductivity approaches infinity and Q_c^{-1} approaches zero. Furthermore, if the openings are small enough, the radiation losses could be neglected in comparison to the dielectric losses. Therefore, the unloaded quality factor can be written as in eq. 3.3, where $\tan \delta$ is the dielectric loss tangent. The loss tangent is not constant but increases with frequency driving to higher losses [181].

$$\frac{1}{Q_o} \approx \frac{1}{Q_d} \approx \tan \delta \quad (3.3)$$

The calculations of these parameters or the EM fields distribution are difficult to be carried out accurately by hand in geometrically complex structures. Several methods were developed and implemented in computational environments to facilitate this task. Integral equation technique [182], mode matching [183], or finite-element analysis [184] are some of the methods used nowadays in commercial microwave simulation software. The resonator was designed to operate in the C-band implementing the fundamental mode TE_{101} . The tuning posts were carried out with a PEC via short-circuited on the

bottom metal layer and isolated from the top face with a rectangular opening. The connection and disconnection is performed during the simulations adding or removing a metallic link which represents a switch located here on the ON and OFF states from the top pad to the cavity metal plate. The post was represented with a parallelepiped via connected to a squared metallic pad. A cylindrical via post shape was utilized during the device fabrication for a better adaptation of the design to 3-D printing process. In this framework, the design parameters exhibit five degrees of freedom: the pad width (W_{PAD}), the post width (W_{POST} or D_{POST}), the opening gap (G), the metal link width (W) and the post x-/y- location from the center of the resonator (POS).

Post location (POS) and number of connections

The via post location within the resonator $POS(x, y)$ is the main parameter to perturb the TE_{m0p} modes. The frequency shift was studied fixing the rest of the design parameters. The established criteria to choose these values was based on the manufacturing processes contemplated for real samples. On one side, the minimum size of the tuning post was restricted to $W_{POST} = D_{POST} \geq 0.5 \text{ mm}$ to ensure a correct via plating with the available metallization processes. On the other side, the square opening gap G was chosen to be the same as the CPW lines gap presented in Section 3.2.1 depending on the substrate material. The minimum pad width was set to $W_{PAD} \geq W_{POST} + 2G_{PAD}$ since in some ceramic SLA processes sharp edges can be rounded between 0.1 to 0.2 mm. $G_{PAD} = 0.2 \text{ mm}$ is the minimum pad space needed for placement of SMD components. Additionally, some extra area is required to solder bond wires or assemble devices on the pad. In regard to the metal link width (W) its value was arbitrarily chosen to be $W = 0.25 \cdot W_{PAD}$.

The post was placed in three different positions P1, P2 and P3 as depicted in fig. 3.7. The magnitude of the fundamental mode TE_{101} is represented in each case. The rest of the cases could be considered as a combination or intermediate states between these three points. In P1, the post is placed at the corner of the resonator where minimum values of E-field can be found. The influence of the tuning element in this case has no great impact on the mode and the resonance frequency suffers almost no change. In the second case, the post located at P2 is placed in a maximum of H-field and closer to the maximum E-field than in the first case. A perturbation on the field distribution can be observed from this position causing a higher frequency shift. Finally, the addition of the short-circuited tuning post (referred from now on as ON state) in the position P3 causes an important change on the resonant mode when

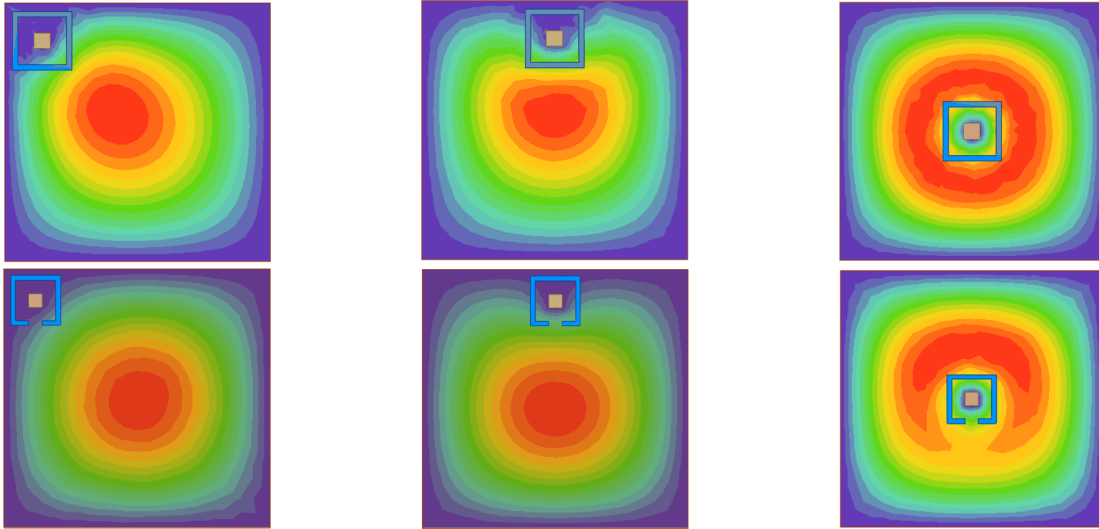


Figure 3.7: Magnitude of the E-field distribution of two states (ON/OFF) for three tuning post positions: corner (P1), center edge (P2) and center (P3).

placed in the area of maximum E-field and minimum H-field, producing the greatest possible frequency shift possible with this method. On the contrary, when the post is disconnected and isolated from the metallic plate (OFF state), it can be seen that the fields pattern resembles to the original TE_{101} mode.

In [160] the utilization of multiple interconnections was suggested as a technique for the current density flow control and the creation of multiple tuning states. This idea was also explored in the simulation realm at different post positions to investigate their influence on the distance between the different states. As proposed in [160], up to four connections were performed by metal links placed on every edge of the square opening. The joint effect of the post position within the resonator and the number of connections on Δf_0 and ΔQ_0 is summarized in fig. 3.8 for a substrate thickness of $H_{RES} = 0.12.W_{RES}$. Zero connections represent the OFF state ($N_{con} = N_0 = 0$), whereas connections from $i = 1$ to 4 corresponds to $N_{con_i} = N_i = i$ (ON state). The frequency shift Δf_0 is normalized to $f_0(N_0)$ in every via post position ($\Delta f_{0_N} = \Delta f_0(N_i)/f_0(N_0)$). The resonator shows a great frequency shift Δf_0 from N_0 to N_1 and a moderate variation between the ON states (N_1 to N_4 in fig. 3.8.a). This effect is amplified as the tuning post is displaced, for example, from P1 to P3.

The dominant mode is shifted depending on the post position and the boundaries conditions imposed by the plated via and the isolated metal pad. These elements act as an additional shunt capacitor connected to the resonator that decreases the original resonance frequency [180]. In the position P1 the effect is less evident owing to the minimum E-field in the surroundings. When the post is connected, the magnetic

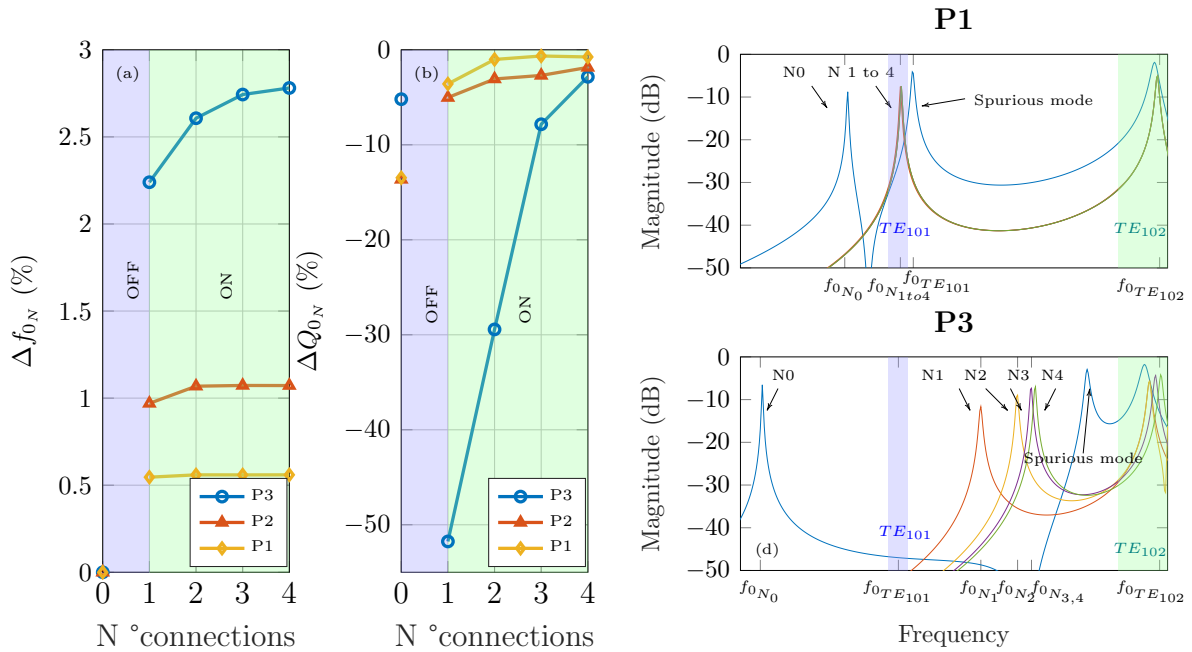


Figure 3.8: Normalized frequency shift Δf_0 (a), unloaded quality factor ΔQ_0 (b), and simulated S-parameters (S_{21}) (c and d) of a ceramic-filled rectangular cavity resonator for different via post positions and number of connections.

field generated disturbs the field, reduces the cavity space in the corner, and causes a resonance of the TE_{101} mode at higher frequencies. In P3, the maximum E-field increases the capacitive effect, thus shifting the resonant mode towards even lower frequencies and disturbing the fundamental mode TE_{101} field distribution. When the post is connected, the disturbance in a region of maximum field distribution provokes a greater effect than in P1. On the contrary, the via post effect at these positions has less impact on the TE_{102} mode since the minimum E-field magnitude is located at those points. Furthermore, the transmission zero resulting from the cancellation between TE_{101} and TE_{102} [185], [186] shifts its position depending on the post location.

Additionally, the apparition of a spurious mode between the fundamental and the second mode is observed in the OFF state. To the best of our knowledge this effect has not been reported in similar works that implements lower permittivity substrates. The investigation of this particular resonant mode performed by means of EM simulations points out to the combined effect of an spurious resonance frequency on the isolated via post coupled to the cavity resonator EM fields, that can be controlled with the substrate height or the pad width. The influence of this mode should be taken into account during the design to void insufficient attenuation in the filter stop band.

In regard to the quality factor, a more pronounced degradation effect is shown as the

post is displaced from P1 to P3. The variation of the Q-factor (ΔQ_o) in fig. 3.8.b has been normalized to the maximum quality factor that can be achieved in each case if no air gap is engraved into the metallic surface ($\Delta Q_{oN} = \Delta Q_o(Ni)/Q_o(max)$). Moreover, as the number of metal links increases, the square opening is reduced and the Q-factor converges to the typical resonator case that could be a bit lower owing to the ohmic losses introduced by the plated via.

Tuning post design parameters

The study of the plated via physical parameters and the understanding of the impact of each parameter on the tuning effect behaviour is a challenge owing to the correlation between them. Each element determine a particular state where the specific value of the other parameters affects the result. Therefore, we are heading towards a multidimensional analysis where a space of potential solutions could be found with different

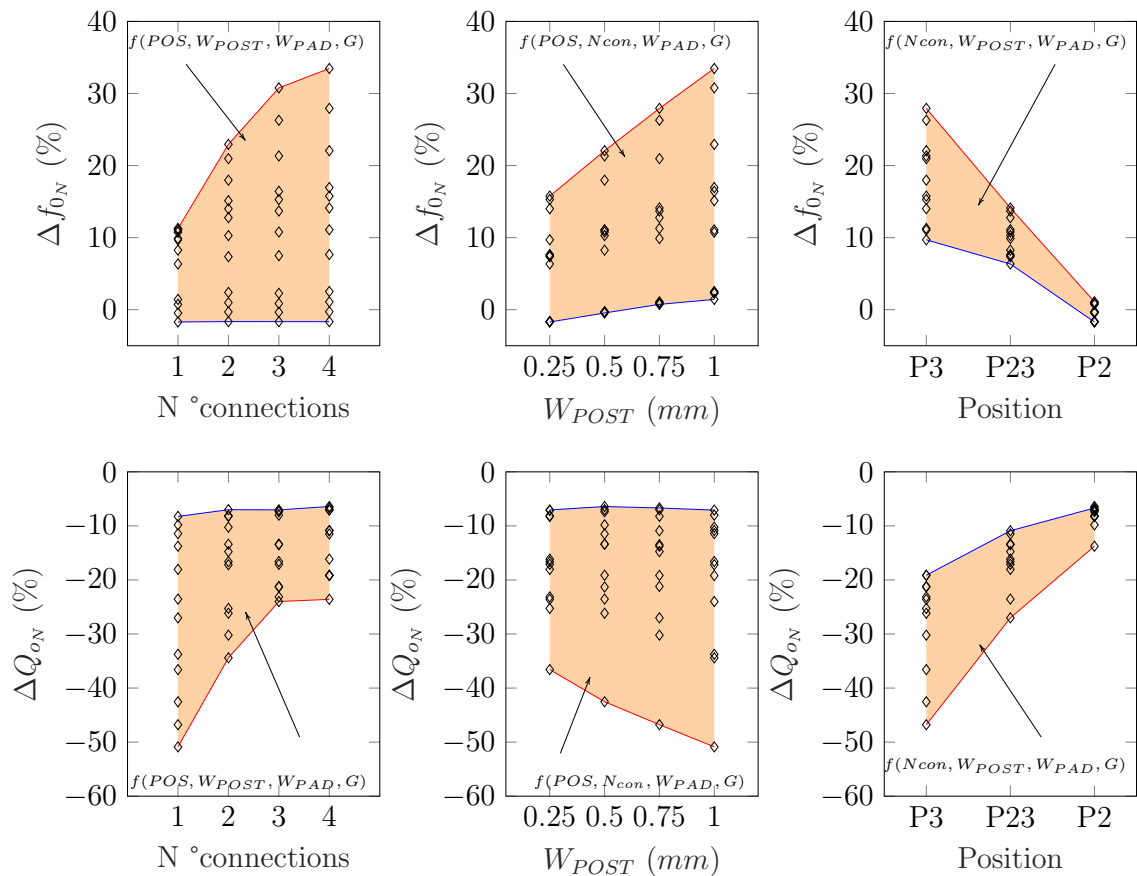


Figure 3.9: Alumina-filled rectangular cavity resonators study of quality factor (a) and frequency tuning range (b). Several substrate thickness (t) and post positions ($D_{post} = 1 \text{ mm}$) were used to adjust the design to the specifications.

set of values. In order to face this problem, a possible strategy to be followed could be finding optimum solutions for this particular design with the use of advanced optimization tools. As starting point, an approximate result can be achieved with the use of the information provided in the previous sections. The different criteria explained so far can help to choose the resonator dimensions H_{RES} , W_{RES} and L_{RES} , the post position (POS), and the number of connections. The initial design parameters of the via can be then slightly optimized to obtain the required Δf_0 and Q_0 . However, in order to provide more information about the space of solutions, a multi-parameter sweep analysis has been carried out with $0.25\text{ mm} \leq W_{POST} \leq 1\text{ mm}$, $1 \leq N^{\circ}\text{connections} \leq 4$, W_{PAD} , G and POS . A position P23 between P3 and P2 was added to include an intermediate case with more impact than in P1. The space of solutions obtained are illustrated in fig. 3.9 where the normalized Δf_{0N} and ΔQ_{oN} have been plotted in function of the main variables. As it can be seen, the number of connections from 1 to 4 could vary the frequency up to 35% as well as the increment of post width depending on the other variables. However, wider posts could bring higher losses. In the last case, the tuning post location strongly determines the frequency range and the losses. As closer to the resonator edge, the less the frequency range and the degradation of the quality factor. The highlighted areas in orange remarks the regions where possible solutions can be expected during the optimization. Furthermore, a better decision of initial parameters can be taken by simplifying the set of values based on this information.

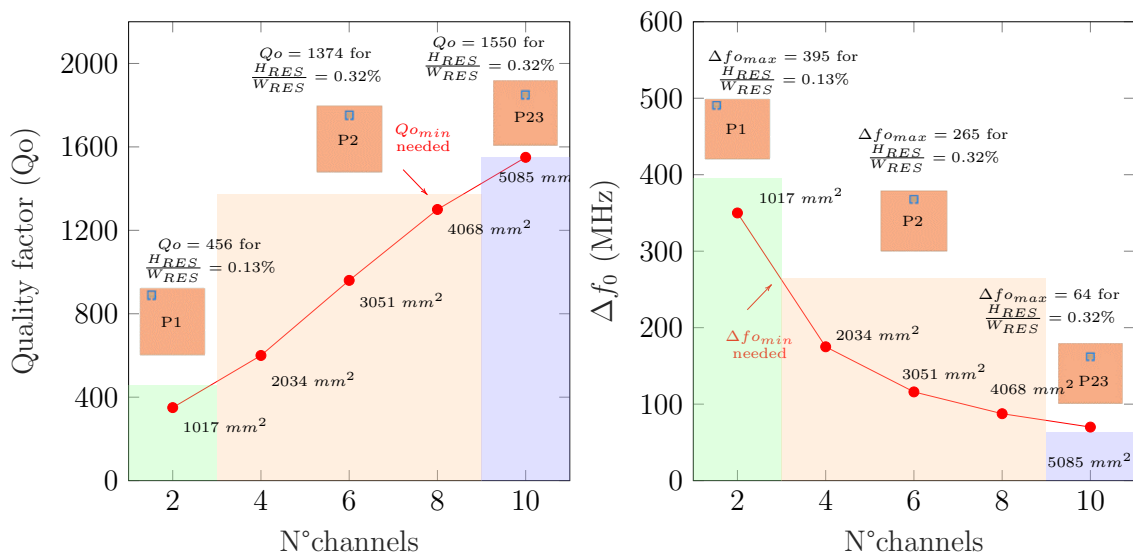


Figure 3.10: Alumina-filled rectangular cavity resonators study of quality factor (a) and frequency tuning range (b). Several substrate thickness (t) and post positions ($W_{post} = 1\text{ mm}$) were used to adjust the design to the channel specifications. The area of each resonator is specified in black.

In addition to the losses introduced by the via post, the substrate thickness limitations imposed by the spurious resonant modes led to the non-compliance of minimum Q-factor required in Zirconium Dioxide resonators. However, Alumina materials can meet the specifications with a reasonable thickness and without compromising the filter stop band with undesired spurious modes. Finite-element simulations were carried out to estimate the tunable resonator performances made with this material. The same fabrication constraints exhibited in Section 3.3.2 were taken into account for the tuning post parameters. The minimum theoretical quality factor and frequency shift per number of channels is cross-checked in fig. 3.10 with the simulation results at P1, P2 and P23. Tunable resonators manufactured with this material could hypothetically offer the quality factor needed for multiple channels. For example, in a 4 channels scenario a 4-states (2 bit) tunable filter is required. The minimum frequency shift needed of 175 MHz and Q-factor of 600 can be fulfilled with the via post placed around P2. Nevertheless special attention must be taken to avoid spurious modes to interfere with the stop band specifications of the filters realized with this technology.

Experimental verification of Δf_0 and ΔQ_0 simulation methods

Nowadays, simulation tools are an essential instrument to predict the behaviour of a system before its implementation in the real world. While these tools can accurately model the physical phenomena, usually a correct workflow implies a loop where the experimental results provides a necessary feedback to refine the model.

In 3-D electromagnetic simulators, the calculation of resonance frequencies and losses is a sensitive matter which must be checked against real measurements. Therefore, in order to verify the correct procedure carried out in previous simulations, a very simple rectangular resonator was designed in the C-band using a Rogers PCB as a low-cost fast prototype. The resonator was machined from a 0.4 mm thick RO4003C substrate. The substrate properties utilized during the simulation were $\epsilon_r = 3.55$ and $\tan \delta = 2.7 \cdot 10^{-3}$. The substrate was pierced during the fabrication with a 1 mm end mill to carry out the through hole via and coated as well as the resonator side walls with an electroless process. The post square openings (P23) and I/O coplanar accesses for RF measurements were carved into the metal layer as after the metallization using fiducial holes for the machine alignment. The measurements were performed in a RF probe station with 0.5 mm pitch GSG tips and connected to a ZVA 87 VNA. The aforementioned fabrication method was also used in other rectangular resonator prototypes introduced in Chapter 5 for the study of support

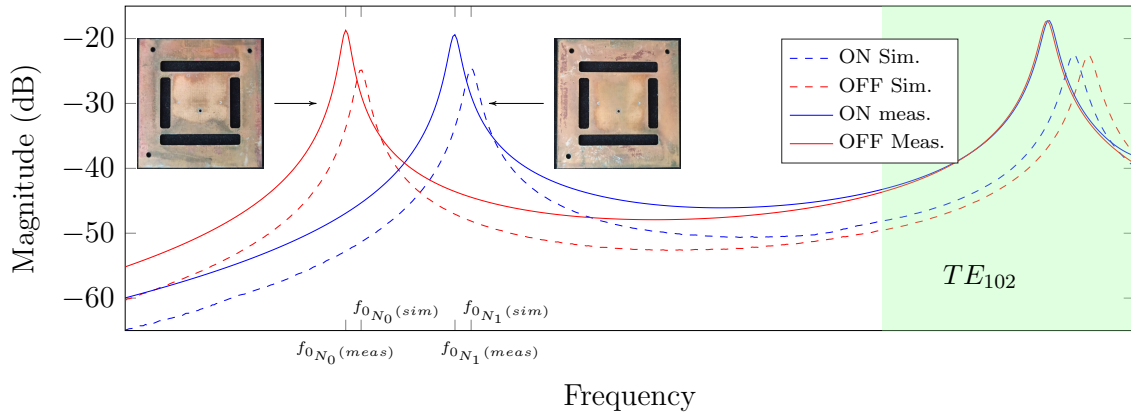


Figure 3.11: Tuning effect simulations and measurements S-parameters (S_{21}) comparison of a 2-state rectangular cavity resonator developed in a 0.4 mm thick RO4003C substrate.

structures. Figure 3.11 depicts the comparison between the simulated and measured scattering parameters of two resonator samples, one of them implementing the OFF state (with the post completely isolated) and the other with one connection (CH1 in the nomenclature or ON state). As it can be seen, measurements are in good agreement with the simulation methodology implemented so far during this study. The whole frequency response is shifted $\delta f = -1.3\% f_{0_{CH_0}}(sim)$ towards lower frequencies with respect to simulations probably owing to the combination effect of permittivity mismatch and fabrication tolerances. However, the device exhibit the same general behaviour and frequency tuning range $\Delta f_0(sim) = \Delta f_0(meas) = 8.77\% f_{0_{CH_0}}(sim)$ between CH0 and CH1. Although measurements show higher external coupling than simulations, the unloaded quality factors were $Q_{o_{CH_1}}(meas) = 103$ and $Q_{o_{CH_0}}(meas) = 112$, a bit lower than the simulated values $Q_{o_{CH_0}}(sim) = 142$ and $Q_{o_{CH_1}}(sim) = 131$. The added losses are caused by the lower conductivity of the deposited metal layer on the side walls and on the plated via as product of the laboratory metallization process.

Although the mentioned differences, the simulation of the tuning effect up to this point seems to fit well with the experimental results. Based on this first step, an electrical model will then be introduced to replace the metal links used so far in order to represent a more realistic approximation with the use of p-i-n diode switches that will provide the frequency tuning of the resonator.

3.4 Modelling and characterization setup

The first part of the present analysis was focused on the choice of the tuning method to be used for the development of a compact 2-state tunable filter, as well as its

implementation on monolithic ceramic substrates. The estimation of the tuning range and the Q-factor in Zirconium Dioxide rectangular resonators led to the conclusion that it is not possible to satisfy the necessary performances for 2-channel tunable filters. Nonetheless, low-loss Alumina substrates may provide the required quality factor. Package parasitics and interconnection losses related to switching devices have not been considered until now in the analysis. Their contribution to extra losses is usually critical and can spoil the good characteristics of low-loss materials and limit their implementation. Switches based on p-i-n diode technology were chosen for our prototypes over MEMS owing to cost and integration size reasons in expense of higher losses. However, the same procedure as explained below can be carried out with RF MEMS switches.

3.4.1 P-i-n diode RF switch

The p-i-n diode is a silicon semiconductor device composed by high resistivity intrinsic region (I) with a P-/N-type regions at each end. The described technology can be seen as a current controlled resistor at microwave frequencies whose impedance is modified with its DC bias level [187]. During the forward bias, the I region is flooded with electron and holes that remains as charges during an average time τ known as carrier lifetime until their recombination. This effect produces an average charge Q that reduces the effective resistance of the region. P-i-n diode devices can handle large amount of RF power with relatively low DC levels. On the contrary, no charge is injected into the I region if the device is subjected to reverse or zero DC bias, leading to a high resistance state and a parallel parasitic capacitance. The switching speed is determined by the I region thickness (T) and the carrier lifetime. Both parameters limit the lowest operation frequency of the device.

The effective resistance and the parasitic capacitance in both forward and reverse states can be represented in a small signal electrical model of the diode (fig. 3.12). In the forward model, the resistance can be calculated as shown in eq. 3.4, where T is the I region thickness, Q is the stored charge determined by $Q = \tau \cdot I_F$, τ is the average carrier lifetime, I_F is the forward bias current, and μ_n/μ_p are the electron and hole mobility. No package or contact parasitic resistance is taken into account in this model, nevertheless, a parasitic inductance $L \leq 1 \text{ nH}$ is usually included. It is also assumed that the RF signal does not significantly affect the stored charge in the I region.

$$R_s = \frac{W^2}{Q(\mu_n + \mu_p)} \quad (3.4)$$

In the case of reverse or zero bias model, the parasitic capacitance is the result of the charges accumulation in the interface between the P-/N-type and the I region that takes the role of an insulator for this case. Therefore, the capacitance can be calculated as a parallel plate capacitor C_p with an area of diode junction A , separation between plates T and permittivity of the I region material ϵ (eq. 3.5). In regard to the resistance R_p , its value is usually higher than the parasitic capacitance reactance, proportional to the reverse voltage and inversely proportional to frequency.

$$C_p = \frac{\epsilon A}{T} \quad (3.5)$$

The equation 3.4 is valid at frequencies higher than the transmit time frequency $f \geq 1300.T^{-2}$ in the I region with f in MHz and T in μm . In the second case, equation 3.5 can be applied at frequencies higher than the dielectric relaxation frequency of the I region $f \geq (2\pi\rho\epsilon)^{-1}$ with ρ the material resistivity. Otherwise, the device behaves as a varactor instead of a p-i-n diode at lower frequencies.

The off-the-self device chosen for the implementation of the tuning effect explained in Section 3.3.1 was the p-i-n diode switch MA4AGSW1. These components are currently offered in the market by the manufacturer of semiconductor products MACOM. This particular product is an Aluminum-Gallium-Arsenide (AlGaAs) single pole, single throw (SPST) switch recommended for its use in defense and aerospace applications. The switch was chosen for its good features in terms of low insertion loss (0.3 dB), high isolation between ports, fast switching speed (10 ns at 10 GHz from 10% to 90% of the RF signal), compact size and thickness, and availability in form of waffle pack. The device can operate between $-55^\circ C$ to $-125^\circ C$ and up to 50 GHz.

In order to bias the device and control the RF signal through the ports a bias network is required to be implemented externally. A circuit schematic of the shunt diodes connection as well as the bias tee recommended by the manufacturer is represented in fig. 3.13. On the one hand, the coupling capacitors $C1$ and $C2$ behave as a high-pass filter for the DC signal. On the other hand, the LC network is a second order low-pass filter that blocks the propagation of the RF signal to the DC source. The second order low-pass filter cutoff frequency $f_c = (2\pi\sqrt{LC})^{-1}$ was designed to be placed more than one decade below the lower frequency of the operating band. Moreover, the coupling capacitors were calculated to attenuate the signals below f_c . The overall network was simulated in the Keysight's circuit simulator Advance Design System (ADS). Figure 3.13 depicts the frequency response of the designed circuits. The p-i-n diode switch could be simulated by implementing the circuit model illustrated in fig. 3.12 if the parameters

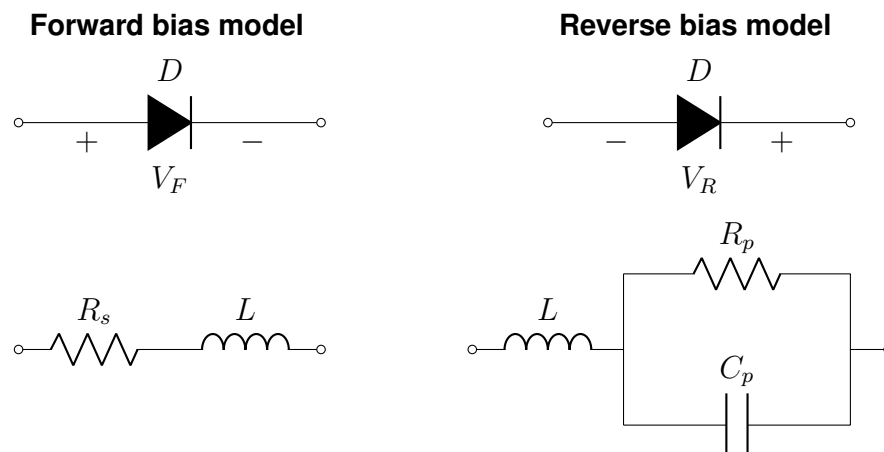


Figure 3.12: P-i-n diode forward and reverse small signal electrical model.

were informed by the manufacturer or if the layout and the technology parameters were publicly available. Another option is to extract these parameters in a characterization setup or to carry out the estimation of the different values through a simulation fit. However, this procedure could result in an inaccurate analysis limited to a restricted frequency range owing to additional parasitics not included into the model. Nevertheless, the manufacturer facilitates measurements data probed on wafer as Touchstone files. These files can be embedded in ADS to work with more precise information of the device behaviour up to the GSG mounting pads interface. Simulations of the complete circuit, in addition to the interconnection CPWG lines effect using these files show a correct behaviour in both forward and reverse bias states.

Additionally, a complementary study is presented in Annex A.1. This study helped to define a model of the bond wires connecting the switch to the top of the 3-D resonators, where the bias network is placed (fig. A.1). The extracted model was implemented in all the designs introduced for the rest of this chapter in order to include the parasitic effects of the wires. Their inclusion was performed by mixing circuit and full-wave EM simulations of the p-i-n diodes and the de-embedded bond wire Touchstone files in HFSS to achieve a more accurate simulation of the tuning behaviour.

3.5 3-D printed tunable resonators: cases of study

In the previous sections we have seen the fundamentals of the frequency shift effect chosen for the development of C-band tunable filters based on ceramic-filled rectangular cavity resonators. Furthermore, we studied the influence of different design variables on Δf_0 and their effect on the quality factor of the resonator. Practical design constraints as

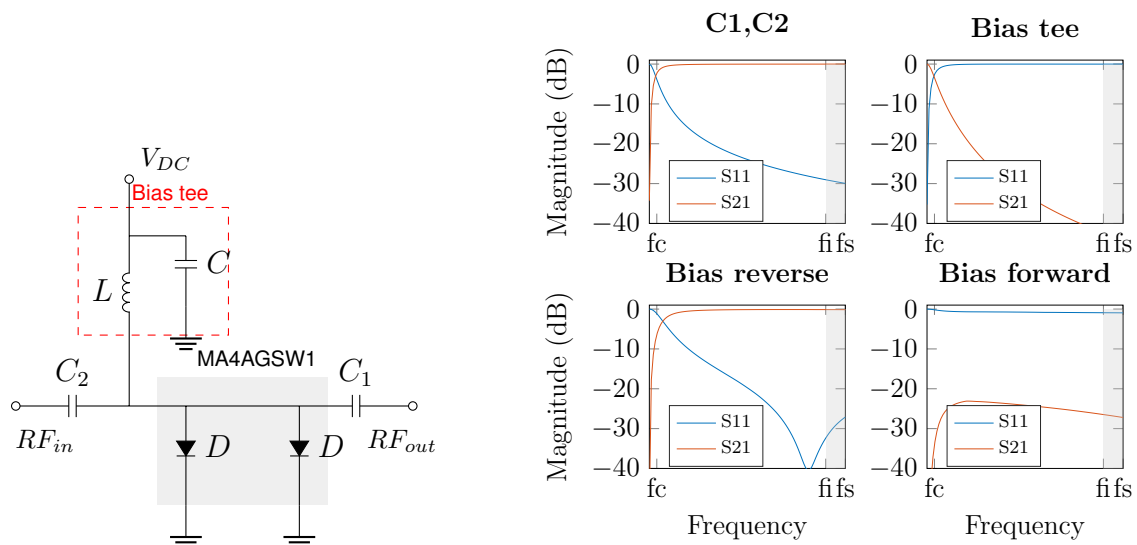


Figure 3.13: Pin-diode and bias network circuit model (left). The component values are $C_1 = C_2 = 10 \text{ pF}$, $C = 39 \text{ pF}$, $L = 8.2 \text{ nH}$. Simulated frequency response of every part of the network (right). f_c stands for the cutoff frequency and f_i and f_s the inferior and superior frequencies of the operating band $BW_{op. band}$.

a consequence of parasitic modes have been identified and exhibited. Furthermore, a modelling of bond wire interconnections and the p-i-n diode switch utilized as a channel selector has been proposed and implemented mixing EM and circuit simulations to provide a better insight of the device performances. The gathered information is indispensable for the evaluation of possible design scenarios.

In this section we will leverage the flexibility of additive manufacturing techniques for the development of 3-D printed ceramic components with the capability to integrate all the required interconnections and control circuits inside as a flip-chip device that could function as SMD 2-state tunable resonator.

3.5.1 Ceramic tunable resonators: general structure

The simulation strategies and models studied were utilized to evaluate the frequency shift and quality factor of flip-chip monolithic ceramic resonators. The purpose of the system modelling is to serve as an input to identify the main sources of electrical losses and design or fabrication constraints. Then, several prototypes can be proposed to enhance the resonator features in terms of size and Q-factor, facilitate the assembly and fulfill the specifications of multiple channels.

The tunable resonators introduced in this thesis were manufactured using stereolithography process with low-loss Alumina material. In general terms, the resonator consists of

a 3-D printed cuboid monolithic block with a via functioning as a tuning post. The device is metal coated and engraved to perform the interconnections lines in the metal surface (fig. 3.14). The overall structure is surrounded by ramps to create an inner pocket where the control circuit devices can be assembled (Level 1). The resonator mounting pads are placed in the second level (Level 2) where RF and DC ports are carried out with CPW lines that connects both levels along the ramps. This interconnection approach was implemented by some research groups in 3-D printed flexible system-on-package (SoP) devices [188], inkjet printed transmission lines on 3-D ceramic semi-spheres and ramps [189], and dielectric ramps for MMICs interconnections[190], [191]. Other interconnection techniques implemented in ceramic SMD filters include vertical coplanar transitions as reported in [192]. The transmission lines were designed to guarantee a 50Ω impedance from the carrier substrate to the termination inside the resonator. Furthermore, the CPW line dimensions in the PCB were chosen to match with a 0.5 mm probe tip pitch. The same design rules were used for the ports and interconnection lines that compounds the p-i-n diode switch network. Therefore, the correct device functioning can be tested before its assembly onto the carrier board. The tuning post diameter was pushed to the minimum possible size feasible to be coated with electroless or aerosol spray processes with a depth of 2 mm. The post was located in a position that provides a frequency shift $\Delta f_0 = 6.9\% f_s$ required for 2-state tunable filters in C-band.

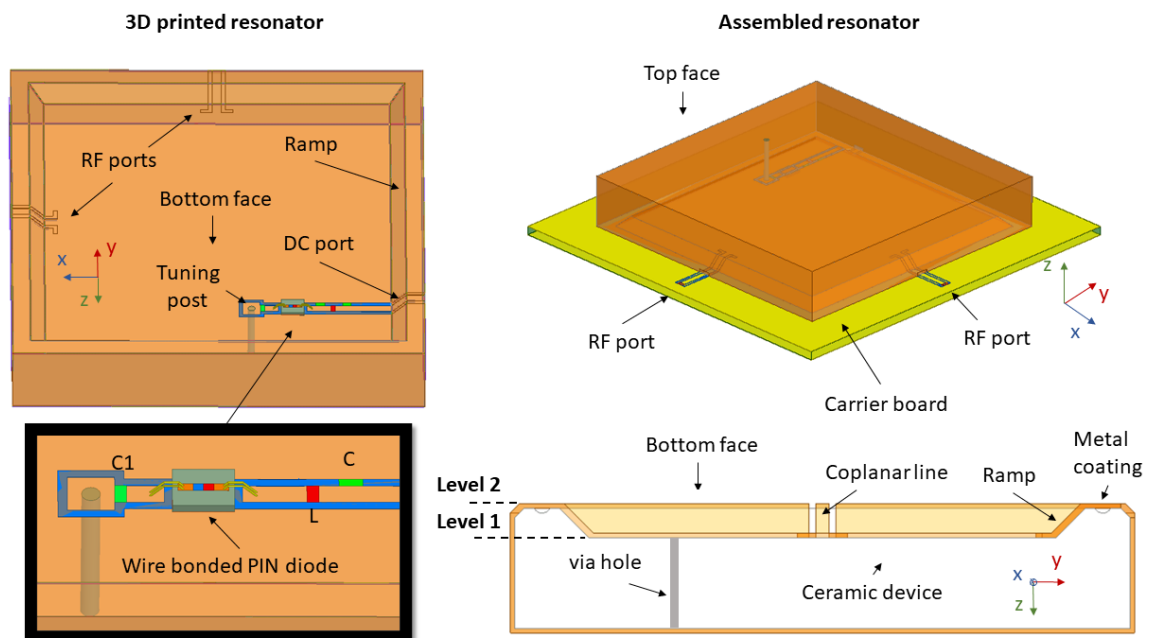


Figure 3.14: 3-D printed flip-chip tunable resonator design.

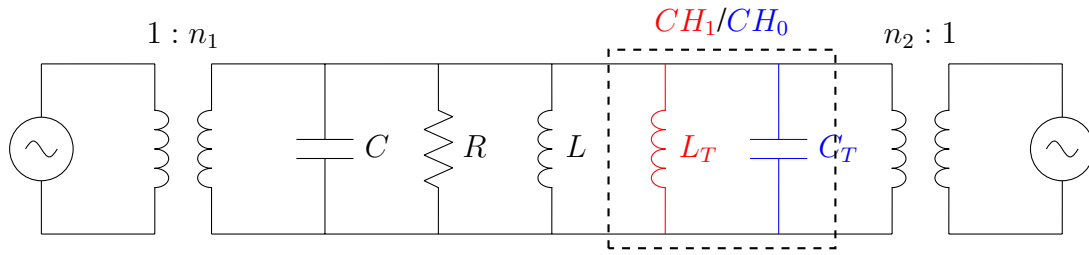


Figure 3.15: Circuit model of the cavity resonator loaded with the tuning via post.

During the simulations of both channels it was noted that the relative location of the switch with respect to the post (*POS*) had a non-negligible impact on the frequency shift that could impose certain design limitations. In order to study the observed effect the system was modelled as an electrical circuit conformed by a L-C tank resonator (fig. 3.15) where the cavity resonance frequency can be calculated as $\Delta f_0 = (2\pi\sqrt{LC})^{-1}$. Otherwise, the tuning post can be modelled as a lossy shunt inductor [159] or capacitor in parallel to the resonator depending the via state. The specific value of the tuning post elements will depend on the via position within the cavity and the electric field magnitude. These values can be calculated with the rectangular cavity electromagnetic field formulas in TE_{101} mode. If the post is connected to the resonator the original resonance frequency Δf_0 is shifted to $\Delta f_0(CH_0) = (2\pi\sqrt{(L//L_T)C})^{-1}$, while if the post is isolated the capacitive effect shifts the resonance frequency to $\Delta f_0(CH_1) = (2\pi\sqrt{L(C + C_T)})^{-1}$. The total resonator losses are included in the resistive element R.

As explained in section 3.3.2, when the via is isolated from the resonator it acts as a transmission line with an open termination, loading the resonator with a capacitive effect. This behaviour will be maintained as long as the total electrical length of the line is less than a quarter wavelength. As a result, a line lengthening will produce a stronger parasitic capacitance that will be reflected as an equivalent resonance at lower frequencies. Otherwise, when the post is short-circuited no strong changes are observed in the via inductance. Therefore, the effect of the switch location can be leveraged as a design variable to increase the distance between the two channels. Nevertheless, the Q-factor degradation should be taken into account when considering this design strategy. A parametric EM simulation of the tunable resonator was carried out in HFSS in order to analyze the behaviour of the frequency shift and quality factor dependency with the transmission line length loading the via post in the OFF and ON state. Figure 3.16 illustrates the effect of the CPW line extension on Δf_0 and ΔQ_o for both cases. The

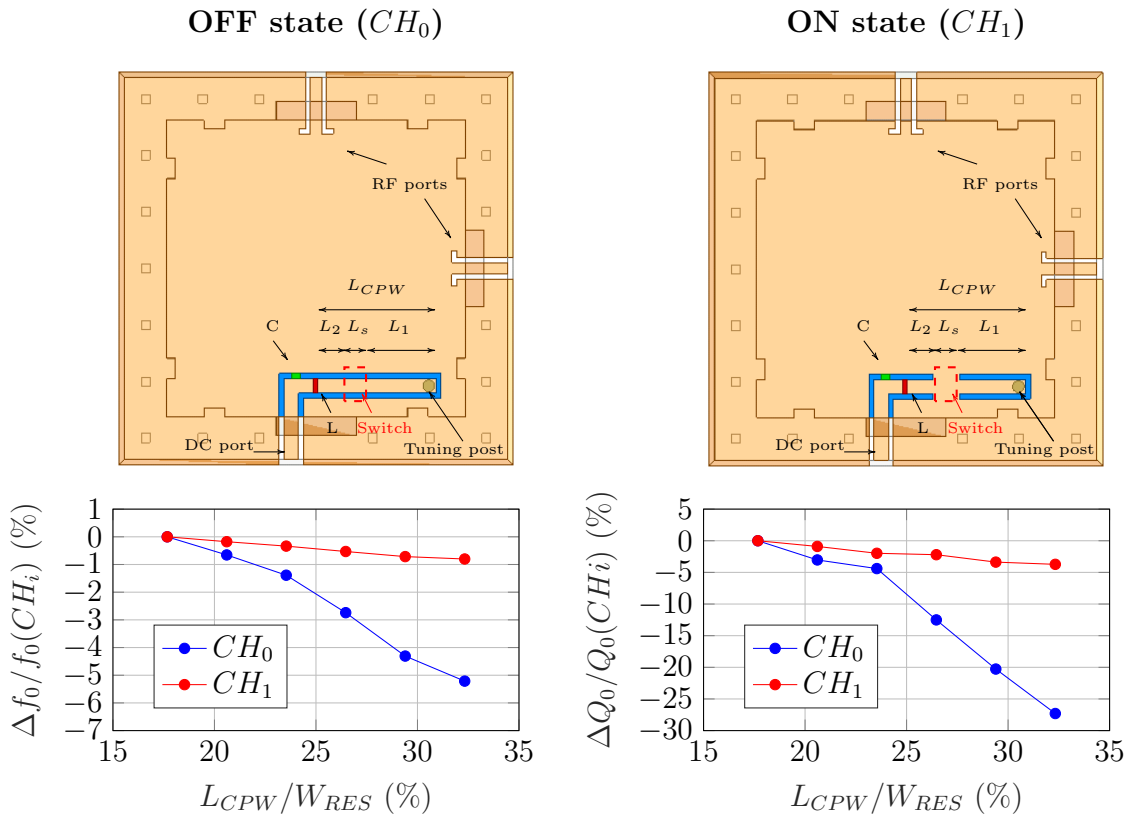


Figure 3.16: Termination line effect on the quality factor and frequency shift for each via post state.

simulations were performed without the switch model to study exclusively the effect of the transmission line on the resonator. Therefore, the switch was replaced by a section of the transmission line in the OFF state (CH_0) and by a short circuit in the ON state (CH_1). The RF path length L_{CPW} between the tuning post and the inductor L has been parametrised between $17.7\%W_{RES} \leq L_{CPWG} \leq 32.3\%W_{RES}$ for the study. The switch position with respect to L has been fixed to $L_2 + L_s = 13.4\%W_{RES}$. In this way, any change in L_{CPW} allows to analyze a line length variation in both states at the same time since it will provoke: a change in the opened line in the OFF state (disconnected post loaded with a transmission line of length $L_{CPW_{OFF}} = L_{CPW}$ ended in an open-termination); and a change in the ON state (via post loaded with a transmission line of length $L_{CPW_{ON}} = L_1$ ended in a short-termination). The minimum line length used as a reference ($L_{CPWG_{min}} = 17.7\%W_{RES}$) was chosen based on the practical limitations imposed by the minimum space needed to place the coupling capacitor C1, the inductor L, the switch and the bond wires on the resonator. The relative channels frequency shift and unloaded Q-factor variation are normalized to the corresponding values of each channel at $L_{CPW_{min}}$. A high f_0 sensitivity to L_{CPW} can be noted in Channel 0 and a fast

decreasing of Q_o as the length is increased. This phenomena results in a frequency shift around 5% with respect to the reference f_0 and an increasing of 4 % in the separation between channels for a length less of one quarter of the resonator size. Furthermore, a reduction up to 26 % of the quality factor can be expected for the same length.

The studied effect can be implemented during the design optimization process as an extra variable to accomplish with the tunable filter specifications. However, as a design rule the tunable resonator prototypes developed in this work will implement the minimum CPW line length to avoid decreasing the quality factor down to values that may compromise the non-compliance with the specifications established for this design. As it can be seen in fig. 3.16 the DC port was placed next to the closest resonator edge to minimize the metal surface engraving and reduce the radiation losses. The features of this prototype will be presented in the following section.

3.5.2 Resonator prototypes

The development of a mixed EM/circuit simulation model that takes into account all the components and loss sources that conform the tunable resonator system, as well as a necessary understanding of the design parameters effect on the electromagnetic behaviour lead to the implementation of several 3-D printed integrated devices scenarios. In microwave filters design the quality factor is one of the most important parameters. During the technology evaluation, this parameter has been constantly monitored to discard the scenarios that could not fulfill the required specifications. The conservation of the Q-factor will be taken as a premise to propose different approaches. As a general guideline the proposed prototypes can be classified in the following categories:

1. All the surface-mounted devices (switch, self inductors, capacitors) integrated in the resonator (Level 1).
2. All the devices placed in the carrier board.
3. Part of the devices integrated in the resonator (Level 1) and part in the carrier board.
4. Multiple switch connections.

Six tunable resonator designs (fig. 3.17) were proposed to explore their advantages and drawbacks. Each prototype implemented an approach of the aforementioned categories using as a basis the structure introduced in the previous section.

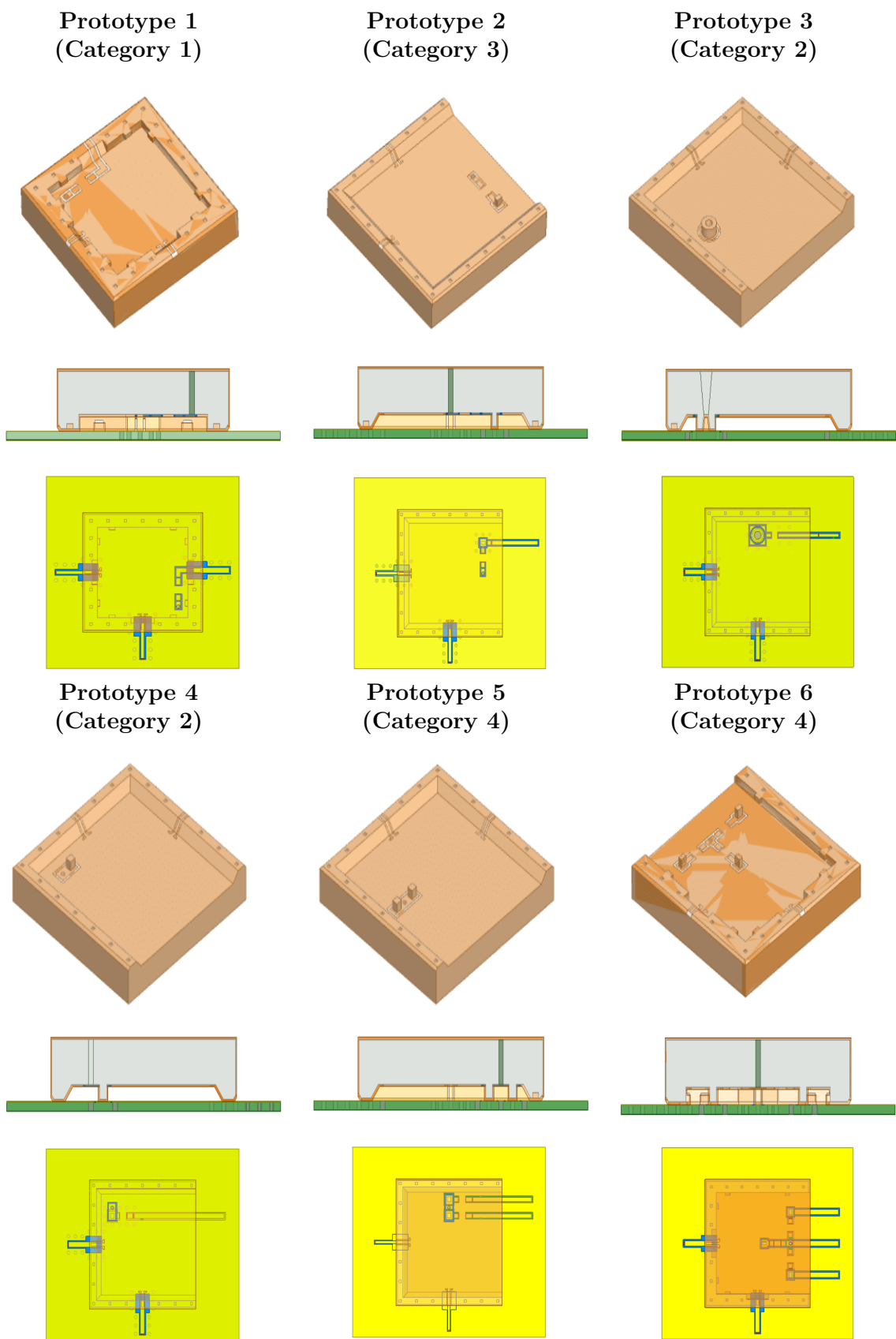


Figure 3.17: Suggested 3-D printed tunable resonator prototypes.

The first prototype (P1) integrates the p-i-n diode switch and the bias network assembled to the resonator. A L-shaped interconnection line layout was designed to provide the shortest path and the minimum metal surface engraving. All the DC and RF mounting pads were placed on the resonator edges.

In the second prototype (P2), the RF network was kept in the ceramic device but the DC bias tee was placed on the carrier board. The connection between both circuits was performed through a vertical bump. The ramps and the electrical connection (Level 2) on one of the resonator edges was removed to let the DC feed line go underneath the device.

The third and fourth designs (P3 and P4) were designed with the intention to study the second category. Both of them are similar to the second prototype, nevertheless, the whole control network is assembled onto the carrier board and connected to the tuning post through vertical bumps. In the case of prototype 3, the bump is a hollow cylinder placed on top of the via to shorten the electrical path between the post and the switch. The cylinder can be seen as an extension of the tuning post with a conical hollow shape to facilitate the inner metallization of the via and the bump. On the contrary, prototype 4 implements a solid parallelepiped bump located next to the post.

Prototype 5 and 6 (P5 and P6) implement several switches connected in parallel as analyzed for multiple post connections. This approach has a double function: to implement multiple connections providing more channels, and to investigate the quality factor enhancement in a 2-state tunable device by reducing the parallel parasitic resistance of the control network. The fifth design is a variation of prototype 4 with two switches placed on the carrier board. Prototype 6 is a mix between the first and second design with three switches where all the devices were placed in the resonator and the DC connections are carried out with vertical bumps.

In the cases, a regular cube hole array was included on the edges of the bottom face (Level 2) to place soldering paste or tin solder balls inside. Two versions of each prototype with conical and cylindrical tuning posts were contemplated to guarantee a correct plating inside the via.

Prototype	1	2	3	4	5	6
Vertical transition	No	Yes	Yes	Yes	Yes	Yes
Control network	Integrated	Partially integrated	On board	On board	On board	Integrated
Switches	1	1	1	1	2	3
Qo enhancement	No	No	No	No	Yes	Yes
Area (mm^2)	13.48 x 13.66	15.36 x 15.56	15.49 x 15.7	15.36 x 15.56	15.36 x 15.56	15.36 x 15.56

Table 3.4: Tunable resonator prototypes features comparison.

Prototype		$\Omega_0(CH_0)$ (MHz)	$Q_o(CH_0)$	$\Omega_0(CH_1)$ (MHz)	$Q_o(CH_1)$	Δf_0 (MHz)
w/o bond wire	1	-227	269	209	179	436
	2	-222	129	1	92	223
	3	-242	294	162	68	404
	4	-246	294	66	159	312
	5	-123	345	137	167	261
	6	-203	301	63	230	266
w/ bond wire	1	-214	219	183	170	397
	2	-246	121	-104	75	142
	3	-305	251	151	47	456
	4	-264	228	96	130	360
	5	-151	283	152	119	303
	6	-215	181	108	156	323

Table 3.5: Simulated surface-mounted resonators resonance frequency, quality factor, and frequency shift between two states (Δf_0) with and without bond wire parasitics for channel 0 and 1.

A summary of the proposed prototypes features can be found in Table 3.4. Moreover, simulations of the surface-mounted prototypes were carried out with and without bond wire parasitics (Table 3.5) in order to foresee the performances to be expected once the devices were manufactured. As it can be seen, the Q-factor in CH_1 is usually lower than in CH_0 presumably owing to the losses generated during the current density flow along the RF path. The quality factor is increased in CH_0 for those cases where the control network is placed on the board and the resonator engraving is reduced. However, as mentioned in Section 3.5.1, the longer extension of the RF path in some cases with vertical connections have an impact on the performances (designs 2, 3, 4 and 5). Additionally, no enhancement can be noticed in the Q-factor of filters with multiple parallel control networks (design 5 and 6) when compared to their single control network version (prototypes 4 and 5, and prototypes 1 and 6). It should be remarked that these results were obtained by synchronizing the switches to the same connection/disconnection state. Nevertheless, multiple channels can be implemented by combining the switches individually. Finally, a degradation on the Q-factor and an impact on the resonance frequency of the channels is observed when considering the bond wire model in the simulations (Table 3.5). From now on, the frequency will be specified as $\Omega = f - (f_i + \frac{BW_{op. band}}{2})$. For the sake of clarity, figure 3.2 is reproduced again in fig. 3.18. In order to address this problem, we try to reduce the contact resistance in the gold bond wire interface by implementing a gold layer on the carrier board and the resonator to match the material compatibility and facilitate the welding.

All the simulated devices were considered for a fabrication run to cross-check the

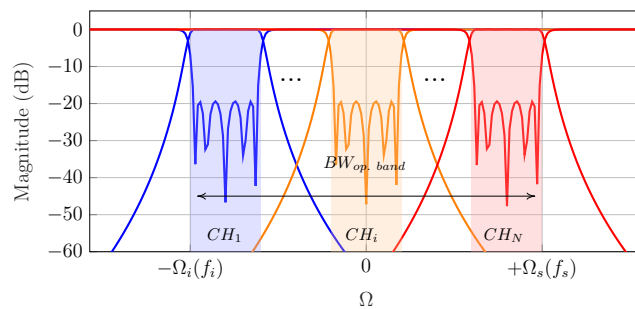


Figure 3.18: Normalized frequency spectrum in the tunable filter operating band.

simulated behaviour to experimental results, address the major difficulties related to the overall manufacturing process of each prototype, and determine the best choice for a potential filter design.

3.6 Manufacturing process

The six prototypes introduced for the study of different integration scenarios were fabricated to verify the compliance between the simulation environment, the models assessment and the experimental results. This is a necessary step to be checked before the design of a monolithic tunable filter developed with this approach. Furthermore, the compatibility of the process materials can be tested as well as the identification of fabrication constraints and the versatility of ceramic 3-D printing processes for the realization of the necessary geometrical shapes. The process can be subdivided in two: the fabrication of the monolithic ceramic resonator, and the carrier board. Each part consist of:

1. Ceramic resonator
 - (a) Ceramic SLA 3-D printing process.
 - (b) Metal plating.
 - (c) Gold electrolysis treatment.
 - (d) Patterns laser engraving.
 - (e) Surface-mounting of p-i-n diode switches and discrete components.
 - (f) Switch die wire bonding.
 - (g) Electrical verification of the correct operation of the control circuit.
 - (h) Solder paste or tin balls placement on Level 2 surface.
2. Carrier printed circuit board
 - (a) Vias layout carving with a milling machine.

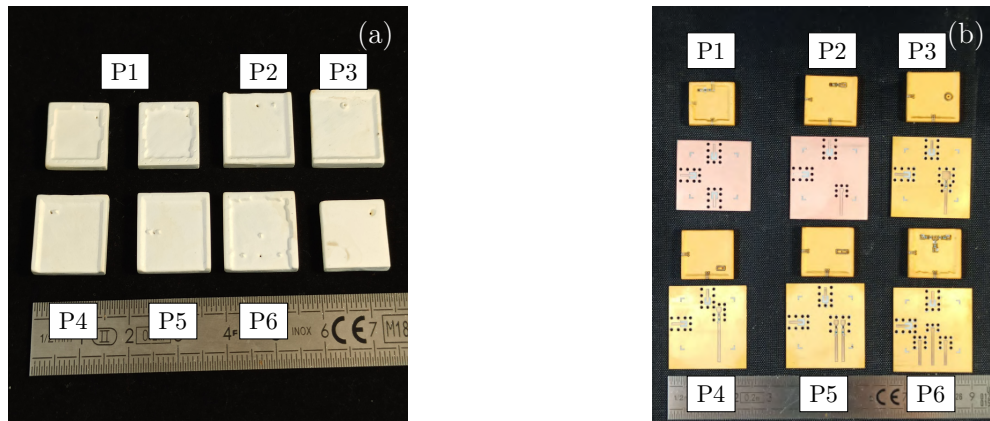


Figure 3.19: Manufactured 3-D printed ceramic resonators and PCB carrier boards without metallization (a) and metallized with all the components surface-mounted before the final assembly (b).

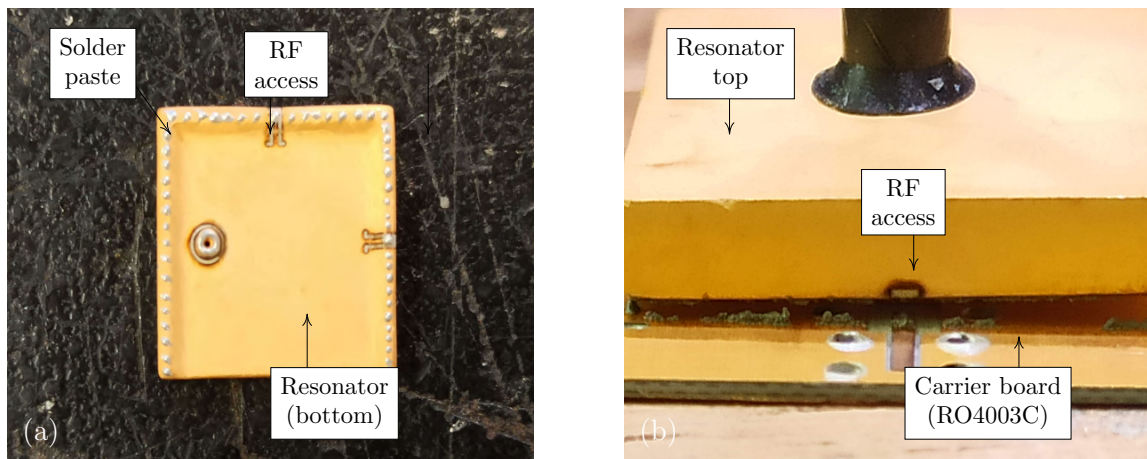


Figure 3.20: Tunable resonator (Prototype 3) solder paste deposition (a) and device assembly with a pick and place machine (b).

- (b) Vias metal coating with electroless process.
 - (c) Gold electrolysis treatment.
 - (d) Circuit layout carving with a milling machine.
3. Both
- (a) Resonator alignment and placement on the carrier board with a pick and place machine.
 - (b) Device welding in a temperature controlled oven.
 - (c) Tunable resonator on-board measurements in a probe station.

The monolithic ceramic parts printed after the end of step 1.a with the SLA additive manufacturing are shown in figure 3.19.a. Figure 3.19.b depicts the finalized prototypes and their respective PCB boards before the assembly. It should be noted the difference

between the PCBs before the electrolysis step and those protected with gold. Figure 3.20 illustrates the solder paste placement inside the device pockets (step 1.h) and the resonator assembly with a pick and place machine (step 3.c). The solder paste used for the prototype's first generation assembly was an alloy Sn63/Pb37 with a low melting point (138 °C). Nevertheless, it is recommended to substitute its use for a lead-free solder paste compatible to spaceborn applications. More details about the steps carried out during the manufacturing processes are given next.

3.6.1 Monolithic ceramic resonators fabrication

The manufacturing process starts with the utilization of 3-D printing stereolithography process (fig. 3.21) using Alumina to build the devices [96], [97], [108], [193]. Other high-performance technical ceramics such as, silicon nitride and beta-tricalcium phosphate could be also used with this process. The design CAD model is exported to industry mechanical formats such as IGES or STL and imported in the printer software. Then, the design is subdivided or sliced in printing layers whose thickness depends on the specific printer. The SLA process principle consist of the slurry paste preparation by mixing the ceramic powder, resin and an initiator sensitive to UV light. The photosensitive paste is stored in a tank inside the machine and spread towards a mobile support plate with a scraper. The support plate moves in the z-direction in equidistant steps equal to the layer thickness. In every step, the paste is exposed to an UV laser light which position in the xy-plane is controlled by a galvanometer mirror. The regions of the paste in contact with the laser are then polymerised forming the sample shape. At the end of the process the part is cleaned in order to remove structural supports or non-polymerized slurry. A debinding process is applied to the device in a furnace with oxygen-containing atmospheres to remove the additives and the organic components present in the ceramic paste. The sintering process is used to compact the ceramic particles by exposing the part to temperatures up to 1800 °C over a long period of time.

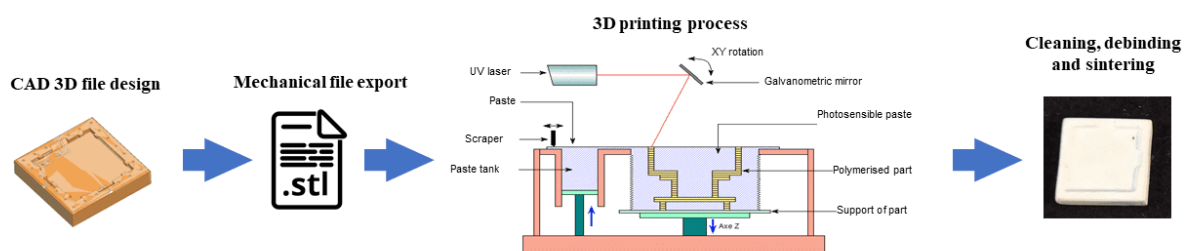


Figure 3.21: Ceramic 3-D printed stereolithography manufacturing process flow.

A good optimization of the part orientation is fundamental for a successful fabrication. Some shapes could suffer deformations depending how the structure is printed. Furthermore, auxiliary supports are usually required to contain overhanging structures during the process. The tunable resonator parts were printed from the so called top face placed on the support plate to the bottom face (Level 2) and no supports structures were required for their fabrication. However, this technique was implemented in the devices developed in Chapter 4.

The manufactured devices were carried out in a SLA process with a fabrication tolerance of $100\ \mu\text{m}$. A staircase effect could appear in ramps and holes as a product of the layer-by-layer fabrication method [79], [193]. Special attention must be taken to avoid discontinuities between the ramp layers metallization as a consequence of this structure termination. Additionally, the metal layer removal during the laser engraving could be hindered if the effect is very pronounced. As a rule of thumb, as higher the ramp slope the less evident the staircase profile.

3.6.2 Metal plating and gold coating

Two methods were considered for the ceramic surface treatment previous to the resonator primary coating layer taken into account the processes compatibility: a copper electroless and a silver spray deposition [194]. The main difference between these two methods is the maximum metal layer conductivity possible to be achieved and the complexity 3-D metallization.

Unlike other processes such as, chemical vapour deposition (CVD) or physical vapour deposition (PVD), chemical deposition with electroless copper process is a simple method to homogeneously coat complex 3-D objects [195]–[197]. No external power supply or electrical current is required in this process to perform the material deposition on the target. Moreover, since the part is immersed in a solution with a constant moving flow it is possible to achieve an uniform metallization of complicated areas such as the vias holes of our designs. This method has been widely utilized in XLIM's projects to metallize polymer-based and ceramic-based microwave devices. A complete description of the electroless copper flow can be found in [195].

Several metallization tests were performed in XLIM's laboratory facilities with electroless copper process in order to estimate the typical metal layer conductivity obtained with the latest products suggested by the industrial supplier for ceramic materials. The tests were carried out in Alumina substrates with a variety of surface roughness aver-

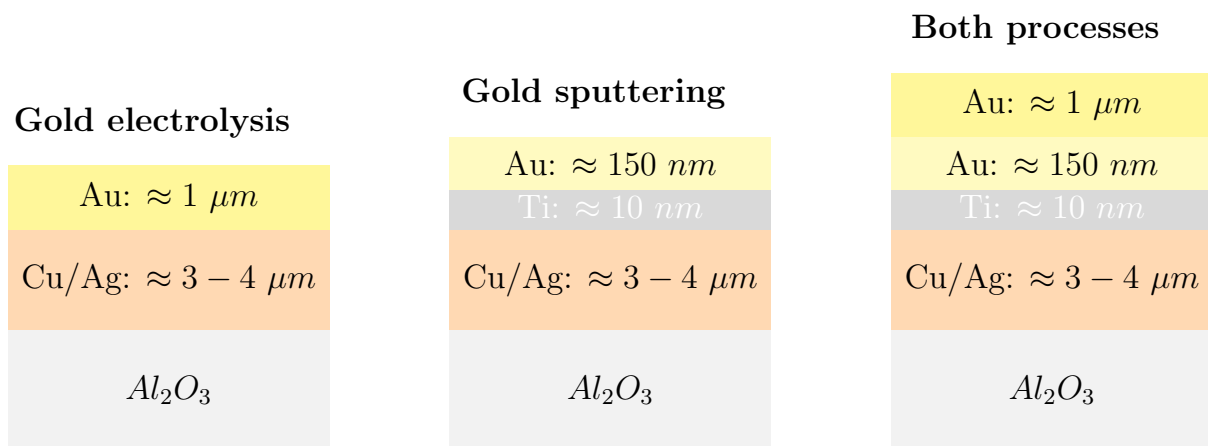


Figure 3.22: Metal stack layers deposited with gold coating processes.

age values characterized with a profilometer. Furthermore, the process was tailored to guarantee a proper copper adhesion and layer deposition between 3 and 4 μm . Conductivity values between $6 \text{ S}/\mu\text{m} \leq \sigma \leq 27 \text{ S}/\mu\text{m}$ were calculated implementing a resonant cavity technique [194] for substrates with a surface roughness range between $289 \text{ nm} \leq Ra \leq 411 \text{ nm}$. However, the average values were concentrated around 16 - 20 $\text{S}/\mu\text{m}$.

The aerosol silver deposition is a technology developed by Jet Metal® [198] which consists of the utilization of an oxidant and reducing agent solution to perform an oxido-reduction reaction. The two aqueous solutions are sprayed into the substrate at room temperature and ambient pressure to coat the 3-D object. The desired metal thickness is achieved by controlling the amount of deposited layers. Once the process is finalized the reaction is stopped using deionized water and dried with compressed air. This process has been exploited for the metallization of most of the ceramic devices developed in this thesis owing to their higher conductivity, leading to a better quality of microwave devices. The typical characterized conductivity in ceramic resonators was around 30 $\text{S}/\mu\text{m}$. Regarding the metal thickness, the same value as in electroless process was implemented to ensure a good coating of the ramps.

The deposition of a protective gold layer is desirable to avoid oxidation of the copper/silver coating and to provide a better compatibility with wire bonding machines and to improve the welding to the board. This step was performed with two plating processes to compare the adherence of the material and to determine the best method to be used: gold sputtering and gold electrolysis (shown in fig. 3.22).

On the one hand, the sputtering process allows to have a very good control of the deposition parameters and the layer thickness. Nevertheless, it is usually a long procedure, it requires a clean room, a costly setup, and the metallization is done on one side at the time. On the other hand, the layer thickness in gold electrolysis can be finely controlled once the setup is well characterized, it requires a few minutes to deposit hundreds of nanometers and is cheaper than sputtering.

The sputtering-metallized resonators were only coated on the face in contact with the SMD components (bottom face) and finished with gold electrolysis. The devices exposed to gold electrolysis were completely plated. A successful application was observed in both cases. A stack of Titanium (10 nm) and Gold (150 nm) was implemented in the case of gold sputtering to enhance the adherence to the silver layer. On the other side, a gold layer thickness of $1 \mu\text{m}$ was deposited on the device with gold electrolysis.

The protective layer demonstrated a remarkable improvement in the bond wire soldering process in comparison to naked copper/silver tests. Nonetheless, the bonding pads show a fragile adherence that is exposed when a welded SMD device or gold wire is removed. Furthermore, since these pads are isolated from the rest of the metal coating, they are partially thermally isolated. This virtual isolation hinders the surface heating during the bonding process. Since no specific advantage was observed between the different gold coating tests in terms of adherence or surface quality of the deposited layer, gold electrolysis was implemented in the majority of the devices owing to the simplicity of the process and the reduced time required in comparison to gold sputtering.

3.6.3 Printed shapes characterization

A verification of the three main 3-D structures (ramps, parallelepiped and hollow-cylindrical bumps) was conducted by means of a digital microscope in order to determine the constraints and design limitations that current ceramic SLA processes could impose in these particular cases. The comparison between the CAD design and the actual fabricated results may serve as useful information for the development of future designs. As it can be seen in figure 3.23, the measured profiles exhibit rounded borders and irregular shapes. In principle, the fabricated dimensions roughly matches with the design. In the case of the ramp, a 37° slope was measured in the structure instead the 45° slope of the design. The measured height difference between Level 1 and 2 with respect to the design is of $\Delta H(L2 - L1) = 33 \mu\text{m}$. Additionally, the interconnection pad placed on Level 2 exhibit a poor flatness. However, the most important aspect could be pointed out towards the vertical bumps height mismatch. These structures

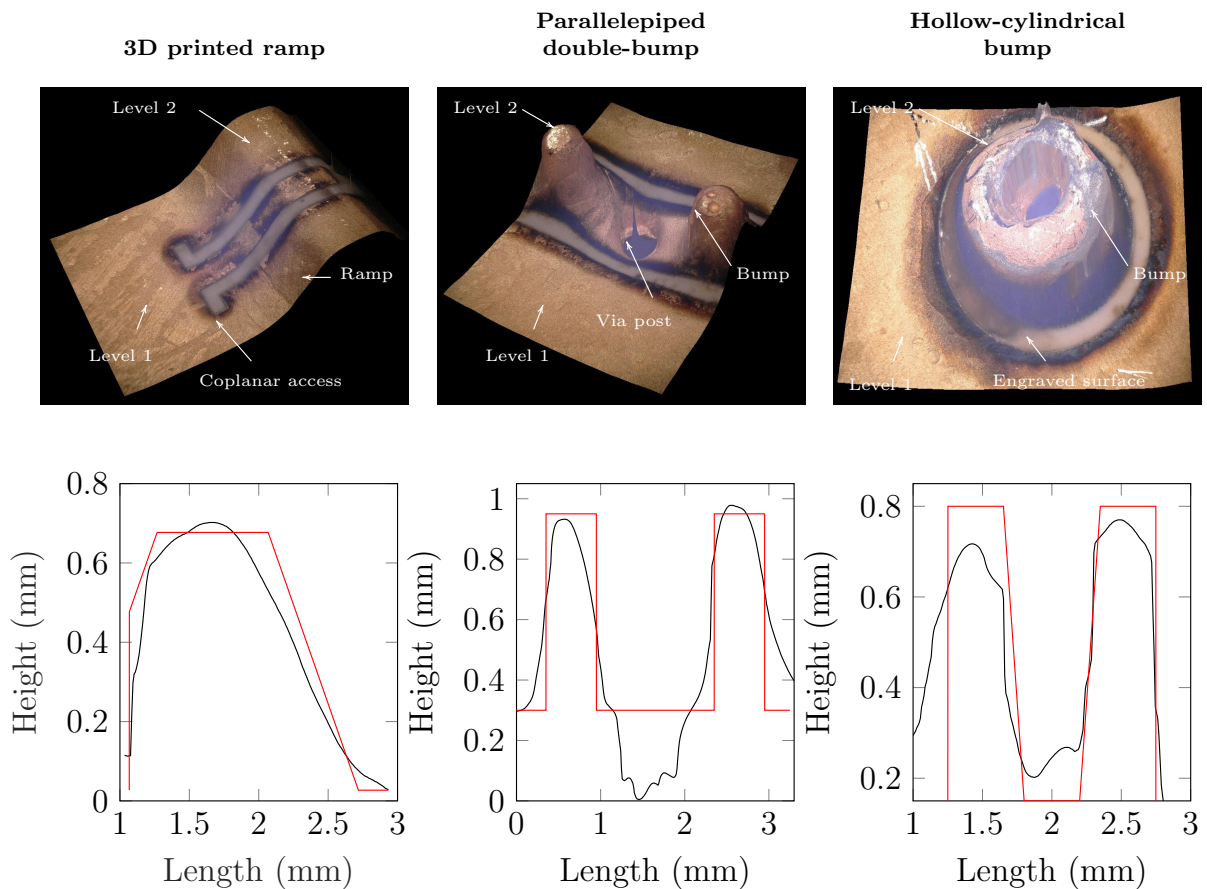


Figure 3.23: 3-D scanned profiles of ramps and bumps manufactured with ceramic SLA. The ideal design profiles are highlighted in red to facilitate the comparison.

are conceived to function as the connection links between the board and the resonator. Therefore, a high reduction of their size introduces a gap that could cause an electrical disconnection of the device during the assembly. The size difference can be attributed to several factors: an excessive rounding of the bump edges, the manufacturing tolerances inherent to the process and a underestimation of the object shrinkage in the z-direction during the sintering process. The estimated air gap between Level 2 and the bump surface was $30 \mu m \leq G \leq 83 \mu m$. This gap was filled with solder paste to ensure the connection during the device assembly.

Although major deformations can be observed in the structures, the cylinder and via holes show a good agreement with the expected dimensions and a good metal coating inside. Finally, it should be remarked the neat layout engraving of the metal surface carried out in the irregular 3-D objects. No major complications or short circuits were detected in the coplanar lines.

3.7 Experimental validation of manufactured devices

Owing to the large amount of steps required to manufacture the devices, intermediate verification procedures were implemented in order to identify fabrication failures and correct or minimize errors.

The first verification procedure is performed at the end of step 1.d (see Section 3.6) to search for short-circuits or disconnections that could occur as a consequence of an insufficient laser engraving penetration depth or unsatisfactory metal layer thickness (e.g. excessive staircase effect on ramps). The proceeding is carried out with DC electrical measurements and visual verification with a digital microscope.

The resonator is tested once again when the control network is soldered to the device and the switch die is bonded. In this case, the circuit is biased with an external source associated to DC probes and the resonator accesses are connected to a two ports vector network analyzer (VNA) by means of GSG RF probes (fig. 3.24.a). The devices are measured and tuned to verify the proper operation of the tuning control circuit. During a correct operation scenario the device consumes a forward bias DC current of $I_{DC}(forward) = 10 \text{ mA}$ and $V_{DC}(forward) = 1.3 \text{ V}$, while for reverse bias these values are around $I_{DC}(reverse) \ll -1 \text{ mA}$ and $V_{DC}(reverse) = -2.5 \text{ V}$.

Once the tuning tests show that the device is operative, the component is assembled to the PCB and ready to be measured from the carrier board using the same measurement setup as in the previous test (fig. 3.24.b).

Furthermore, a peltier cell and a temperature sensor were included into the setup to effectuate thermal characterization analysis at ambient pressure.

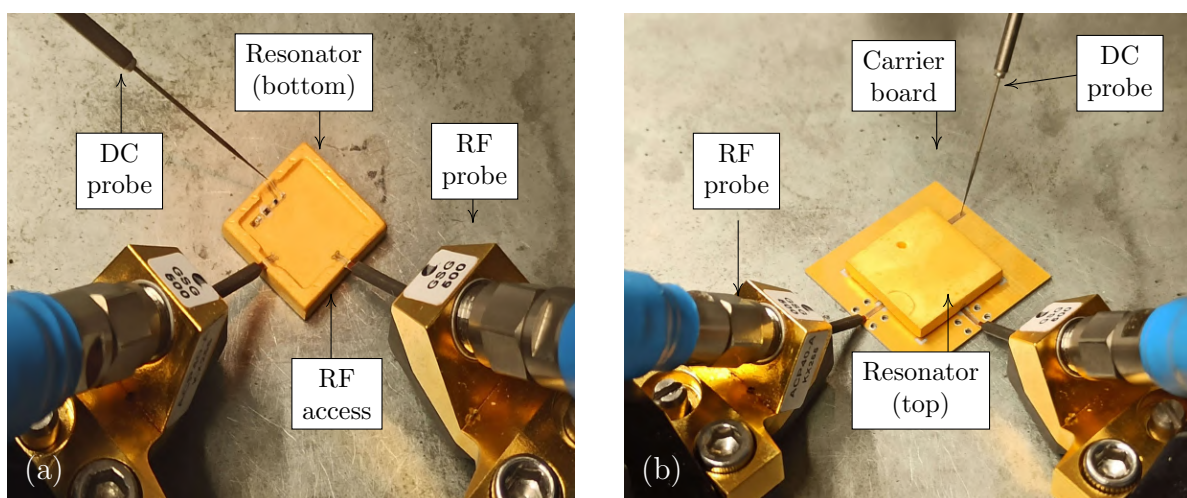


Figure 3.24: Tunable resonator functioning tests performed (a) before and (b) after the assembly onto the carrier board.

3.7.1 Measurement campaign at room temperature

All the prototypes were directly measured on the resonator at room temperature (fig. 3.24.a) and then again on the board after the assembly (fig. 3.24.b). Some devices without the integrated control network such as, prototypes 3, 4 and 5 were switched manually with a wire during the first measurement to experimentally assess the resonator quality factor without the influence of external parasitics.

The analysis of experimental data summarized in fig. 3.25 shows that:

- in **prototype 1** the measured scattering parameters are in good agreement with the behaviour expected from simulations. Both channels show a frequency shift of $\Delta f_0(CH_{0_{sim}} - CH_{0_{meas}}) = +33 \text{ MHz}$ and $\Delta f_0(CH_{1_{sim}} - CH_{1_{meas}}) = +86 \text{ MHz}$ with respect to simulations. The measured tuning ratio was (1.09:1), whereas the simulated tuning range was (1.11:1). The difference in resonance frequency can be attributed to a material permittivity mismatch that may vary within the manufacturing tolerance range. In this design it is not possible to discern between the resonator Q-factor and the control network added losses. Nonetheless, measurements performed before the resonator assembly onto the board exhibit a Q-factor of 114 and 178 for CH0 and CH1, respectively. Measurements of the soldered device performances expose the degradation driven by new sources of losses during the assembly. The impact of their effect on channel 1 is remarkable.
- in the second prototype (**prototype 2**) the difference between the simulated and measured resonance frequency is more notorious than in the previous case ($\Delta f_0(CH_{0_{sim}} - CH_{0_{meas}}) = +121 \text{ MHz}$ and $\Delta f_0(CH_{1_{sim}} - CH_{1_{meas}}) = +173 \text{ MHz}$). On the other hand, the measured tuning ratio is (1.04:1) versus (1.03:1) for the simulated results. Pre-assembly measurements (on resonator) are not possible in this case owing to the bias tee network is placed on the PCB. The expected quality factor for this design is rather low, probably due to the added losses introduced by the extended DC feed line and the vertical transition. Moreover, the low transmission level (S_{21}) is driven by an excessive gap and a deficient connection between the resonator mounting pads and the board transitions.
- in the case of prototypes 3, 4 and 5 all the tuning devices are placed on the board. Therefore, the unloaded quality factor of the engraved resonators can be directly measured. The results exhibit a maximum unloaded Q-factor of 483, 534 and 282 for resonators 3, 4 and 5 when measured before their assembly and with the via post disconnected. The Q-factor is reduced from channel 0 to 1 when

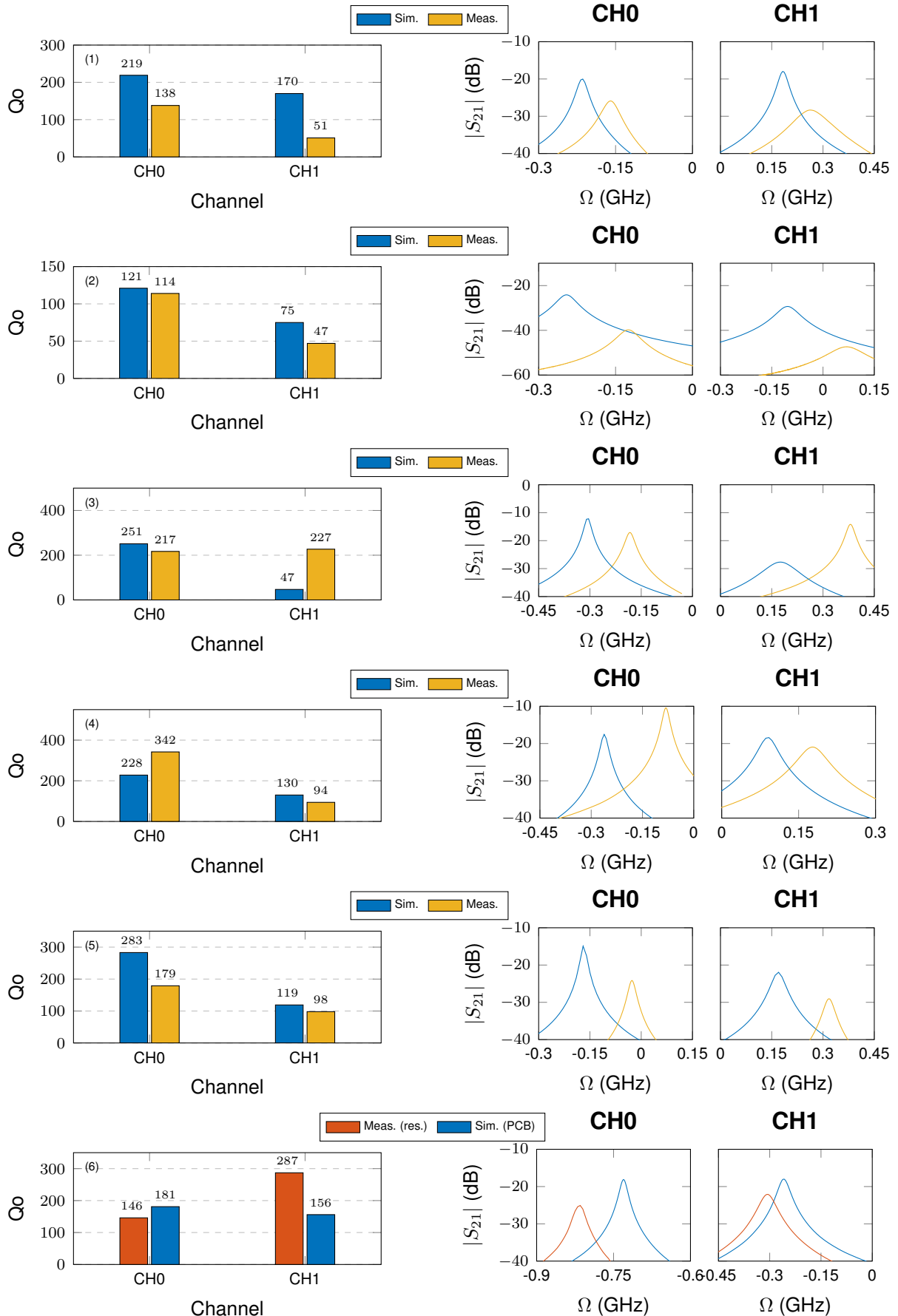


Figure 3.25: Measured Q-factor and frequency shift for the six prototypes (1 to 6) tested before and after the device assembly onto the carrier board.

manually connecting the via post with a wire, as a result of the current density flowing through the via. Additionally, the performances decrease even more when measured from the carrier board with the operative control network. Once again, the same tendency as in the other prototypes of the channel's resonance frequency placed at higher frequencies is found in the measured samples.

- the prototype 5 shows no particular improvement with respect to the single p-i-n diode version (prototype 4) in terms of quality factor but its application can extend the number of channels up to 3. In the case of prototype 6, the complexity of the assembly of three p-i-n diodes and their associated control networks could lead to several sources of errors and complications during the final placing on the carrier board. No specific conclusions could be obtained from this case. However, direct on-resonator measurements shows the maximum quality factor feasible to be obtained. It can also be noted that f_0 is located at lower frequencies in both channels as a consequence of the shortened via path when measured directly on the resonator. Nevertheless, the channels should be relocated at the correct frequency once assembled.

Although the shift exhibited by all prototypes studied in this section, the simulations seems to predict the resonators behaviour quite well. However, the estimation of the quality factor differs from measurements mainly due to the multiple sources of losses introduced by the manufacturing imperfections such as, the conductive epoxy glue and solder paste contact resistance, the air gap between the resonator and the board produced by irregularities on the printed structure. Furthermore, in the designs where the devices are placed on the board (see prototype 3, 4 and 5) the simulations overestimate the losses.

Prototype 3 shows the best results in terms of quality factor thanks to the design focused on shorten the via post path and the reduction of the resonator engraving layout. However, the deformation of the hollow cylinder bump requires a good control of the soldering paste to ensure the electrical connection and at the same time avoid short-circuiting the line.

In regard to the assembly, the alignment procedure in the first prototype was easier than in the rest of the designs thanks to the location of the RF and DC ports on the edges of the resonator, thus facilitating the visual verification. The utilization of vertical transitions inside the resonator could lead to short circuits if the alignment is not accurate enough and if the resonator deformations are too extreme. Additionally, bumps and RF mounting pads alignment in same connection plane (Level 2) introduces a constraint

hard to achieve with this technology. Otherwise, the device tilting could lead to the disconnection of one or multiple ports.

3.7.2 Thermal characterization

The characterization of the frequency dependency with temperature is an essential analysis to establish the operation range of the devices working under harsh conditions. The tunable resonators were exposed to a simple thermal cycle study to foresee the component response in terms of electrical behaviour and mechanical constraints as it could be desoldering of the device or other problems related to temperature. The maximum operating temperature of the system is established by the switch around 125 °C. A measurement campaign was carried out using Prototype 3. The device assembled to the carrier board was exposed to three thermal cycles which consisted of the device heating from room temperature ($T_{min} = 23\text{ °C}$) and $T_{max} = 70\text{ °C}$ and cooling back to room temperature in steps of $\Delta T = 5\text{ °C}$. The setup consisted of a peltier cell, a controlled temperature source, a temperature sensor, a VNA and a probe station. Figure 3.26 illustrate the results obtained in one thermal cycle. Both channels show a sensitivity to temperature of $\Delta f_o(T) = -364\text{ kHz/°C}$. However, the degradation of the quality

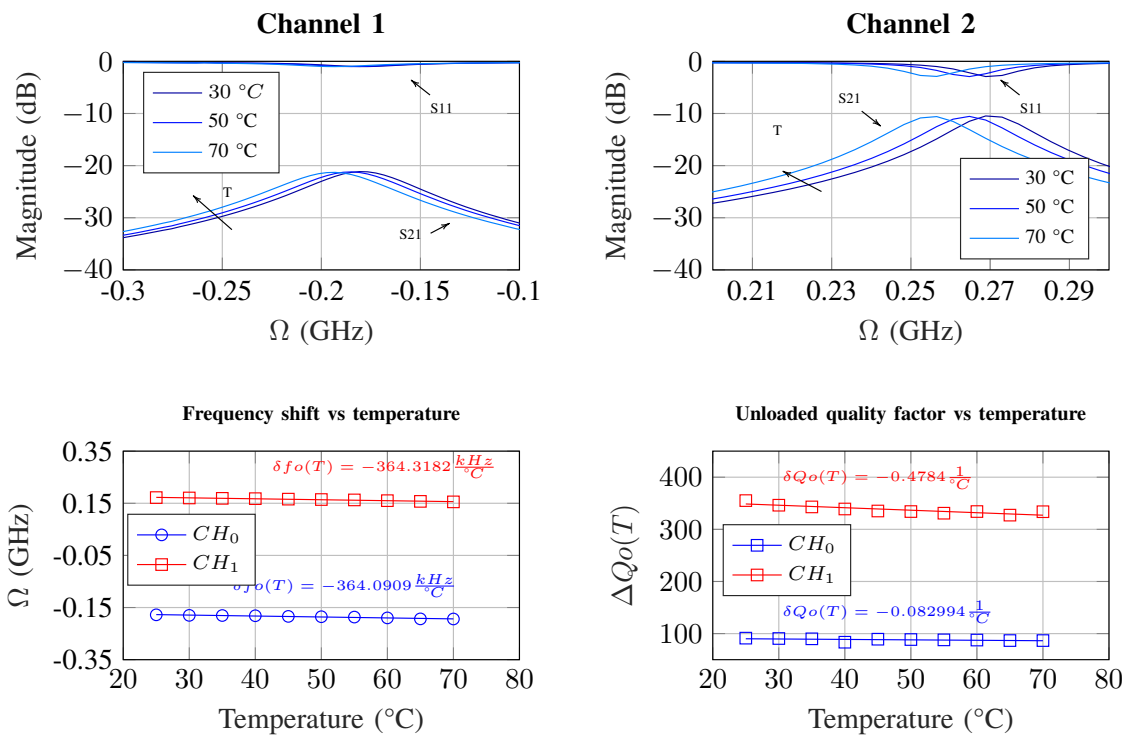


Figure 3.26: Measured and simulated S-parameters (S_{21}) and Q-factor of Prototype 3.

factor seems to be steeper in the channel with higher Q (CH1). Concerning structural or assembly problems, no particular damage was detected on the resonator metal surface nor the soldered joints after three cycles. This observations were confirmed with electrical measurements since no changes were observed in the frequency response.

3.8 Envisioning a monolithic 2-state tunable filter

The scenarios investigated in the electrical simulations realm and in the manufacturing domain served to provide a better insight of the advantages and the limitations encountered in the six proposed approaches. Based on these results, a 2-state tunable filter was designed implementing a 4-pole Chebyshev topology. The filter was synthesized using an arrow topology whose resulting target coupling matrix is shown in equation ??.

$$M_{filter} = \begin{bmatrix} 0 & 1.04 & 0 & 0 & 0 & 0 \\ 1.04 & 0 & 0.91 & 0 & 0 & 0 \\ 0 & 0.91 & 0 & 0.70 & 0 & 0 \\ 0 & 0 & 0.70 & 0 & 0.91 & 0 \\ 0 & 0 & 0 & 0.91 & 0 & 1.04 \\ 0 & 0 & 0 & 0 & 1.04 & 0 \end{bmatrix} \quad (3.6)$$



In order to perform the physical filter structure, the resonators were placed in an square-fashion arrangement with the RF ports facing each other. The inter-resonator couplings $m_{12} = m_{21}, m_{23} = m_{32}, m_{34} = m_{43}$ were performed with inductive irises. The irises size was calculated by performing the even- and odd-mode analysis [199], [200] in the EM simulator and obtaining the dimension-dependent coupling law. This method consists of the frequency split of an electromagnetically coupled system into two modes (even and odd) comprised of two resonators synchronized at f_0 . Equation 3.7 depicts the calculation of the normalized coupling coefficient M carried out with this method, where f_0 and BW are the center frequency and the ripple bandwidth of the filter, and f_e and f_o are the resonance frequency of the even and odd mode. Usually, the odd mode is found at higher frequency than the even mode for inductive coupling.

$$M = \frac{f_0}{BW} \frac{f_o^2 - f_e^2}{f_o^2 + f_e^2} \quad (3.7)$$

Furthermore, the external coupling Q_e can be calculated with equation 3.8 in the 3-D full-wave simulator, where f_0 is the resonance frequency of the coupled resonator and $\Delta f_{\pm 90^\circ}$ is the frequency at $\pm 90^\circ$ phase shift from f_0 .

$$Q_e = \frac{f_0}{\Delta f_{\pm 90^\circ}} \quad (3.8)$$

Resonators based on prototype 1 were selected for the implementation of a first filter design owing to simulations proved to be the most accurate between all the prototypes (in terms the channels frequency location in the frequency spectrum), and to avoid alignment difficulties and vertical bumps short-circuits. The via posts were located in the only corner without a direct connection to the inductive irises to avoid undesired modifications of the inter-resonator couplings and enough space to place the control network. The design integrates all the functionalities implemented in prototype 1: flip-chip device with ramps, printed via hole, integrated control network, and solder paste pockets (fig. 3.27). The optimized C-band filter footprint measures 24.81 mm x 27.02 mm x 2.5 mm. In order to simplify the manufacturing difficulties of a very first prototype, the design was not intended to provide a tunable bandwidth but to accomplish the specifications only with the resonance frequency tuning. Consequently, the bandwidth of one of the channels will be wider than then other because of this limitation. The specifications were achieved as shown in figure 3.28 by optimizing the numerous resonators, irises and control network design variables in the optimizer. The optimization stage was implemented by applying the methodology developed in [201]. It should be mentioned that in order to properly perform this procedure, it is mandatory to optimize both channels

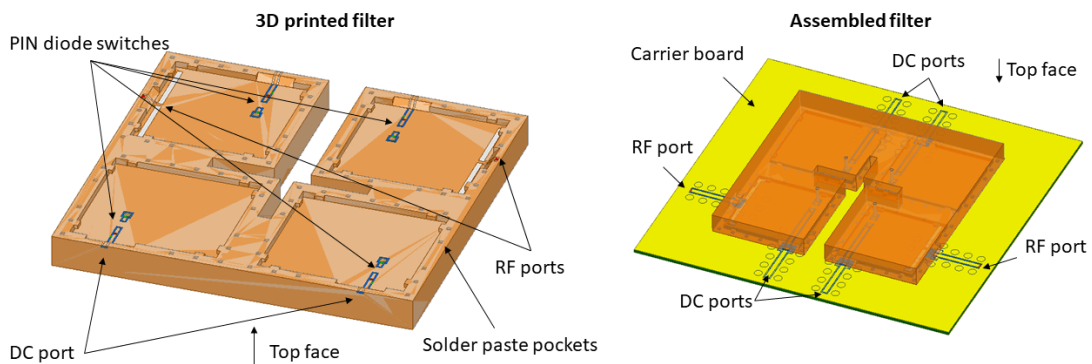


Figure 3.27: 2-state tunable filter design. The tuning method is based on prototype 1.

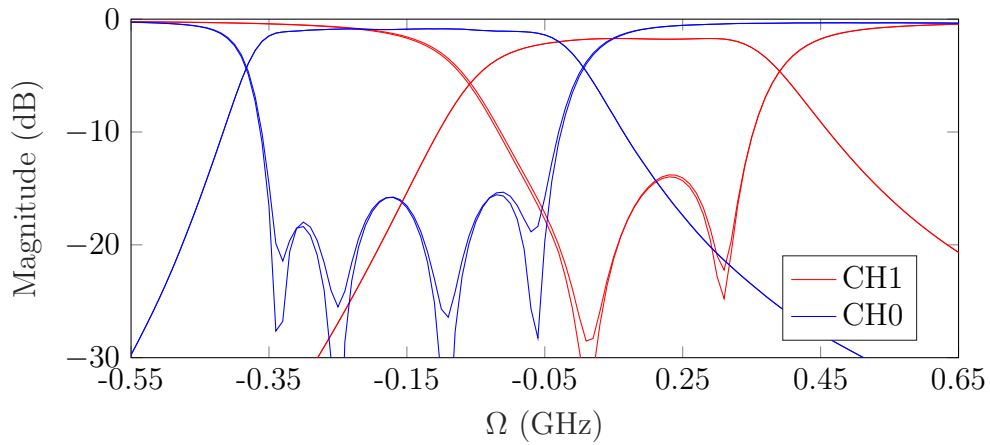


Figure 3.28: Tunable filter simulated S-parameters.

at the same time to address the effect of every tuned variable in the filter. With the resulting quality factor from measurements the minimum filter mismatch within the pass band was set to $|S_{11}(CH_0)| = -15 \text{ dB}$. The simulated S-parameters show total losses of $|S_{21}(CH_0)| = -0.88 \text{ dB}$ and $|S_{21}(CH_1)| = 1.76 \text{ dB}$ within the band. The effective filter quality factor estimated was $200 \leq Q_{eff} \leq 400$ and the tuning range was designed to be (1.08:1).

The coupling matrices extracted from the simulated S-parameters show the trade-off between the channels to accomplish with the target matrix by only switching the center frequency. The matrices were normalized to the target filter bandwidth $FBW = 7.1\%f_0(CH_1)$ and to the respective target center frequency of each channel.

$$M_{filter(CH_0)} = \begin{bmatrix} 0 & 0.99 & -0.06 & 0.02 & 0 & 0 \\ 0.99 & 0 & 0.92 & -0.08 & 0 & 0 \\ -0.0 & 0.92 & 0 & 0.76 & -0.08 & 0 \\ 0.02 & -0.08 & 0.76 & 0 & 0.96 & -0.06 \\ 0 & 0 & -0.08 & 0.96 & 0 & 1.01 \\ 0 & 0 & 0 & -0.06 & 1.01 & 0 \end{bmatrix} \quad M_{filter(CH_1)} = \begin{bmatrix} 0 & 1.21 & -0.06 & 0.03 & 0 & 0 \\ 1.21 & 0.42 & 0.99 & -0.10 & 0 & 0 \\ -0.06 & 0.99 & 0 & 0.74 & -0.10 & 0.04 \\ 0.03 & -0.10 & 0.74 & 0 & 0.99 & -0.06 \\ 0 & 0 & -0.10 & 0.99 & 0.43 & 1.21 \\ 0 & 0 & 0.04 & -0.06 & 1.21 & 0 \end{bmatrix}$$

Concerning to the manufacturing process, the monolithic ceramic filters can be fabricated following the process detailed for the tunable resonators. The accuracy of the printed parts can be enhanced by implementing the observations made during the resonators printing. Moreover, the complexity of vertical bumps is removed in this design, thus avoiding connection problems during the assembly. In addition, tolerances can be improved by mixing a more costly but more precise state-of-the-art SLA printing process ($100 \mu\text{m}$) and a post-fabrication machining step. Tests carried out in several samples

Sample	Dimension			
	X (mm)	Y (mm)	Z (mm)	Via diameter (mm)
Reference	24.81	27.02	2.50	0.5
1	24.69	27.03	2.57	0.503
2	24.66	27.02	2.54	0.502
3	24.68	27.02	2.58	0.505
4	24.68	27.06	2.57	0.505
5	24.69	27.06	2.54	0.507
Average	24.68	27.04	2.58	0.504
Difference	-0.13	+0.02	+0.08	+0.004

Table 3.6: Tunable filter samples tolerance comparison. The printed devices were exposed to a milling process to enhance the structure tolerance and definition.

exhibit a better definition than previous devices. A comparison between the target design and the manufactured parts are shown in Table 3.6. Figure 3.29 illustrates the manufacturing steps of a dummy device realized in order to test the process modifications and to address the overall results.

The samples were metallized with copper electroless and aerosol silver deposition in order to test the two metal coating processes exhibited in section 3.6.2. Both approaches were covered with a simple 1 μm gold layer deposited with electrolysis. The SMD components assembly onto the filter also yielded an improvement thanks to the better manufacturing quality. Nonetheless, adherence problems were detected on the resonator metal layer after applying a mechanical stress on the welded devices, partially lifting the metal lines. Furthermore, even though the wire bonding process

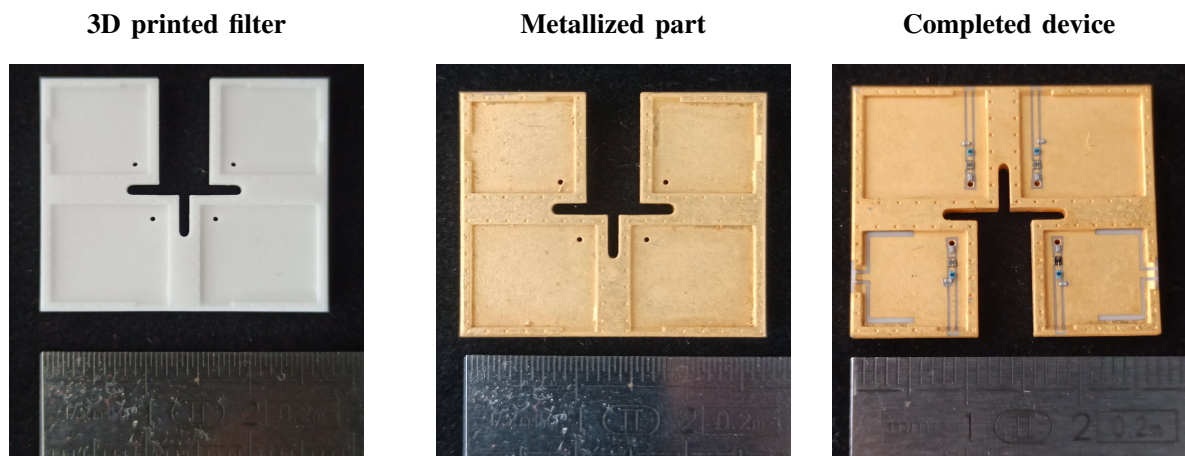


Figure 3.29: All the manufacturing steps of a SMT monolithic ceramic tunable filter.

was realized more easily as a result of the better surface termination, the air gap of the engraved coplanar lines still isolates the pads and hinders the heat transmission from the heating plate in the wire-bonding machine.

On the other side, short-circuited lines were found on the ramps in some samples as a consequence of the staircase effect product of the printing process. Although the good definition of the laser machining engraving this problem is difficult to remove without an over-etching of the resonator.

It is evident that the complexity and the extensive number of steps required for the development of these devices poses a challenge to finely control the manufacturing parameters in a custom fabrication process. However, the experience obtained from the analysis, design and fabrication of SMD monolithic tunable devices introduced along this chapter could be utilized to be implemented in an industrial environment where the all parameters can be better monitored.

3.9 Conclusions and perspectives

In this chapter, the integration of heterogeneous technologies was investigated in the frame of sub-6 GHz communication applications. The project was faced from the point of view of 3-D printing technologies to leverage their flexibility for the conception of surface-mounted system-on-package microwave tunable filters. Moreover, the access to high-tech ceramic materials developed in research institutes in Limoges, as well as their interesting mechanical, electromagnetical and thermal properties, among others, motivated the utilization of ceramic stereolithography as the main thread for the exploration of many integration scenarios.

On the one hand, the realization multiple-band devices such as filter banks usually demands a large space and weight in the system board; an undesirable fact in the majority of cases. On the other hand, the implementation of tunable filters, either by mechanical movable parts or electrical reconfiguration present great performance constraints in every channel, especially as the frequency range increases. The study of an hybrid scenario could leverage the advantages of both approaches, miniaturizing the component size and maintaining the channel performances.

A widely used method to perform electrically-tuned filters is done with varactors. However, the parasitics introduced by these devices usually increase the losses and degrade the quality factor. Another interesting technique proposed in the bibliography is related to the utilization of a controlled magnetic field effect generated by a via post inside the cavity resonator. Demonstrations show higher Q-factors than with the former varactor

technique. Nevertheless, the majority of the examples reported by the researchers were SIW devices fabricated in organic PCB.

We focus our efforts on the development of a 2-states filter (ON/OFF) as part of the basic building block required for the creation of a complex hybrid tunable filter bank operating in the C-band.

The theoretical study of the channel specifications set a limit to the possible materials to be used depending on the amount of channels. Even though, Alumina seems to be a good candidate to fulfill the requirements thanks to their good electrical permittivity and low losses. However, special attention must be taken to keep the good performances of the system once the device is integrated with the tuning control circuit.

A very first simulation campaign carried out in HFSS helped to observe the impact of the tuning effect on the fundamental and spurious modes, and understand the capacitive and inductive nature produced by the short-circuit or isolation of the via. This two effects lead to a frequency shift of the mode towards opposite directions, thus increasing the tuning range. On the other side, the augmentation of the number of via connections also lead to an increase of the current density and an increase of the inductive effect. Hence, this effect can be leveraged to implement extra channels with lower frequency range between them. In addition, a spurious mode was observed in the OFF state in thick ceramic materials. To the best of our knowledge this mode that could greatly affect the upper filter stop band was not reported in other works. Most likely, the spurious resonance frequency was hidden at higher frequencies owing to the PCB permittivity used in SIW (at least three times lower than in the materials studied in this thesis). We understand that the nature of this resonance is introduced by the tuning post resonance frequency capacitively coupled to the cavity resonator. Moreover, RF line length associated to the via control network was another key parameter found that loads the tuning post modifying the final result.

The investigation of the design variables influence in the frequency shift and the quality factor shed some light to the identification of coarse and fine tuning parameters, and the available range covered by all of them. We consider this as a fundamental piece of information that facilitates the design and optimization tasks.

The multi-variable tuning study performed with EM simulations was contrasted in a cavity resonator manufactured in a Rogers substrate. Furthermore, the control circuit carried out with a SPST p-i-n diode switch was tested in a separated board to check the feasibility of the manufacturing steps needed in the laboratory facilities. Additionally, the results obtained served for the de-embedding of the bond wire frequency response, the consequent modelling and the lumped elements extraction of the network. The extracted

model in addition to the p-i-n diode switch Touchstone files led to the implementation of the most important effects in a mixed EM/circuit simulation environment of the overall tunable resonator structure.

This mixed simulation model was the main tool for designing several flip-chip tunable resonators approaches that could be manufactured in a 3-D printed process. The six prototypes proposed were intended to analyse different aspects of the tuning effect and the device assembly: a complete integration of the system parts on the flip-chip resonator; a separation between the resonator structure to minimize the losses and the control network placed on the carrier board below the device; the RF circuit integrated on the resonator and the DC bias tee on the board; and multiple switches connected in parallel to reduce the parasitic losses. Ramps and bumps with different geometries were designed to perform the component mounting pads and realize the interconnections between the different elements. Pockets were also implemented around the resonator contact surface to contain the solder paste and enhance the ground connection.

In order to validate the fabrication process, 30 samples were printed with ceramic SLA and subjected to different metallization processes (copper electroless, aerosol silver deposition, gold electrolysis and sputtering). The parts showed a good coating, both inside the vias as in every other part of the structure. Even more, the laser engraving process exhibited a good efficiency to finely remove the metal layer in flat as inclined surfaces. Concerning the SMD devices assembly, the low melting point solder paste matched well with the ICs and the resonator coating maximum temperatures. However, the thickness was not monitored which may result in an excessive contact resistance. The wire bonding of the switch die was another challenge to overcome owing to the irregularity of the resonator printed surface and the deficiency of heat transmission from the resonator isolated engraved lines that hinder the wire melting. Several tests were realized to adjust the machine parameters and solve this inconvenient for these particular prototypes.

The assembled resonators exhibited a constant shift with respect to simulations owing to the the combined effect of the permittivity mismatch and the manufacturing tolerances. However, in general terms the channels behaviour seems to be in good agreement with the model. The quality factor shows a variety of results where in some cases the degradation is overestimated and in others is underestimated. This fact manifests the challenges of modelling the multiple sources of losses lead by the custom fabrication process (air gaps, deficient ground connection, inaccurate alignment, excessive solder paste deposition, etc.). However, based on the previous results, we can conclude that:

- the control network split in two parts (RF on the resonator and DC on the carrier board) shown in prototype 2 leads to poor quality factors as a consequence of the extension of the RF line from the via to the board.
- the control network fully integrated on the resonator exhibit quality factors between 100 and 200 but the assembly is a critical aspect that could drastically reduce the performances. The same implementation with three switches in parallel (prototype 6) could help to increase the channel's Q-factor at expense of more costly devices.
- the placement of the whole control network on the board reduces the resonator engraving thus increasing the quality factor. The connection path shortening between the via and the network could provide good results as it was observed in prototype 3 ($200 \leq Q_o \leq 300$). Prototype 4 shows an imbalance between the quality factor of both channels, where one of them is higher than 300 and the other is less than 100. The combination of two switches (prototype 5) seems to slightly equalize this problem.

The tunable resonator performances can be also enhanced with the use of RF MEMS switches instead of the p-i-n diode switch reducing extra losses, intermodulation distortion and power consumption.

The scenario analysed in prototype 1 was chosen as a candidate for the development of a first version of a tunable filter owing to the relative ease of the device alignment and assembly thanks to the possibility of visual verification of every port during the process. The actions taken to enhance the printed part finishing with a post-fabrication machining were translated into an easier assembly of the SMD components on the resonator and bond wire welding. However, a weak adherence of the metal layer to the resonator was also noted. Although, the fabricated part shows a correct definition of the structure and the designed dimensions.

For future prototypes it is suggested the implementation of printed pockets to contain the switches, removing the bond wires and replacing them with aerosol jet printing technique to perform the interconnection lines. This technique was investigated in several research projects and could introduce the needed improvements for the development of 3-D printed monolithic tunable filters. Finally, the implementation of under development low-loss thermal stable ceramic materials could improve the channels thermal stability caused by temperature drift in order to be applied in telecommunication applications working in harsh conditions such as in satellite payloads.

4

Bulky 3-D printed ceramic microwave devices

ADDITIVE manufacturing (AM) emerged as a promising technology exponentially growing during the last decade in many industry sectors such as automotive, aerospace, military, medical and electronics, among others [65]. The increasingly demand of microwave devices, mainly due to the popularization of 5G communications encouraged the exploration of new ways to conceive electronic devices. The implementation of massive Multiple-Input Multiple-Output (MIMO) beamforming systems [36], [126], Internet of Things (IoT) applications [14], [24], and the deployment of nanosatellite constellations [32] demands low-cost highly-integrated hardware [49]. AM could be utilized as a new approach to replace traditional manufacturing processes. Different perspectives were explored thanks to the continuous advancements in 3-D printing technologies [76]. The realization of complex geometrical structures in one single piece extends the manufacturing flexibility, simplifies the assembly procedures and encourages the arise of innovative solutions. Additionally, the selective layer-by-layer fabrication minimizes process wastes and reduces the production time. The high versatility of available materials in addition to the good fabrication accuracy achieved by modern 3-D printers motivated the utilization AM for the conception of innovative RF

devices before unthinkable [79].

Exceptional work has been done towards the implementation of 3-D printing technology in microwave applications. Several multifunction (electrical, thermal or structural) designs were developed driving to miniaturized and lighter components. Monolithic band-pass filters, orthomode transducers, directional couplers and horn antennas are some examples of microwave devices reported using Stereolithography (ceramic and photopolymer resins), and Selective Laser Melting (metals) processes[202]. Inkjet and Aerosol Jet Printing technologies were also used for printed electronics such as interconnection lines, planar circuits and antennas on flat flexible substrates and 3-D surfaces [67], [189], [191], [203]. There is a particular interest to integrate heterogeneous technologies in printed circuit boards (PCBs) to provide novel functionalities or improved features at subsystem level. Furthermore, massive MIMO beamforming transceivers are usually developed in printed-circuit boards [44], [48] as shown in figure 4.1. These transceivers could also implement metal shielding structures to reduce possible interferences and improve the channels isolation.

Efforts were made towards the fabrication of 3-D printed multi-chip modules (MIMs) and the integration of embedded devices [204]. These modules could be directly printed with the PCB or assembled onto a carrier substrate using surface mount technology (SMT) [205] as a more traditional solution. There are many examples in the bibliography of SMT cavity microwave components mostly manufactured with traditional methods [206]–[213] and some 3-D printed devices [214] that implements monoblock filters assembled in an

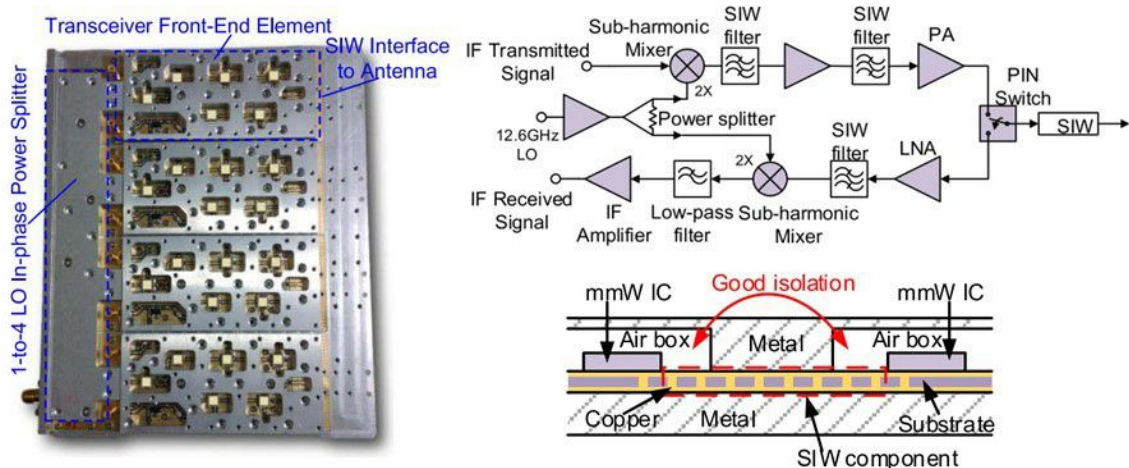


Figure 4.1: 5G MIMO beamforming transceiver board and mm-Wave front-end schematic circuit [44]. Auxiliary metal structures are utilized to electromagnetically isolate the different regions of the system.

horizontal-fashion position onto the carrier board. These bulky devices provide higher quality factors and power handling than planar devices directly integrated in the PCB. Owing to their good electromagnetic properties, ceramic-filled cavity devices are an interesting option for hyper-frequency applications, specially in microwave bands where good performances and compact dimensions are required. Microwave filters with relatively good quality factors and temperature stability could be developed with low-loss ceramics commercially available in SLA processes and thermally compensated dielectrics under development. However, the actual ceramic printing resolution allows the fabrication of better defined structures operating at higher frequencies. Most of the designs found in the literature leverage the 3-D printing capabilities to build compact monoblock devices in a 2D-fashion [105], [106]. To the best of our knowledge, the development of fully 3-D SMD ceramic components and their integration with heterogeneous technologies has not been widely investigated. Massive MIMO beamforming transceivers could be an interesting target application for this technology since these systems are usually developed in printed-circuit boards [44], [48] as shown in figure 4.1. Metal shielding structures are often utilized to minimize interference and improve channel isolation. In this scenario, additively manufactured microwave devices could be distributed on the

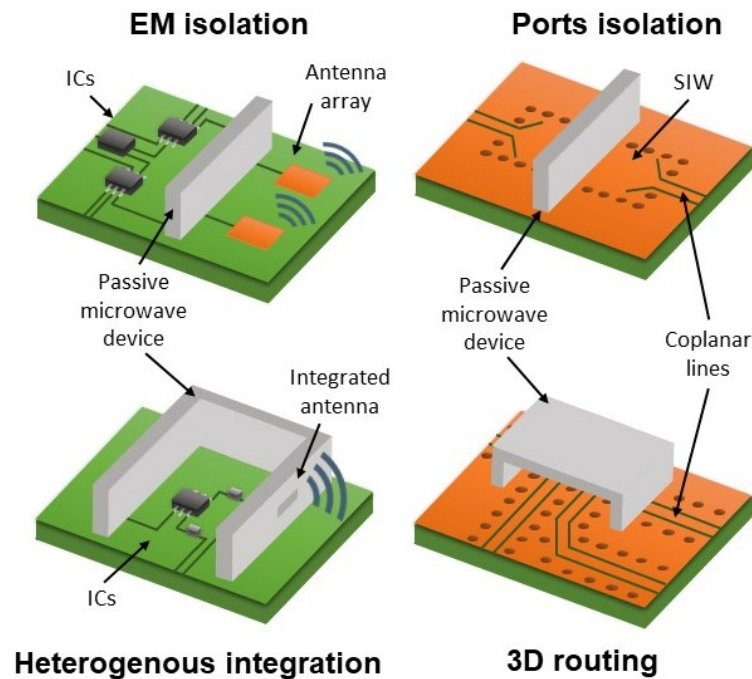


Figure 4.2: Examples of surface-mounted 3-D printed ceramic devices adapted to different scenarios.

RF front-end and adapted to the layout to: facilitate the board floor planing and routing; isolate electromagnetically specific areas; integrate disparate technologies and functionalities in the same space; and reduce the interconnection paths (fig. 4.2). Terrestrial and non-terrestrial communication applications could benefit from this concept, particularly, satellite and nano-satellite payloads where good-performance and compact devices are required. These features could be exploited in RF transceivers [44] to enhance the board layout, improve the system performances and increase the integration. In this chapter, SMD band-pass filters are introduced making use of 3-D printing technologies. The fabricated devices served as a proof of concept to address the manufacturing limitations observed for this approach and to test different scenarios. A transition is proposed for the specific interconnection of coplanar lines to TE_{101} rectangular cavity resonators mounted vertically on a PCB. Laser tuning techniques are used to correct the filter response and overcome the manufacturing dispersion. The obtained results are intended to provide useful information towards the future implementation of complex subsystems embedded in 3-D ceramic microwave devices.

4.1 SLA ceramic devices: previous work

The utilization of additive manufacturing processes to manufacture 3-D printed ceramic microwave devices has been investigated in the laboratory XLIM of the University of Limoges in previous PhD projects [108], [109], [193], [195]. The development of ceramic microwave filters was particularly studied with stereolithography. Fabrication tolerances are a critical aspect in filter design that can limit the application of these AM technologies specially in narrow-band filters. These constrains should be taken into account during the design stage to foresee the feasibility of the project. Many methods have been proposed to compensate the effect of manufacturing tolerances in metal and plastic printed air-filled cavity devices such as tuning screws used to disturb the electromagnetic field inside the filter [215]. Other examples in the bibliography present movable parts that modifies the inner dimensions of the resonators [216]. The optimization of the screws position or movable parts in every cavity is performed with the support of a specialized algorithm [217]–[219]. However, none of these methods fit the needs of ceramic cavity devices. As shown in Chapter 2, laser engraving techniques are usually utilized to selectively remove the metal coating of the devices to create planar patterns. These patterns could be used to generate transmission zeros, interconnect heterogeneous technology devices, create accesses and transitions or to correct the frequency response of a filter [220], [221].

An example of how manufacturing tolerances of ceramic SLA can affect the behaviour of microwave filters can be found in [109], where 3-D printed filters were designed at 40 GHz with low-loss ceramic resins. The tested devices resulted in an unsatisfactory behaviour owing to the AM process tolerances. A laser engraving tuning method was proposed for the correction of ceramic microwave filters to overcome the problems observed in the experimental results. This approach will serve as a necessary strategy to be implemented in this thesis for the integration of more complex 3-D printed ceramic devices potentially useful in scenarios as the ones shown in fig. 4.2.

4.1.1 Laser engraving tuning methodology

The conception of 3-D printed mm-Wave filters was explored in [109] to test the feasibility of SLA ceramic devices at 40 GHz bands. As a result, the process tolerances observed drove to the conclusion that a post production tuning step was required for these technologies. Additively manufactured TM_{110} resonators and filters at 8 GHz were fabricated in [193] to validate a laser-based methodology proposed as frequency tuning strategy. The operating band of the devices under test (DUTs) was shifted to lower frequencies in order to facilitate the samples manipulation and to continue in line with previous works. The tuning methodology consists of the metal surface engraving of specific patterns that cause specific effects on the resonance mode of the component. Coplanar accesses were engraved on the devices metallic surface to be measured and tuned at the same time in a setup comprised of a laser machine, a probe station and a Vector Network Analyser. Figure 4.3 summarizes the tuning process flow developed in [193] for the correction of 3-D printed ceramic filters.

During the first step, the filter is synthesized to determine the topology and number of poles required to satisfy the specifications such as the center frequency, bandwidth, out-of-band rejection and losses within the band, among others. Then, the filter is physically designed in a full-wave electromagnetic simulator. Sensitivity analysis are performed during this step to estimate the feasibility of the device production with the technological process chosen (ceramic SLA in this case).

Once the device is printed, a metal coating is deposited on the surface by means of an electroplating process. Coplanar port terminals are engraved on the surface to finalize the fabrication.

If the measured response does not match with the specifications, the filter coupling matrix (CM_{meas}) is extracted and compared to the initial design to determine the correction required in every part of the structure. The patterns are chosen based on the

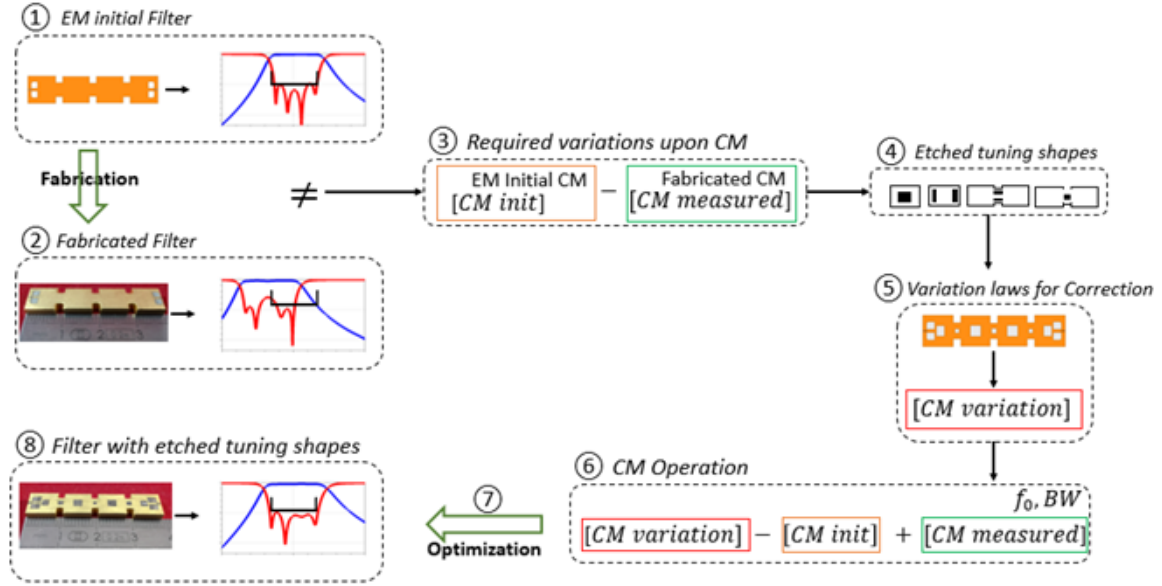


Figure 4.3: Post-fabrication tuning method process flow [193].

study explained in the following Section. The extraction of all the coupling matrices coefficients normalized to the filter center frequency and bandwidth are carried out with a software developed by INRIA called Presto [201].

The required tuning patterns are applied in the reference design EM simulation to assess their effect in the filter response (CM_{init}). The initial size is chosen arbitrarily as starting point and optimized to achieve the filter specifications. The optimization is driven by a sensitivity analysis of the filter behaviour as function of the individual variation of the patterns geometry. Every parameter modification is simulated and extracted by Presto until obtaining a set of N matrices (CM_{var}) that describes the effect of the N pattern modifications on the coupling coefficients in the reference filter.

The variation of the coupling coefficients on the measured filter should be similar than in the case of the reference filter if the corrections are within the method limitations defined in the next section. Hence, in order to associate the variations obtained in the previous stage to the manufactured filter, the reference coupling matrix is extracted to the set of simulated coupling matrices with the variations (eq. 4.1) and added to the measured coupling matrix (eq. 4.2).

$$\Delta CM = CM_{var} - CM_{init} \quad (4.1)$$

$$CM_{meas_{opt}} = \Delta CM + CM_{meas} \quad (4.2)$$

The response of the measured filter with the initial tuning patterns is compared to

the specifications. The patterns dimensions are then optimized by classical methods to fulfill the filter requirements [108]. The inputs utilized for the optimization process are the geometrical variation of the tuning patterns simulated during the previous stage. As a result, the process is optimized until converge to the criteria established by the specifications and the final dimensions of the patterns are obtained. Finally, the optimized patterns are engraved on the sample with a laser. If the method was correctly performed, then the new filter response should be closer to the expected behaviour. The process could be re-started in case of unsatisfactory results and new patterns calculated until achieving the desired specifications.

4.1.2 Laser tuning patterns

Several kind of tuning patterns were analysed to provide the electromagnetic effect required to shift in frequency the resonance frequency of the ceramic cavity or to modify the coupling between adjacent resonators. The impact on the coupling coefficients variation of a filter can be controlled with a proper pattern located in the right position and with the correct dimensions. Table 4.1 depicts the coplanar tuning patterns studied



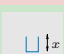

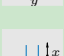
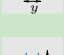
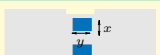
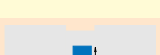
Tuning pattern		Main effect
Square slot		Frequency ↑ as area ↑
Rectangular slot		Frequency ↑ as length ↑
U-shape slot		Frequency ↓ as length ↑
Hairpin-shape slot		Frequency ↓ as length ↑
2 U-shape slots		Frequency ↓ as length ↑
H-shape slot		Frequency ↓ as length ↑
2 Rectangular slots		Coupling ↑ as length ↑
Hole in the coupling section		Coupling ↓ as diameter ↑

Table 4.1: Different coplanar tuning patterns case of study [193].

on TM_{110} single mode resonators and 2-pole filters for the correction of a 4-pole in-line filter. The engraving areas are represented in black and the different colors group the patterns with the same effect. The parameters x and y constitutes the pattern size being x the most sensitive dimension. Electromagnetic simulation results obtained in ANSYS HFSS show a higher sensitivity of frequency shift effect for the square tuning pattern and a lower impact for the H pattern when placed in the center of the resonator. However, the H pattern is more sensitive when shifted towards the edges of the structure. The H pattern can be substituted by a rectangular pattern to avoid high accuracy constraints during the laser engraving, acquiring better performances in terms of frequency shift and quality factor degradation.

The frequency shift effect provoked by these two patterns can be better understood with a study of the EM field. As it can be seen in fig. 4.4, the square pattern strongly interacts with the maximum E field located in the center of the resonator for the mode TM_{110} . In this framework, an effect is caused by the opening on the metal surface that is proportional to the dimension x , driving to an increment of the resonance frequency. On the contrary, the rectangular patterns interacts with the maximum H field located on the sides. A complementary effect can be associated to this case, decreasing the resonance frequency by increasing the length x .

The same principle could be implemented to modify the inter-resonator couplings by applying the square and rectangular patterns on the inductive irises. In this way, the even and odd mode that defines the coupling factor between two resonators [52] can be controlled separately depending on the chosen pattern.

A drawback of this tuning strategy is related to the inherent process of openings on the cavity metal surface. In every case if the corrections required to tune the filter response are too strong, the radiated field through the apertures would decrease significantly the

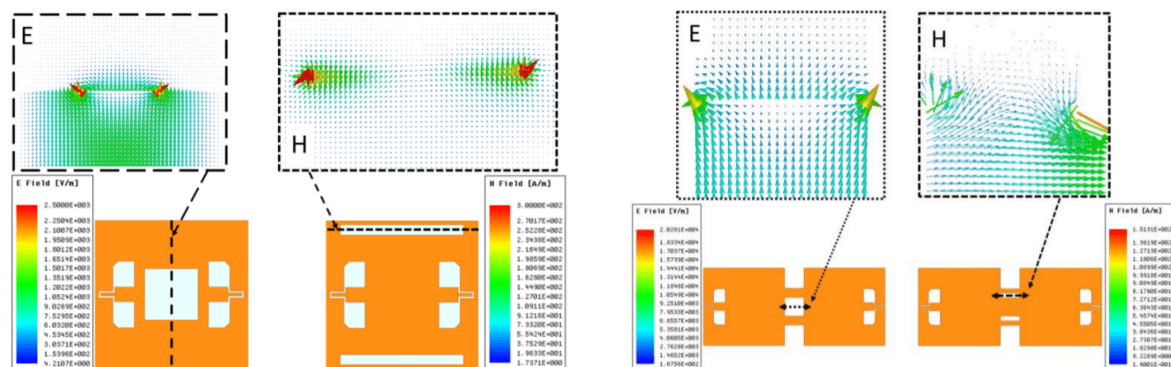


Figure 4.4: Electromagnetic field on the different tuning patters for the case of resonance frequency shift (left) and inter-resonator coupling factor (right) [193].

quality factor. The examples described in [193] show a degradation of 40 % in Q_0 for a frequency shift of 400 MHz for resonators working around 8 GHz, and 78 % in Q_0 for a frequency shift of 270 MHz; both tuned with square patterns. As a rule of thumb for such tuning patterns, compensating a frequency shift higher than the filter bandwidth ($\Delta f_0 > BW$) brings such unacceptable degradation in the resonators Q-factor.

4.1.3 Demonstration of laser tuned 4-pole ceramic cavity filter

The concepts developed for resonators and 2-pole filters were implemented to correct the manufacturing tolerances of a 3-D printed in-line Chebyshev filter. The band-pass filter was designed to operate at 8 GHz with a frequency bandwidth of 350 MHz. The Alumina utilized for the fabrication was developed in the project ATOMIQ [193] and possess an electrical permittivity of $\epsilon_r = 9.1$ and $\tan \delta = 7.10^{-5}$ at 40 GHz. Figure 4.5.a shows the three stages performed after the 3-D printing process: (A) metal coating, (B) laser engraving of terminal ports and (C) laser engraving of tuning patterns. The devices were tested and tuned in a testbench designed for the continuous monitoring of the filter response by means of a VNA and a laser machine. Figure 4.5.b depicts the successful tuning of two filter samples implementing this method. Furthermore, the filter tuning process limitations were identified. Experimental results shows a maximum relative frequency tuning $\Delta f_0 = +5/ - 4\%$ and coupling factor $m = +66/ - 36\%$. A pre-evaluation study is necessary to determine the feasibility of components correction before experimental tuning.

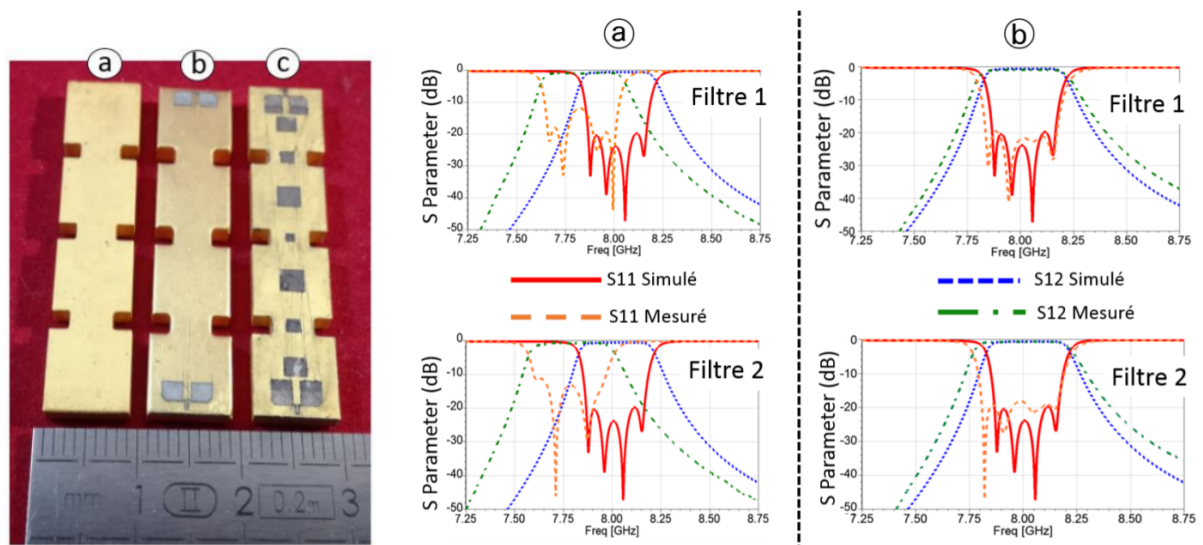


Figure 4.5: Manufactured cavity filters (a). Simulation and measurements of ceramic filters (b): manufactured (A) and tuned (B) device [193].

The successful demonstration of a laser tuning methodology for Alumina-based microwave filter devices manufactured by means of ceramic stereolithography processes served as a motivation on this thesis for the exploration of more complex structures. The in-line filter will be taken as a reference design in the following sections where a similar example is utilized at 9.4 GHz. Fully SMD 3-D folded structures based on this topology are developed to be integrated in the different scenarios described in figure 4.2. Finally, the laser tuning patterns introduced so far will be implemented on the devices to compensate the manufacturing error inherent to AM processes.

4.2 Fully 3-D printed SMD ceramic filters

The implementation of folded structures fabricated with AM techniques could be adapted to different assembly scenarios. Ceramics such as Alumina and Zirconia are commercially available for SLA process [70]. Compact devices can be developed with these materials thanks to their relatively high permittivity. Moreover, a great variety of topologies could be developed by modifying the spatial inter-resonator configuration. Even though a good trade-off between ceramic SLA fabrication tolerances and device miniaturization could be obtained in the X-band, the results of the following analysis could be extrapolated to lower frequency applications.

4.2.1 I/O terminal structure analysis

As mentioned earlier, SMT cavity devices are generally performed in an horizontally-oriented structure such as millimeter-wave crystalline quartz filters shown in [50]. The

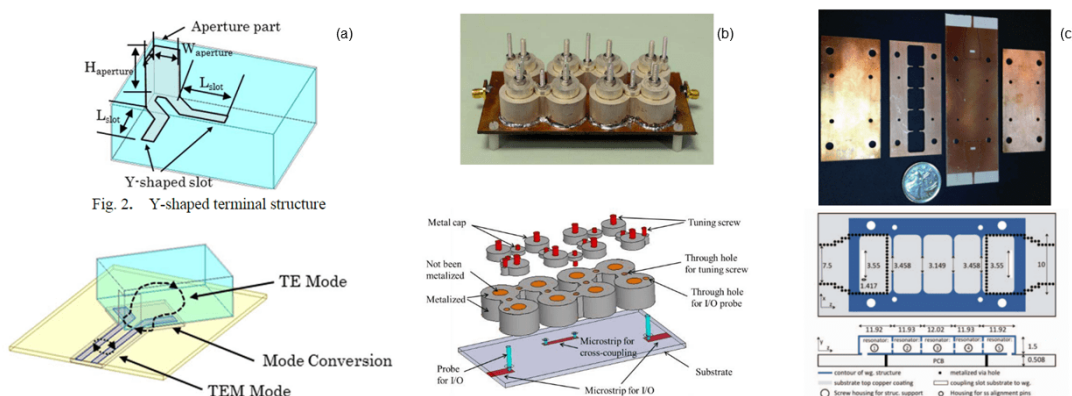


Figure 4.6: SMT I/O terminal port transitions: Y-shaped terminal [50] (a), vertical posts excitation [205] and SIW to SMW transition [211].

resonators excitation is generally carried out through coplanar transitions (fig . 4.6). Several designs have been introduced using asymmetrical Y-shaped terminal for rectangular cavity TEM-TE mode transitions [50], [209], conductive strip lines coupled with microstrip lines or coplanar lines on a PCB [222], I/O vertical posts inside cylindrical cavity resonators fed by microstrip lines [205], [210], or vertical transition vias such as the ones applied in [213] for the connection of a substrate integrated coaxial line filter. SIW to surface-mounted waveguide (SMW) transitions can be also found carried out by means of apertures on the interface [211]. However, these configurations occupies more area on the board and hinders the design of fully 3-D structures. In the fundamental mode TE_{101} , rectangular cavity resonators have a symmetric distribution of the electromagnetic (EM) field with maximum magnitude of magnetic field on the sides. Additionally, no spurious modes are located at lower frequencies, thus facilitating the design. The described features could be leveraged for the development of magnetically-coupled transitions by placing the resonator sideways on a PCB carrier. Furthermore, thanks to the symmetry of the field, the structure could be rotated and placed on any side using the same configuration. Proper transitions are needed to perform the assembly between interconnection lines on the PCB and the ceramic filter terminal ports. In figure 4.7, a magnetically-coupled excitation is proposed for a rectangular resonator with $L_{res} = W_{res} = 7\text{ mm}$ and $H_{res} = 2\text{ mm}$. The transition is comprised of a $50\ \Omega$ CPWG line ($G = 169\ \mu\text{m}$ and $W = 610\ \mu\text{m}$ for a 0.4 mm RO4003C substrate) and terminated in a short circuit to provide maximum magnetic field below the ceramic resonator. Moreover,

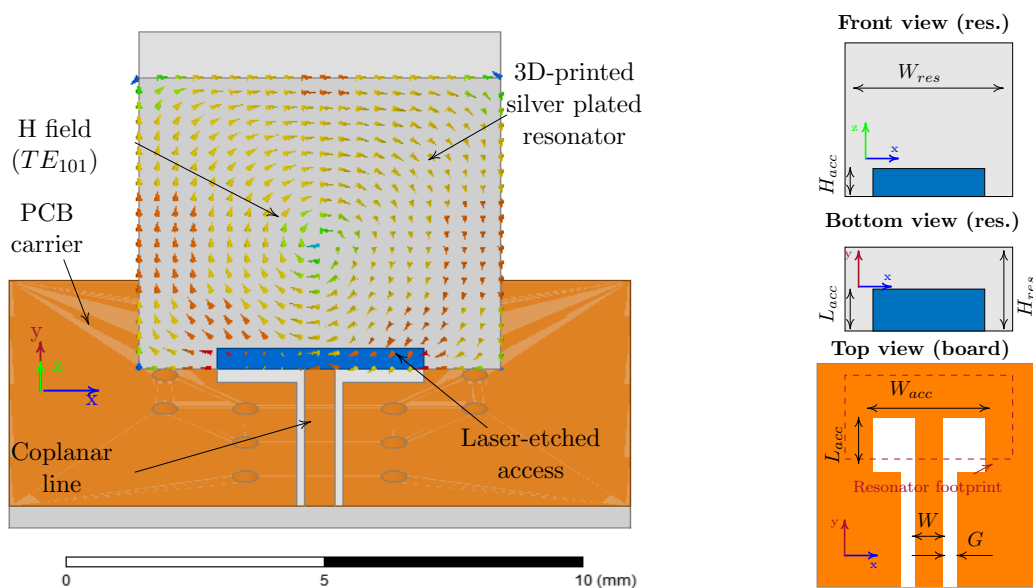


Figure 4.7: Coplanar to TE_{101} cavity resonator transition: magnetic field and surface-mount assembly.

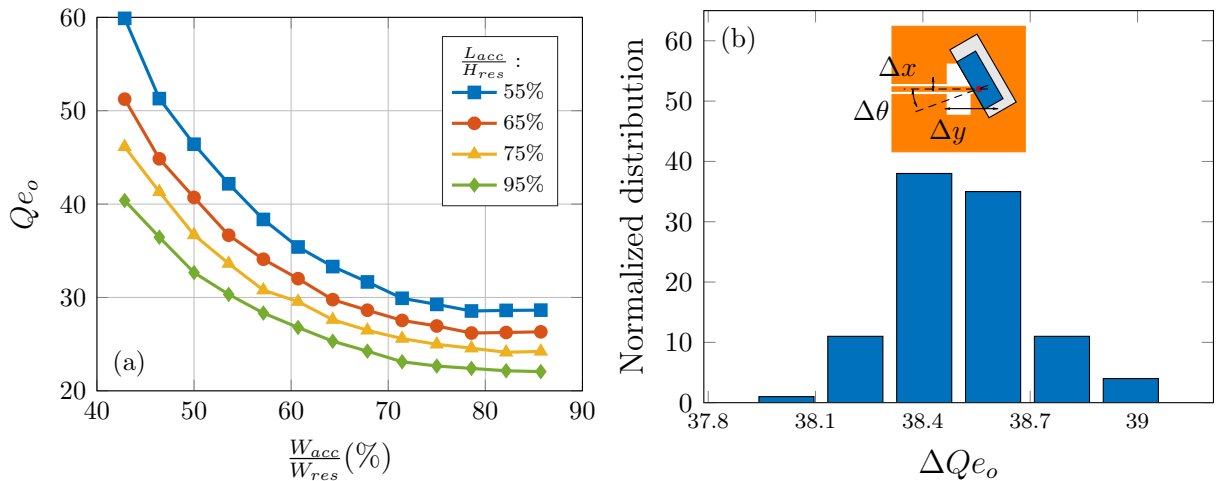


Figure 4.8: I/O terminal external quality factor analysis: (a) dependency with geometrical dimensions ($H_{acc} = 0.2 \text{ mm}$) and (b) variability due to misalignment.

the line gap is enlarged to boost the magnetic field radiation in the nearby area. With this configuration, the radiated magnetic field partially matches with the TE_{101} magnetic field distribution in the resonator-board interface. A rectangular opening is performed on the metallic coating of the ceramic resonator to propagate the radiated field into the device. Both, the access and the CPWG line are centered with respect to the structure. The external coupling Q_{e_o} can be tuned by changing the length (L_{acc}), width (W_{acc}) and height (H_{acc}) of the access (fig. 4.7 and 4.8.a).

Even though no particular measures should be taken to avoid short circuits during the device placement, Q_{e_o} could be affected by the misalignment between the coplanar line termination and the resonator access. A statistical analysis was performed to address the misalignment effect with industrial pick and place setups. The analysis was implemented in resonators with access dimensions of $W_{acc} = 4 \text{ mm}$, $L_{acc} = 1.1 \text{ mm}$ and $H_{acc} = 0.2 \text{ mm}$ and external coupling of $Q_{e_o} = 38.5$. A placement uncertainty in x -, y - and θ described by a normal distribution with deviations of $\Delta x|_{\pm 6\sigma} = \Delta y|_{\pm 6\sigma} = \pm 80 \mu\text{m}$ and $\Delta \theta|_{\pm 6\sigma} = \pm 0.01^\circ$ were considered in the analysis (fig. 4.8.b). A Gaussian distribution fit of the statistical analysis exhibits a $Q_{e_o} = 38.51 \pm 0.19$ which represents a variation of $|s_{11}(dB)| = \pm 1 \text{ dB}$ and $|s_{21}(dB)| = \pm 0.01 \text{ dB}$ within the filter pass band designed in this work.

Nevertheless, unlike the I/O terminals utilized in Chapter 3, no measurements could be implemented to test the devices before their assembly into the board. This could be considered as a drawback and a limiting factor in terms of design flexibility owing to the components should contemplate the tuning process employed for the frequency response correction. Some examples will be presented below.

4.2.2 Band-pass filter design

The magnetically-coupled rectangular cavity resonators were implemented to study the different scenarios highlighted in fig. 4.2. Several 4-pole Chebyshev band-pass filters were designed to be manufactured in Alumina ($\epsilon_r = 9.15$, $\tan \delta < 10^{-4}$) as a generic proof of concept. In all the cases, the devices were designed to meet the same specifications. A typical In-line topology with a center frequency $f_o = 9.45 \text{ GHz}$, bandwidth $BW = 200 \text{ MHz}$ ($FBW = 2.11\%$) and size $32.1 \text{ mm} \times 7 \text{ mm} \times 2 \text{ mm}$ was taken as a reference for comparisons with other arrangements (fig. 4.9). This base design was then modified to apply the aforementioned transitions and 90° inter-resonator irises to fold the whole structure. Rounded corners were performed ($r_j = 1.7 \text{ mm}$) to reduce the losses due to the high current density on the edges (fig. 4.10). Four filter examples were designed and optimized in HFSS (fig. 4.10) to achieve the original specifications and provide different features:

1. *C-shaped filter (Cs)*: this design implements a 90° bending on the irises between resonators 1 - 2 and 3 - 4 to surround other associated devices placed inside (red area in fig. 4.11.a). These devices could be interconnected to the filter from both sides of the resonator thanks to the symmetry of the transition. Thus, the required area on a PCB carrier is better utilized and the interconnection paths could be reduced enhancing the performances. The C-shaped filter could be also used to reflect EM fields or isolate particular regions of the board. The inductive irises were not centered with respect to the resonators to maximize the surface contact between the filter and the board, enhancing the electrical connection and the part assembly.

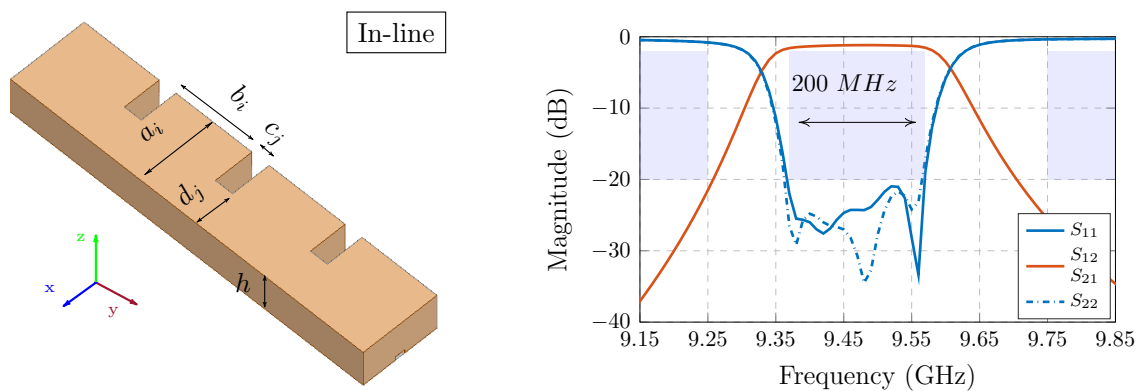


Figure 4.9: Reference In-line filter design and frequency response.

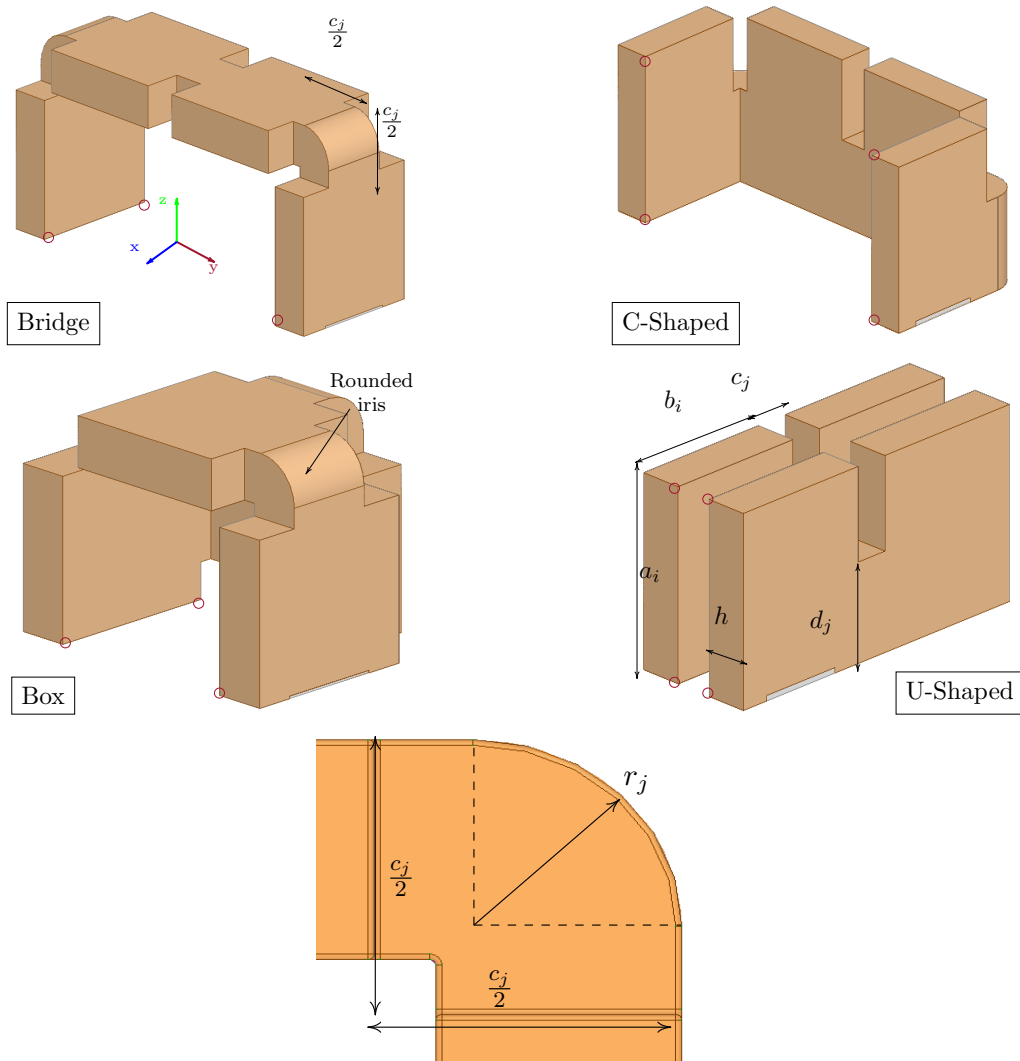


Figure 4.10: 3-D Alumina-based designs: Bridge, C-shaped, U-shaped and Box filters. Support anchor points are highlighted in red.

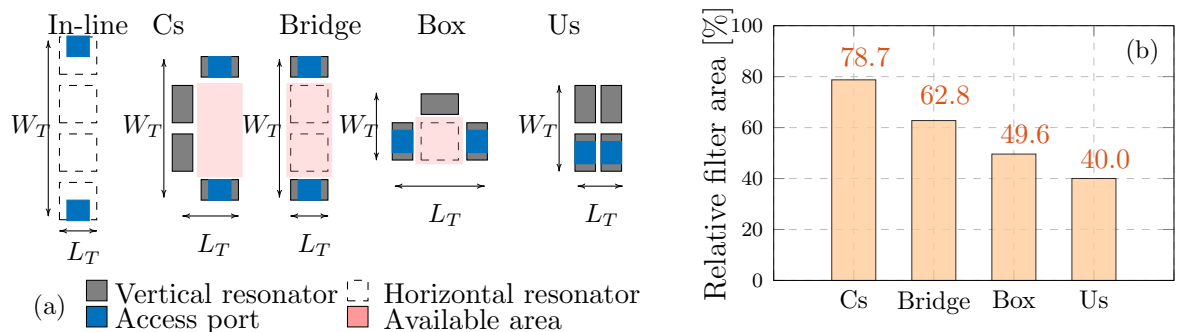


Figure 4.11: 3-D printed filters footprint (a) and relative area ($W_T \times L_T$) comparison (b).

2. *Bridge filter*: the possibility to rotate the rectangular resonators while maintaining the same access configuration is exploited in this case. The C-shaped filter design was flipped to create a version where interconnection lines could cross underneath, thus facilitating the PCB layout routing. Moreover, integrated circuits or microwave planar structures could leverage the area below the filter. Unlike the C-shaped filter, the irises are placed symmetrically to the resonators to balance the weight. Another advantage of this design is that a waveguide version could be implemented by just extending the iris width to the whole extension of the resonator. Real 3-D interconnections could be performed facilitating the board floor planing. A simulated result of such a potential waveguide is depicted in fig. 4.12.

3. *Box filter*: size reduction is fully exploited in this design. The box filter was developed as a first approach towards the implementation of a heterogeneous integrated subsystem where the other parts of the circuit are interconnected from the inside such as the 3-D printed origami antenna published in [82]. Another possible scenario could be the development of dual-band antenna arrays printed on ceramic blocks as suggested in [223]. Additionally, this design removes the inter-resonator connection constraints. Non-adjacent resonators can be linked more easily facilitating the conception of diverse filter topologies.

4. *U-shaped filter (Us)*: a complete folded version of the In-line filter. The design is focused on the area reduction and no other components could be embedded inside the device.

Figure 4.10 and Table 4.2 show the dimensions of the different designs, where $i = 1, 2, 3, 4$ represents the resonator number and $j = 1, 2, 3$ the iris number. The substrate

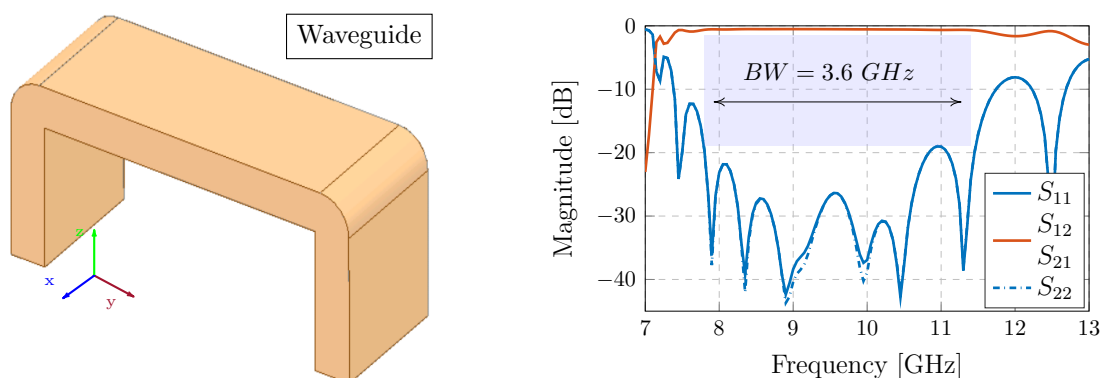


Figure 4.12: 3-D printed waveguide design derived from the Bridge filter.

Table 4.2: Filter design dimensional parameters.

Dimension (mm)	Bridge	C-shaped	U-shaped	Box
$a_{1,2,3,4}$	6.998	6.998	6.998	6.966
$b_{1,4}$	6.396	6.453	6.679	6.866
$b_{2,3}$	6.704	7.007	7.249	6.492
$c_{1,3}$	5.000	5.000	1.566	5.000
c_2	3.527	1.639	1.804	5.000
$d_{1,3}$	2.997	3.922	3.6	3.469
d_2	1.639	3.614	3.75	3.274
L_{acc}	1.293	1.133	1.054	1.113

thickness $h = 2 \text{ mm}$, the access dimensions $W_{acc} = 4 \text{ mm}$ and $H_{acc} = 0.2 \text{ mm}$ are the same for all cases. The designs were conceived in order to let all the resonators and irises faces exposed for the post-fabrication tuning stage. Furthermore, the horizontal resonator arrangement of some designs such as the Box and Bridge filters is a convenient feature for automated assembly processes. Despite the access ports were intentionally placed in line to meet industry preferences, other orientations are also possible by bending the irises at different angles. Figure 4.11 illustrates the footprints of the four examples and their relative size reduction in comparison to the In-line filter. The relative filter area is calculated as the ratio between the 3-D filters area ($W_T \times L_T$) and the surface reference (233 mm^2) of the In Line filter once mounted on a PCB. It has to be considered that in the case of the Bridge, the Box and the C-shaped filters the surface gain is not only represented by the device area but also by the available surface below and inside that could be utilized for any other devices on the board.

4.2.3 3-D printed filters manufacturing characterization

The realization of some devices such as the Box filter would be difficult to carry out with classical manufacturing methods. AM is an useful tool for the creation of complex structures. However, the sintering process in ceramic SLA is a critical step since part of the accuracy could be lost due to the material shrinkage. Special attention must be taken to avoid undesired bending that could affect the quality of the sample [94]. In order to maintain the devices fixed and avoid deformations as a consequence of the stress relief during the sintering, mechanical links were added in specific joints highlighted in red in fig. 4.10. The supports were removed once the process had been completed.

The devices were printed prioritizing maximum flatness for the surface in contact to the board to ensure a good assembly on the PCB. Sensitivity analyses were performed during the design to take into account the effect of rounded corners and manufacturing tolerances. Typical dispersion of $\Delta X = \pm 100 \mu m$ was implemented in the every dimension. Simulations showed an reasonable variation of the filter response that could be corrected in a post-fabrication tuning stage as it will be explained in the following sections. Nevertheless, geometrical irregularities, asymmetries and deformations are difficult to address and to estimate without any experimental feedback, specially in complex parts with suspended structures.

The devices were manufactured using a low-loss ceramic (Alumina) SLA process with $\epsilon_r = 9.15$ and $\tan \delta = 6.9 \cdot 10^{-5}$ (see fig. 4.13.a). The samples were measured with a digital microscope to characterize the mismatch between the design and the printed samples and to identify fabrication tendency. Figure 4.14.a depicts the dispersion observed between the ideal dimensions and measurements in every direction for all the filter designs. Vertically printed structures such as the input/output resonator of the Bridge filter and horizontally suspended parts, such as resonators 2 and 3 of the bridge filter, were grouped to help with the recognition of common manufacturing deviations. A priori, no particular differences were observed depending on the structure orientation (horizontally suspended or vertically placed) showing similar fabrication dispersion. However, the printing accuracy in the z-axis seems to be better controlled than in the other directions due to the well controlled layer-by-layer 3-D printing process.

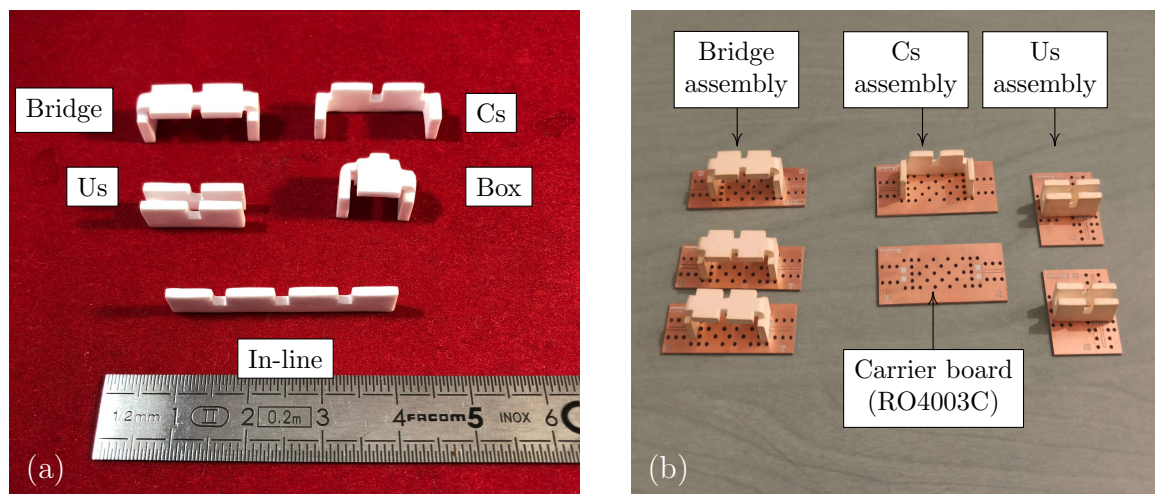


Figure 4.13: Manufactured ceramic filters placed in the printed orientation (a) and surface-mounted devices into the carrier board (b).

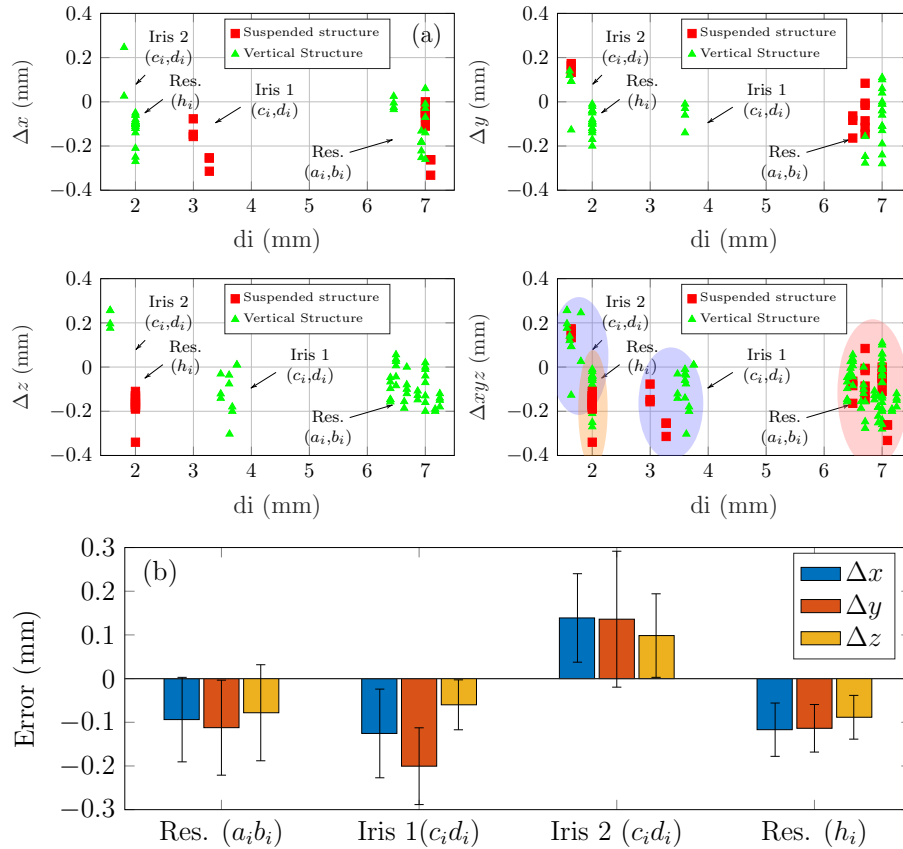


Figure 4.14: Measured manufactured filters dispersion (Δx , Δy and Δz) of every sample dimension (d_i) in the x-, y- and z- direction (a). The terms Suspended and Vertical structure refer to a resonator or iris in contact to the board (e.g. resonator 1 or iris 1 in Cs filter) or hanging as in resonators 2 and 3 of the Bridge filter. The mean filter manufacturing tolerance and dispersion is shown in (b), discriminated by the printing direction and the part of the device.

As it can be seen, for these designs the dispersion highly exceeds the pre-estimated tolerances informed by the manufacturer, in the majority of cases towards smaller sizes. This mismatch could be a product of an excessive shrinkage and stress relief during the sintering process.

Observations show a maximum deviation range between $-270 \mu m \leq \Delta x \leq 60 \mu m$, $-280 \mu m \leq \Delta y \leq 170 \mu m$ and $-200 \mu m \leq \Delta z \leq 256 \mu m$. Deviations seem to be contained in the specified ranges regardless the printing position in the z-axis. Sharp corners and edges show a rounded aspect with a radius less than $r_j \leq 0.2 \text{ mm}$. The process can be tuned using this information by resizing even more the design to counterbalance the shrinkage effect and enhance the final result. The different parts of the device can be identified by their dimensions and analysed separately. Figure 4.14.b exhibits the mean value and the standard deviation to be expected from the resonator

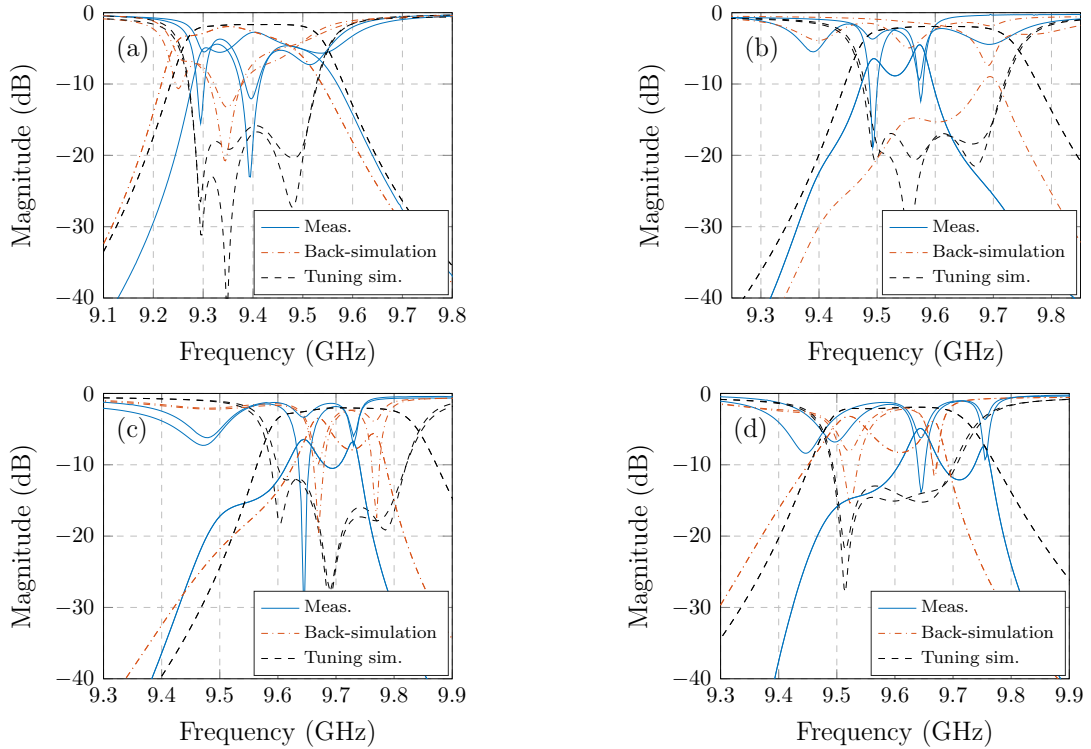


Figure 4.15: 3-D printed filters back-simulations and simulated tuning: C-shaped (a), Bridge (b), Box (c) and U-shaped (d).

and iris dimensions. Resonator width and length (ai, bi): $\Delta x = -94 \mu m \pm 97 \mu m$, $\Delta y = -112 \mu m \pm 108 \mu m$, $\Delta z = -78 \mu m \pm 110 \mu m$; resonator thickness (hi): $\Delta x = -117 \mu m \pm 61 \mu m$, $\Delta y = -114 \mu m \pm 54 \mu m$, $\Delta z = -50 \mu m \pm 88 \mu m$; iris case 1 (Iris 1): $\Delta x = -126 \mu m \pm 102 \mu m$, $\Delta y = -200 \mu m \pm 88 \mu m$, $\Delta z = -57 \mu m \pm 60 \mu m$; iris case 2 (Iris 2): $\Delta x = 139 \mu m \pm 101 \mu m$, $\Delta y = 136 \mu m \pm 156 \mu m$, $\Delta z = 96 \mu m \pm 99 \mu m$.

The dimensions measured with the digital microscope were used to perform back-simulations in HFSS. These simulations helped to obtain a first order estimation of the filters response before their assembly on the PCB (see fig. 4.13.b) and to choose those samples feasible to be tuned before their assembly onto the board. The simulated scattering parameters can be consulted in fig. 4.15. The tuning patterns introduced in Section 4.1.2 were considered for the analysis of a possible correction of the manufactured devices. These patterns were added into the back-simulations and optimized to analyse the feasibility of the filter response reconstruction once mounted on the board. As it can be seen, in some cases the resonance frequency of the resonators does not accomplish the minimum frequency shift $\Delta f_o \leq BW$ (Section 4.1.2) to re-locate the center frequency to the target owing to the high error to compensate. However, the filters were relocated to a new center frequency that respects this criteria and maintains a reasonable quality factor value. Simulations indicate that filter response corrections

are possible even with the high manufacturing errors observed (fig. 4.15).

All the devices were metallized utilizing an aerosol silver coating process [198]. The typical conductivity achieved by this process is between $20 S/\mu m \leq \rho \leq 30 S/\mu m$ for a deposited layer of $3 - 4 \mu m$. The accesses were laser engraved to finalize the fabrication before soldering them on the PCB. A mean overall weight of 1.39 g was measured for several samples of the different filter designs. The devices were welded onto a RO4003C board (0.4 mm thick) with alignment patterns to facilitate the placement. The coplanar line dimensions were $W = 0.61 mm$ and $G = 0.169 mm$. The surface-mounted filters were measured with a setup comprised of a ZVA 87 VNA connected to $500 \mu m$ pitch GSG probes. Figures 4.13.b and fig. 4.15 show the manufactured devices assembled on the carrier substrate and the measured filters response. Furthermore, the extracted coupling matrices ΔCM_{meas} (blue), $\Delta CM_{back-sim}$ (orange), and $\Delta CM_{tuning sim}$ (black), can be consulted in eq. A.10 to A.13 (Annex A.2). The normalization values utilized for the extraction were: $f_{0_{Bridge}} = 9.6 GHz$ and $BW_{Bridge} = 200 MHz$ for the Bridge filter; $f_{0_{Cs}} = 9.6 GHz$ and $BW_{Cs} = 200 MHz$ for the C-shaped filter (Cs); $f_{0_{Box}} = 9.7 GHz$ and $BW_{Box} = 200 MHz$ for the Box filter; and $f_{0_{Us}} = 9.5 GHz$ and $BW_{Us} = 200 MHz$ for the U-shaped filter (Us). As expected, back-simulations do not totally yield the measurements owing to the contribution of the structure asymmetries and deformations in addition to the difficulties to properly model the samples. It should be also noted that the soldering paste thickness was not taken into account during back-simulations. As a result, the normalized external couplings ($m_{S1}, m_{1S}, m_{L4}, m_{4L}$) extracted on the coupling matrices are lower than in back-simulations.

Due to the impossibility to accurately assess the devices structural deformations with a digital microscope, the samples were digitally reconstructed using a 3-D laser scanner. For instance, figure 4.16.a shows the scanned 3-D image of a Box filter sample. The fabrication mismatch can be obtained by overlapping the 3-D image and the design CAD file used as reference for the comparison (fig. 4.16.b). The areas colored in yellow highlight the regions of the manufactured device that surpass the volume of the design. A shrinkage of the device as well as a slight deformation of the resonator can be observed on the inner side. Irregularities on the device surface can also be analysed in more detail in figures 4.16.c and 4.16.d, where the mismatch is represented in 3-D with a heat map. Green colors depict a better matching to the reference structure while bluish and reddish colors illustrate a higher dispersion. Rounded corners and curved faces can be distinguished both in resonators and irises.

As a general conclusion, filter corrections should be carried out using the measurement results instead of back-simulations. In the following section the tuning procedure

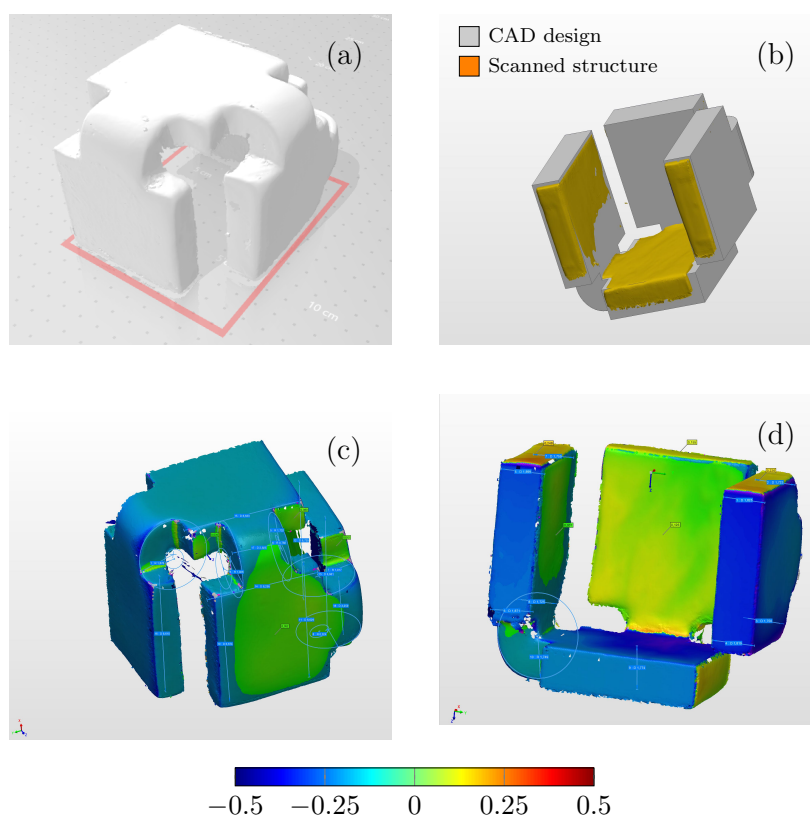


Figure 4.16: Laser scanned 3-D reconstruction of the Box filter (a). Scanned structure and reference CAD design comparisons (b). Deformations characterization of the manufactured device in millimeters (c, d).

explained in Section 4.1.1 will be implemented to the ceramic components to achieve a frequency response similar to those shown on simulations.

4.2.4 Laser tuning strategy implemented in complex-shape 3-D printed filters

The data experimentally obtained through measurements resulted in a non-negligible dispersion of the filter response in every tested sample driven by the manufacturing errors inherent of ceramic SLA process. However, optimization procedures carried out in full-wave simulations helped to anticipate this behaviour and determine the possibility of frequency response corrections in a post-fabrication step [224].

As already mentioned, tuning procedures based on back-simulations are not applicable in this context owing to the complications to perform a precise geometrical model of the device in a computerized environment. The deformations and asymmetries observed in the structure are difficult to be accurately reproduced in a custom design.

Hence, the simulated coupling matrix CM_{meas} used to represent the measurements as starting point for the tuning process will differ from the real response resulting in a false solution. A proof of this concept can be obtained by comparing the measurement and back-simulation coupling matrices depicted in equations A.10 to A.13 in Annex A.2. In this framework, another option is to carry out a different approach by implementing the tuning procedure explained in Section 4.1.1. The ideal filter design is used as a reference CM_{init} to estimate the coupling value variations ΔCM to be applied to tune the filter back to the expected specifications. These variations are added to the measured coupling matrix CM_{meas} extracted with Presto to calculate the tuning pattern dimensions. The effectiveness of this method will depend on the proximity between the target and the measured response that could be translated to the magnitude of the error to be corrected. Therefore, the smaller the coupling coefficients error the lower the sensitivity mismatch calculated. As a rule of thumb, accurate optimizations could be obtained for corrections within the ideal filter bandwidth. The filters were welded into small boards as shown in fig. 4.13 to facilitate the rotation of the components during the laser engraving process. This is a weak point of the methodology since measurements cannot be performed before the filter assembly with this approach to determine the corrections required. Alternative accesses etched on the filters could be developed for direct GSG probe measurements that could function afterwards as a coplanar transitions, nevertheless more restrictive alignment tolerances will be required for a successful operation. As in the case of back-simulations optimization, some devices exhibit a resonance mode shifted more than $\Delta f_o = BW$ from the target frequency. In these cases, the quality

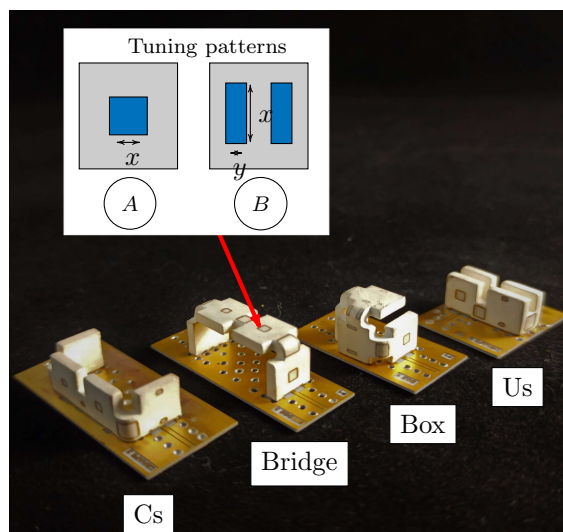


Figure 4.17: Surface-mounted and laser-tuned devices (a). Patterns (A) and (B) are the typical tuning square and rectangular patterns used for the frequency tuning.

factor degradation and inaccuracy driven by the relocation towards the target would be unacceptable. For that reason, the filters were re-centered to a new target frequency. Moreover, the filter bandwidth was adjusted to match with the measured external coupling values in each scenario since it is not possible to tune this parameter with the proposed transition. The coupling matrices of the manufactured filters were re-extracted using different normalization parameters. New target matrices were established to accomplish with the tuning method condition depending on each case and taking into account the current experimental Q_e . The coupling matrix of the Bridge filter was extracted with $f_{0_{Bridge}} = 9.55 \text{ GHz}$ and $BW_{Bridge} = 100 \text{ MHz}$ for normalization and in the case of the C-shaped, Box and U-shaped these parameters were $f_{0_{Cs}} = 9.45 \text{ GHz}$, $BW_{Cs} = 160 \text{ MHz}$ and $f_{0_{Box}} = f_{0_{Us}} = 9.6 \text{ GHz}$, $BW_{Box} = BW_{Us} = 130 \text{ MHz}$, respectively. Two tuning patterns were adopted from the corrected in-line filter presented in [193] as a case of study and implemented to correct the fully 3-D printed filters in both irises and resonator structures (inset in fig. 4.17). Pattern (A) is a square opening on the metal coating positioned in the area of maximum electric field for the TE_{101} resonators mode. A capacitive effect provided by this pattern raises the resonator resonance frequency or the inter-resonator coupling factor. The opposite effect could be generated by implementing a rectangular pattern in the position of maximum magnetic field (pattern (B)). This pattern was used in both edges of the resonator to perturb the field symmetrically.

The proposed tuning strategy was applied to the printed devices to enhance their frequency response. The implementation of a laser machine in the process provides the

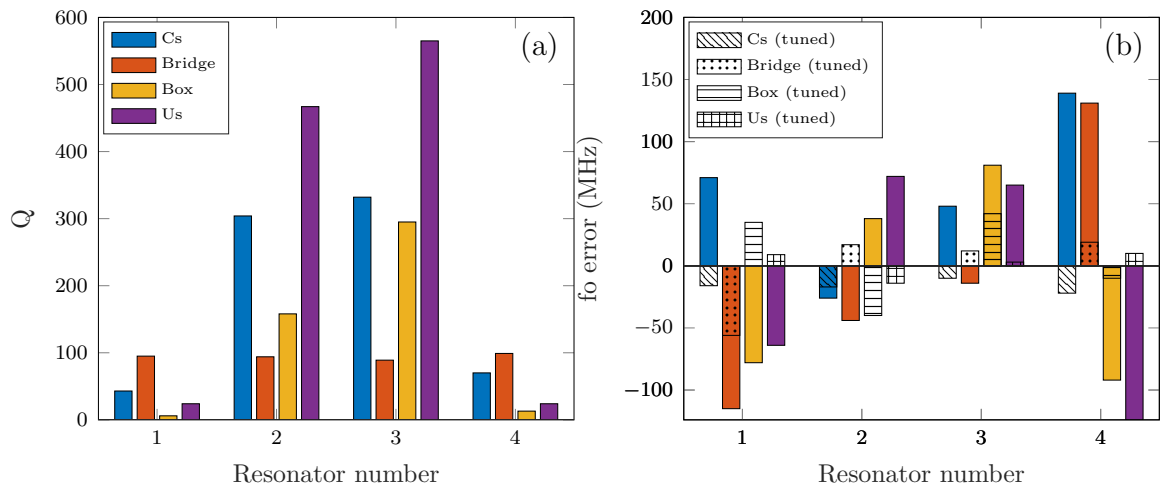


Figure 4.18: Equivalent quality factor extracted after laser tuning (a) and resonance frequency error correction (b).

advantage of engraving complex shapes in regions of difficult access while maintaining the integrity of the sample. A comparison between the resonance frequency error before and after the tuning procedure and the equivalent Q-factor extracted for each design can be consulted in fig. 4.18. High losses are observed driven by the strong corrections required in every case as it was observed in [193]. Figure 4.19 shows the pre- and post-tuning S-parameters of the measured filters. Final results reveal a good agreement between the target and tuned filter response in the C-shaped sample as a result of the tuning methodology. The filter shows post-tuning insertion losses between 2 dB and 3 dB in the pass band. This effect is the result of radiation losses related to the EM field leakage through the metal layer apertures. The method provides an accurate correction for the filters with a response closer to the final target as it can be seen in the case of the C-shaped filter. In the other examples, since the initial errors are quite elevated, the optimization process manages to re-center the filter and enhance the response. However, the final result is not so accurate as in the first case. Table 4.3 summarizes the measured parameters for all the designs after the tuning stage and equations A.14 to A.17 (Annex A.2) depicts the extracted coupling matrices for the pre-tuned (blue), simulated target (black) and tuned (red) filters. In equation A.15, the

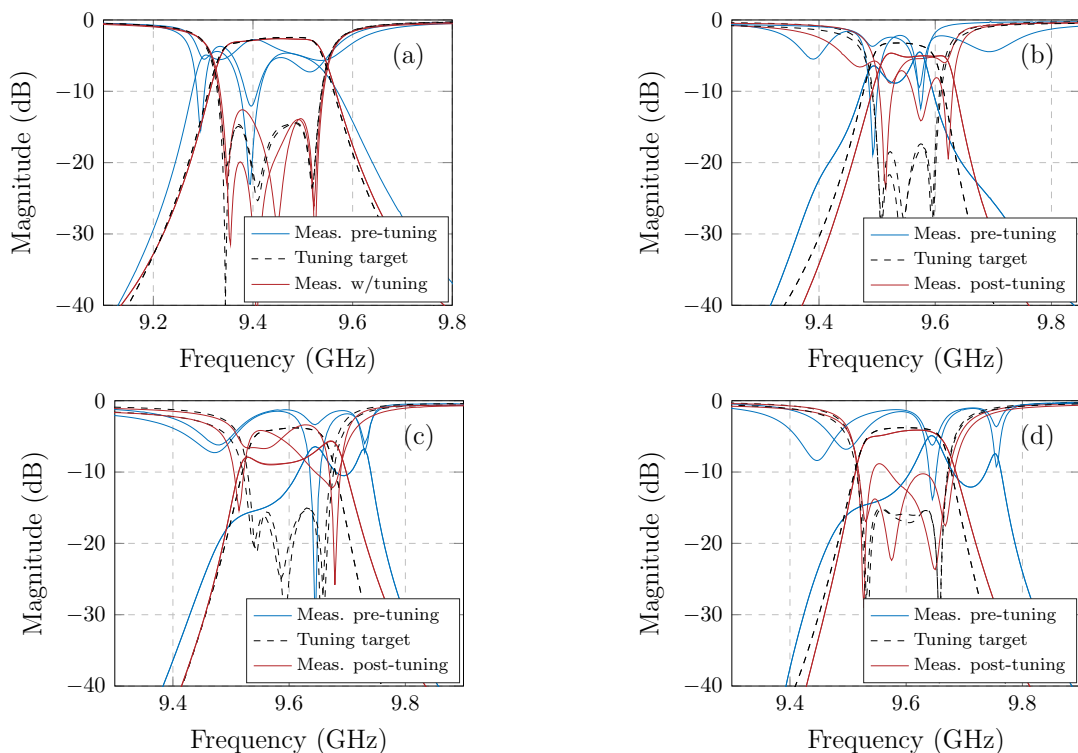


Figure 4.19: Pre-tuning and post-tuning measured S-parameters of 3-D printed filters: C-shaped (a), Bridge (b), Box (c) and U-shaped (d).

Table 4.3: Filter design dimensional parameters.

Parameter	Bridge	C-shaped	U-shaped	Box
Center freq. (GHz)	9.567	9.455	9.598	9.596
Bandwidth (MHz)	135	200	164	190
Return Loss (dB)	8	12.65	8.82	3.39
Insertion Loss (dB)	5	2.636	4.892	5.62
Quality factor	370	550	330	300
Ripple (dB)	0.34	0.29	0.78	3.32
Weight (g)	1.44	1.39	1.44	1.35

unsatisfactory response is driven by a tuning error in the resonance frequency of the output resonator and a very high coupling between resonator 2 and 3. In the U-shaped filter, inter-resonator couplings match quite well with the target and the resonance frequency of the resonators was improved but still a bit shifted. A fine tuning could be applied to correct these imperfections with the risk of degrading the quality factor even more. Finally, even though the inter-resonator couplings were successfully enhanced, insufficient correction can be seen in the input/output resonator. As in the case of the U-shaped filter, the device could be re-tuned to achieve the specifications but adding more losses within the pass band.

4.3 Temperature drift characterization

An experimental temperature analysis was carried out in order to characterize the robustness of the fabricated samples and their behaviour to temperature variations. The setup (fig. 4.20.a) consisted of a Microtech probe station with GSG 0.5 mm probe tip connected to a Rhode & Schwartz ZVA 87 VNA. The DUTs were placed on a Peltier cell handled with a temperature controller. A temperature sensor was placed on top of the devices (fig. 4.20.b) and connected to a digital multimeter to monitor the temperature difference between the board and the DUT during the experiment. The main goals of the analysis were to:

1. determine the dependency between the filter response and the temperature drift.
2. examine possible damages on the device (metal layer or the ceramic) or unsoldering as a consequence of the coefficient of thermal expansion (CTE) mismatch between the board and the ceramic device.

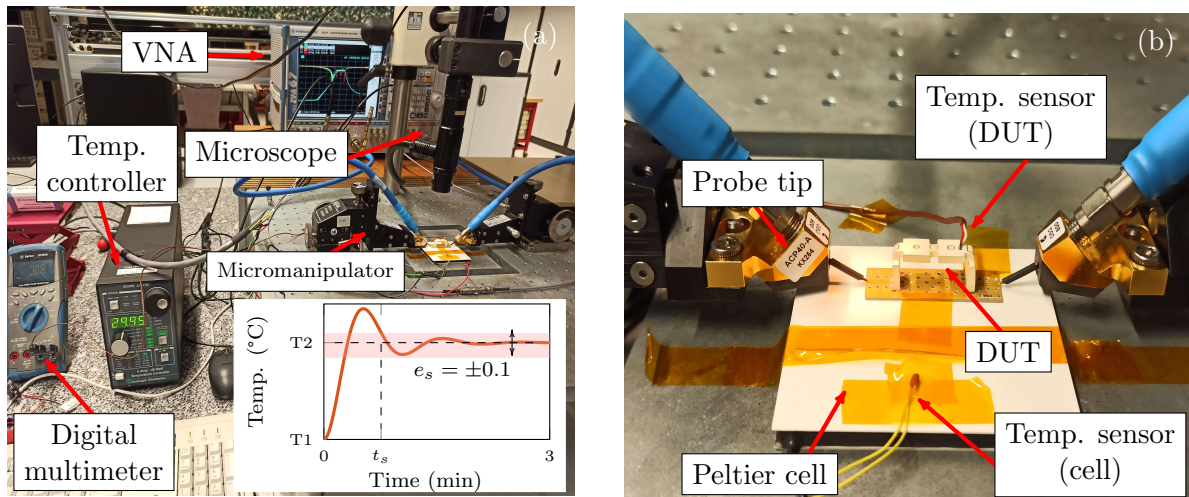


Figure 4.20: 3-D printed filters temperature characterization setup (a) and probe tips and sensing elements (b).

3. verify the correct operation after a few temperature cycles from room temperature up to 80 °C.

All the devices studied so far were exposed to three temperature cycles which consisted of: 1) heating stage from room temperature ($T_{min} = 23\text{ °C}$) up to $T_{max} = 80\text{ °C}$ (maximum temperature supported by the Peltier cell) in steps from temperature T1 to T2 of $T_2 - T_1 = \Delta T = 5\text{ °C}$ (see insight in fig. 4.20.a); 2) cooling from T_{max} to T_{min} in steps of $\Delta T = -5\text{ °C}$, finalizing the cycle; and 3) repeating the whole process two more times. The maximum settling time Δt_s monitored on the samples by the sensor between two temperature steps was less than 3 minutes in every case. The error band established to define the settling time was $e_s = \pm 0.1\text{ °C}$ (insight in fig. 4.20.a). Despite the fact that in the majority of the cases a typical temperature difference between the Peltier cell and the temperature sensor was of a few degrees, the temperature gradient in the case of the Bridge filter shows a higher difference that becomes more pronounced as the temperature increases. This effect could be produced by the non-homogeneous distribution of temperature along the structure driven by the conduction heat transfer from the carrier board to the input/output resonators through the contact interface between them. Moreover, the great device surface in contact with the surrounding air could be facilitating the heat evacuation more than the other designs. As a consequence, the electrical permittivity and the dilatation of the structure present in all the DUTs could be slightly different at different points of the Bridge filter. The thermal characterization of this device during the experiment was limited up to 60 °C to avoid damaging the Peltier cell owing to the temperature difference observed. On the other side, the C-

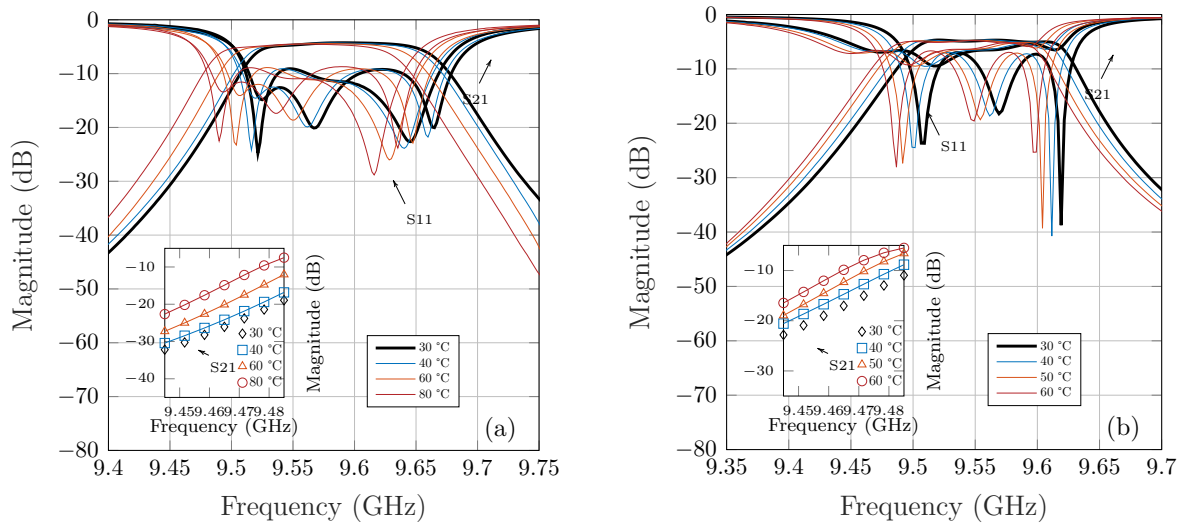


Figure 4.21: C-shaped filter pre-tuning (a) and post-tuning (b) measured S-parameters.

shape and U-shape filters are completely in contact with the board showing a more homogeneous heating of the overall sample. The Box filter results in an intermediate case between C-/U- shaped and Bridge filters.

Figure 4.21 shows the U-shape and the Box filter scattering parameters measured at several temperatures.

Although the plot exhibits a frequency shift $\Delta f_o(T) \simeq f_o(T) - f_o(23^\circ\text{C})$, the filter shape remains similar with a slight compression of the pass band $\Delta BW(T) = BW(T) - BW(23^\circ\text{C})$ around a few MHz in both cases. Alumina-based substrates usually possess a negative thermal coefficient of frequency τ_f that added to the device dilatation, could shift $\Delta f_o(T)$ towards lower frequencies [214]. This effect can be more clearly seen in the scatter plots exhibited in fig. 4.22. The data analysed during a complete thermal cycle shows a linear progression with temperature leading to a linear regression fitting of Δf_o , ΔBW and the losses. The maximum relative center frequency shift observed in fig. 4.22.a for temperatures up to 80°C is between $-42 \text{ MHz} \leq \Delta f_o(T) \leq -29 \text{ MHz}$. The linear regression slope obtained ranges between $-766 \text{ kHz}/^\circ\text{C} \leq \frac{\delta f_o}{\delta T} \leq -554 \text{ kHz}/^\circ\text{C}$, being the Box filter the less sensitive and the Bridge filter the most sensitive. The center frequency behaviour with temperature in the case of the U-shaped and the C-shaped filter is similar ($\frac{\delta f_o}{\delta T}(Us) \approx -637 \text{ kHz}/^\circ\text{C}$ and $\frac{\delta f_o}{\delta T}(Cs) \approx -629 \text{ kHz}/^\circ\text{C}$). The variation of the resonance frequency from the measured filter at room temperature was also extracted from the coupling matrix main diagonal factors $\Delta m_{ii}(T) = m_{ii}(T) - m_{ii}(23^\circ\text{C})$ and plotted in fig. 4.23.a. The picture shows the linear evolution of $m_{ii}(T)$ with $i = 1$ to 4 for all the resonators of the different DUTs.

In regard to the bandwidth variation (fig. 4.22.b), the filters seem to be divided again

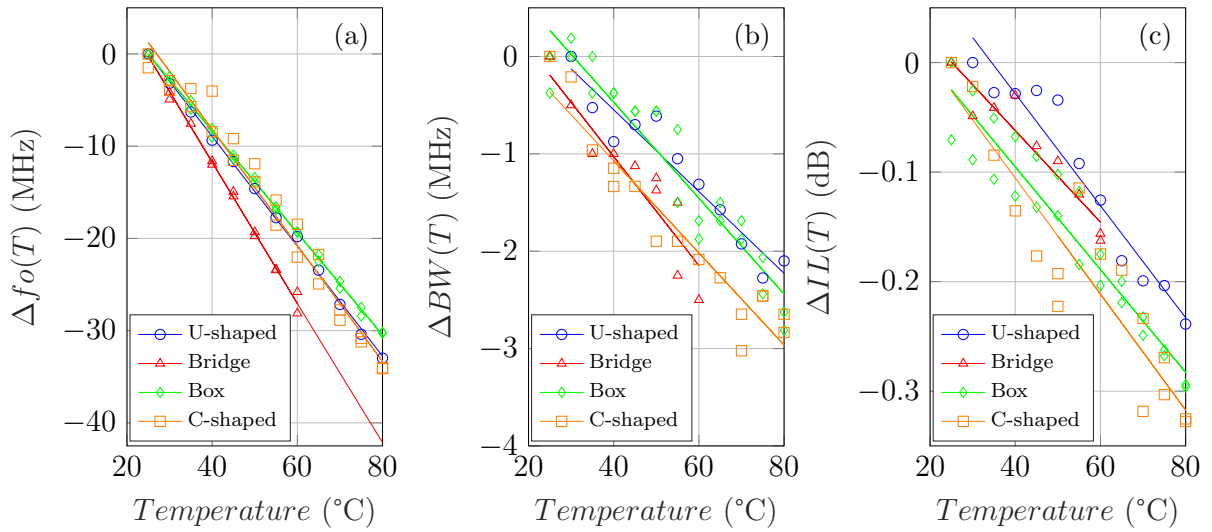


Figure 4.22: Additively manufactured ceramic filters response evolution with temperature in one cycle: relative frequency shift (a), relative bandwidth variation (b) and relative increment of losses (c).

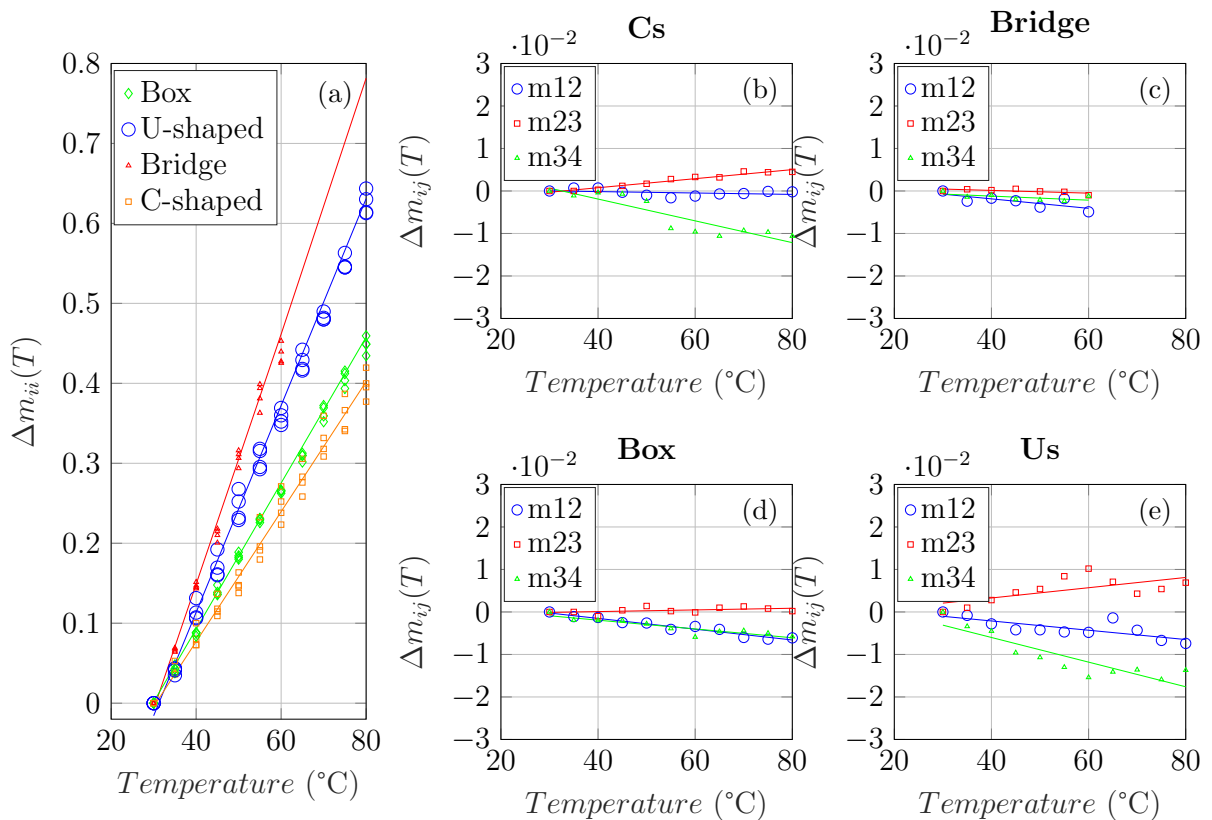


Figure 4.23: Normalized coupling matrix factors dependency with temperature extracted from DUTs measurements: main diagonal factors m_{ii} (a) and inter-resonator coupling factors m_{ij} for the C-shaped (b), Bridge (c), Box (d) and U-shaped (e) filters.

in two groups: on one side the C-shaped and U-shaped and on the other side the Box and Bridge filters. These designs show a similar behaviour that could be related to the device heating. In the first group the filters irises and resonators are soldered to the carrier board. On the contrary, the irises and some resonators of the second group are not placed on the PCB and therefore, not directly heated. The relative bandwidth fluctuation with temperature is $\frac{\delta\Delta_{BW}}{\delta T} = -0.042 \text{ MHz}/^\circ\text{C}$ for the C-shaped and $\frac{\delta\Delta_{BW}}{\delta T} = -0.047 \text{ MHz}/^\circ\text{C}$ for the U-shaped filter. In the second case these variations are $\frac{\delta\Delta_{BW}}{\delta T} = -0.049 \text{ MHz}/^\circ\text{C}$ for the Box and $\frac{\delta\Delta_{BW}}{\delta T} = -0.055 \text{ MHz}/^\circ\text{C}$ for the Bridge filter. The consecutive inter-resonator couplings m_{ij} with $i = 1, 2, 3$ and $j = 2, 3, 4$ illustrated in fig. 4.23.b to e exhibit also the same tendency between the C-shaped and U-shaped on one side, and between the Bridge and Box filter. As it can be seen, in the first case the coupling factors are more affected by temperature, while in the second case are less dispersed. Furthermore, the coupling factor m_{23} that corresponds to the iris between resonator 2 and 3 shows a lower variation in the last case. This part of the structure should be the colder in these DUTs. The same observations could be applied to the added losses within the pass band in fig. 4.22.c, where the filters behaviour can be subdivided into the same two groups. The highest losses (up to $\Delta IL = IL(T) - IL(23^\circ\text{C}) = 0.3 \text{ dB}$) were identified in the C-shaped filter. Based on the experimental results, the calculated loss rate with temperature expected for these devices is $0.004 \text{ dB}/^\circ\text{C} \leq \frac{\delta IL}{\delta T} \leq 0.006 \text{ dB}/^\circ\text{C}$. Depending on the particular application some designs could be preferred respect to the others. The losses increasing are attributed to the metallization conductivity degradation as well as the degradation of the dielectric loss tangent when the materials temperature increases [214].

No structural damages on the metal surface of the device were detected during the three temperature cycles performed. Furthermore, no appreciable degradation of the frequency response was observed in any of the DUTs at the end of the experiment.

4.4 Application example: Filtenna

In previous sections we studied the challenges of SLA 3-D printing for complex-shape microwave filters developed with low-loss ceramic materials to be implemented in different scenarios as a surface-mounted device. The area reduction is possible to be achieved on the one hand thanks to the permittivity of ceramics and on the other hand owing to the distribution and integration of the device to other components of the subsystem on the carrier board. It is also of our interest to provide other functionalities to the device to boost the advantages of 3-D printed technology applied to electronics.

The integration of filter and antenna components, also known as filtenna is a topic that has been investigated by the community during the last years in different technologies [225]–[227] specially utilized for communication front-ends.

In this section we will introduce the implementation of the ideas exposed so far during the chapter to integrate a 3-D printed filter as part of a planar antenna by means of full-wave simulations. This approach could be identified as the EM isolation scenario illustrated in fig. 4.2.

In [44], an array of Yagi-Uda planar antennas were fabricated in several Rogers RT/Duroid 5880 substrate boards for the construction of a 5G digital MIMO beamforming transceiver. Each antenna was connected to a SIW waveguide and 4-pole band pass filter placed on a daughter board of the mm-Wave front-end. These antennas are promising elements for mm-Wave communication owing to their high gain, low cost and compact size [81], [228], which is an interesting feature for the integration with the devices developed during our work. Inkjet printed Yagi-Uda antennas manufactured on flexible substrates were also reported in [81]. Therefore, this case served as inspiration for the proof-of-concept of a 3-D printed in-line filter placed sideways used as reflector of these antennas (fig. 4.24). To be consistent with the work previously shown the filter specifications were chosen to be the same as the filter reference presented in Section 4.2.2. Furthermore, the metal coating of the device should ensure the penetration depth condition at the operating frequency band in order to provide a shielding function. Equation 4.3 depicts the minimum metal layer thickness needed where $f = 9.8 \text{ GHz}$ is the upper cutoff frequency of the filter in $[Hz]$, μ is the magnetic permeability of the material ($\approx \mu_0$) in $[T.m.A^{-1}]$, and σ is the conductivity of the metal layer in $[S/m]$. For the plating

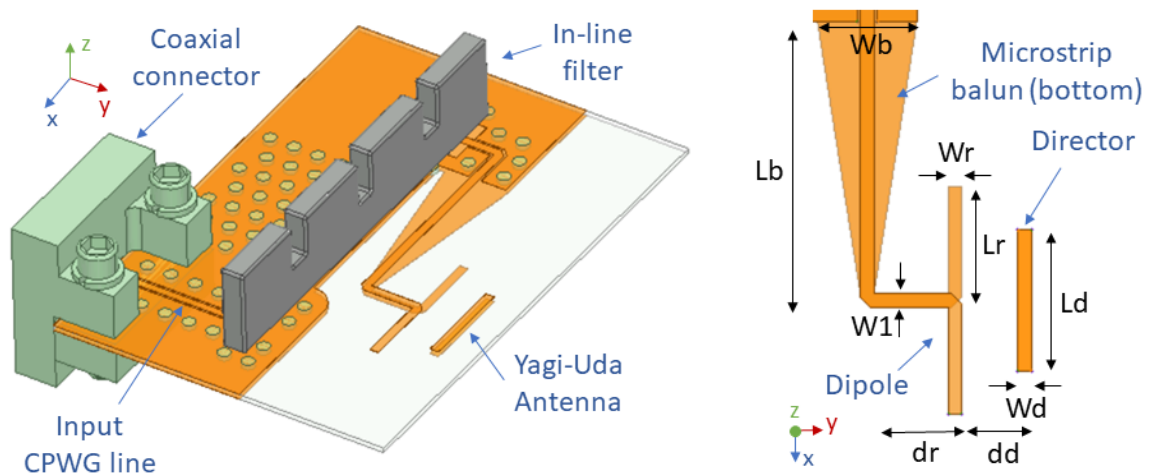


Figure 4.24: CAD model of filtenna design. The in-line BPF is placed on a side to be used as the reflector of a Yagi-Uda antenna element.

processes used in this thesis (copper electroplating or aerosol silver deposition) with $15 \text{ S}/\mu\text{m} \leq \sigma \leq 30 \text{ S}/\mu\text{m}$ the minimum metal layer thickness required is less than $1 \mu\text{m}$, which means 3 to 4 times less the typical deposited thickness for our technology.

$$t_{\text{metal}} \geq \frac{1}{\sqrt{\pi \mu \sigma f}} \quad (4.3)$$

The filter output port is connected to the antenna termination while the input is connected to a CPWG line. Both ports implements the transition analysed in Section 4.2.1. The CPWG line dimensions are $W = 0.61 \text{ mm}$ and $G = 0.169 \text{ mm}$ and the carrier board chosen is a 0.4 mm thick RO4003C ($\epsilon_r = 3.55$, $\tan \delta = 2.7 \cdot 10^{-3}$) with $18 \mu\text{m}$ of copper cladding. The other end of the line is linked to an edge mount connector via a coplanar-to-coaxial transition. The connector (145-0701-802) is intended to be used to feed the filtenna during experimental measurements on an anechoic chamber. The vias are separated a distance $d = 1 \text{ mm}$ and their diameter is $D = 1 \text{ mm}$ which is the minimum size of the drilling machine mills utilized in the laboratory for electronic boards manufacturing. The planar Yagi-Uda antenna is comprised of a microstrip balun, a reflector, a dipole and a director. The microstrip balun helps to adapt the antenna element input impedance to the downstream circuit. The reflector is carried out with a planar metal line on bottom while the top planar reflector is replaced by the metallic surface of the 3-D filter placed on a side. The antenna element dimensions are $W_b = 5.13 \text{ mm}$, $L_b = 14.71 \text{ mm}$, $W_1 = W_r = W_d = 0.7 \text{ mm}$, $L_r = 6.22 \text{ mm}$, $L_d = 7.32 \text{ mm}$, $d_r = 4.55 \text{ mm}$, $d_d = 3.59 \text{ mm}$. On the other side, the band-pass filter dimensions are $a_1 = a_2 = a_3 = a_4 = 7 \text{ mm}$, $b_1 = b_4 = 6.634 \text{ mm}$, $b_2 = b_3 = 7.168 \text{ mm}$, $c_1 = c_3 = 1.612 \text{ mm}$,

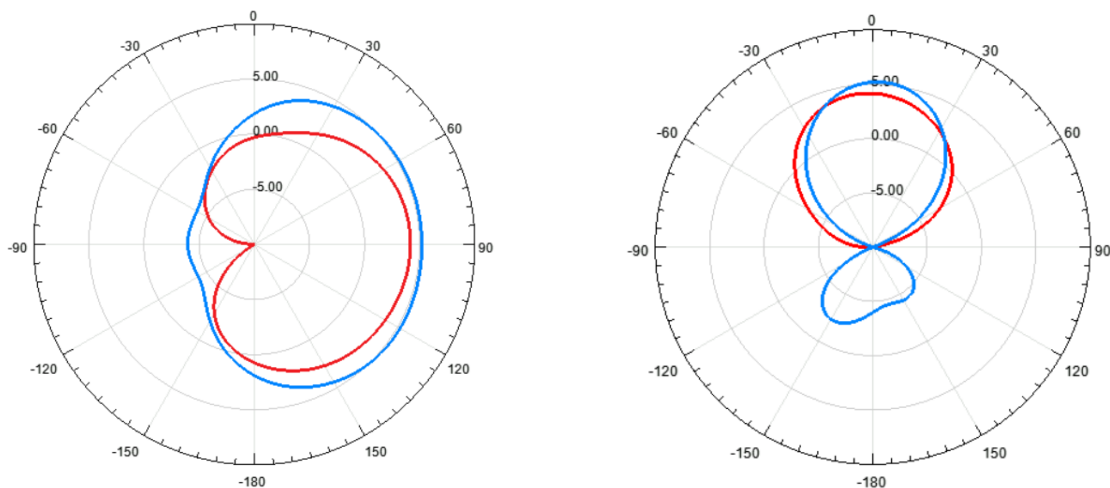


Figure 4.25: Simulated radiation patterns comparison of the single Yagi-Uda antenna element (blue) and the integrated filtenna (red): H plane (left) and E plane (right).

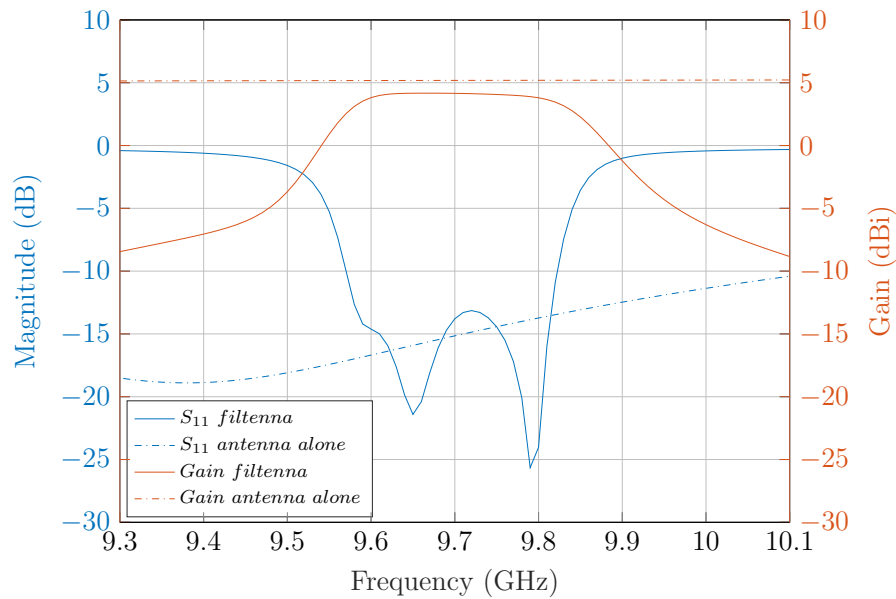


Figure 4.26: Simulated gain and reflection coefficient of the filtenna design.

$c_2 = 1.639 \text{ mm}$, $h = 2 \text{ mm}$, $H_{acc} = 0.2 \text{ mm}$, $L_{acc} = 4 \text{ mm}$, $W_{acc} = 1.173 \text{ mm}$.

The single element antenna and the filtenna gain simulated in HFSS are illustrated in fig. 4.25. As it can be seen, the Yagi-Uda antenna alone used as reference shows a low backlobe of -4 dBi and a wide half-power beamwidth of 164° in the H-plane and a higher backlobe of -2.3 dBi and lower beamwidth of 54° in the E-plane.

The implementation of the 3-D printed In-line filter as the antenna reflector to perform the reference antenna reduces the radiated field on the backlobe in both E- and H-planes below -10 dBi , thus improving the isolation of the circuit behind it and enhancing the utilization of the carrier board area. As a drawback, the antenna gain is reduced when compared to the reference antenna. However, a future study on this subject could be carried out to optimize the antenna gain performances. The half-power beamwidth is 125° and 67° for the H- and E- planes, respectively. Figure 4.26 shows a comparison between the gain and reflection coefficient for both designs. The reflexion coefficient is less than -13 dB in the operating band between 9.6 and 9.8 GHz. The antenna gain is greater than 5.1 dBi while the filtenna gain is 4.2 dBi in the pass band.

4.5 Conclusions and perspectives

Throughout this chapter, an approach towards the utilization of additive manufacturing processes for the conception of passive surface-mounted microwave devices was presented. To the best of our knowledge, most of the works realized related to 3-D SMT

ceramic filters found in the bibliography are monoblock components horizontally-placed on the carrier board. However, the possibility of printing complex-shape ceramic objects opens the way for the exploration of new scenarios where heterogeneous technologies could be integrated inside compact 3-D devices.

The implementation of rectangular cavity resonators placed sideways driven by the necessity of a better use of the vertical dimension and the board area requires the design of a specific transition. The magnetic field in TE_{101} rectangular resonators was leveraged to develop a SMT transition compatible to industrial pick and place misalignment tolerances. The vertically-positioned resonator brings two main advantages: an important area reduction in comparison to traditional designs, and a natural tendency to build the structure in volume. Moreover, since in this mode the quality factor increases with the resonator thickness (h_i), a wider resonator base gives more stability to the device, enhances the ground contact to the board, facilitates the welding and improves the electromagnetic performances of the filter. As a drawback, this approach makes impossible the component direct testing with a probe station, thus hindering the engraving of tuning patterns before their assembly. Alternative transitions should be investigated to achieve the benefits of both accesses. A transition with these characteristics will be introduced in the next chapter. Vertically-oriented cavity resonator filters could be designed in order to adapt the device to the board floor-planing needs, surround or contain other elements of the circuit, integrate more functionalities in the same space, simplify the layout or help to electromagnetically isolate determined regions of the system.

Four different scenarios were proposed for the implementation of ceramic devices in the X-band with different advantages in terms of space consumption and applications. Even though only band-pass filters were studied in this line of work, other passive circuits such as waveguides, diplexers or power splitters could be designed with the same approach. Moreover, in the framework of front-end transceivers reflectionless techniques applied to band-pass filters could be an interesting feature to be explored [138]. In previous works, mm-Wave ceramic SLA band-pass filters were manufactured to operate at 40 GHz. Nevertheless, reports show a high mismatch between simulations and measurements as a consequence of the current manufacturing tolerances of the fabrication process. A tuning methodology for cavity filters was proposed to overcome this obstacle. The correction process was tested on rectangular parallelepiped cavity BPFs specifically designed for this purpose at 8 GHz, demonstrating a good agreement between the target

frequency response and measurements. Based on previous experience, the 3-D filters proposed in this chapter were manufactured with ceramic Stereolithography to operate in the X-band as a first approach taking into account the manufacturing tolerances for sensitivity analysis. Sensitivity analysis performed during the design stage confirmed the necessity of a post-fabrication step to correct the frequency response of the filters. Ceramic supports were utilized to limit deformations, avoid cracks and the collapse of overhanging structures. Nevertheless, these defects are difficult to predict during the design step. The manufacturing orientation was chosen to prioritize a flat surface on the interface in contact to the board. The fabricated samples showed manufacturing tolerances up to $\pm 350 \mu m$ in some cases. No particular trend was noted depending on the orientation of the structures except for a tendency to smaller dimensions compared to the design in the x-/y- direction. This tendency could be a product of an excessive shrinkage of the samples during the sintering step and could be corrected in the future by updating the manufacturing process based on the analyzed information. The manufacturing dispersion observed was rather homogeneous in every case.

The impossibility to model the complex structural deformations observed during a laser scan reconstruction and to properly simulate their EM effect motivated the utilization of the tuning methodology explained in 4.1.1 to perform the frequency response compensation. The samples were assembled onto a board and measured showing a high dispersion. A closer look of the extracted coupling matrices allowed to evaluate the tuning patterns required in every part of the component to compensate the manufacturing errors effect. The tuning pattern dimensions were obtained by calculating the relative variation of the coupling matrix and engraved on the metal coating with a laser. Post-tuning measurements showed an improvement of the filter response and a good agreement between the target and tuned filter for those filters with lower initial error. In these particular cases, a great enhancement was noted but the final filter features were still not satisfactory. Furthermore, high corrections are equivalent to high losses and reduction of the quality factor. Nevertheless, future advancements in 3-D printing technologies could bring better fabrication tolerances, requiring less corrections and better features. It should be also remarked that the laser scanner reconstruction could be an interesting technique to potentially develop an exact 3-D model of the devices. The scanner provides a cloud of points in STL format that could be imported to ANSYS HFSS or CST. Nevertheless, the obtained object is not recognized as a solid body and has to be reconstructed by hand, losing the advantages of the scanner accuracy. Furthermore, the complexity of an automated tool to generate external IGES or GDS

files that could be easily imported to the EM simulators is not trivial. Some CAD softwares as SolidWorks offer similar tools but usually the end of the process has to be ended by hand. The development of a specific automated tool that accomplishes the requirements of these applications would be a great step towards the enhancement of tuning optimization methods.

On the other hand, the ceramic devices exposed to thermal characterization between room temperature and 80°C provided some clues about proper design guidelines to be followed depending on the application. In principle, no damages or anomalies were observed on the structure or the frequency response after a few temperature cycles. The analysis should be extended to a great number of cycles to validate the reliability of the filters under real conditions. Several humidity and low temperature conditions could be also performed in a climatic chamber to complete the reliability characterization of the devices. For these experiments, coaxial connectors could be implemented for external connections to the measurement equipment by applying the transitions shown in Section 4.4.

Finally, the results obtained are a very first step towards the miniaturization and integration of heterogeneous microwave technologies in a flexible way. Once overcame the technological milestones exhibited in this thesis, future efforts could focus in the development of complete integrated subsystems such as the filtenna application presented in Section 4.4.

5

Passive ceramic devices development for mm-Wave band applications

THE rapid expansion of mobile applications and IoT evolution during the last decade resulted in the necessity of low latency high-speed systems. The important growth of data transfer foreseen in the wireless communications sector led to the implementation of wider broadband channels. As a consequence, new mobile networks such as the fifth generation and upcoming sixth generation demand more capacity and data rate performance than previous technologies [17]. These requirements encouraged researchers to push conventional communication systems from sub-6 GHz bands to higher frequencies such as Q-band, V-band and E-band, mostly used so far for military and radar applications. For the first time, millimeter-wave bands have been implemented in the new generations of mobile communications to increase the bandwidth and leverage the underutilized frequency spectrum. Several new bands have been treated recently by WRC-19 [27] for the standardization of 5G worldwide deployments (24.25 – 27.5, 31.8 – 33.4, 37 – 40.5, 40.5 – 42.5, 42.5 - 43.5, 45.5 - 47, 47 - 47.2 and 47.2 - 50.2 GHz). Millimeter-wave broadcasting emerges as a promising solution to provide higher spectrum efficiency for point-to-point communications, inter-satellite links, semi-autonomous 5G networks, vehicular communication, and health care applications, among others.

In order to provide continuous service to every part of the planet numerous terrestrial and satellite link networks are currently being deployed globally, while MIMO beam-forming systems are more and more utilized in those scenarios. The application of MIMO technologies requires a large amount of antenna arrays and electronic systems associated [36]. Low-cost hardware comprehended of reliable devices are needed to work under harsh conditions [26]. As seen in previous chapters, additive manufacturing could be a very useful approach to integrate heterogeneous technologies at device and subsystem level, reduce the footprint area and adapt the designs to space constraints. However, today's technological limitations of 3-D printing ceramic technologies hinder the development of additive manufactured microwave devices at K-, Ka- and millimeter-wave bands. The current minimum fabrication accuracy available and the manufacturing tolerances required at higher frequency bands cannot be still provided and tuning methods would drastically degrade the performances. Therefore, typical processes such as subtractive manufacturing could be still implemented for the conception of mm-Wave 5G devices. Unlike additive manufacturing, subtractive manufacturing consist of the material removal from a solid block by means of a controlled machining method such as cutting, boring, drilling, or grinding.

Many technological approaches [229] were implemented so far for mm-Wave applications with a trade-off between manufacturing dispersion, cost, fabrication steps, size, electromagnetic (EM) performances and temperature stability. For example, in multi-step processes such as LTCC, high 3-D integration can be obtained at expense of demanding alignment constraints and elevated prototyping costs [229]–[232]. Technologies such as stacked micro-machined silicon wafers [233], [234] and miniature coaxial resonators [235] must be fabricated in clean rooms or very well monitored environments. An alternative technology based on laser micro-machined process and 3-D plating was proposed in [236]. In organic-substrate SIW, temperature instability and high loss tangent limit the quality factor (Q), a problem that was successfully solved by air-filled SIW and ESIW technology [237]–[239].

Substrate integrated waveguide (SIW) filters have been widely utilized in communication applications, specially in radio-frequency front-ends due to their low-loss, low-cost, compact, flexible, and mass-producible features [44], [240]. Furthermore, their implementation in ceramic materials could provide compact devices with good EM properties and power handling capability.

During this chapter we will explore the application of subtractive methodologies for the conception of compact passive devices for 5G applications, mainly focused in mm-Wave bands suggested in WRC-19. The development of a three-step fabrication method, the

utilization of temperature-stable materials and the implementation of surface-mount technologies (SMT) for the integration of the devices in printed circuit boards systems will be introduced to the reader.

5.1 Laser Micro-machined Substrate Technology

Laser beam machining is a process that uses thermal energy focused in a confined spot to remove material from a target. The impact of high frequency photons on the target surface heats and vaporizes the material. Lasers are widely utilized for surface treatment, drilling and cutting processes. This manufacturing methods stand out for their good accuracy and low manufacturing dispersion. The laser beam can be focused to a small diameter producing high power density per area unit. Furthermore, no additional finishing is usually required and since no physical contact exists between the machining tool and the substrate, the maintenance costs are reduced. Moreover, laser machining can be applied to a great variety of materials ranging from metals to polymers and ceramics. The selection of the laser type and wavelength depends on the material to be treated. Solid-state lasers based on crystals such as yttrium aluminum garnet ($Y_3Al_5O_{12}$) or YAG became popular in the 1960s. Nd-YAG lasers emit light waves with high energy at the near infrared region and can cut high reflecting materials such as aluminium or copper.

The aforementioned characteristics are interesting properties for the development of microwave devices at mm-Wave bands. The development of a generic three-step manufacturing process based on laser beam machining is discussed in this section. The process named Laser Micro-machined Substrate Technology (LMST) has been mainly focused on laser-carved Alumina passive filters and enhanced to obtain the best possible performances through several generations. Many filter topologies were implemented in this technology as proofs of concept for millimeter-wave communication applications. Thanks to the the experience obtained several upgrades were applied to enhance the process performance.

5.1.1 Fabrication flow

LMST technology is a simple three-step generic manufacturing process [236], [241], [242] that consists of the device layout etching on the substrate (STEP 1); the component plating with a metallic coating (STEP 2) and the final details engraving such as ports or transmission lines on the metal surface (STEP 3). Fig. 5.1 describes

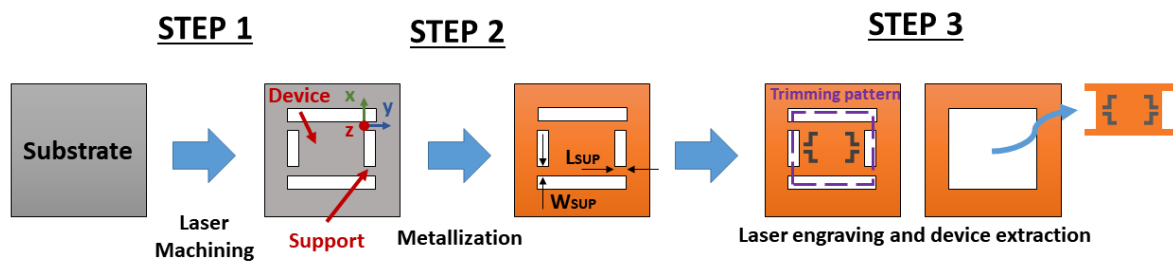


Figure 5.1: Laser micro-machined fabrication flow.

generically the fabrication flow developed for resonant cavity microwave components. In order to achieve a balance between size reduction, low manufacturing cost and EM performances, the process was specifically enhanced for mm-Wave devices developed on ceramic substrates. Ceramic materials are an attractive option for these applications thanks to their good properties such as low losses, high ϵ_r and acceptable thermal stability. However, the fabrication flow is independent to the substrate material since almost any material could be machined by selecting the right laser.

The first step consists of the device layout carved out of the substrate. The required manufacturing accuracy will depend mostly on the frequency range of the device. For Q-band applications, the dimensions of ceramic devices in the order of millimeters requires low tolerances to avoid post-fabrication corrections. To meet the specifications of 5G mm-Wave bands at 26 GHz and 40 GHz without extra tuning steps, all the components exhibited along this Chapter were manufactured using a $25 \mu m$ spot YAG laser with an accuracy of $10 \mu m$. The ceramic wastes that does not form part of the original design are carefully removed from the substrate until the main structure is completed.

The substrate is cleaned with an airbrush before the metallization process to remove potential ceramic particles that could remain attached after the machining, immersed in Isopropyl alcohol (C_3H_8O) and Acetone (C_3H_6O) to prepare the surface and improve the adherence of the metal particles. As explained in Chapter 3, the metal coating of Alumina substrates could be realized using electroless copper or aerosol silver deposition. The metal layer thickness greater than $3 \mu m$ allows to obtain an attenuation higher than seven times the penetration depth for the operating frequency band. In the case of electroless copper a final protective layer ($0.2 \mu m$) could be applied with gold electrolysis. The metallization processes were tested with different ceramic substrates utilized for every new generation to verify the correct deposition.

Once the substrate is completely coated (STEP 2), planar structures can be engraved into the metal surface to finalize the port terminals, circuit interconnections or any other required pattern (STEP 3). Special attention must be taken to avoid laser overpower that

could damage or lift the metallic plating during the process. The laser power is adjusted to prevent overetching into the ceramic and burning the structure. Tuning corrections such as those explained in Chapter 4 could be also carried out with this methodology. During the first and second generation (G1 and G2) the devices were directly extracted from the main substrate in STEP 1. After the third generation (G3) the components were extracted at the end of the process after the metal surface engraving during STEP 3. The reason for this modification is related to the process enhancement as a result of the observations made during previous fabrication tests and will be explained in the following sections.

5.1.2 LMST First Generation (G1)

The first manufacturing tests were carried out in a commercial 0.25 mm thick Alumina substrate with $\epsilon_r = 9.75$ and $\tan \delta = 3.3 \cdot 10^{-3}$. The purpose of the first generation was to test the methodology and highlight the main fabrication constraints. Every component was individually carved into the substrate and separated before the second step. Electroless copper process was implemented in this generation for metal coating. As a result, a 3 μm copper layer was deposited simultaneously on all the devices and covered in gold as an antioxidant protective layer.

A 4-pole dual-mode Chebyshev and a 6-pole quasi-elliptic filters were designed as devices under test [241] operating at $f_o = 39 \text{ GHz}$ with a bandwidth equals to $BW = 1.5 \text{ GHz}$. Additionally, TE_{201}/TE_{102} dual-mode ceramic resonators were fabricated to characterize the overall losses of the technology and estimate the copper layer conductivity. Resonator measurements exhibit a maximum unloaded quality factor of $Q_o = 150$ and a resulting conductivity of $\rho = 10 \text{ S}/\mu\text{m}$ at the resonance frequency. Manufacturing inaccuracies showed an average tolerance of $\pm 10 \mu\text{m}$ with a maximum deviation of 27 μm in the device pattern and $\pm 3 \mu\text{m}$ and $\pm 15 \mu\text{m}$ on the top face engraving, respectively. The measured filters response (fig. 5.2) depicts a center frequency shift of $f_o = 300 \text{ MHz}$ and a total insertion loss of 3.5 dB due to the low quality factor.

Two factors were clearly identified as limitations in this generation: the losses inherent to the Alumina substrate and the low quality of the metallic coating deposited with electroless copper plating. Figure 5.3 illustrates the theoretical influence of the metal layer conductivity, substrate loss and thickness on the unloaded quality factor (Q_o) in a TE_{102} rectangular cavity resonator. As it can be seen, an increment of the conductivity up to 20 $\text{S}/\mu\text{m}$ together with a higher quality ceramic substrate ($\tan \delta = 5 \cdot 10^{-4}$) could enhance Q_o up to 320 at 39 GHz. Moreover, the substrate thickness in TE_{m0p} modes

may help to increase the performances. For instance, a Q_0 around 700 could be achieved with a thickness of 0.6 mm.

5.1.3 LMST Second Generation (G2)

The conclusions obtained during the experiments performed in the first generation were considered during the design of the second generation. The electroless copper plating was replaced by an aerosol air-brushing silver coating with higher quality and better deposition control. A typical conductivity of $30 S/\mu m$ at 39 GHz was expected for a $3 \mu m$ to $4 \mu m$ silver layer deposited with this process. Additionally, a low-loss Alumina ($\epsilon_r = 9.94$ and $\tan \delta = 2.5 \cdot 10^{-4}$) developed in Limoges Research Institutes [236] was implemented to boost the filter performances. The substrates were characterized electromagnetically at the operating frequency and used as inputs for the design. The dual-mode filters manufactured in this generation showed a significant Q_0 improvement of 250% ($Q_0 \approx 400$) and an insertion loss reduction of 2 dB in comparison with previous devices (fig. 5.2.a). The measured dimensions were 5.98 mm x 2.76 mm x 0.6 mm. Even though very compact filters were achieved, the individual fabrication of the devices hindered their manipulation during the aerosol deposition process. As a consequence, the process control was affected reducing the quality of the metal layer and resulting in a poor conductivity. Nevertheless, an important improvement was observed in comparison with the previous generation in terms of performances and manufacturing accuracy. A frequency shift of 200 MHz, insertion loss of 1.65 dB and 1.34 GHz bandwidth were measured on the fabricated filters.

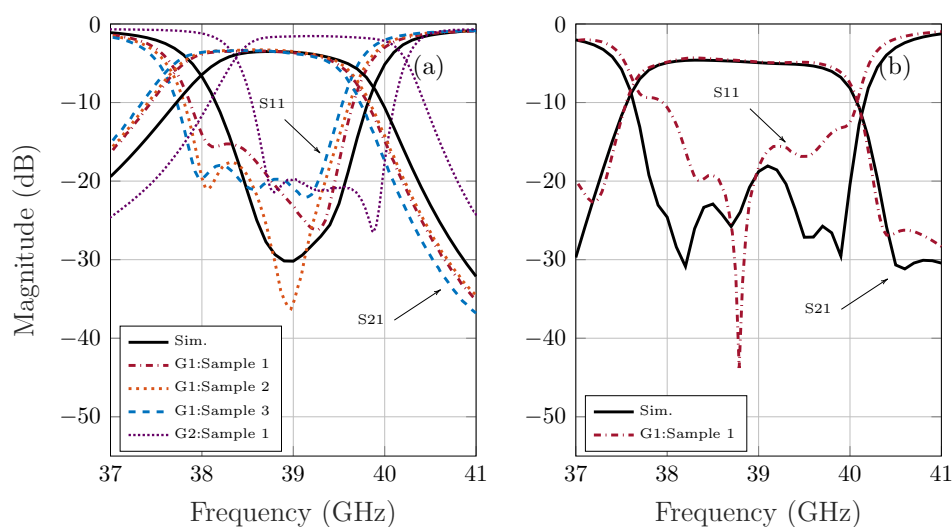


Figure 5.2: LMST filters: (a) 4-pole dual-mode Chebyshev (G1 and G2), (b) 6-pole quasi-elliptic (G1).

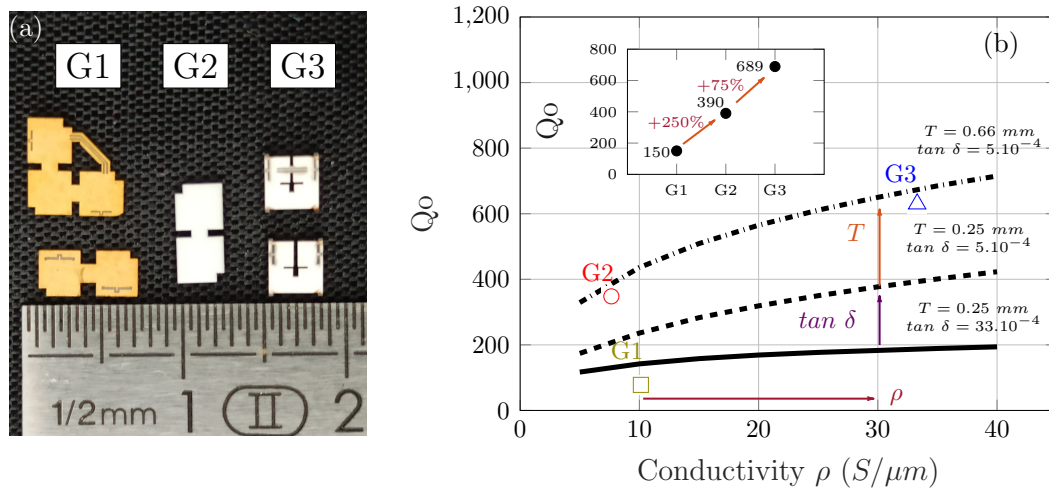


Figure 5.3: LMST evolution: (a) passive microwave filters and (b) quality factor dependency with the substrate loss ($\tan \delta$), electrical conductivity (ρ) and thickness (T) for a TE_{102} rectangular resonator.

5.1.4 LMST Third Generation (G3)

The problems observed in G2 were addressed in the following run. In this generation, a CMOS-like approach was employed to reduce the fabrication time and cost. Unlike in previous runs, the components are removed at the end of the process (STEP 3) instead of at the beginning. In this way, the substrate is more easily handled facilitating the silver coating process. Furthermore, the devices could be tested on-frame before the extraction to verify their compliance with the specifications. Broken or out-of-specifications devices could be identified in early stages and be discarded or tuned. After the second generation some critical points of the ongoing manufacturing process were corroborated showing sufficient technological maturity to move from individual to collective fabrication. Even more, a new batch of state-of-the-art ceramics developed in Limoges [243] were used for the study. As shown in fig. 5.3.b, the quality factor could be increased using thicker substrates. However, the maximum thickness observed is limited to approximately 0.7 mm due to laser focus constraints. Moreover, mechanical weaknesses observed during the laser machining of quasi-elliptic filters (G1) on narrow ceramic structures were also taken into account [241]. In the third generation the technology was pushed to the limits and deeply characterized to provide the designers with useful design rules [242]. Trenches were added during STEP 1 (fig. 5.1) in order to avoid frictions between the device and the substrate walls that could hinder the component removal. The spacing created by the trenches also improves the silver deposition during the metal coating process. The devices are held attached to the

substrate by supports as shown in fig. 5.1. The minimum trench size characterized in Alumina substrates is $160 \mu m$ while the minimum width to avoid cracks on the supports is $200 \mu m$. A theoretical $Q_o \approx 700$ is expected for devices fabricated with low-loss ceramics and coated with Jet Metal© silver coating.

Side walls and laser engraving characterization

The side walls machined in a 0.66 mm thickness (H_{SUS}) Alumina block were characterized to determine their manufactured quality and dispersion. Figure 5.4 depicts the images obtained with a digital microscope Keyence VHX-5000 utilized to estimate the size of the structures. Even though a maximum substrate thickness $H_{SUS} = 698 \mu m$ was measured (fig. 5.4.a), a separation of $50 \mu m$ between the microscope stage and the substrate was observed. As shown in figure 5.4.b the side walls surface exhibit a rough termination around the middle of the substrate. These imperfections are a consequence of the pulsed laser utilized in the fabrication process. Furthermore, in order to increase the maximum possible substrate thickness to be machined, the substrate was cut from one side (1st etching) to half the height and then flipped, aligned and machined again from the bottom (2nd etching). This approach allows to reduce the laser dispersion and to machine thicker substrates. Nevertheless, the misalignment could cause a discontinuity between the upper and the lower side of the wall increasing the manufacturing dispersion (fig. 5.4.a). A typical difference of $\Delta X = 8 \mu m$ was observed in the measured sample profiles.

To better characterize the side wall imperfections as well as the profile and the surface roughness the substrate was measured with a Scanning Electron Microscope (SEM) and a profilometer. Measurements performed in the cross section of a silver plated support extracted from the substrate reveal a total substrate thickness of 0.66 mm (fig. 5.5.a). The surface imperfections on the trimmed face can be clearly seen in the picture. 3-D profilometry tests performed on the trimmed support concentrated in this region exhibit an Alumina surface average roughness of $Ra_{subs.} = 716 \text{ nm}$ as a consequence of the grooves left by the laser machining. Similar measurements realized in the silver layer shows a surface roughness of $Ra_{silver} = 556 \text{ nm}$. A metal layer thickness dispersion was also noticed as a product of the irregular deposition around the device surface (fig. 5.5.b). Considering that the laser inaccuracy increases with the etching depth, the lateral walls profile was characterized for the maximum substrate thickness. Measurements obtained with a stylus profilometer reveal a slight slope on the lateral walls with an average deviation of $4 \mu m$ to $5 \mu m$. The combined effect of the laser inaccuracy with the

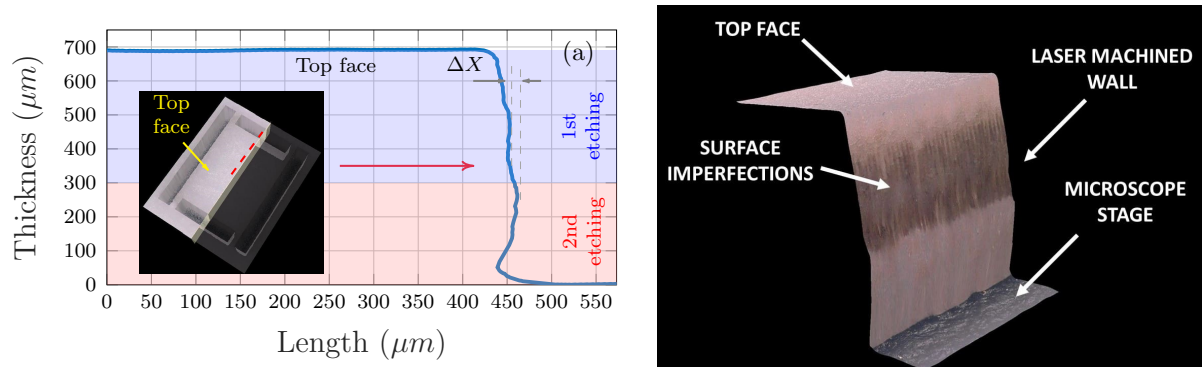


Figure 5.4: Rectangular resonator profile (a) and 3-D reconstruction of the side wall (b) measured with a digital microscope.

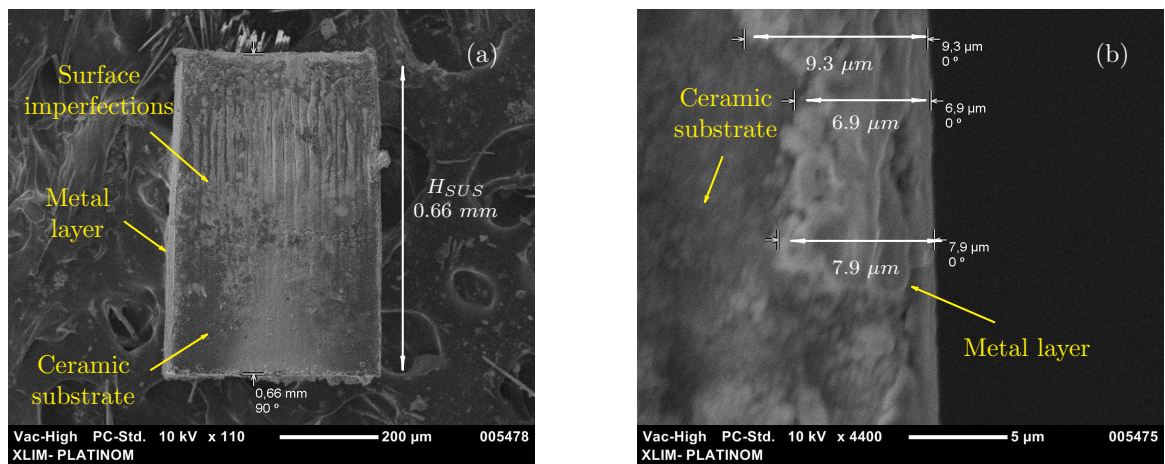


Figure 5.5: SEM images of LMST structures fabricated in G3. Cross section of silver coated Alumina substrate (a). Metal layer after support trimming (b).

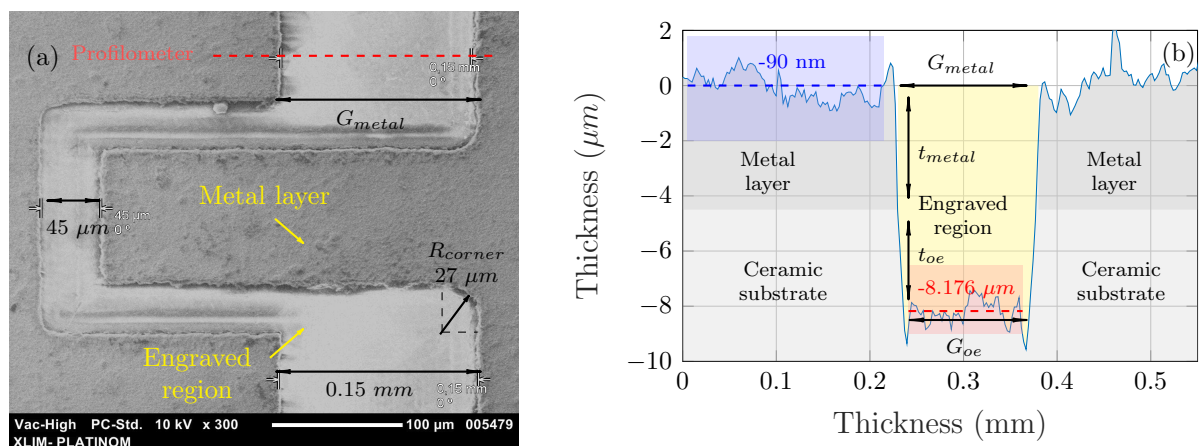


Figure 5.6: Coplanar access engraving on silver layer: (a) SEM and (b) profilometer measurements. A total ceramic substrate over-etching (t_{oe}) of 3.586 μm is measured.

lateral walls imperfections results in a fabrication tolerance of $15 \mu m$ and a maximum deviation of $30 \mu m$. Even though the side walls dispersion cannot be neglected and should be taken into account during the design, the manufacturing deviation results in a lower dispersion than typical PCB or LTCC processes. The characterized tolerances are in a good compromise between Q-factor improvement and fabrication accuracy. In regard to the engraving of planar structures, the ceramic substrate over-etching caused by the laser was characterized on the fabricated components metal surface. Figure 5.6 shows the measurements performed with the SEM and the profilometer in the coplanar accesses realized. No burned regions or metal layer lifting were observed on the engraved surface. A closer look with the profilometer served to estimate the quality of the patterns. In order to discern between the metal layer and the engraved substrate depth, the data contained into the highlighted regions (red and blue in fig. 5.6) was utilized to calculate the average vertical positions. As a result, a total engraved depth of $t_{metal} + t_{oe} = 8.086 \mu m$ was measured. Additionally, the boundary between the deposited metal layer and the ceramic substrate can be identified at $-4.5 \mu m$ ($t_{metal} \simeq 4.49 \mu m$). Hence, an over-etching of $t_{oe} = 3.586 \mu m$ into the ceramic substrate can be expected for the laser parameters selected. The laser accuracy could also be corroborated by comparing the dimensions measured with the SEM and the profilometer. In the case of a target gap of $G_{metal} = 150 \mu m$, measurements show a fabricated gap of $G_{metal (SEM)} = 0.15 mm$ and $G_{metal (prof.)} = 154.7 \mu m$, respectively. Furthermore, the measured gap is reduced down to $G_{metal (prof.)} = 147.2 \mu m$ in the metal layer/ceramic substrate interface and $G_{oe (prof.)} = 137.2 \mu m$ in the over-etched substrate. Straight angles show a maximum rounding corner radius of $R_{corner} = 27 \mu m$. The manufacturing tolerances and roughness observed on the side walls can be used to perform useful sensitivity analysis during the design and estimate the performances of the devices. Moreover, the substrate over-etching on planar structures can also slightly modify the external coupling as in the case of coplanar access ports, affecting the frequency response of passive microwave components. Therefore, the manufacturing process characterization provides essential information for designing.

Collective manufacturing

The necessity to facilitate the handling of the devices added to the high manufacturing time and costs motivated the search for a solution to both problems. In CMOS processes, the silicon wafer surface is distributed between dies of standard area that contains the integrated circuits. The devices are fabricated in parallel and tested on-wafer to

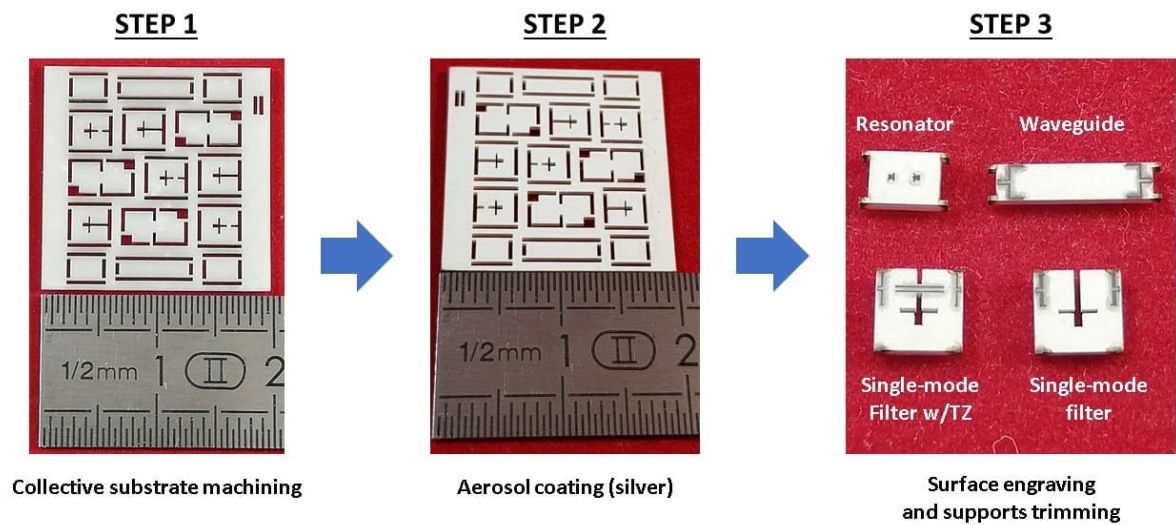


Figure 5.7: LMST collective fabrication (G3) of microwave passive devices: 4-pole band-pass filters, waveguides and cavity resonators.

identify failed dies. At the same time, the highly integrated technologies and parallel manufacturing approach enhance the production efficiency in less time and lower costs. CMOS fabrication process was the inspiration for the conception of affordable ceramic microwave devices in LMST G3. The devices were contained in frames and attached to the substrate until the end of the process by mechanical supports with negligible electromagnetic impact on the filters. Trenches and supports were carved into the substrate during the first step to create those links. The filters were designed in a square fashion arrangement (G3 in fig. 5.7) for future surface-mount assembly compatibility with industrial pick and place machines. The devices were more easily manipulated thanks to the surrounding substrate frames. Besides, the use of trenches helped to improve the aerosol silver particle deposition during the metallization process. No special considerations were taken during the metallic layer laser etching since no structural or adherence problems were identified. The substrate thickness was measured at several positions to determine the dispersion ΔH_{SUS} since in TE_{m0p} modes the quality factor is sensitive to this parameter. As a result, $\Delta H_{SUS} = 30 \mu m$ and a slight $55 \mu m$ substrate bending were found. Flatness is a critical parameter for SMD devices that could affect the final performance of the device. A surface polishing treatment could be applied to the surface before the laser micro-machining to ensure a correct roughness and flatness. Figure 5.7 depicts the collective manufacturing implementation of several passive components. Every component is confined in frames and linked to the substrate by mechanical supports. The devices were placed along the substrate in a zig-zag pattern

to make the best possible use of the available surface. The supports were designed to have no influence on the device and avoid EM field leakage in the surrounding area during the preliminary measurements.

Electromagnetic study of supports

The main function of auxiliary support structures is to maintain the devices fixed to the substrate facilitating the handling of the part during the metallization. The minimum length of the supports should guarantee a separation from the substrate wide enough to ensure the correct deposition of a thick layer of metal particles on the side walls. The correct metallization quality will determine the effective conductivity of the metallic layer and the device performances. Once the patterns are engraved, the device is separated by trimming the mechanical supports to finalize the process. Nevertheless, their utilization could interfere with the proper operation of the devices. On the one hand, they could propagate the EM field from the device to the substrate during measurement tests before their separation. On the other hand, once the metallic coating is removed from the support termination during the device extraction, the EM field could radiate to the surroundings through the supports [244]. For that reason, the negative effect of supports on the process needs be addressed in order to reduce their influence.

The first resonance modes in rectangular cavity resonators are usually TE_{m0p} (m and $p \in \mathbb{N}$) if the substrate thickness is much smaller than the device area. The minimum magnitude of both electric (E) and magnetic (H) fields can be found in the corners of the resonator. This is an attractive region to place the supports since the EM field is less sensitive to shape irregularities. The supports act as rectangular waveguides excited by the resonator in a position where EM field magnitude is minimum. In this frame, there are two parameters to control the EM field leakage of a resonator: the support length (L_{SUP}) and the width (W_{SUP}), as shown in fig. 5.1. Given the thickness homogeneity H_{SUB} throughout the substrate the only parameter left to control the waveguide cutoff frequency (f_c) is the width. If $W_{SUP} \ll W_{RES}$ the TE_{10} cutoff frequency is placed at higher frequencies than the operating band owing to W_{SUP} is always smaller than the resonator width ($W_{RES} = \lambda/2$), thus preventing the EM field to propagate [245]. However, the waveguide exhibits a rapid attenuation from the resonator-support to the support-air interfaces below the cutoff frequency (f_c) [246], [247]. As shown in eq. 5.1, the magnitude of the electromagnetic field at the support-air interface could be modified with L_{SUP} . E_o is the E-field along the x- direction in the resonator-support interface, β is the propagation constant in rad/s (eq. 5.2), v is the velocity of propagation in the

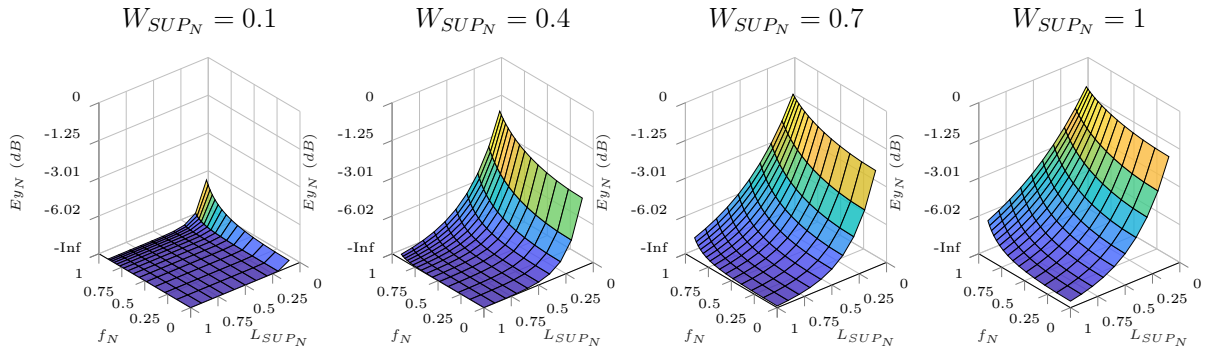


Figure 5.8: Electromagnetic field attenuation in function of normalized (N) values for the guided wave frequency ($f < f_c$ or $f_N < 1$), support length and width.

dielectric in m/s and f the frequency in Hz.

$$E_y = E_o(x) \cdot e^{-\beta L_{SUP}} \quad (5.1)$$

$$\beta = 2\pi \cdot v^{-1} \sqrt{f_c^2 - f^2} \quad (5.2)$$

The attenuation of the evanescent modes could also be controlled by modifying $f_c(T E_{10}) = v \cdot (2 \cdot W_{SUP})^{-1}$ with W_{SUP} . The structures could be dimensioned to reduce the EM field leakage and avoid strong radiation losses. Figure 5.8 depicts the attenuation of the E-field along a dielectric-filled rectangular waveguide $E_y(L_{SUP}, W_{SUP}, f)$ (normalized to $E_y(0, W_{SUP}, f_c)$: $Ey_N = E_y(L_{SUP}, W_{SUP}, f) / E_y(0, W_{SUP}, f_c)$). Since the waveguide cutoff frequency depends on W_{SUP} , the frequencies below $f_c(W_{SUP})$ has been normalized as $f_N = f / f_c$ for every width to provide a direct comparison of the E-field attenuation. As it can be seen, the E-field diminishes when W_{SUP} decreases (normalized to W_{RES} : $W_{SUP_N} = W_{SUP} / W_{RES}$) or when L_{SUP} increases (normalized to L_{RES} : $L_{SUP_N} = L_{SUP} / L_{RES}$). The control of the support parameters could be also useful to modify the behaviour of resonance modes and to finely tune the frequency. This concept will be introduced in Section 5.5. The dimensions of the supports can be calculated for a given attenuation of the EM field based on the conditions established in equation 5.1. Nevertheless, the design rules suggested in [242] should be considered when determining the supports size. On the one hand, the minimum support length ($160 \mu m$ or $4.3\% L_{RES}$) is limited to ensure the proper deposition of a thick metal layer on the side walls. On the other hand, the support size is restricted to a minimum width, typically $200 \mu m$ in order to avoid cracks or structural damage on the substrate.

5.1.5 Manufactured millimeter-wave devices

The information gathered during the characterization tests was utilized to design and manufacture a set of low-loss Alumina-based passive devices. The substrate was characterized in the laboratory [248] before the design stage showing a permittivity of $\epsilon_r = 9.8 \pm 0.4$ and $\tan \delta = 5.10^{-4}$ at 42 GHz. A collective fabrication approach was implemented to meet the specifications of potential 5G front-ends using the suggested design rules in the full-wave EM simulator and designed to operate in the European millimeter-wave band (40.5 - 43.5 GHz) [26]. A set of 15 passive devices were engraved in a 20 mm x 20 mm x 0.66 mm Alumina substrate and coated in silver with aerosol deposition. Four rectangular cavity resonators, two rectangular waveguides and several band-pass filters were developed to test the process enhancement and analyze the performances. The devices were directly machined into the substrate in confined regions (see fig. 5.7) and linked to the substrate with supports designed using the methodology explained in the following section. Additionally, the coplanar accesses were optimized for direct probe testing.

Rectangular cavity resonator

Resonators are key design blocks for passive cavity filters since they allow to estimate the resonance frequency, the substrate permittivity and the overall losses of the technology. Rectangular resonators operating in the fundamental mode TE_{101} are smaller than higher order modes and ideal for compact single-mode filters. However, these resonators exhibit lower Qo and are more sensitive to fabrication dispersion. For instance, considering manufacturing tolerances of $\pm 30 \mu m$, a 1.6 mm x 1.6 mm dielectric-filled resonator presents a frequency shift of $\Delta f_{TE_{101}} = 808 MHz$ at 42 GHz while a 2.12 mm x 2.70 mm TE_{102} resonator shows a frequency shift of $\Delta f_{TE_{102}} = 511 MHz$ for the same conditions. Furthermore, an increment of 19.5% Qo could be obtained when using the TE_{102} mode in expense of 46.8% more area. In regard to permittivity discrepancies, the resonance frequency is identically shifted in both modes. For example, a variation of $|\Delta \epsilon_r| = 0.2$ produces $|\Delta f_{TE_{101}}| = |\Delta f_{TE_{102}}| = 436 MHz$. As a conclusion, TE_{102} resonators are less affected by manufacturing dispersion and more suitable for electrical characterization in expense of higher area consumption and less spurious modes frequency separation in the stop-band.

Several TE_{102} rectangular cavity resonators were designed in order to characterize the EM properties at 42 GHz of the low-loss ceramic substrate chosen for this generation. Figure 5.9.a illustrates the electric and magnetic fields distribution simulated

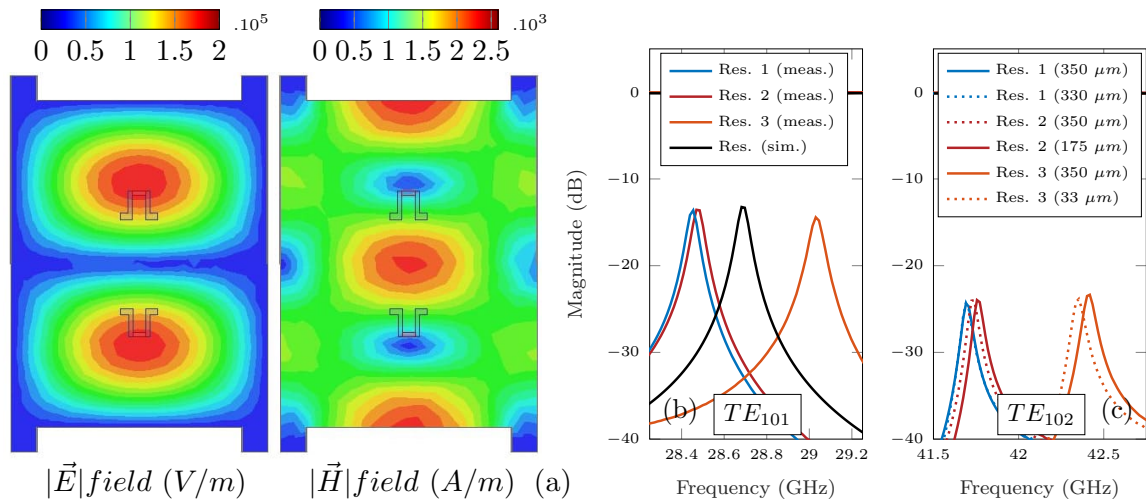


Figure 5.9: Simulated EM fields of a ceramic rectangular cavity resonator at 42 GHz (TE_{102} absolute values) (a). S-parameters comparison of three ceramic-filled rectangular cavity resonator samples: TE_{101} mode resonance frequency measured on-frame (b), and measured TE_{102} modes before ($L_{sup} = 350 \mu m$) and after the device separation from the substrate, testing different lengths for L_{sup} (330, 175 and $33 \mu m$) (c).

in HFSS at this frequency. Firstly, the S-parameters of the resonators were tested on-frame before their separation from the substrate ($L_{SUP} = 13.04\%L_{RES}$) with a Rohde & Schwarz ZVA67 VNA connected to a probe station with a $125 \mu m$ pitch GSG tip. The devices were externally excited by coplanar ports engraved on the metal surface. Figures 5.9.b and 5.9.c show the TE_{101} and TE_{102} resonance modes measured on different samples. The accesses were designed to provide low coupling to TE_{102} mode, neglect the influence of the external coupling in the loaded Q, and facilitate the direct measurement of Q_0 . A frequency shift can be noticed in both modes as a consequence of the manufacturing tolerances. For instance, fig. 5.9.b illustrates the TE_{101} mode S-parameters of three samples measured on-frame compared to the simulated design. The different resonator samples were characterized in size with a digital microscope revealing a tolerance up to $30 \mu m$. The combined effect of manufacturing dispersion and permittivity mismatch leads to a maximum frequency shift of $|\Delta f_o(TE_{102})| = 331 MHz$ (see fig. 5.9.b) for resonator 2. On the one hand, the effect of frequency shift owing to the actual resonator dimensions can be contemplated in a simulation environment. Full-wave back-simulations performed using the measured size reflect a frequency shift of $|\Delta f_o(TE_{102})| = 425 MHz$ to higher frequencies for resonator 2. Therefore, it is possible to extract with this information the electrical permittivity of the Alumina substrate. A parametric analysis of the permittivity shows that in order to shift f_0 to lower frequencies the permittivity should augment from 9.8 to 10.1. The difference of $\Delta\epsilon_r = \pm 0.3$ is within

Table 5.1: Measured dispersion in two manufactured resonator samples.

Parameter	Resonator 1	Resonator 2
$Width(W)$	2.090 mm	2.102 mm
$Length(L)$	2.676 mm	2.687 mm
$ \Delta W $	30 μm	20 μm
$ \Delta L $	24 μm	13 μm
$ \Delta f_o(T E_{102}) _{@42GHz}$	331 MHz	296 MHz
$ \Delta f_o(T E_{101}) _{@28.72GHz}$	249 MHz	223 MHz
$\epsilon_r_{@42GHz}$	10.16	10.08
$Q_{@42GHz}$	689	673

the dispersion range informed during the substrate characterization. The calculated ϵ_r was also verified in resonator 1 implementing the same methodology. In regard to the losses, loaded quality factors ($Q_L \approx Q_o$) between 673 and 689 were measured in the manufactured resonators. These values are very close to the expected quality factor of 700 demonstrating a significant improvement and maturity of the technology. Table 5.1 summarizes the measured size, frequency shifting, ϵ_r and Q for two manufactured $T E_{102}$ resonators with the fundamental mode located at 28.72 GHz.

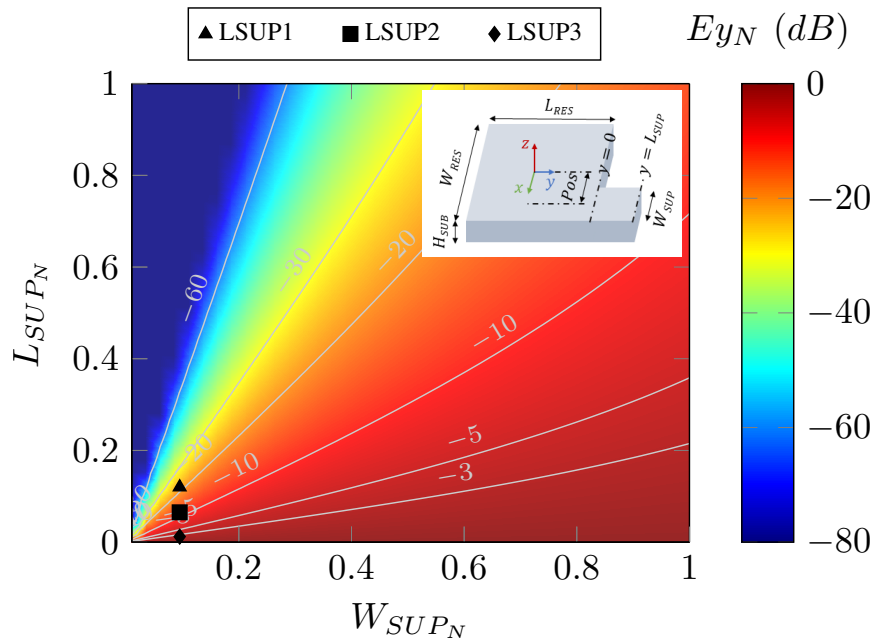


Figure 5.10: Attenuation of E_y at $f_0 = 42 \text{ GHz}$ for a given L_{SUP} and W_{SUP} . The markers indicates the supports size used in LMST G3.

In regard to the supports design, an arrangement of four supports was applied in every corner of the manufactured ceramic resonators (fig. 5.9.a). The support width was fixed to the minimum recommended size for a 0.66 mm thick Alumina substrate ($W_{SUP} = 200 \mu m$ or $9.5\%W_{RES}$) to shift the support cutoff frequency towards high frequencies ($f_c \geq 225 GHz$). The maximum support length $L_{SUP_{max}}$ was chosen to be approximately the double of the minimum trench size to guarantee a good metal coating on the side walls and avoid a brittle structure. The resonators were carved into the substrate with a support length of $L_{SUP_{max}} = 350 \mu m$ ($L_{SUP_{max}} = 13.04\%L_{RES}$) and trimmed at $L_{SUP1} = 330 \mu m$ ($12.3\%L_{RES}$), $L_{SUP2} = 175 \mu m$ ($6.5\%L_{RES}$) and $L_{SUP3} = 33 \mu m$ ($1.2\%L_{RES}$), respectively. Figure 5.10 depicts the computed E-field attenuation in the support/air interface ($y = L_{SUP}$) for these dimensions at the resonator operating frequency ($f_0 = 42 GHz$). As it can be seen, the attenuation increases with the support length. This observation can also be noted in fig. 5.9.c, where the frequency shift and Q-factor variation increase as L_{SUP} is shortened. Measurements performed before and after the resonators trimming exhibit a relative resonance frequency variation less than 100. $|f_0(sep.)/f_0(substrate)| \leq 0.3\%$ and a relative degradation of the quality factor of 100. $|Qo(sep.)/Qo(substrate)| \leq 2\%$ for the different support lengths. For the worst case ($L_{SUP3} = 1.2\%L_{RES}$) the attenuation of 3 dB represents a frequency shift of 126 MHz and a Q-factor reduction of 14. However, since the center frequency and the Q-factor degradation have an exponentially decreasing trend with the support length, it is recommended to set $L_{SUP_N} \geq 10\%$ to be closer to the horizontal asymptote and better attenuation than 20 dB.

Rectangular waveguide

Waveguides are other basic passive element useful for EM wave transmission in microwave systems. Nevertheless, these devices were never fabricated in LMST technology until now. In LMST G3 a 1.45 mm x 6.00 mm rectangular waveguide was designed for Q-band applications. The fundamental mode cutoff frequency $f_c(TE_{10})$ is located at 34.5 GHz with these geometrical dimensions, while for the next mode $f_c(TE_{20})$ is placed higher in frequency at 66 GHz. The coplanar to waveguide transition is often the most challenging part in these kind of designs, especially when implemented on thick substrates with high electrical permittivity. Some transitions were proposed in [249] where a dipole termination with series stub is employed to adapt the line. In [250], two resonators are coupled to the access ports to excite the waveguide. However, this approach increases the bandwidth (BW) by sacrificing area. The waveguide ports were

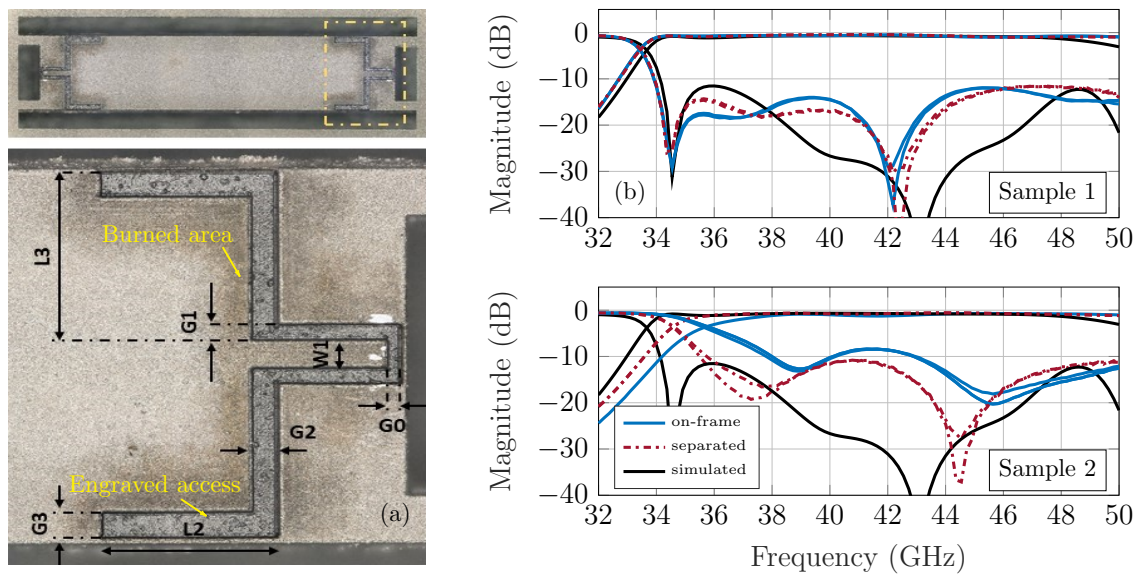


Figure 5.11: Manufactured ceramic rectangular waveguide: engraved coplanar access (a), and simulated and measured S-parameters of two samples (b).

performed through coplanar accesses (fig. 5.11.a) engraved in the metal layer. In order to perform the transition in the desired frequency band, the coplanar accesses were optimized with 3-D EM simulation software to increase the coupling in the desired frequency range. The optimized access dimensions are $G_0 = G_1 = 61 \mu\text{m}$, $G_2 = G_3 = 100 \mu\text{m}$, $W_1 = 104 \mu\text{m}$, $W_2 = 1.2 \text{ mm}$, $L_1 = 450 \mu\text{m}$, $L_2 = 500 \mu\text{m}$ (fig. 5.11.a). Although a change of color could be noticed in the machined surrounding area as a result of the metal surface heating, a clean fabrication of the pattern is observed. The devices were tested on-frame in parallel with the rest of the devices and re-measured after their separation. As in the case of the rectangular cavity resonators, the arrangement utilized for the supports design also contains four structures on the corners of $W_{SUP} = 200 \mu\text{m}$ and trenches of $L_{SUP} = 350 \mu\text{m}$. In this occasion, the supports were trimmed at the maximum support length. The measurements of the S-parameters performed in the two fabricated samples are exhibited in fig. 5.11.b. Sample 1 shows a return loss and attenuation better than 14 dB and 0.13 dB/mm, respectively, in the range of 34.2 GHz to 43.8 GHz for the tested on-frame device. The final separated device response slightly changes its bandwidth to 34.0 - 44.7 GHz and the maximum attenuation increases to 0.15 dB/mm. It has to be noted that an important mismatch between the simulations and the measured results is present between 38 GHz to 48 GHz. Mismatches observed could be due to manufacturing imperfections in the coplanar accesses and differences between simulation ports and probes position. The measured response obtained during the testing stage of sample 2 revealed an unsatisfactory operation of the waveguide in

comparison to the results obtained for the same structure in the first sample. A visual verification of the structure corroborated the suspicions of failures in the fabricated device since coating damages were found on the back side, probably as a result of the substrate manipulation. However, on-frame testing demonstrated to be a valuable approach to identify failed devices in early stages.

5G millimeter-wave band-pass filters

As it has been explained throughout this thesis, band-pass filters are crucial devices in communication applications and highly demanded components in transmitter and receptors systems. Owing to their relevance, different filters were developed in LMST technologies as proof of concept to assess their performances. During this generation, two band-pass filter topologies were designed to operate in the European 5G mm-Wave band at 40 GHz and extend the studied cases: a single-mode filter (SMF) and a single-mode filter with two transmission zeros (TZ). Despite LMST dual-mode filters (DM) designed in previous generations [251] exhibited good performances, their attenuation was limited owing to the spurious fundamental mode TE_{101} located at lower frequencies. A Chebyshev topology was implemented using the fundamental TE_{101} mode to enhance the rejection at low frequencies and obtain the most compact filter size as possible in expense of lower quality factor. Simulations performed in a 5.11 mm x 2.68 mm

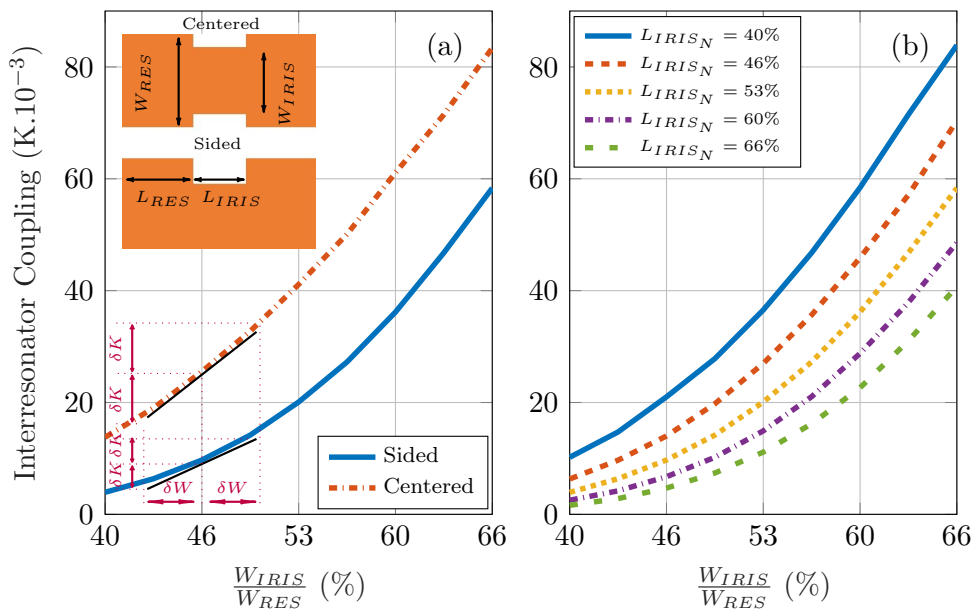


Figure 5.12: Inter-resonator coupling variation with: iris position ($L_{IRIS_N} = \frac{L_{IRIS}}{L_{RES}} = 53\%$) (a) and length (sided) (b).

DM filter with the aforementioned specifications show filter rejection up to 23 dB at 34 GHz. In order to accomplish a return loss better than 20 dB and pass band ripple below 0.5 dB, the coupling matrix for a 4-poles filter with these characteristics should match with the target matrix shown in equation 5.3. One way to reduce the filter sensitivity to manufacturing tolerances is to perform inter-resonator couplings with inductive irises placed on one side (fig. 5.12.a and 5.12.b). Despite having less coupling factor than a centered iris for the same length (fig. 5.12.a), the fluctuation linked to size dispersion is diminished (see the slope of the tangents shown in fig. 5.12.a), thus partially compensating the sensitivity to fabrication inaccuracy.

$$M_{SMF} = \begin{bmatrix} 0 & 1.04 & 0 & 0 & 0 & 0 \\ 1.04 & 0 & 0.91 & 0 & 0 & 0 \\ 0 & 0.91 & 0 & 0.70 & 0 & 0 \\ 0 & 0 & 0.70 & 0 & 0.91 & 0 \\ 0 & 0 & 0 & 0.91 & 0 & 1.04 \\ 0 & 0 & 0 & 0 & 1.04 & 0 \end{bmatrix} \quad (5.3)$$

Additionally, this approach saves time during the substrate machining by simplifying the pattern, leads to increasing the width for a given coupling and avoids violating size restrictions that could damage the device during the cutting process. The iris length (L_{IRIS}) could also be modified to adjust the coupling to more convenient values (fig. 5.12.b). The final design should show a good trade-off between mechanical robustness, sensitivity and total size. A second filter was synthesized from the SMF to improve the selectivity of the filter in the transition and the stop band, adding two transmission zeros by means of a coplanar line between the input and the output resonators. As in can be seen in eq. 5.4 the target coupling matrix values are similar as in the case of the SMF with the addition of $m_{41} = m_{14} = -0.17$.

$$M_{TZ} = \begin{bmatrix} 0 & 1.02 & 0 & 0 & 0 & 0 \\ 1.02 & 0 & 0.87 & 0 & -0.17 & 0 \\ 0 & 0.87 & 0 & 0.77 & 0 & 0 \\ 0 & 0 & 0.77 & 0 & 0.87 & 0 \\ 0 & -0.17 & 0 & 0.87 & 0 & 1.02 \\ 0 & 0 & 0 & 0 & 1.02 & 0 \end{bmatrix} \quad (5.4)$$

The band-pass filters described in equations 5.3 and 5.4 were designed, simulated and

optimized in HFSS. Unlike the inter-resonator couplings, the coplanar line implemented in TZ was centered to the resonators to provide better control on the coupling with minimum influence of the iris below the line. The coplanar line used to implement the transmission zeros presents a resonance at 33.3 GHz, limiting the attenuation at low frequencies.

A sensitivity analysis was also performed implementing the manufacturing tolerances extracted from the process characterization in Section 5.1.4 to estimate the worst filter response to be expected. The analysis over 100 simulations applied to all the geometrical parameters of the design shows as a result a minimum return loss better than $RL \geq 15.45 \text{ dB}$, insertion loss $IL \leq 0.82 \text{ dB}$ and frequency shift lower than $\Delta f_o \leq 162 \text{ MHz}$ (see fig. 5.13). The total filter size for the SMF is a 3.07 mm x 3.26 mm and slightly larger (3.13 mm x 3.24 mm) for the modified version with transmission zeros. The S-parameters measurements were carried out with the same setup as the resonators and waveguides. Figure 5.13 depicts the measured S-parameters of several 3.13 mm x 3.24 mm x 0.66 mm filter samples manufactured during the third LMST generation. The obtained results show a return loss of $RL \geq 17.7 \text{ dB}$ and $IL \leq 1.1 \text{ dB}$ between 40.35 GHz to 43.10 GHz for the SMF, and $RL \geq 15.5 \text{ dB}$ and $IL \leq 1 \text{ dB}$ between 40.45 and 43.28 GHz for the TZ.

Although the filters are shifted due to the combined dispersion of the substrate permittivity and the process tolerances, the manufactured devices fit properly with the simulations and the sensitivity analysis in both cases. Three samples of each topology

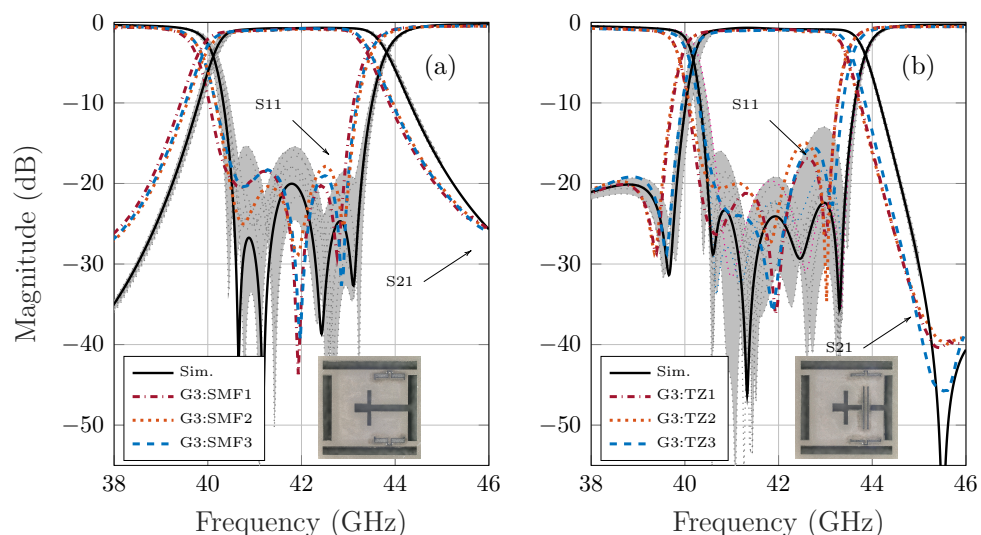


Figure 5.13: LMST filters: 4-pole single-mode Chebyshev G3 without (a) and with transmission zeros (b). The area colored in gray illustrates the simulated geometrical parameters sensitivity analysis.

Table 5.2: LMST G3 measured filters performances.

Sample	Area (mm x mm)	BW (GHz)	RL (dB)	IL (dB)	Atten. @ 34 GHz (dB)	Atten.@ 50 GHz (dB)	Ripple (dB)
SMF1	3.38 x 3.11	40.2 - 42.9	18.4	0.78	34	29	0.25
SMF2	3.37 x 3.11	40.4 - 43.0	17.9	0.86	35	30	0.31
SMF3	3.37 x 3.11	40.4 - 43.0	18.1	0.77	34	30	0.41
TZ1	3.34 x 3.12	40.2 - 43.1	16.5	0.87	18	31	0.31
TZ2	3.35 x 3.12	40.2 - 43.1	14.9	0.89	18	32	0.23
TZ3	3.32 x 3.10	40.4 - 43.3	15.5	0.94	17	32	0.21

were fabricated to test the process repeatability. Measurements shows a consistent frequency response with good characteristics in all the samples. Filter performances can be consulted in Table 5.2 for both topologies. Supports were taken also into account during the design, and their size and position were optimized in HFSS to reduce their impact on the final response. Comparisons between filters with and without supports show negligible changes and fit with the specifications for all cases. Measurements show a good repeatability for the same run. Return losses between 15 and 18 dB were obtained for single-mode Chebyshev topologies while insertion losses do not exceed 0.95 dB in any case. A maximum frequency shift of 300 MHz was found as a consequence of permittivity dispersion while the bandwidth reduction ranges between 100 and 400 MHz. Post-manufacturing laser corrections could be performed to overcome this problem and achieve the final specifications.

Measurements show a good repeatability between samples and a clear improvement in comparison with the previous generations.

5.2 Temperature stability and surface-mount devices

There is a constant necessity for electronic devices to provide better features in terms of area, performances, reliability and costs for communication applications. In the case of ceramic technologies, they are usually more expensive than SIW devices manufactured in organic PCB substrates and rather costly for large-scale production. Hence, affordable fabrication strategies are required to reduce the manufacturing costs. In CMOS processes, scaling and collective fabrication have been widely used in the semiconductor industry to increment the density of integrated circuits on wafer and maximize the

profits [252]. As part of the upgrades introduced in LMST G3, collective manufacturing was successfully implemented to leverage the substrate area, enhance the metallization deposition process control and identify failed devices before the final extraction. Ceramic materials present good performances in terms of loss tangent and require less area thanks to their permittivity, contributing to increase the scale of integration. Additionally, this approach provides higher flexibility for the creation of micro-machined discrete surface-mount components or monolithic subsystems developed in ceramic substrates. The implementation of collective fabrication in LMST technology could reduce the production time and cost, lead to the automation of technology within an industrial process.

Temperature stability and power handling capability are major aspects in electronic systems reliability under harsh environments. Heating due to power dissipation or environmental temperature fluctuations could produce malfunctions or working frequency band shifts. Under these conditions, bulk components as waveguide technologies provide better power handling capabilities than planar technologies. Spacecraft systems, satellite communications links and military applications demand high-performance devices working in a wide temperature range (-55°C to 125°C). Even more, temperature issues in mobile phones were reported in the first 5G generation devices as a consequence of the high data rate handled [20]. Even though nowadays there are several temperature stable technologies, ceramic materials have the ability to support repeated temperature fluctuations, dissipate heat and remain functional at higher operating power levels and temperatures. Therefore, ceramic materials are an interesting choice for reliable devices under harsh conditions. Hence, it is of our interest to provide LMST ceramic microwave devices that could accomplish the necessities and requirements of these industrial sectors.

The specifications in terms of thermal stability and standard surface-mount technology (SMT) were addressed in the fourth generation (G4) of LMST. The technology improvements during G3 were implemented on a off-the-shelf thermally-stable substrate for 5G millimeter-wave (mm-Wave) filter development. Problems caused by temperature drift were addressed to extend the operating range for communication applications under harsh environments. The results obtained from a thermal reliability study were compared to the Alumina filters manufactured in the previous generation. Furthermore, the coplanar access used for probe station measurements were designed to provide a flip-chip SMT transition once the device is separated.

5.2.1 Thermal study of LMST G3

In order to characterize the temperature constraints of LMST G3 Alumina filters, a non-destructive thermal analysis was performed in a test bench compound by a Peltier cell controlled by a temperature source (fig. 5.14.a). The devices under test (DUTs) were separated from the frame and measured with a ZVA 87 VNA connected to a 125 μm pitch GSG probe tip. The DUTs were gradually heated with a Peltier cell in steps of 10 $^{\circ}\text{C}$ between 30 $^{\circ}\text{C}$ and 80 $^{\circ}\text{C}$ while device temperature was monitored with a sensor placed on the top of the device. A total frequency shift around 200 MHz (0.48% of the center frequency) giving a frequency drift of $f_0(T) = -2.1 \text{ MHz}/^{\circ}\text{C}$, and a degradation of Q_0 from 689 to 667 was measured in Alumina resonators. In the case of passive filters, the pass band shifts towards lower frequencies while the bandwidth remains relatively stable due to the homogeneous temperature distribution on the device (fig. 5.15). Results show a center frequency ($\Delta f_0(T)$), bandwidth ($\Delta BW(T)$) and insertion losses ($\Delta IL(T)$) dependency to temperature of: $\Delta f_0(T) = -2.45 \text{ MHz}/^{\circ}\text{C}$, $\Delta BW(T) = -483 \text{ kHz}/^{\circ}\text{C}$, and $\Delta IL(T) = 7.8 \cdot 10^{-4} \text{ dB}/^{\circ}\text{C}$ for the single-mode filter; and $\Delta f_0(T) = -2.56 \text{ MHz}/^{\circ}\text{C}$, $\Delta BW(T) = -392 \text{ kHz}/^{\circ}\text{C}$, and $\Delta IL(T) = 1.05 \cdot 10^{-3} \text{ dB}/^{\circ}\text{C}$ for the single-mode filter with transmission zeros. This is an undesirable effect that strongly depends on the system specifications. For instance, the thermal stability of tunable filters or filter banks utilized in RF transceiver front ends is of the utmost importance since the filter shift could provoke an overlap between adjacent channels.

A second study was performed to determine the technology breakdown limits. In the first

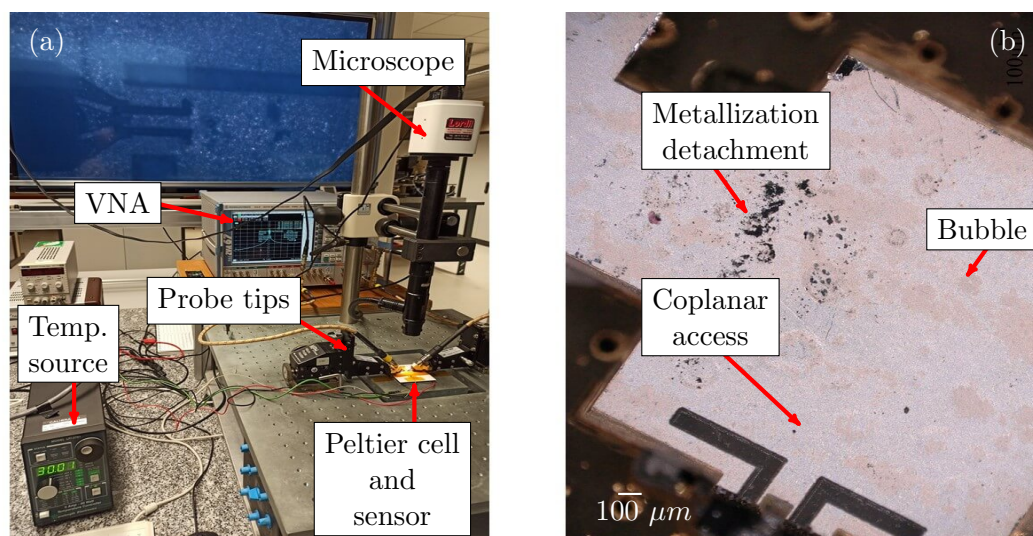


Figure 5.14: LMST devices temperature characterization setup (a). Defects in aerosol-deposited silver layer after exposure to temperatures greater than 200 $^{\circ}\text{C}$. (b)

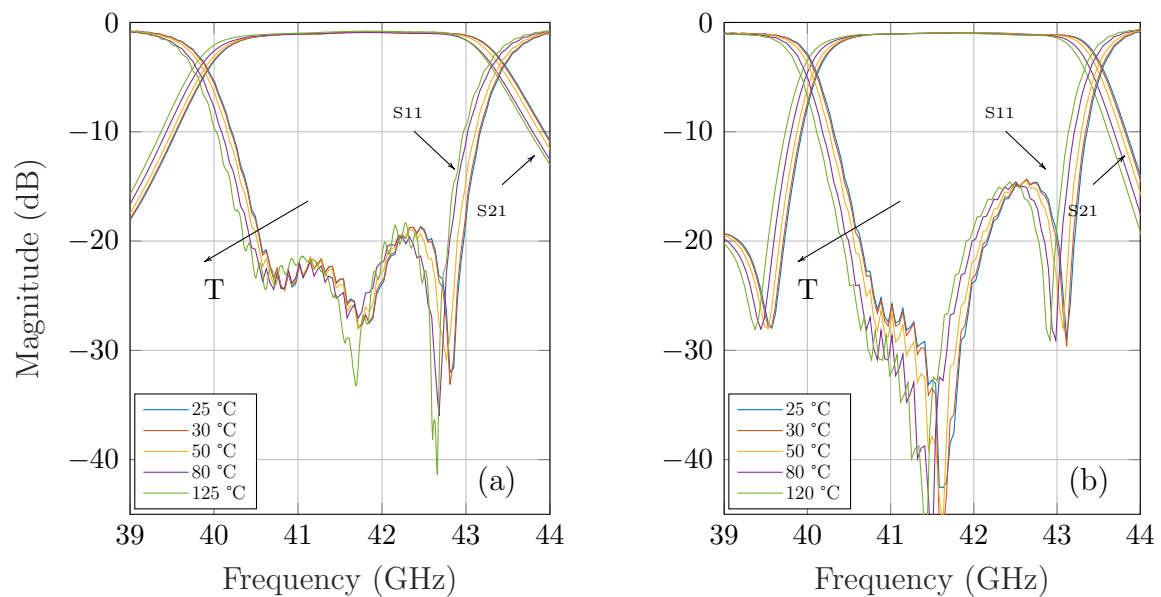


Figure 5.15: Alumina band-pass filters exposed to several temperatures: (a) single-mode filter and (b) single-mode filter with transmission zeros. Temperatures up to 123 °C were obtained heating the device in a furnace.

place, the devices were heated in an furnace during two hours and stressed with three different temperature profiles. The maximum operating temperatures in each case were 80 °C, 123 °C and 200 °C. The frequency shift and Q_0 measured at these temperatures were in good agreement with previous test and subsequent measurements at room temperature exhibited no difference when compared to the fresh device. This behaviour suggests that no permanent damage was realized on the Alumina or metallic structure after being exposed to several temperature cycles. Bubbles and material detachment were observed on the silver coating after exposing the devices to temperatures greater than 200 °C (fig. 5.14.b). Further measurements reveal malfunctions on the frequency response. The test was repeated on DUTs metallized with a fine copper layer ($3 \mu\text{m}$) and protective gold. No structural damage or imperfections were observed this time on the metallic layer after stressing the devices with temperatures up to 300 °C.

5.3 Thermally-stable devices (G4)

The resonance frequency of regular Alumina devices typically decreases when the temperature increases. To minimize the frequency shift, thermally-stable materials are developed to compensate the drift with a positive temperature coefficient. The strategies and experienced gathered in previous generations were implemented in a commercially available ceramic substrate provided by Exxelia Temex to design thermally-stable mi-

crowwave devices. The substrate (E7024) is made of a ceramic known as BMT ($\text{Ba}(\text{Mg}_{1/3}\text{Ta}_{2/3})\text{O}_3$) with a coefficient of thermal expansion $CTE = 10 \text{ ppm}/^\circ\text{C}$ and a thermal coefficient of frequency $\tau_f = (0 \pm 2) \text{ ppm}/^\circ\text{C}$. The electrical permittivity and losses were characterized with a split cylinder resonator cavity method (SCR) [248] at 26 GHz. Measurements exhibit a $\epsilon_r = 24.1 \pm 0.7$ and $\tan \delta = (8.5 \pm 5.2) \cdot 10^{-5}$ at room temperature. The high Q_o and electrical permittivity together with the temperature coefficient make the material ideal for compact filter applications like satellite multiplexing filter devices, radio-links for communication systems (LMDS), military radars, among others.

Five TE_{101} resonators and twelve single-mode 4th order Chebyshev band-pass filters (BPF) were fabricated in a 25 mm x 25 mm x 0.65 mm substrate for 5G applications at 26 GHz mm-Wave band (fig. 5.16.a). This 5G lower band was selected instead of the 42 GHz band owing to the higher permittivity of the material, otherwise the device shrinkage would be so high that would hinder the device manipulation and the assembly on a carrier board. Collective fabrication and surface-mount transitions were taken into account for the design. Thanks to the high substrate permittivity, the filters show a high area reduction similar to the Alumina filters fabricated at 42 GHz (see Table5.4). The final resonator and filter size measures 1.63 mm x 1.93 mm and 3.08 mm x 3.48 mm, respectively. Electroless copper coating was chosen to increase the operating temperature range, in spite of performance degradation as a consequence of the combined contribution of the lower conductivity and the higher substrate losses. Resonator measurements reveal a maximum Q-factor between $360 \leq Q_o \leq 378$ for

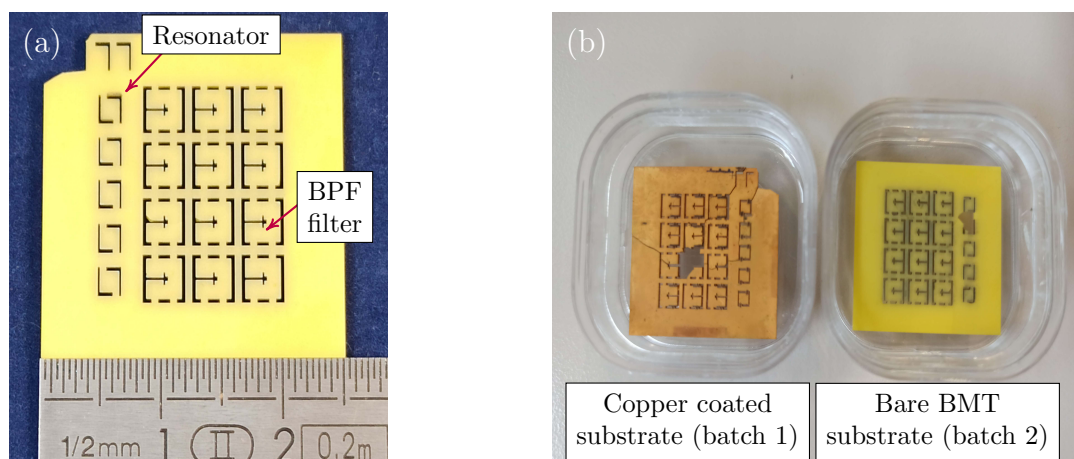


Figure 5.16: Laser micro-machined fabrication of BMT substrates ($\epsilon_r = 24.1$): (a) collective manufacturing (STEP 1) and (b) exposed structural weaknesses using straight corners (left) and rounded corners (right).

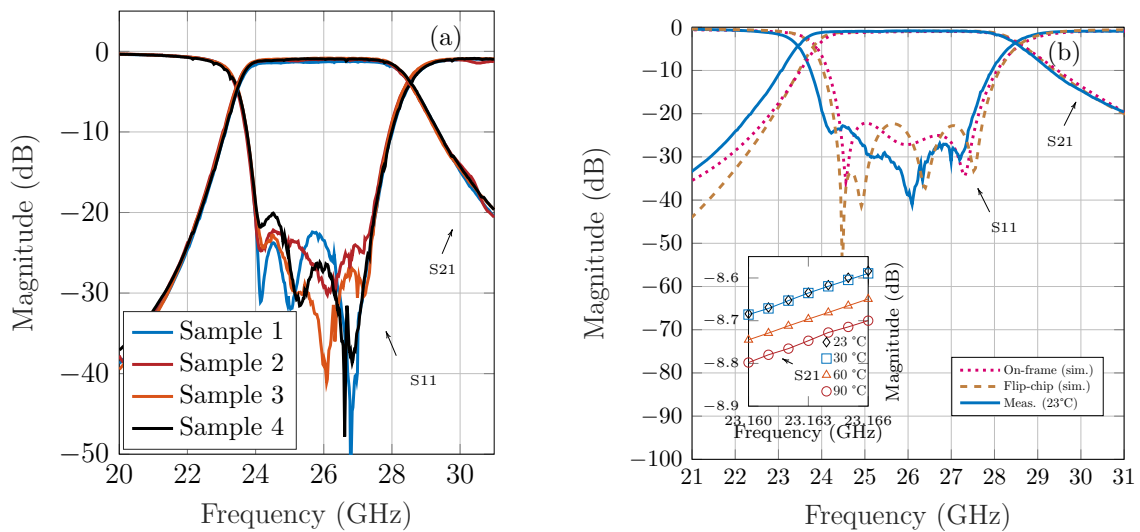


Figure 5.17: Measured S-parameters on-frame of 5G mm-Wave band thermally-stable filters: (a) frequency response comparison between four samples of the same run and (b) on-frame/SMD simulations and measurements (23 °C, 30 °C, 60 °C and 90 °C).

copper coated resonators. If necessary, the quality factor could be enhanced up to 600 by implementing TE_{102} modes filters [251] and silver plating. The coplanar access transitions were optimized to be assembled on a 0.4 mm thick RO4003C board. The board was chosen due to its proximity to the ceramic substrate CTE for a temperature range between -55 to 288 °C (11 ppm/°C and 14 ppm/°C in x- and y-direction). Figure 5.17.a depicts the measured S-parameters for several filter samples at room temperature T_{RT} , while figure 5.17.b shows the filter simulations for the optimized on-frame/SMD transitions and the fabricated filter measured at room temperature. The devices were tested using the same temperature characterization setup as shown in fig. 5.14.a. Measurements are in good agreement with simulations and the expected performances of the technology (insertion losses lower than 1 dB and 3.41 GHz bandwidth). It is worth to be mentioned that no tuning corrections were implemented on these filters. As in Alumina devices, a thermal analysis was performed in BMT filters and resonators from $T_A = 30$ °C to $T_B = 90$ °C (inset in 5.17.b). In the case of BMT resonators, a degradation of Qo from 376 to 332 was measured in Alumina resonators for the worst Q-factor observed.

In the case of the band-pass filters, the center frequency shift measured in several samples was found to be between $3.2 \text{ MHz} \leq \Delta f_0(T) \leq 6.5 \text{ MHz}$ ($0.01\% f_0 - 0.02\% f_0$) within the temperature range, and $-1.5 \text{ MHz} \leq \Delta BW(T) \leq -9 \text{ MHz}$ of bandwidth. Therefore, the parameters gradient with temperature is $-53 \text{ kHz/}^\circ\text{C} \leq \Delta f_0(T) \leq -108 \text{ kHz/}^\circ\text{C}$ and $-25 \text{ kHz/}^\circ\text{C} \leq \Delta BW(T) \leq -150 \text{ kHz/}^\circ\text{C}$, representing a significant

Table 5.3: Temperature-stable band-pass filters technology comparison.

Technology	f_0 @ 23 °C (GHz)	IL @ 23 °C (dB)	FBW @ 23 °C (%)	Δf_0 (kHz/°C)	δf_0 (ppm/°C)	ΔBW (kHz/°C)	ΔIL (dB/°C)	Reference
LMST G3: SMF	41.700	0.780	6.230	-2450	-58.75	-483	$7.08.10^{-4}$	[242]
LMST G3: TZF	41.700	0.890	6.950	-2560	-61.39	-392	$1.05.10^{-3}$	[242]
LMST G4: SMF	25.890	0.840	16.580	44 - 108	1.70 - 4.17	25 - 150	$1.20.10^{-3}$	[253]
Compensated AFSIW	21.003	1.080	1.600	35	1.67	35	-	[238]
AFSIW	21.006	0.700	1.590	-386	-18.38	-17	-	[238]
AFSIW	12.993	0.625	3.125	-300	-23	-29	-	[239]
ADLS	13.213	4.470	2.695	-328	-24.82	-86	-	[239]
ESICL	12.982	0.801	2.943	-213	-16.41	-200	-	[239]

improvement when compared to regular Alumina devices. A comparison between G3 Alumina devices and other thermally-stable technologies is exhibited in Table 5.3, where δf_0 is the center frequency thermal stability in ppm/°C (eq. 5.5) within the temperature range T_{RT} to T_B studied in this analysis.

$$\delta f_0 = \frac{1}{f_{T_{RT}}} \frac{f_{T_B} - f_{T_{RT}}}{T_B - T_{RT}} = \frac{\Delta f_0}{f_{T_{RT}}} \quad (5.5)$$

LMST G4 filters show a clear improvement with respect to LMST G3 devices in terms of center frequency ($1.7 \text{ ppm}/^\circ\text{C} \leq \delta f_0 \leq 4.17 \text{ ppm}/^\circ\text{C}$) and bandwidth thermal-stability. Furthermore, the band-pass filters exhibit a thermal stability features comparable to self-compensated air-filled technologies. However, the Q-factor is lower than the previous generation and significantly less than air-filled components.

A special remark should be done in regard to the laser machining of BMT substrates. Despite the good electromagnetic performances, this material presents lower mechanical resistance than Alumina substrates. The implementation of the standard laser machining process utilized so far reveals these weaknesses. Several superficial and deep cracks were observed during the etching, damaging the devices on the corners or even breaking the substrate (fig. 5.16.b). Even though, some parts of the substrate were broken during the process, most of the devices were completely fabricated and tested with good results. A second version was designed taken into account these problems. All the straight corners present in the devices, trenches and supports were replaced by rounded corners to avoid the concentration of hot spots during the laser path that could affect the structure. A better result was observed this time on the overall substrate. The rounded corners favored the quality of the components termination and

reduced the amount of cracks. However, in future developments it is recommended to utilize more robust temperature-stable materials for compatibility with our technology.

5.3.1 Surface-mount transitions

Surface-mount technology (SMT) is a widely implemented approach in the electronic device industry. Its utilization in discrete components, ICs or sensors for wireless communication and control systems facilitates the assembly to carrier boards and promotes the manufacturing automation. These characteristics are interesting features to be integrated in LMST devices to provide compact reliable devices. The development of surface mounting I/O terminal structures are a challenge at millimeter-wave bands owing to the reduced size and the higher precise control needed during the assembly. Some transitions were reported in the bibliography for SMT millimeter-wave filters ranging from microstrip lines with radiating slots [254] to Y-shaped coplanar terminals [50]. In order to integrate the latest upgrades shown in G3, the SMT assembly should contemplate a coplanar line termination for on-frame probe station testing while providing a surface-mount transition. In the generations implemented so far, the components were excited by a coplanar access carved into the metal layer. The layout of the access was always entirely located on the filter resonator. Nevertheless, nothing prevents extending the CPW lines from the resonator to the substrate using the supports. In that case, the supports usually placed on the corners should be shifted to be aligned to the access. This approach brings multiple functionalities to the process. On one side, it keeps the device testing before the device separation. On the other side, the coplanar lines are cut during the supports trimming, thus automatically creating the SMT transitions without any extra step. Finally, depending on the resonance mode, the supports position could be placed to a region of higher EM influence. Instead of being a disadvantage, this effect could be also used to tune the resonance frequency of every resonator and adjust the filter response measured on-frame. This topic will be explained with more details in Section 5.6.

Transitions optimization methodology

This new approach was implemented during the design of temperature-stable resonators and filters in G4. Figure 5.18.a shows the implementation of a common coplanar access for both on-frame (case 1) and SMT transition (case 2) in a resonator. The ports were extended from the device to the frame using the mechanical supports centered to the CPW line. The transmission line was designed to match a 125 um pitch GSG

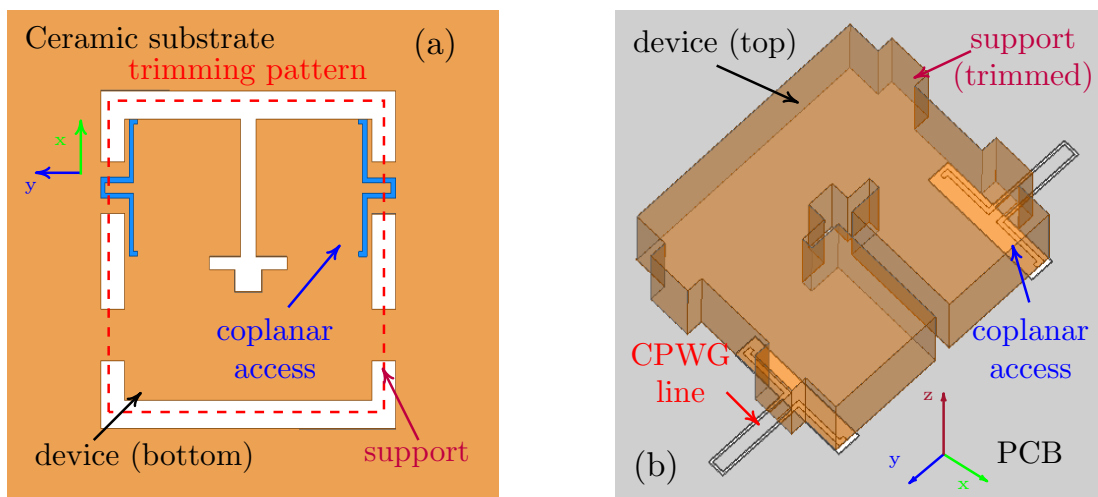


Figure 5.18: Coplanar access transition on: ceramic substrate (a) and carrier PCB (b).

probe to 50Ω within the operating band. Once the device is tested, the supports that link it to the substrate are trimmed providing two functionalities: to separate the device from the substrate and to create the new transition. Finally, the device is flipped, surface-mounted on the PCB carrier, and connected to a 50Ω CPWG line with a rectangular termination (fig. 5.18.b).

A proper design should ensure a similar frequency response for case 1 and 2 so the final SMD response could be predicted during preliminary measurements. Then, tuning strategies such as resonance frequency corrections could be implemented in each resonator during the testing stage by modifying the trimmed supports length. It should be taken into account that the boundary conditions in both cases are different. On one side the permittivity on top of the transmission line is entirely air (case 1). On the other side, the transition from the carrier board to the device is partially covered with the ceramic material next to the termination. Therefore, the implementation of this approach should be faced by simultaneously optimizing the designs to overcome this problem. The strategy applied in the filters developed during G4 consisted of mixing 3-D full-wave and circuit simulations as presented in [224].

Both cases are modeled with coupling matrices that describes the desired filtering laws. The models are developed by extracting the coupling matrices obtained by means of full-wave simulations performed in HFSS. These simulations contemplates the initial design of case 1 and 2 and variations of all the geometrical parameters [255], [256]. The set of matrices obtained for all the variations are used to calculate sensitivity expressions related to the geometrical changes of the device. Then, these expressions are added to the initial coupling matrix of both cases. In this way, it is possible to describe the coupling/frequency laws in the proximity of an initial point for

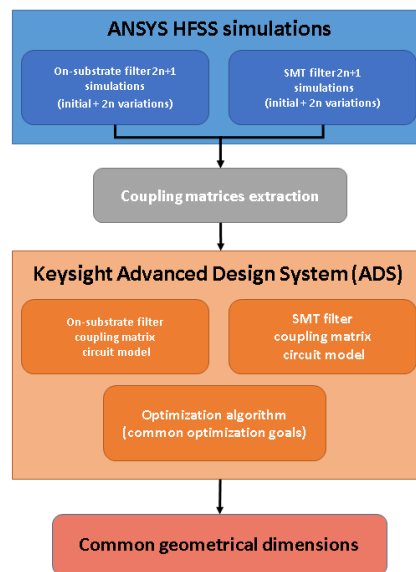


Figure 5.19: Laser Micro-Machined Substrate Technology fourth generation (G4) filters and transitions optimization flow.

every variation. Since two variations per geometrical parameter were utilized for the complete modelling of each case, a total amount of $2(2n+1)$ simulations were carried out for n geometrical parameters.

Then, an equivalent circuit model developed in Keysight ADS was implemented to represent the coupling matrices response obtained from the EM simulations. Since the geometrical parameters are shared for both cases, classical optimization algorithms with common goals could be set to minimize the error and achieve a similar filter response. Finally, the same geometrical dimensions are obtained as output of the optimization process. These results could be implemented as input for HFSS simulations to check the accomplishment of the filter specifications and the matching between both transition cases. A comparison between the EM simulations of both design cases (on-frame and flip-chip) can be consulted in fig. 5.17.b. The filter footprint dimensions as well as the coplanar access parameters can be consulted in Table A.1 in Annex A.3.

Practical implementation

Surface-mount transitions were considered to be implemented in previous generations for LMST millimeter-wave Alumina devices at 40 GHz. Nevertheless, experimental demonstrations showed unsatisfactory results with extremely low external coupling values. The feedback obtained during these tests served as useful input for new designs. Observations performed with a microscope of the assembled transitions (fig.

5.20.a) exhibited failures owing to three main causes: an excessive separation in the board/device interface as a consequence of non planar substrate surface; a deficient electrical connection between the device and the PCB metallic plates; and damages on the silver coating as a consequence of the temperature profile required during the soldering process (over 200 °C). These problems were addressed in G4 where CPWG to ceramic-filled cavity transitions were implemented in a 0.4 mm thick RO4003C carrier substrate with a copper cladding of 18 μm . The board copper layer was removed during the PCB manufacturing process and replaced by a multi-metal layer stack of Copper (2 μm), Nickel (2 μm) and Gold (0.5 μm) to enhance the device soldering. The commercial BMT substrate is machined by the manufacturer to ensure a good surface flatness and a thickness tolerance below 10 μm . Two fabrication batches were launched using this temperature stable material. As explained in Section 5.3, copper coated devices were utilized in a first batch to be soldered with lead-free solder paste with a melting point over 200 °C. Moreover, a second batch was manufactured using aerosol silver coating process and soldered with a low-temperature alloy based on Sn-Bi with a fusion temperature of 180 °C. Several band-pass filters and TE_{101} single-mode resonators were assembled on the carrier board using an industrial pick and place machine to improve the alignment and to test the devices compatibility in a real industrial setup. The alignment tolerances are the same as the ones used during the transition sensitivity analysis explained in Chapter 4: $\Delta X|_{6\sigma} = \pm 50 \mu\text{m}$ and $\Delta\theta|_{6\sigma} = \pm 0.01^\circ$. Figure 5.20.b shows the copper and silver coated devices assembled on the manufactured board. The devices were sorted in rows depending their functionality (resonators or

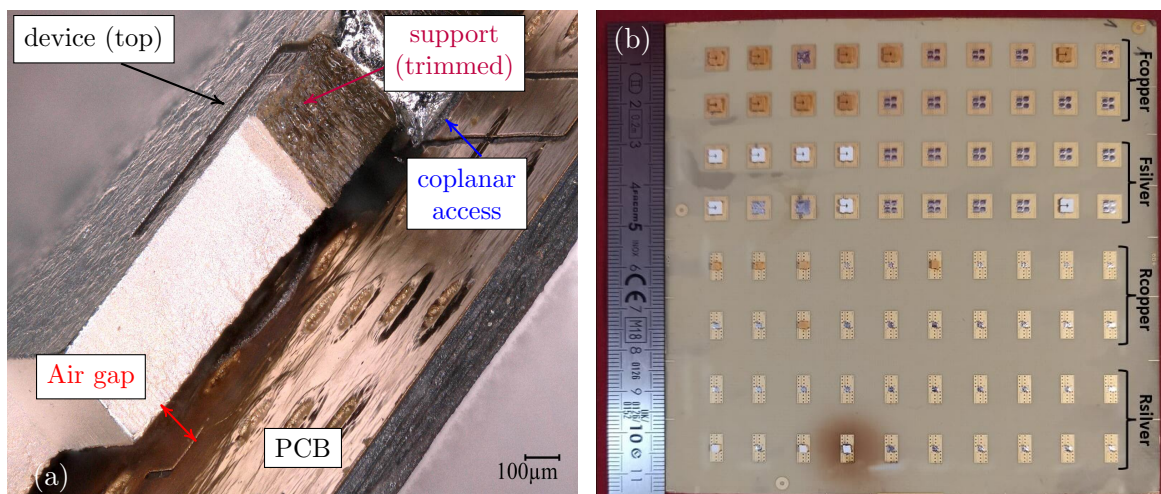


Figure 5.20: Photography taken with a digital microscope of a LMST ceramic device surface-mount transition (a). Excessive separation from the substrate and electrical disconnections can be observed. Surface-mounted components on a PCB carrier board (b).

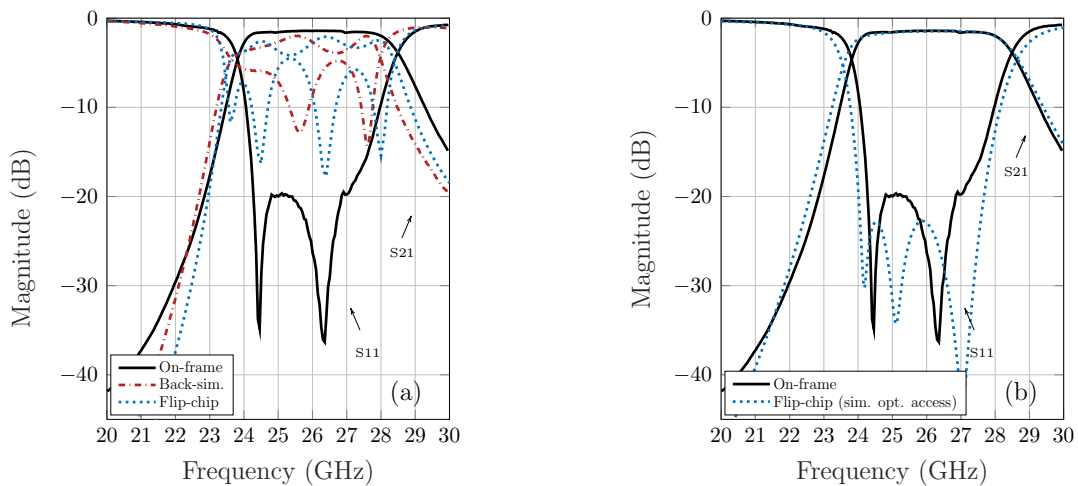


Figure 5.21: BMT substrate-based manufactured filters in G4 scattering parameters. On-frame, surface-mounted and back-simulations (a). Optimized coplanar access simulations for $60 \mu m$ separation gap (b).

filters) and their coating process (copper or silver). Even though the original support length utilized during the design stage was $L_{SUP} = 200 \mu m$ the devices were trimmed at different lengths ($50 \mu m$, $100 \mu m$, $150 \mu m$, $200 \mu m$ and $250 \mu m$) to test the frequency shift effect and ordered in different columns for better identification.

The measured scattering parameters exhibit a lower external coupling than expected in both resonators and filters. On one side, the surface-mounted resonators show a reduction between $4.2 dB \leq \Delta S_{21} \leq 10.6 dB$ when compared to the measurements carried out before the device extraction at the resonance frequency. On the other hand, the reduction of Q_e was also corroborated in the assembled filters. Measurements show a return loss of 5 dB and insertion loss of $2 dB \leq IL \leq 4 dB$ within the pass band in the best case as illustrated in figure 5.21.a. The high discrepancies between the expected results and measurements could be attributed to the excessive gap between the board and the substrate. The separation between these two interfaces depends on the amount of solder paste deposited during the screen printing process and the melting flow control. Back-simulations show a gap separation between $40 \mu m$ to $100 \mu m$ for a decrease between $4.2 dB \leq \Delta s_{21} \leq 10.6 dB$ in the case of the resonators and to obtain $R_L = 5 dB$ in the case of the filters. In order to check the deficient external coupling effect the filters coupling matrices were extracted from the measured scattering parameters. Equations 5.6 and 5.7 shows the on-frame (green), surface-mounted (red) and back-simulated (blue) extracted coupling matrices.

$$M_{SMF} = \begin{bmatrix} 0 & 1.22 \setminus 0.97 & -0.07 \setminus -0.05 & 0.02 \setminus 0.00 & -0.01 \setminus 0.00 & 0.00 \setminus 0.00 \\ 1.22 \setminus 0.97 & 0.21 \setminus 0.60 & 1.00 \setminus 0.87 & -0.12 \setminus -0.07 & 0.01 \setminus -0.02 & 0.00 \setminus -0.02 \\ -0.07 \setminus -0.05 & 1.00 \setminus 0.87 & 0.15 \setminus 0.12 & 0.74 \setminus 0.71 & -0.11 \setminus -0.08 & 0.00 \setminus 0.08 \\ 0.02 \setminus 0.05 & -0.12 \setminus -0.07 & 0.74 \setminus 0.71 & 0.09 \setminus 0.32 & 1.09 \setminus 0.74 & -0.07 \setminus -0.09 \\ -0.01 \setminus 0.00 & 0.01 \setminus -0.02 & -0.11 \setminus -0.08 & 1.09 \setminus 0.74 & 0.01 \setminus 1.02 & 1.26 \setminus 0.69 \\ 0.00 \setminus 0.01 & 0.00 \setminus -0.02 & 0.00 \setminus 0.08 & -0.06 \setminus -0.09 & 1.26 \setminus 0.69 & 0 \end{bmatrix} \quad (5.6)$$

$$M_{SMF} = \begin{bmatrix} 0 & 0.67 \setminus 0.97 & -0.09 \setminus -0.05 & 0.03 \setminus 0.00 & -0.01 \setminus 0.00 & 0.00 \setminus 0.00 \\ 0.67 \setminus 0.97 & 0.39 \setminus 0.60 & 0.87 \setminus 0.87 & -0.08 \setminus -0.07 & 0.01 \setminus -0.02 & -0.02 \setminus -0.02 \\ -0.09 \setminus -0.05 & 0.86 \setminus 0.87 & 0.19 \setminus 0.12 & 0.76 \setminus 0.71 & -0.09 \setminus -0.08 & 0.03 \setminus 0.08 \\ 0.03 \setminus 0.05 & -0.09 \setminus -0.07 & 0.76 \setminus 0.71 & 0.2 \setminus 0.32 & 0.86 \setminus 0.74 & -0.07 \setminus -0.10 \\ -0.01 \setminus 0.00 & 0.01 \setminus -0.02 & -0.09 \setminus -0.08 & 0.86 \setminus 0.74 & 0.40 \setminus 1.02 & 0.67 \setminus 0.69 \\ 0.01 \setminus 0.01 & -0.02 \setminus -0.02 & 0.04 \setminus 0.08 & -0.10 \setminus -0.09 & 0.67 \setminus 0.69 & 0 \end{bmatrix} \quad (5.7)$$

It could be noticed that the measured inter-resonator couplings are in good agreement with the target coupling matrix ($m_{21} = m_{12} = m_{34} = m_{43} = 0.9$ and $m_{23} = m_{32} = 0.7$) for $f_o = 26.15 \text{ GHz}$ and $BW = 3.5 \text{ GHz}$. Besides, the resonators resonance frequency (main diagonal in eq. 5.6) are shifted to lower frequencies. This shift is the result of the filter support length sample ($L_{SUP} = 100 \mu\text{m}$) chosen to extract the coupling matrix. It can also be noted that the external coupling values are lower than the required for a correct operation of the device ($m_{S1} = m_{4L} = 1.03$). Moreover, the coupling values are not symmetrical suggesting a tilting of the device on one of its sides. Back-simulations were performed by increasing the solder paste thickness and the filter titling angle to cross-check the data extracted from the coupling matrices. Comparisons between back-simulations and measurements show a good agreement for a gap between $50 \mu\text{m}$ to $70 \mu\text{m}$ and a titling angle around 0.4° (eq. 5.7). The estimated parameters were verified on measurements taken with the digital microscope (fig. 5.22). The pictures exhibit a good device alignment and welding to the board. Sensitivity to the accesses separation is mainly a consequence of the high difference between BMT substrate permittivity ($\epsilon_{r(BMT)} = 24.1$) and the carrier board/air interface ($\epsilon_{r(air)} = 1$), hindering the EM field penetration into the material. Measurements of the diverse samples served to better characterize the typical device separation and titling. These parameters are valuable data to adjust the overall manufacturing flow and to be used as design rules. The external coupling deficiency could be easily corrected by optimizing the access dimensions on the filter to the worst identified case. Figure 5.21.b depicts the simulated filter response for a gap of $60 \mu\text{m}$ by optimizing the coplanar access dimensions. These modifications could be applied in a future manufacturing batch, repeating the same

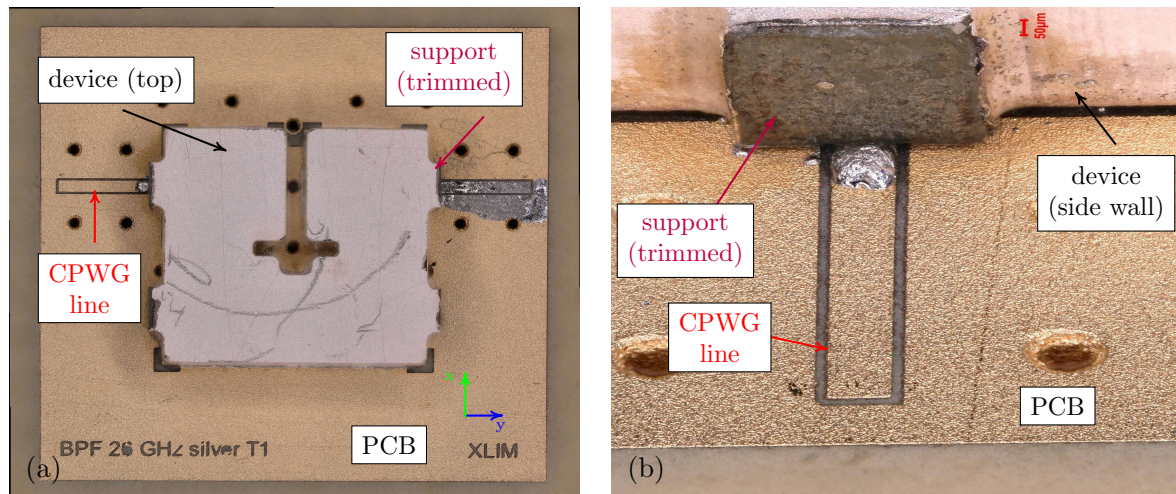


Figure 5.22: Photography taken with a digital microscope of a LMST ceramic device surface-mount transition. Excessive separation from the substrate and electrical disconnections can be observed.

manufacturing process to corroborate the correct operation of the assembled filters.

5.4 Technology comparison

Many manufacturing technologies were implemented by the scientific community during the last years to satisfy the need of microwave and millimeter wave communication devices. The developments reported exhibit different trade-offs in terms of manufacturing complexity, size, performances, weight and cost, among others. The utilization of one or the other technology will mostly depend on the particular requirements of the applications.

In order to determine what are the features of ceramic-based LMST devices and their potential target applications, an objectively technological comparison should be carried out. Table 5.4 lists the most common characteristics analysed by the microwave filter community for several manufacturing technologies in K-, Ka- and Q-band, and sorted by the quality factor. Crystalline quartz micro-machining exhibits the highest Q_0 among the rest of the technologies and a similar number of manufacturing stages as LMST. Additionally, surface-mounted filters were reported in the literature. Nevertheless, owing to the relative low permittivity of these materials compactness is not a strong point of this technology and the substrate material could be rather costly. Four-pole filters at 60 GHz consume 7.44 times more area than LMST filters at 42 GHz. High quality factors can also be achieved with air-filled SIW technology. Furthermore, these devices

Table 5.4: Millimeter-wave filters manufacturing technologies.

Technology	Frequency (GHz)	Qo	Filter order	Size (mm x mm x mm)	Area (mm ²)	Ref.
LTCC	41.80	333	4	5.50 x 2.30 x 0.60	12.65	[257]
DRIE SOI	38.00	343	3	7.41 x 15.32 x 1.50	113.52	[233]
	29.40	500	4	8.90 x 11.60 x 1.17	103.24	[234]
Fuse Silica laser micro-machining	36.20	550	4	5.90 x 24.40 x 0.76	143.96	[258]
B259MC1S	25.88	65*	4	5.50 x 2.30 x 1.80	12.65	[259]
B385MD0S	38.50	150*	4	6.99 x 2.03 x 1.91	14.19	[260]
LMST G4	26	360	4	3.08 x 3.48 x 0.65	10.72	[253]
LMST G3	42.00	689	4	3.38 x 3.11 x 0.66	10.51	[242]
u-coax	35.90	829	1	3.33 x 3.33 x 0.70	11.09	[235]
Air-filled SIW	38.00	1065	4	7.11 x 24.42 x 4.57	173.67	[261]
ESIW	12.99	1400*	5	25.00 x 90.00 x 3.00	2250.00	[239]
Crystalline Quartz	28.00	1500	8	3.40 x 33.70 x 1.50	114.58	[50]
micro-machining	60.00	1230-1470	4	5.75 x 13.6 x 1.8	78.20	[262]

* Effective quality factor estimated from an equivalent Chebyshev band-pass filter with the same order, f_0 and bandwidth.

are directly integrated on the carrier board, low-cost and could be self-temperature compensated [237]–[239]. However, since the cavities are filled with air their are usually larger in size and thicker due to the substrate stacking. A compact 3-poles band-pass filter was reported in [261] with $Q = 1065$ and a size of 7.11 mm x 24.42 mm x 4.57 mm. Micro-coaxial technology can reach good performances but the manufacturing process is usually more complex and requires a clean room to perform the fabrication. DRIE SOI and fused silica laser micro-machining technologies have lower quality factor than LMST and in the case of laser-micromachining [258], the components size is larger due to the lower permittivity of the substrate. Finally, nowadays LTCC is a mature technology widely implemented in several applications. LTCC millimeter-wave filters reported in the bibliography provides very compact highly-integrated devices but with low quality factors. LMST millimeter-wave band-pass filters developed in G3 shows a good unloaded Q around 689 at 42 GHz, better than typical SIW or LTCC processes and comparable to fused silica laser micro-machining and DRIE SOI.

Even though the quality factor is lower than other mm-Wave manufacturing technologies around 40 GHz, 4-pole filter features comparison suggests that ceramic-based LMST filters are in a good balance between miniaturization in terms of footprint and thickness (normalized to the free space wavelength λ_0), quality factor and maximum operating frequency (fig. 5.23). Moreover, passive filters designed with this technology are light and as compact as LTCC filters [242] and the utilization of temperature-stable ceramic substrates as demonstrated in LMST G4 could be interesting features for satellite and airborne applications. Commercially available off-the-shelf SMD temperature-stable ceramic filters operating at 38.5 GHz such as B385MD0S (Dielectric Laboratories) [260]

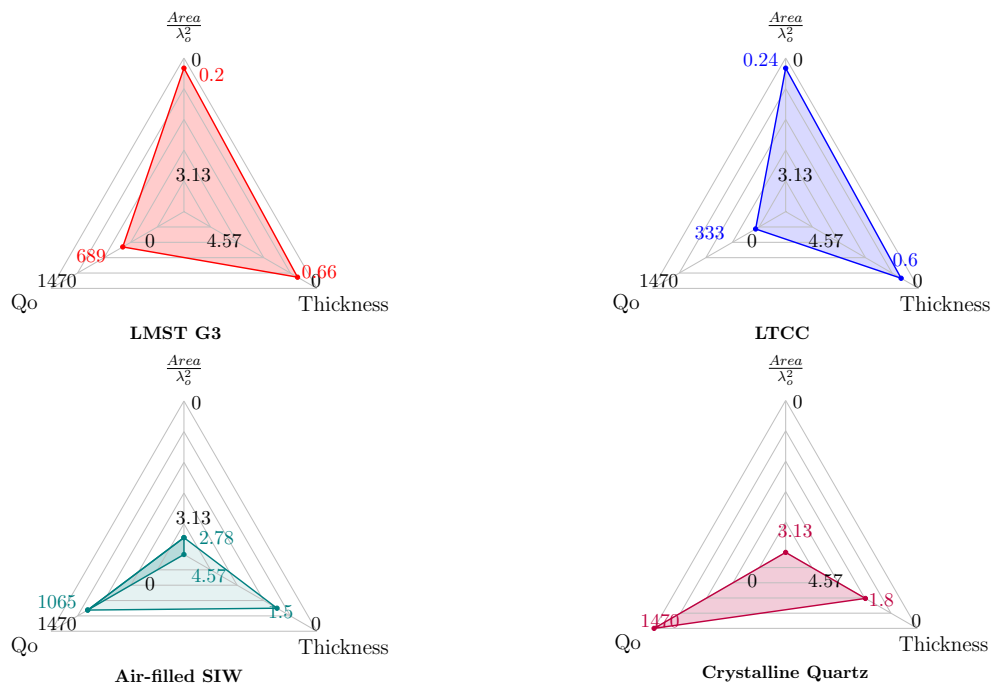


Figure 5.23: Relative features comparison between LMST G3 filters [242] and 40 GHz mm-Wave band fabrication technologies (LTCC [257], air-filled SIW [261], and crystalline quartz [254]) [236]. The device thickness is represented in millimeters.

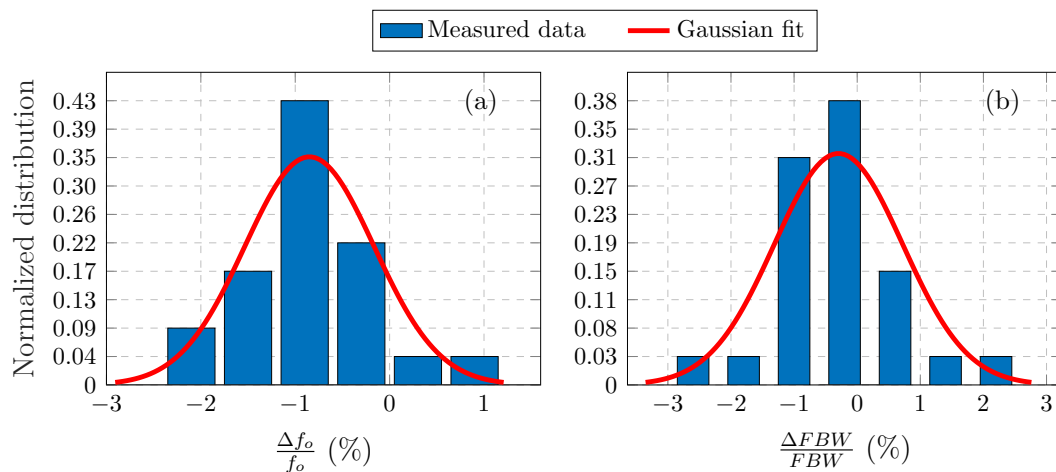


Figure 5.24: LMST filters relative frequency shift (a) and fractional bandwidth mismatch (b) statistics and Gaussian distribution.

shows slightly larger area and thickness, and a typical $RL = 10 \text{ dB}$ and $IL = 2.5 \text{ dB}$. Furthermore, this BPF weights 3.68 g versus 26.7 mg and 44.8 mg of the heaviest filters measured in LSMT G3 and G4, respectively. Manufacturing costs could be one of the main drawbacks of ceramic-based LMST filters due to the higher price of Alumina substrates in comparison with less expensive technologies as organic PCB SIW. The devices manufactured throughout the different generations provide valuable infor-

mation about the process dispersion for industrial massive production of mm-Wave LMST ceramic devices. A statistical analysis of band-pass filter central frequencies and bandwidth mismatch was performed using the available data of 24 devices between the different topologies fabricated with this technology (fig. 5.24). The data fitted with a Gaussian distribution exhibits a mean frequency shift of $\mu(\frac{\Delta f_o}{f_o}) = -0.85\%$ with a standard deviation of $\sigma(\frac{\Delta f_o}{f_o}) = 0.69\%$ and a mean bandwidth mismatch of $\mu(\frac{\Delta FBW}{FBW}) = -0.29\%$ with a standard deviation of $\sigma(\frac{\Delta FBW}{FBW}) = 1.02\%$. The analysis contemplates all the process variable tolerances including the substrate permittivity characterization inaccuracy. A better estimation of this value could be achieved in an industrial environment where a better adjustment of the process is possible through several batches for the same substrate material. Although the manufactured devices show a correct filter response, the center frequency and the fractional bandwidth dispersion suggest that small post-fabrication corrections could be performed to compensate the effect of the fabrication tolerance.

5.5 Supports as tuning structures

During the third generation, the LMST fabrication flow was modified to maintain the devices attached to the substrate with supports. Their main function was to facilitate the substrate manipulation and enhance the metal coating process control. Nevertheless, some design constraints related to the metal coating process and the structural integrity of the substrate that should be considered as design rules. On the one hand, the minimum support length should be such that allows the proper deposition of a thick metal layer on the side walls. This is a critical step since a good plating control will determine the effective conductivity and the performances of the device. On the other hand, the minimum support width is restricted to avoid cracks or structural damages on the substrate.

The supports utilized so far in LMST were conceived to show a negligible influence on the resonance frequency modes of the devices, as explained in Section 5.1.4. However, the same effect can be leveraged to control the resonance frequency by distorting the fields inside the cavity. Therefore, these structures could be rethought as tuning elements already integrated in the LMST fabrication flow by giving them an electromagnetic functionality. Among the upgrades introduced in the third generation, the complete fabrication of the device before its separation from the substrate allows the implementation of a testing stage to check the correct functioning of the components. Consequently, failed or unsatisfactory devices can be detected beforehand. In this

frame, the corrections needed to improve the filters response can be assessed during this stage. The device adjustment is performed by calculating the support length to re-center the resonators. An advantage of this approach is that the tuning step is carried out at the same time as the device is trimmed in STEP 3, thus maintaining the simplicity of the process.

5.6 Frequency shift effect

The interpretation of the electromagnetic behaviour is fundamental for the design of different support arrangements. As explained in section 5.1.4, the supports can be seen as dielectric-filled rectangular waveguides excited by the device field at the operating frequency. The waveguide cross section dimensions are W_{SUP} and H_{SUP} along the x- and z-axis, respectively. However, since H_{SUP} is fixed, three degrees of freedom can be identified to control the electromagnetic field of a resonator: the support length (L_{SUP}), the width (W_{SUP}) and the support relative position on the resonator (Pos). For instance, a support position centered with the resonator width corresponds to $Pos = 0$. Equation 5.1 could be rewritten to include the dependency of the support position in the electric field propagating through the support as shown in eq. 5.8, where $k_x = \pi W_{RES}^{-1}$ is the wavenumber along the x-axis. As the support position is shifted from the middle to the corners of the device, the excitation of the waveguide suffers a sinusoidal decay and the impact on the EM fields of the structure is reduced.

$$E_y = E_o(x) \cdot \cos(k_x \cdot Pos) \cdot e^{-\beta \cdot L_{SUP}} \quad (5.8)$$

In comparison to higher TE_{m0p} modes, TE_{101} mode exhibits a larger distance between the location of maximum and minimum field. The available space could be useful to implement wider supports and enhance the sensitivity control of the inner fields disturbance. Therefore, the analysis introduced in this work will be focused on rectangular cavity prototypes based on the fundamental mode TE_{101} .

Owing to the intrinsic nature of the manufacturing process, the supports end lack of metal coating after the device extraction in STEP 3. As a result, a radiation boundary is created in the air/support interface, leaking part of the field present in the waveguide into the surroundings and disturbing the resonant mode of the device. Figure 5.25, depicts the effect on the electric field of a double-support resonator for several support lengths. As the length is reduced, the radiated field increments its impact on the inner field and boosts the frequency shift towards lower frequencies. Nonetheless, it is logical

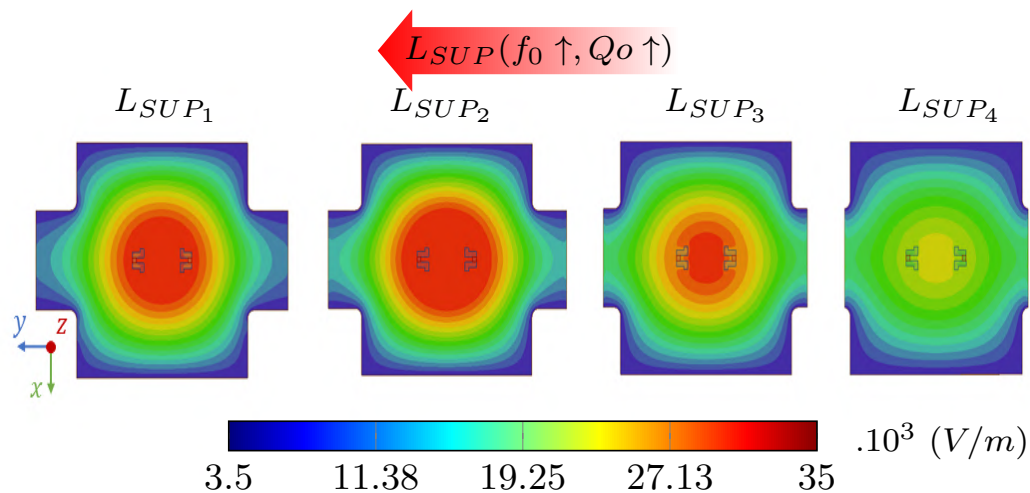


Figure 5.25: Rectangular cavity resonator TE_{101} electric field distribution evaluated at different support lengths ($W_{SUP_N} = 50\%$) for a support located at $Pos = 0$. $L_{SUP_1} = 25\%$, $L_{SUP_2} = 19.5\%$, $L_{SUP_3} = 10\%$, $L_{SUP_4} = 2.5\%$.

to expect a degradation in the quality factor owing to the radiation losses, an important fact to take into account when implementing the tuning with supports. The Q-factor constraint could be considered as the limiting factor to be addressed in advance during the design stage to determine the correction boundaries.

5.6.1 Device tuning

In order to understand how to effectively use the supports as tuning elements, an analysis based on full-wave electromagnetic simulations was conducted and compared against experimental results. Rectangular cavity resonator prototypes with different support arrangements were designed to evaluate the frequency shift and Q-factor degradation. The simulated electromagnetic effect estimated was tested in prototypes implemented in low-cost RO4003C boards to develop a great quantity of samples and carry out the experimental tests. An equivalent circuit model based on numerical fit approximations of the variation laws analysed in HFSS simulations could be also implemented using these results to simplify the computation time during the estimation of the final support length.

Resonators frequency tuning

The devices under test (DUT) were manufactured in a RO4003C substrate owing to its fast-prototyping and low-cost features. However, the methodology and conclusions

obtained in this analysis could be extrapolated to other dielectric materials. The substrate thickness is $t = 400 \mu m$, the copper cladding $18 \mu m$, the electrical permittivity $\epsilon_r = 3.55$ and $\tan \delta = 0.0027$. All the prototypes were manufactured by means of a milling machine respecting the same LMST fabrication flow. The fabrication tolerance of this machine was $\pm 200 \mu m$. Dummy resonators with negligible EM effect supports were fabricated implementing the criteria established in Section 5.1.5 (Prototype 1 in fig. 5.26), and coated with an electroless copper process plus gold electrolysis. The dummy resonators served as reference devices to estimate the equivalent metal layer conductivity coated with these processes and obtain the typical Q-factor. The equivalent conductivity is the result of the thick $18 \mu m$ copper layer on the top and bottom face ($58 S/\mu m$) and $1 \mu m$ metallic layer on the device walls. An effective conductivity between $6 - 12 S/\mu m$ was estimated and used as input for the designs. The total device losses could be calculated as shown in equation 5.9, where Q_o is the unloaded quality factor, Q_{rad} represent the radiation losses, Q_{cond} is the ohmic losses due to a finite conductivity of the metal walls and $Q_{tan\delta}$ are the intrinsic losses of the substrate. A TE_{101} resonator with four supports (Prototype 1 in figure 5.26) was fabricated as reference to estimate the losses. The supports were located in the regions of minimum EM field to reduce the radiation leakage and isolate Q_{cond} and $Q_{tan\delta}$.

$$\frac{1}{Q_{rad}} = \frac{1}{Q_o} - \frac{1}{Q_{cond}} - \frac{1}{Q_{tan\delta}} \quad (5.9)$$

The simulated maximum quality factor expected for a TE_{101} resonator realized on this

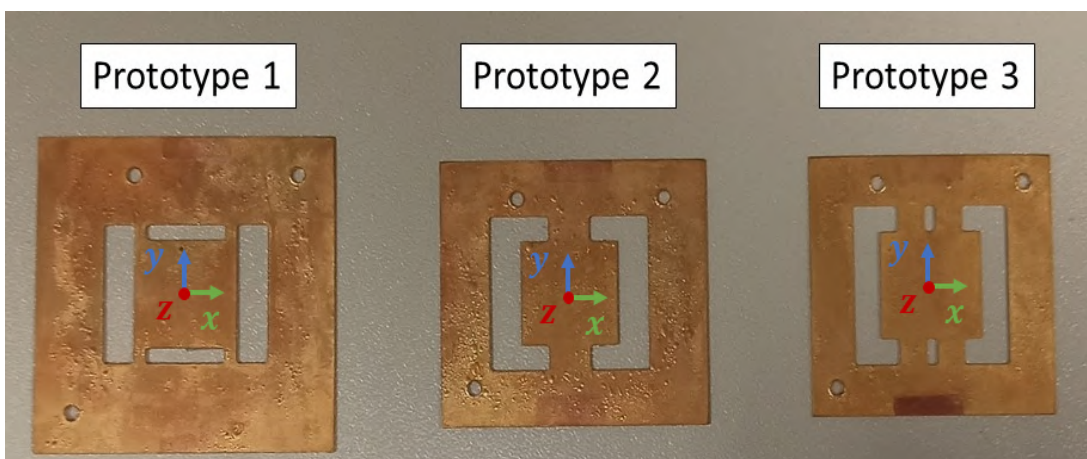


Figure 5.26: LMST resonator examples manufactured in organic PCB substrates: quad-support with no EM influence (Prototype 1), double-support with high-frequency tuning range (Prototype 2), and quad-support with medium frequency shift tuning range (Prototype 3).

Table 5.5: Measured dispersion in manufactured dummy resonators.

Parameter	Sample 1	Sample 2
Size (mm x mm)	13.29 x 13.09	13.29 x 13.09
W_{SUP} (mm)	2.687	2.676
ϵ_r	3.58	3.58
$f_{o_{frame}}$ (GHz)	8.197	8.208
Q_o	136	132
$ \Delta f_o $ (MHz)	3	3
$ \Delta Q_o $	1	1

substrate is 354 with $\rho \rightarrow \infty$ and 142 with $\rho = 8 \text{ S}/\mu\text{m}$. Unloaded quality factors of 136 and 132 were measured on-substrate in two different dummy samples fabricated in the same batch. The negligible effect of the radiation losses was checked by cross-checking the on-substrate and trimmed device data. As a result, no significant variations were observed neither on the quality factor nor the resonance frequency for $L_{SUP_N} = 25\%$ (sample 1) and $L_{SUP_N} = 2.5\%$ (sample 2) at 8.2 GHz (Table 5.5). Owing to all the prototypes implemented the same resonator design and were fabricated in the same fabrication batch, the measured f_0 and Q_o are used as references to assess the tuning range and extra radiation losses introduced in every case.

The first case of study proposed was intended to provide the maximum frequency tuning range possible by adding two wide supports ($P_{os} = 0$) centered with the resonator (Prototype 2). The utilization of two supports in this location extends the tuning range, provides mechanical stability and a symmetrical EM field disturbance. The initial $L_{SUP_N} = 25\%$ was designed to greatly attenuate the evanescent mode during the device measurement before trimming the support. On-substrate measurements allow to back-simulate the device and optimize the support length necessary to shift f_0 towards the target frequency.

In order to provide higher flexibility to correct the resonance frequency towards higher or lower frequencies it is suggested to include the supports as part of the structure during the design stage. Then, the following procedure steps are recommended:

1. Set the simulated support length (open termination) to the middle of the frequency tuning range (dashed line in fig. 5.27). This point (f_{mid}) will provide the maximum frequency tuning range towards either direction. The combined resonator-supports structure designed should resonate at the target frequency f_0 .
2. Fabricate the devices using the maximum support length in the tuning range (e.g.

$$L_{SUPN_{max}} = 25\%).$$

3. Measure the resonance frequency before the trimming step (on-substrate) and compare it to the resonance frequency of the simulated design at the same support length ($L_{SUPN_{max}} = 25\%$).
4. The difference between both frequencies ($\delta f_0 = f_0(meas) - f_0(sim)$) indicates the frequency shift owing to the manufacturing tolerance. Then, the final support length to be trimmed and to compensate the deviation can be obtained by calculating L_{SUP} for $f_{mid} + \delta f_0$ (dotted line in fig. 5.27).

Several samples were manufactured and measured to experimentally determine the tuning range of the prototype. Each sample was trimmed at $L_{SUP_{1N}} = 25\%$, gradually sanded down to $L_{SUP_{4N}} = 2.5\%$ and measured at intermediate lengths. Back-simulations were performed in HFSS to compare the experimental results with the simulated model. Figure 5.28 shows the simulated far field radiation pattern of the resonator with the opened supports terminations placed in the y-axis. As it can be seen, the EM field leakage to the media increases as the support length is reduced, which is in good agreement with the expected behaviour.

Figure 5.27 depicts the frequency tuning range for Prototype 2 and the radiated field effect translated in terms of unloaded quality factor degradation. Both parameters are normalized and relative to the reference f_0 and Q_o values. Simulations are in a good agreement with measurements for both, frequency range and quality factor degradation. This approach allows to perform a tuning correction up to $\Delta f_0 = 3.8\%$ of the resonance frequency. Nonetheless, the relative degradation of the quality factor measured on-substrate as a result of the radiation losses could scale up to $\Delta Q_o = 27\%$.

One way to achieve a scenario with lower radiation losses could be done by reducing the support width or by shifting the support position. A third prototype (Prototype 3) is proposed as an intermediate scenario between Prototype 1 and 2 by implementing a quad-support structure as shown in fig. 5.26. The minimum separation between the supports is limited by the diameter of the mill or the laser spot (in the case of the laser-machined ceramic substrate) and the minimum trench size recommended for a good metal plating. Electroless copper process was successfully tested on 0.5 mm wide trenches realized in the PCB substrate. As in the second prototype, the same methodology was implemented to characterize the tuning range. The maximum frequency shift observed was $\Delta f_0 = 1.57\%$ while the measured radiation losses show a degradation of $\Delta Q_o = 8\%$. In comparison with the former method, the frequency range is 58% lower but the quality factor degradation decays by 70%.

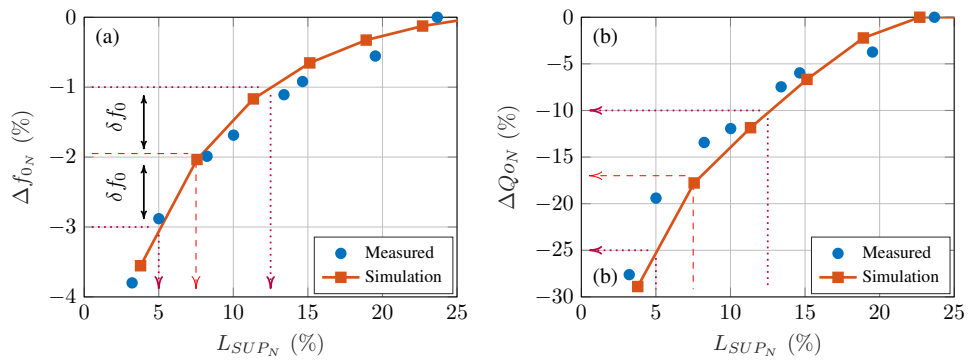


Figure 5.27: Frequency tuning range (a) and unloaded quality factor degradation (b) observed on prototype 2.

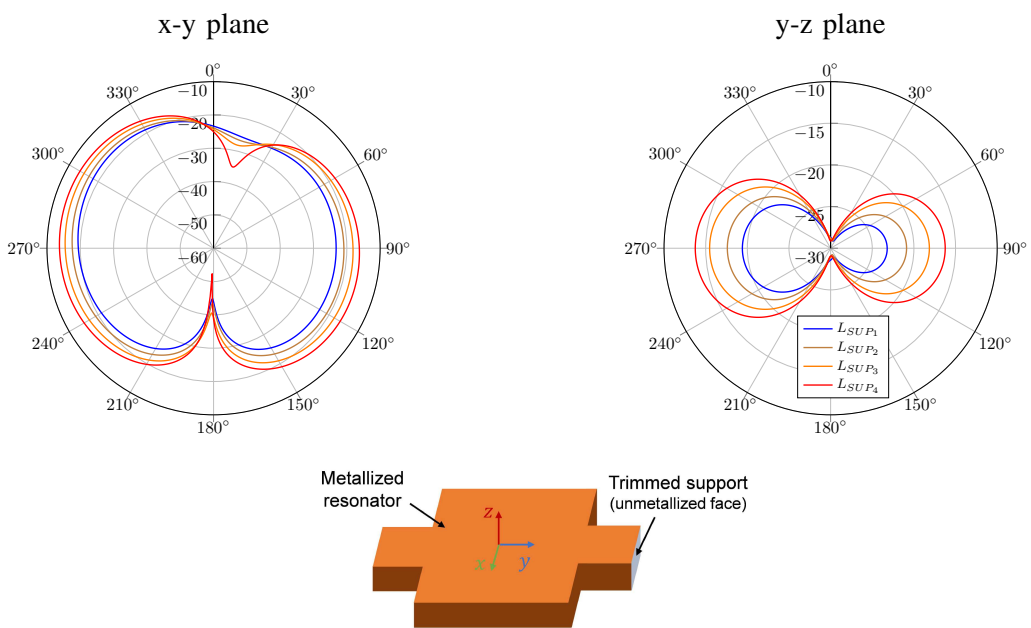


Figure 5.28: Simulated double-support resonator radiation pattern in decibel.

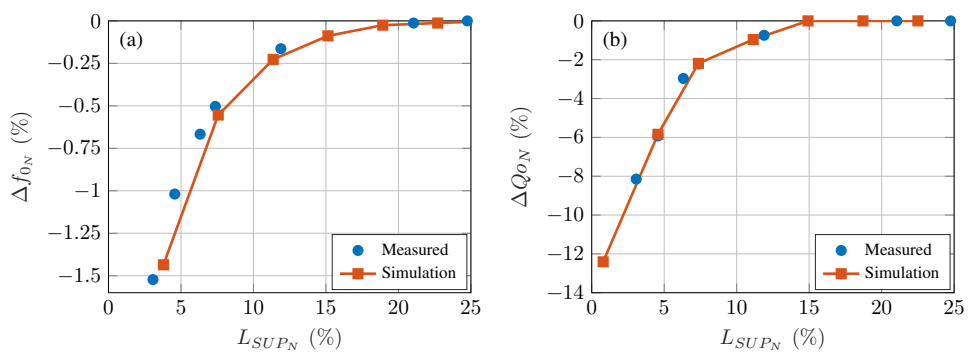


Figure 5.29: Frequency tuning range (a) and unloaded quality factor degradation (b) observed on prototype 3.

To summarize, the choice of the supports size and position depends on the particular specifications of every case. The manufacturing dispersion, the tuning frequency range and the target frequency accuracy will be decisive elements for the final choice.

Inter-resonator coupling tuning

A frequency shift effect could be implemented when the supports are correctly designed. Nevertheless, a particular study should be carried out to tune the inter-resonator couplings. The couplings utilized for the conception of cavity filters in the LMST filters usually implement inductive irises. It is well known that the coupling can be augmented by increasing the iris width or decreasing the length [242]. To be compatible with LMST technology, the irises could be partially trimmed (L_{trim} in fig. 5.30.a) during STEP 3 in order to reduce the coupling. The trimmed width exhibits a negligible effect on the coupling modification. The position of the milling tool is centered with the iris to avoid an undesired machining of the resonators side walls. Figure 5.30.a shows the simulated and experimental results of the coupling factor for several L_{trim} values. The axes were normalized to the nominal iris width and to the nominal coupling value ($L_{trim} = 0$). W_{trim} was fixed to 1 mm which is the end mill diameter utilized to tune the devices. Measurements show good agreement between the simulated coupling trend and the experimental results for several trimming lengths. However, full-wave simulations seems to underestimate the coupling factor up to 15%. The measured data is a valuable

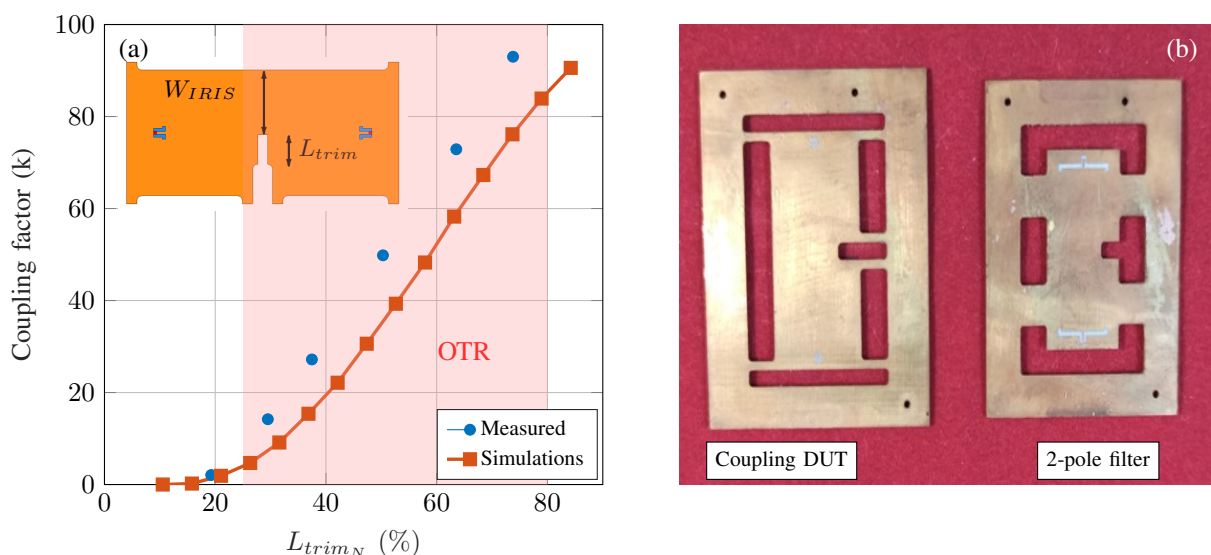


Figure 5.30: Iris trimming coupling factor (a) and LMST 2-pole filter (b) manufactured in organic PCB substrates: inter-resonator coupling tuning example (left) and 2-poles tunable filter example at 8 GHz (right).

resource to adjust the simulation dispersion or to be used as a look-up-table (LUT). In both cases a quasi-linear response is observed between $30\% \leq L_{trim} \leq 80\%$. A good trade-off between substrate machining and coupling tuning can be achieved within the so called operating tuning region (OTR). However, the higher the filter correction the higher the trimming length and the radiation losses.

5.6.2 2-pole filter tuning

The design utilized for the experimental validation of the inter-resonator tuning was adapted to develop a 2-pole filter (fig. 5.30.b) with $f_0 = 7.9 \text{ GHz}$ and $BW = 400 \text{ MHz}$. The resonance frequency and inter-resonator coupling tuning strategies were applied to correct the initial response. The coplanar accesses were re-designed to obtain the necessary external coupling and the supports (inspired from Prototype 1 in fig. 5.26) were replaced with supports with electromagnetic influence (Prototype 2 from fig. 5.26). The maximum simulated frequency shift for a resonator manufactured on a milling machine with a $200 \mu\text{m}$ manufacturing tolerance is around 300 MHz ($\Delta f_{0N} = 3.62\%$). Therefore, the support arrangement needed to accomplish the specifications is the one used in Prototype 2. Pre-tuned measurements show a center frequency $f_0 = 8.2 \text{ GHz}$ and $BW = 555 \text{ MHz}$ (fig. 5.31). The extracted coupling matrix normalized to the specifications is shown in eq. 5.10, where the measured pre-tuned values are highlighted in green and the target matrix is colored in blue. The geometrical parameters L_{SUP} and L_{trim} were estimated and utilized to set the trimming pattern. The measured tuned filter coupling matrix is depicted in red in equation 5.10. An improvement in the inter-

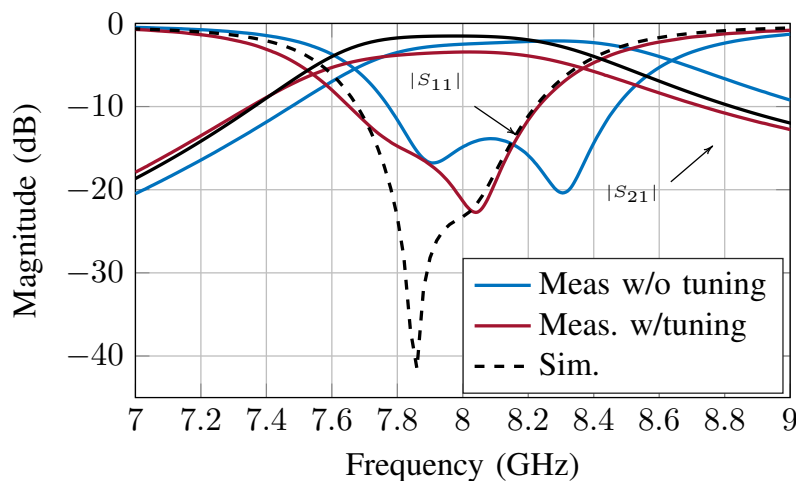


Figure 5.31: 2-pole filter S-parameter comparison: simulated design (black), manufactured prototype without corrections (blue), and post-tuned device (red).

resonator couplings from $m_{12} = m_{21} = 1.85$ to $m_{12} = m_{21} = 1.67$ (target value 1.66) can be observed. Moreover, the resonance frequency of the resonators was shifted around $f_o = 7.9 \text{ GHz}$ ($m_{ii} \leq \pm 0.11$) and the bandwidth is equal to $BW = 440 \text{ MHz}$ (fig. 5.31).

$$M_{2pfilter} = \begin{bmatrix} 0 \setminus 0 \setminus 0 & 1.22 \setminus 1.22 \setminus 1.19 & 0 \setminus -0.11 \setminus -0.09 & 0.02 \setminus 0.02 \setminus 0 \\ 1.22 \setminus 1.22 \setminus 1.19 & 0 \setminus -1.07 \setminus -0.11 & 1.66 \setminus 1.85 \setminus 1.67 & 0 \setminus -0.11 \setminus -0.09 \\ 0 \setminus -0.11 \setminus 0.09 & 1.66 \setminus 1.85 \setminus 1.67 & 0 \setminus -1.11 \setminus 0.10 & 1.22 \setminus 1.20 \setminus 1.16 \\ 0 \setminus 0.02 \setminus 0.02 & 0 \setminus -0.11 \setminus -0.09 & 1.22 \setminus 1.97 \setminus 1.16 & 0 \setminus 0 \setminus 0 \end{bmatrix} \quad (5.10)$$

To estimate the extra losses added when tuning the iris, a lossless substrate and perfect conductivity was taken into account during the simulation. The additional losses due to the corrections can be obtained by analysing the relative quality factor degradation on every resonator. As a result, the quality factor diminished from $Q_{O(on-substrate)} = 65$ to $Q_{O(tuned)} = 47$ representing a degradation of 27.7%.

The methodology explained along this section using PCB substrates could be also implemented on other substrate materials as ceramics and automatized to measure the device response, and to estimate the trim path autonomously.

5.7 Conclusion

Laser Micro-Machined Substrate Technology (LMST) is a generic technology for the fabrication of microwave and millimeter-wave passive devices. LMST is a flexible technology with a good trade-off between size, quality factor and manufacturing complexity. The utilization of lasers to machine the components and engrave planar patterns provides the technology the versatility and accuracy necessary for its implementation in several communication applications at frequencies where the actual 3-D printed ceramic tolerances cannot fulfill. The machining of different substrate materials like organic or ceramic substrates is also possible implementing the same methodology.

The characterization and the evolution of the technology applied to commercial and custom ceramics has been presented in this chapter. The fabrication flow was enhanced to provide compact devices with good EM performances. The identification of the main technological constraints throughout the different generations was a critical aspect to overcome the process limitations and enhance the features. Several prototypes of waveguides and band-pass filters with different topologies (Chebyshev/Quasi-elliptic, 4-poles/6-poles, single- and dual- mode, with and w/o TZ) were designed as proof of

concept and fabricated in Alumina substrates at 40 GHz for 5G mm-Wave front-ends. A closer study of the manufacturing constraints allowed to provide design rules to facilitate the tasks of designs during the developments. The combination of the laser spot uncertainty, side walls slopes and misalignment measured and tested in single-mode cavity resonators resulted in a maximum fabrication dispersion of $23 \mu m$. Alumina substrates up to 0.7 mm thick were successfully machined within the estimated process accuracy. Furthermore, the utilization of low-loss Alumina substrates developed during research activities helped to improve the components performances. Special attention must be taken during the metal surface planar engraving since excessive laser power could cause burnt regions or coating lifting. Furthermore, the substrate overetching could affect the external coupling. In order to reduce device sensitivity to the manufacturing tolerance, design strategies were introduced and applied to fulfill the filter specifications. The manufactured filters show good performances and fabrication repeatability with a typical return loss over 16 dB and unloaded quality factor around 700. To the best of the authors knowledge, the ceramic filters developed with LMST are one of the most compact devices when compared to other technologies. Nevertheless, ceramic technologies are usually expensive for its implementation in the industry. A collective fabrication approach inspired on CMOS fabrication processes was implemented in LMST G4 in order to automatize the process, reduce fabrication costs and ease the substrate manipulation during the metallization. Moreover, the process modifications introduced naturally the possibility device testing and failures detection in early stages (STEP 3). The application of SMT assembly encouraged the creation of a common transition for both testing and SMD connections. An hybrid circuit/EM simulation design strategy was utilized to design and optimize these transitions. The thermal behaviour of Alumina devices was analysed to evaluate their application for military and satellite communication systems. Experiments realized at $f_o = 42 GHz$ show a maximum frequency shift of $0.48\% f_o$ for operating temperatures up to $80 \text{ }^\circ C$ ($-2560 kHz/^\circ C$). Bubbles and cracks were identified on the aerosol-deposited silver coating over $200 \text{ }^\circ C$. Extra tuning step could be implemented in case of more restrictive specifications. The temperature stability was enhanced by implementing collective-fabrication passive filters in a commercial low-cost high-Q thermally compensated substrate. The devices were coated in copper to increase the maximum supported temperature. Surface-mount filters as compact as the filters developed in LMST G3 were designed as a case of study for 5G mm-Wave band applications at 26 GHz. Highly-integrated and large temperature operating devices were obtained as a result of the application with significant thermal stability improvements (center frequency temperature stability of $-4.17 kHz/^\circ C$).

Problems observed during a first generation of SMD devices were taken into account during LMST G4. The devices were designed to be placed with an industrial pick and place machine to reduce the misalignment and fabricated in a surface machined substrate to improve the flatness and the contact in the device-board interface. The carrier board was fabricated in a Rogers board for microwave applications, re-metallized and covered in gold to enhance the compatibility with the solder paste. Despite these considerations measurements show a deficient external coupling owing to the solder paste thickness. The high permittivity difference between the substrate and the air-board results in a high sensitivity to this parameter. A reduction of this layer and a better thickness control as well as an optimization of the coplanar accesses could overcome this final outcome.

The data gathered through the different fabrications provided valuable information to assess the typical frequency shift and bandwidth deviation to be expected from this technology.

Machining tests carried out in custom low-loss temperature stable ceramic substrate developed in Limoges exhibit a good fabrication quality without structural damages in thicknesses up to 0.75 mm. Millimeter-wave components such as power splitters, directional couplers or diplexers as well as more complex mm-Wave subsystems are expected to be developed in future LMST generations on this material. Finally, an electrical model of the frequency shift and quality factor degradation will be developed to reduce the calculation time during the supports length estimation to tune the devices. The model could be integrated to automate the industrial production using the test measurements as input and returning the trim path for the optimized filter.

6

Conclusions

IN this thesis we have studied the utilization of ceramic materials to perform the integration of microwave technologies focused on wireless communication systems. All the devices investigated were designed to fulfill the specifications of massive MIMO front-ends in the microwave and millimeter-wave bands, standardized during the recent years for 5G and beyond. Additive and subtractive manufacturing techniques were equally implemented for the development of 2.5-D and 3-D components based on ceramic-filled cavity devices for terrestrial, aerial and space applications. Special attention was given to the development of components compliant to the surface-mount methods utilized nowadays in the industry sector.

The main goals pursued in this thesis were the fundamental guidelines for the establishment of the different lines of work. The common objectives comprehended the minimization of the space occupied by passive elements in receptor/transmitter front-ends while providing good EM performances, the technological integration of subsystems and functionalities in reduced areas, and the weight reduction and temperature stability required for affordable satellite networks deployment. Additionally, a discussion of the major difficulties observed during the fabrication of metal coated state-of-the-art 3-D printed ceramic devices was held throughout this work. The observations made in

every project served also as useful feedback information for the application of different strategies and the resolution of these problems in other lines of work. In the same way, the study of different transitions was carried out in the different projects to gather enough information in regard to the SMD assembly of these devices.

6.0.1 Surface-mount transitions

In general terms we can conclude that:

1. In the case of utilization of coplanar ports for the excitation of TE_{10p} modes, it is better to place the patterns on the metal surface of the resonator owing to the better accuracy of lasers machine in comparison to PCB milling machining.
2. The use of coplanar ports as the examples shown in Chapter 3 and 5 allows to test the correct operation of the devices before the final assembly on the carrier board. As a result, it is possible to detect out-of-specification or failed devices during the fabrication stage and carry out correction techniques.
3. Coplanar ports require a good alignment to avoid short-circuits and are highly sensitive to the the gap between the board and the device, thus greatly affecting the filter's external quality factor. The application of transitions as the ones shown in Chapter 4 for resonators turned sideways are less sensitive to alignment mismatch and air gap separation, whereas risk of short-circuit are less likely. However, the device testing functionality during the fabrication stage is not available in this case.

The placement of the 3-D printed devices as well as the LMST components was realized successfully by means of a pick and place machine in every case, excluding some particular cases as the C- and U-shaped filters. Even though the solder paste deposition was controlled manually in the laboratory facilities, the observed results seems to be good enough for proof-of-concept demonstrations. Nonetheless, better results can be achieved in an industrially controlled process, specially in the case of millimeter-wave applications such as the LMST SMD band-pass filters.

6.0.2 Low-loss ceramics and metallization tests

The utilization of low-loss ceramic substrates developed in dedicated research activities carried out in the laboratories of the University of Limoges, in addition to the experimental tests performed with electroless copper metallization, aerosol silver plating, gold sputtering and electrolysis, helped to determine the general fabrication process to be followed for all the devices.

On the one hand, the electroless copper plating tests performed in the laboratory exhibited a conductivity between $7 S/\mu m \leq \rho \leq 27 S/\mu m$ for Alumina substrates with average surface roughness between $289 nm \leq Ra \leq 716 nm$. The same tests performed on Rogers RO4003C PCBs demonstrated a lower maximum conductivity for the same process between $6 - 12 S/\mu m$. On the other hand, the tests conducted in LMST G3 resonators plated by aerosol silver deposition shown a maximum conductivity around $30 S/\mu m$.

In regard to the metal layer adherence on the ceramic substrates implemented in this thesis, even though both processes seem to work properly in the deposition of the material, the silver coating seems to be more fragile to scratches, to lift more easily under mechanical stress, and to support lower temperatures than the copper layer. However, no conclusive tests were carried out in this work to study and properly estimate the adherence level of both methods.

The protective gold plating process was implemented in all the devices to avoid oxidation and to enhance the material compatibility with bonding wire machines and their assembly on carrier boards with a gold layer termination. Gold electrolysis and sputtering tests realized in both copper and silver coated ceramic devices shown a negligible difference in terms of the material deposition quality and adherence. The only remark that can be done in this regard is related to the processes themselves. Gold sputtering requires the utilization of expensive equipment and a considerable amount of time (several tens of minutes) to plate one surface of the device, while gold electrolysis can be done in a couple of minutes in the whole component.

6.0.3 3-D printed designs and technology integration

The popularity of ceramic technologies in microwave applications is nowadays eclipsed by cost-effective polymer or metal printed devices. Nevertheless, the numerous useful features of ceramics such as compact size, low-loss, light weight or temperature stability should motivate their implementation in modern communication systems. The utilization of ceramic 3-D printed devices was explored as a tool for the conception of SMD components that can make part of complex RF front-ends. In Chapter 3, we investigated the application of SLA process for the creation of flip-chip compact tunable filters with a SoP-like methodology by integrating the control circuit inside or below. This approach can be extended to the inclusion of planar devices (low-pass filters, power splitters, etc.) or other active circuits of the transceptor such as LNAs or mixers. The study carried out with single-mode cavity resonators shows that good quality

factors can be achieved with Alumina substrates. Nevertheless, the Q-factor is rapidly degraded when integrating external devices to the component. The utilization of p-i-n diode switches instead of varactors was intentionally chosen to minimize this problem. Nevertheless, the contribution of the laser engraved patterns, in addition to the wirebond parasitics and other sources of loss such as the solder paste contact resistance or a poor ground connection due to the device tilting during the placement conspire against the success of the method. Many of these constraints can be enhanced in a well controlled industrial environment. Moreover, the replacement of switches by MEMS technology and the substitution of bond wires by aerosol jet printed lines can help to improve the RF performances. Emerging RF switches technologies such as resistive memory devices are also a promising solution for near future developments in the field of tunable filters [263]. The exploration of several resonator prototypes opens the possibility to different interesting approaches for N-bit microwave filters. However, further investigations are required to provide an appropriate conclusion about the best trade-off between the designs.

In the case of the filters developed in Chapter 4, many common scenarios were identified where the application of ceramic additive manufacturing can provide several functionalities to the system, adapt to the PCB (facilitating the floor planing), and reduce the consumed area. Envisioning a SoP subsystem and the integration of antenna elements is also possible with these designs, specially in the case of the Box filter. This approach should be explored in future work by implementing the co-design of filtenna components.

The accurate fabrication of real 3-D devices is a constraint to take into account that can limit the application of these technologies at higher frequencies than the X-band. The laser tuning strategies discussed can provide a solution up to certain point, however, further efforts should be done to improve this limiting factor.

The complex deformations generated during the ceramic sintering process are difficult to model and back-simulate to foresee the device behaviour. Nevertheless, 3-D laser scanning techniques can be an useful tool for the reproduction and simulation of a more accurate model in 3-D full-wave EM simulators. The major complications come from the programming point of view, since the reconstruction of the cloud of points file obtained as a result of the scanning is not trivial. Some CAD software provide this functionality in a semi-autonomous way with the user assistance. Dedicated activities based on fully autonomous reconstruction techniques could provide useful solutions in this topic.

6.0.4 LMST millimeter-wave devices for 5G applications

The development of LMST led to the evolution of the fabrication flow throughout the different generations thanks to the characterization of the technology and the correction of the observed difficulties in every step. Several functionalities such as the collective fabrication, the device's pre-testing before the extraction, the supports tuning strategy and the SMD transitions were included in the process. Different band-pass filter topologies and waveguides were used as DUTs to enhance the technology. We agree on the fact that the process is mature enough for the industrial automation and the creation of more complex filters and millimeter-wave components based on low-loss Alumina substrates. However, there is still a way to go to improve the quality factor of temperature stable devices and their assembly. New undergoing tests and fabrication runs could shade some light towards the correct approach to be taken.

6.0.5 Temperature stability and weight

The characterization in temperature (higher than room temperature and at ambient humidity) of SMD 3-D printed band-pass filters based on regular Alumina substrates reveals a central frequency shift $\delta f_0 = -364 \text{ kHz}/^\circ\text{C}$ for the tunable devices operating in the C-band, $\delta f_0 = -766 \text{ kHz}/^\circ\text{C}$ in the worst case for the Bridge filter operating in the X-band and $\delta f_0 = -2.56 \text{ MHz}/^\circ\text{C}$ in LMST G3 filters working in the Q-band. These results represent a frequency shift of -36.4 MHz, -76.6 MHz and -256 MHz, respectively, within 25 - 125 °C. Even though, the frequency shift may be low enough for certain applications and the filter's frequency response is maintained with the temperature drift, the temperature stability can be enhanced for more stringent specifications.

As shown in LMST G4, the use of commercial thermally stable substrates can compensate the effect of temperature drift while conserving the miniaturization, performances and light weight. Measurements exhibit a maximum central frequency shift between $44 \text{ kHz}/^\circ\text{C} \leq \delta f_0 \leq 108 \text{ kHz}/^\circ\text{C}$ (4.4 - 10.8 MHz between 25 - 125 °C), close to state-of-the-art temperature compensated air-filled SIW technologies ($\delta f_0 = 35 \text{ kHz}/^\circ\text{C}$). Furthermore, custom-made low-loss temperature stable ceramics are currently under development in Limoges. Their implementation might allow to: optimize the mechanical resistance for the processes contemplated in this work, compensate the effect of temperature, and set the desired substrate permittivity. Its application in 3-D printed processes could extend these features to all the designs introduced in this thesis.

Regarding to the total size and weight observed in the fabricated components, the devices seem to be more compact and lighter than other technologies thanks to the intrinsic characteristics of ceramics. The 4-pole LMST filters realized for 5G millimeter-wave bands exhibit a total weight of 27 mg and 44 mg for regular Alumina and BMT substrates, while the weight of commercial SMD devices at the same frequency bands is around the order of grams. In regard to the size, LMST devices seem to be one of the most compact technologies, close to LTCC components found in the literature.

The aforementioned features may be a promising solution for satellite or aerospace communication applications. However, further experiments should be realized at low temperatures and several humidity conditions in a climatic chamber before considering their implementation in such systems.



Annexes

Summary

A.1	Wirebonds interconnections model	212
A.1.1	Estimation of bond wire S-parameters with de-embedding technique	214
A.1.2	Generic π -circuit Y-parameters (left) and bond wire model (right).	217
A.2	3-D printed filters extracted coupling matrices	221
A.2.1	Untuned devices	221
A.2.2	Tuned devices	222
A.3	LMST G4	223

A.1 Wirebonds interconnections model

The MA4AGSW1 switch is designed to assemble the die back plate with electrically conductive silver epoxy or with a low temperature solder paste connecting the device ground to the carrier board. Gold bonding pads are placed on the top to bond wire the ports terminal. Bond wires usually introduce a parasitic inductive effect on the transmission lines that could degrade the circuit response as the frequency increases [264], [265]. The correct modelling of bond wires allows to identify their contribution to the resonator quality factor degradation and take actions to minimize their effect. Therefore, these elements should be included in the simulation model. Figure A.1 depicts a widely used model that takes into account the main parasitics of wire bonds, where L_W and R_W represent the wire inductance and resistance, and C_W the capacitive effect between the wire and the board metal plate. Even though the input and output capacitors could be slightly different, they are considered to be the same for the model simplification.

The bias circuit shown in fig. 3.13 was fabricated in order to test the simulation models, verify the proper function of the circuit, estimate the parameters from gold bond wires realized with a bonding machine facility in our laboratory and address possible fabrication or welding problems. A $50\ \Omega$ CPWG line was carved in the first place in a $0.4\ \text{mm}$ RO4003C substrate with a milling machine. The vias were pierced using a $1\ \text{mm}$ diameter mill, covered with conductive epoxy glue deposited in their interior and heated in an oven at 150°C during 2 hours. The central line width was $W = 0.61\ \text{mm}$, the gap between the the line and the ground plane was $G = 0.17\ \text{mm}$ and the total length was $L = 19.125\ \text{mm}$ that corresponds to $\lambda/2$ at $5\ \text{GHz}$. The line was measured with a $500\ \mu\text{m}$ pitch GSG probe station between 1 to $10\ \text{GHz}$ and compared to ADS and HFSS simulations with the same geometrical parameters. Measurements exhibit

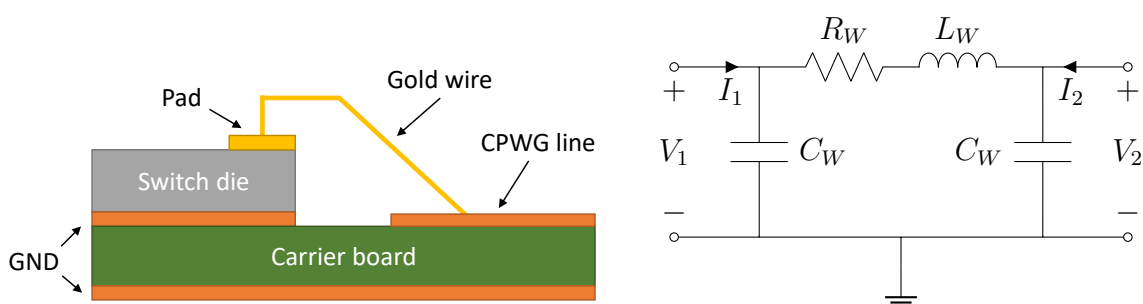


Figure A.1: Typical lumped element bond wire circuit model.

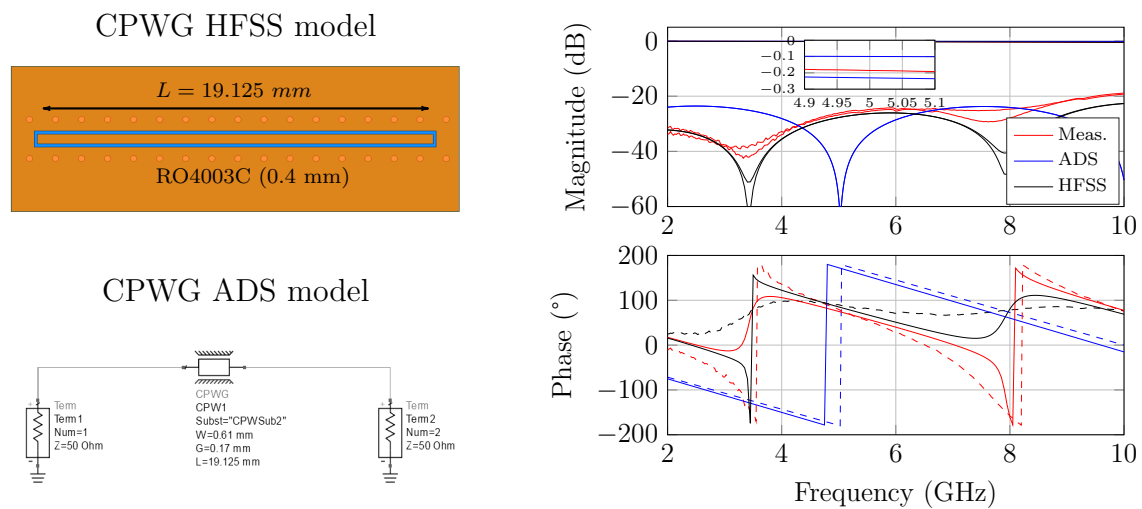


Figure A.2: Manufactured coplanar line S-parameter measurement, and circuit and electromagnetic simulations comparison.

a matching better than -20 dB and losses of 0.012 dB/mm (fig. A.2). Finite-element simulations show a good fit in magnitude and phase for the modelled line while the CPWG line block implemented in ADS shows a good agreement in the behaviour but with a different electrical length (fig. A.2). This behaviour was corrected by adjusting the block parameters to be implemented in future simulations. Furthermore, simulations seem to underestimate the losses probably because of the low via conductivity.

The exact same line was implemented with a p-i-n diode switch in series and its associated bias network (fig. A.3.a). The board was coated in gold using a gold electrolysis process to avoid oxidation on the copper surface and to improve the compatibility with gold bond wires. As shown in figure A.3.b, the device was welded to the board using conductive epoxy glue with the same process as the vias metallization and bonded with $25 \mu\text{m}$ diameter gold wires. Surface-mount discrete components 0201 with self-resonance frequency (SRF) $SRF \geq 60\%f_s$ were used to perform the bias network ($L = 8.2 \text{ nH}$ LQW03AW8N2J00D and $C = 39 \text{ pF}$ GRM0335C1E390JA01D) and the coupling capacitors ($C1 = C2 = 10 \text{ pF}$ GJM0335C1E100JB01D). In order to extract the wire bond parasitics, the wire length was estimated by measuring the distance between the two welding points $P1 = (W1, H1)$ and $P2 = (W2, H2)$ with a digital microscope. The height difference is approximately the switch die thickness $H1 - H2 \approx 110 \mu\text{m}$. Therefore the wire length was calculated as $L_W = \sqrt{(H1 - H2)^2 + (W1 - W2)^2} \approx 367 \mu\text{m}$.

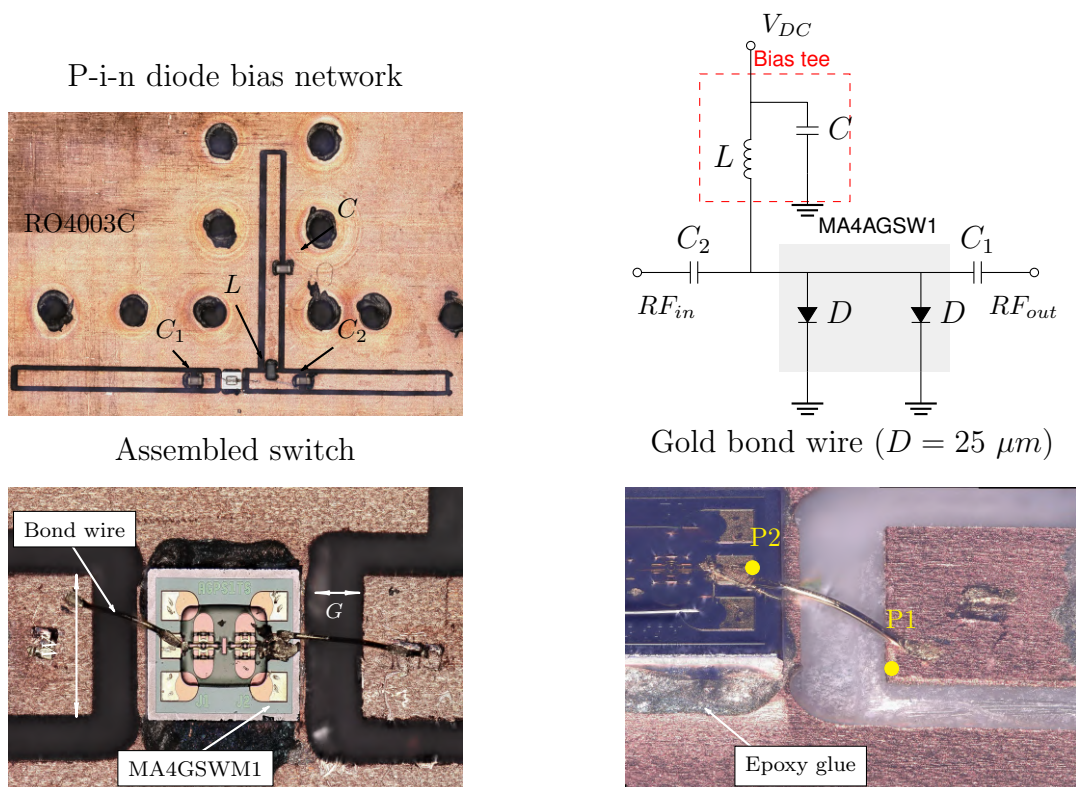


Figure A.3: MA4AGSW1 bias network assembly on a Rogers RO4003C board.

A.1.1 Estimation of bond wire S-parameters with de-embedding technique

The manufactured circuit measurements were compared to electromagnetic and circuit models without taking into account the bond wires effect. The electromagnetic model was developed in HFSS and complemented with the ANSYS circuit simulator to embed the switch Touchstone files. The SMD components were simulated as lumped elements connected to the CPWG lines modelled in the HFSS simulator. As a hypothesis we assume that if the wires contribution to the frequency response at the operating band is negligible, then the overall simulations and measurements behaviour should be similar. Nevertheless, in figure A.4 it can be observed an important difference between simulation and experimental results. Therefore, the effect of the wire bond is non-negligible and must be taken into account to match the simulations with measurements. Based on the experimental results, the objective is to de-embed the parasitics of the two bond wires. For the sake of the analysis simplification we will suppose that both of them are identical and that the contact resistivity in the wire/board interface are included into the wire resistive element. The de-embedding technique consists of the

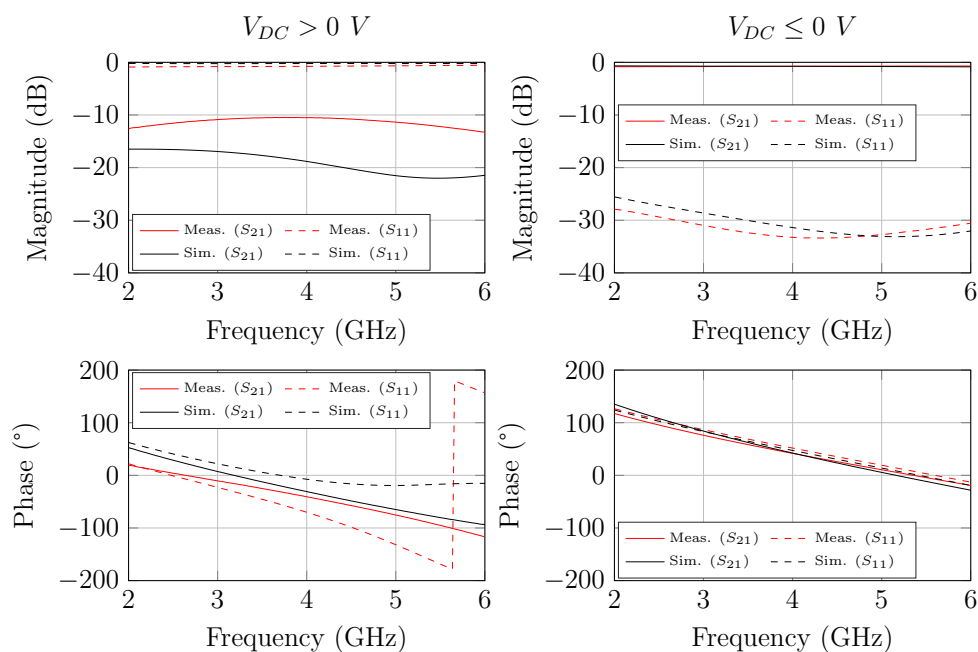


Figure A.4: P-i-n diode switch control network comparison of circuit/electromagnetic model (without bond wires) and measurements.

device under test characterization by removing the effects of external interconnections or elements in the path between the measurement interface and the DUT. Particularly, in the configuration shown in figure A.5 the unknown blocks behaviour (highlighted in red) are the bond wires at each side of the switch. The blocks highlighted in orange such as, the bias tee and the output RF line can be fabricated and measured separately while the S-parameters of the p-i-n diode switch can be characterized with a probe station or replaced by the manufacturer Touchstone files.

The input/output RF line blocks cascaded to the rest of the network can be de-embedded from the measured scattering parameters in order to isolate their effect converting the S-parameters into T-parameters (T_I and T_O). Then, it is possible to calculate the combined bond wires/switch transmission parameters T_D as depicted in equation A.2.

$$[T_m] = [T_I] \cdot [T_D] \cdot [T_O] \quad (\text{A.1})$$

$$[T_D] = [T_I]^{-1} \cdot [T_m] \cdot [T_O]^{-1} \quad (\text{A.2})$$

Similarly, the de-embedded matrix T_D can be expressed as the cascaded T-parameters of the bond wires and the switch. Considering that both wires are exactly the same, the matrix multiplication operation is simplified as shown in equation A.3. As it can be

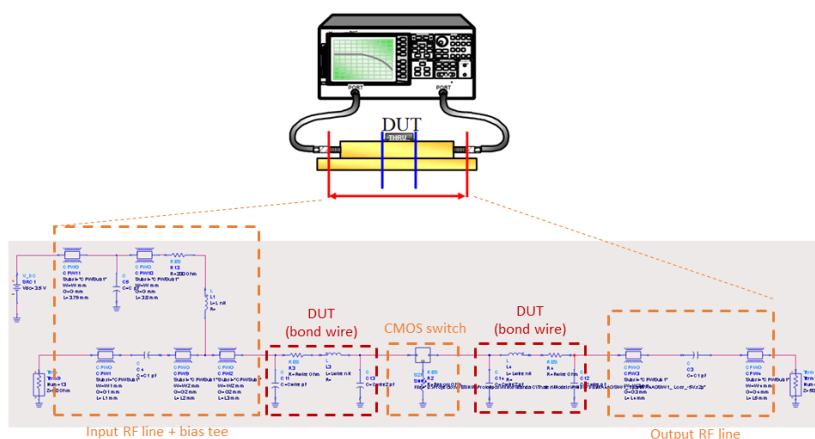


Figure A.5: Scheme of the bias network circuit blocks to be de-embedded.

seen, the matrix results in a system of equations with four unknown variables (T_{w11} , T_{w12} , T_{w21} , T_{w22}) and four equations. The coefficients K_i with $i = 1..8$ corresponds to a combination of the T_{switch} parameters. Then, it is possible to solve the system of equations in a computing software as MATLAB to obtain the transmission parameters at each frequency point.

$$\begin{bmatrix} T_{D11} & T_{D12} \\ T_{D21} & T_{D22} \end{bmatrix} = \begin{bmatrix} T_{w11}^2 \cdot K_1 + T_{w12} \cdot T_{w21} \cdot K_2 & T_{w11} \cdot T_{w12} \cdot K_3 + T_{w12} \cdot T_{w22} \cdot K_4 \\ T_{w11} \cdot T_{w21} \cdot K_5 + T_{w21} \cdot T_{w22} \cdot K_6 & T_{w22}^2 \cdot K_7 \cdot T_{w12} \cdot T_{w21} \cdot K_8 \end{bmatrix} \quad (\text{A.3})$$

The set of solutions calculated with MATLAB is converted from T- to S-parameters. Two of these solutions show the same magnitude and complementary phase and are compliant to the bond wire frequency response while the other two do not show a logical physical behaviour for this case and are not taken into account. The final solution is chosen based on the phase. In one hand the extracted inductance and capacitive parameters are positive in sign and on the other case are negative.

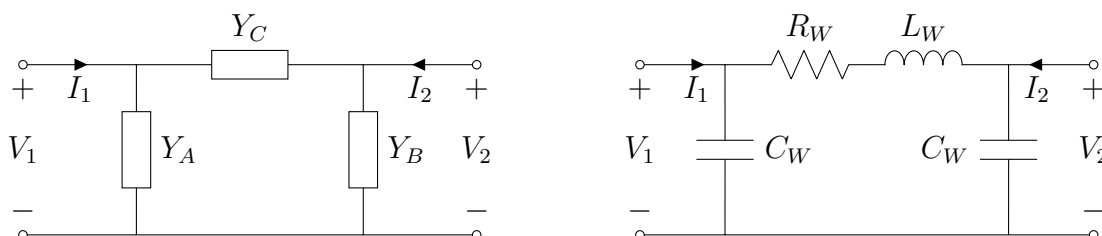


Figure A.6: Reference In-line filter design and frequency response.

A.1.2 Generic π -circuit Y-parameters (left) and bond wire model (right).

Owing to the passive nature of the bond wires, the lumped element model can be associated to the equivalent circuit for Y-parameters of a reciprocal two-port network (see fig. A.6). It is possible to establish a relationship between the π -circuit elements and the 2-port network Y-parameters as exhibited in eq. A.4.

$$\begin{cases} Y_{11} = Y_a + Y_c \\ Y_{12} = -Y_c \\ Y_{21} = -Y_c \\ Y_{22} = Y_b + Y_c \end{cases} \rightarrow \begin{cases} Y_a = Y_{11} + Y_{12} \\ Y_b = Y_{22} + Y_{12} \\ Y_c = -Y_{12} = -Y_{21} \end{cases} \quad (\text{A.4})$$

The bond wire model components can be obtained with these equations by converting the de-embedded scattering parameters to admittance parameters. Consequently, the lumped element values can be expressed as follow:

$$R = Re\left\{-\frac{1}{Y_{12}}\right\}, \quad L = \frac{Im\left\{-\frac{1}{Y_{12}}\right\}}{\omega}, \quad C_w = \frac{Y_{11} + Y_{12}}{\omega} = \frac{Y_{22} + Y_{12}}{\omega} \quad (\text{A.5})$$

The admittances Y_a , Y_b and Y_c as well as the extracted parameters R_W , L_W and were calculated implementing the developed methodology and the equations explained so far within the filter bank operating band (f_i to f_s in C-band). A cross-checked was carried out to evaluate the extracted bond wire parasitics. The verification was contrasted against the theoretical calculation of round wires and the experimental information provided by silicon prototyping for custom and semi-custom ICs services [266]. The wire inductance and the DC resistance can be calculated as shown in equations A.6 and A.9, where L_W is the inductance in μH , d is the diameter in cm, l is the length in cm, f is the frequency in Hz, μ is the absolute magnetic permeability of the conductor and ρ is the resistivity of the conductor in $\Omega.m$.

$$L_W = 0.002.l \cdot \left[\ln\left(\frac{4.l}{d}\right) - 1 + \frac{d}{2.l} + \frac{T(x) \cdot \mu_r}{4} \right] \quad (\text{A.6})$$

$$T(x) = \sqrt{\frac{0.873011 + 0.00186128.x}{1 - 0.278381.x + 0.127964.x^2}} \quad (\text{A.7})$$

$$x = \pi.d \sqrt{\frac{2 \cdot \mu \cdot f}{\sigma}} \quad (\text{A.8})$$

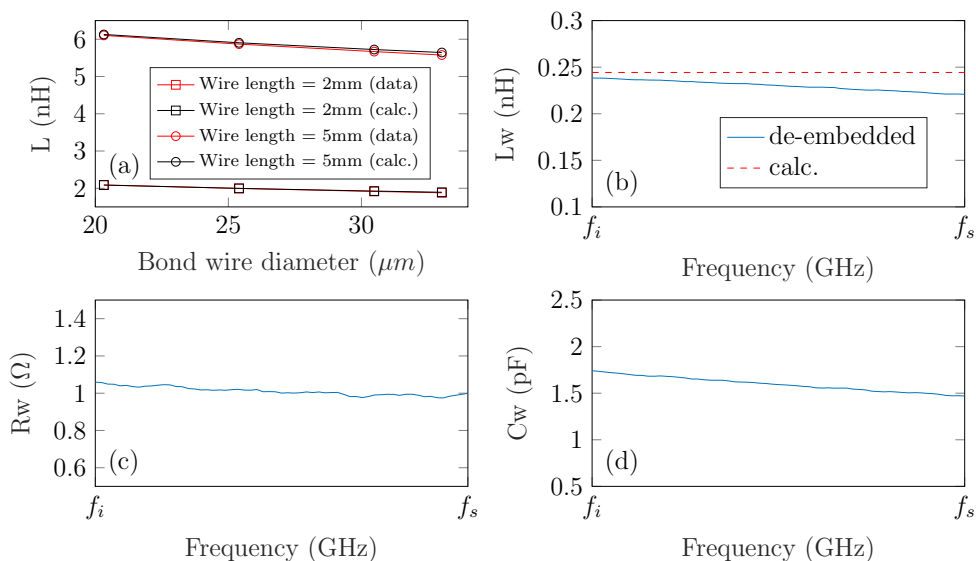


Figure A.7: Cross-check between bond wire inductance theoretical calculation and experimental data (a), and de-embedded bond wire model inductance (b), resistance (c), and capacitance (d).

$$R_{W_{DC}} = \frac{\rho \cdot l}{\pi \cdot (d/2)^2} \quad (\text{A.9})$$

A comparison between the bond wire inductance obtained by the theoretical equations and the experimental data provided by ICs manufacturers depicted in figure A.7 show a good match between several wire diameter and length. The theoretical inductance equation was used as a reference for a $25 \mu\text{m}$ wire diameter compared to L_W obtained with the de-embedding technique. Results exhibit a value between $0.22 \text{ nH} \leq L_W \leq 0.24 \text{ nH}$ against the calculated theoretical value $L_{W_{calc}} = 0.24 \text{ nH}$. All the losses between the CPWCG termination and the switch pad, including the contact resistance are represented in R_W . The wire DC resistance calculated with eq. A.9 is $R_{W_{DC}} = 16 \text{ m}\Omega$ while the total de-embedded losses are around $R_W \approx 1 \Omega$. Finally, the lumped element model capacitance is estimated to be between $1.47 \text{ pF} \leq C_W \leq 1.74 \text{ pF}$.

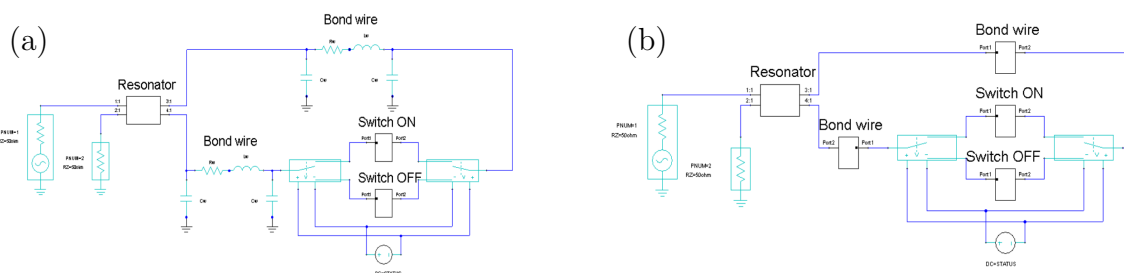


Figure A.8: P-i-n diode switch bias network electromagnetic and circuit simulation implementing the bond wire lumped-element model (a) and Touchstone files (b).

The wire bond model can be implemented in HFSS mixing the rectangular cavity resonator electromagnetic simulations with the switch and the bias network to estimate their impact on the quality factor and frequency shift. The mixed simulation method schematic implemented in the simulator is shown in fig. A.8, where the resonator block provides the simulated EM data of the rectangular ceramic cavity excited through the RF ports 1 and 2 and the bias network carved into the metal surface. Ports 3 and 4 represent the interface of both bond wires welded on the CPW line. The bond wire model are included in the circuit schematic and the ON/OFF p-i-n diode switch S-parameters can be selected by modifying the polarization of the DC bias source. Based on these considerations different scenarios could be evaluated to overcome the additional aggregated losses as a result of the tuning control circuit. When performing the simulations it is possible to choose between two options:

1. implement the lumped element model taking into consideration the frequency dependency nature of the parameters within the band (fig. A.8.a). The plots shown in figure A.7 could be fitted with an approximation function in order to be implemented in the simulator.
2. embed the bond wire 2-ports network S-parameters as a block in HFSS circuit simulator as it has been done previously in ADS with the switch parameters (figure

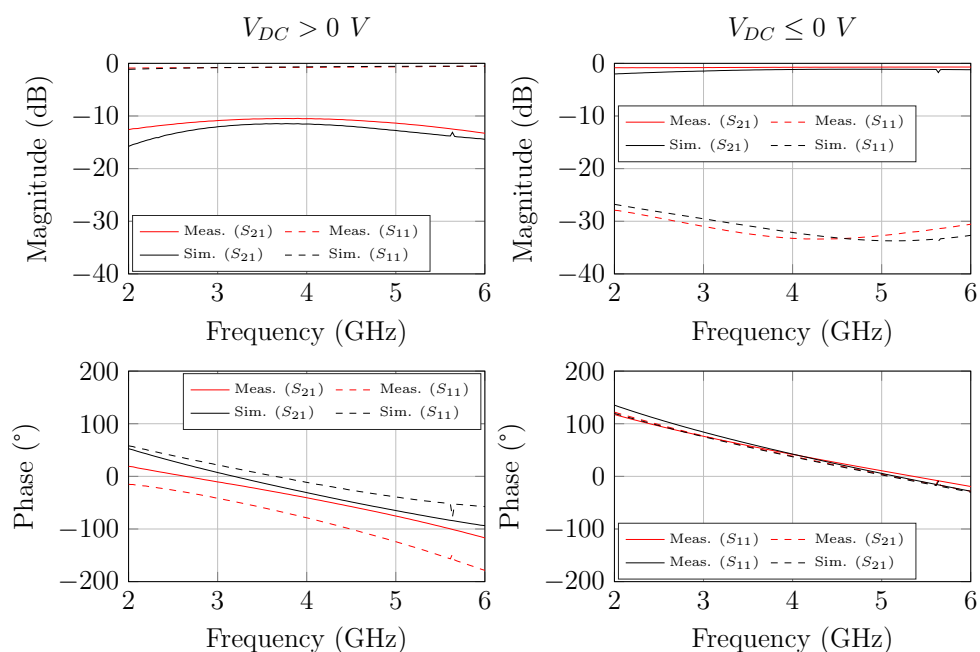


Figure A.9: P-i-n diode switch control network (with bond wires) comparison of hybrid simulation complete model and measurements.

A.8.b).

For the case studies presented throughout this chapter all the designs will be performed mixing circuit and full-wave EM simulations in HFSS implementing the p-i-n diode switch and the de-embedded bond wire Touchstone files (second option) to get a more accurate behaviour and avoid further parameters approximations or simplifications.

Figure A.9 shows that the obtained results using the second option have a more accurate agreement compared to the model without bond wires (see fig. A.4), specially on S_{11}/S_{22} when the p-i-n diode switch is forward biased (switch ON or $V_{DC} > 0 V$).

A.2 3-D printed filters extracted coupling matrices

A.2.1 Untuned devices

The colors in the extracted coupling matrices represent the measured pre-tuned (blue), back-simulated (orange), and simulated tuned (black) filters.

C-shaped filter

$$\begin{bmatrix} 0 \setminus 0 \setminus 0 & 0.96 \setminus 1.16 \setminus 1.17 & -0.02 \setminus -0.02 \setminus -0.03 & 0.01 \setminus 0.01 \setminus 0.01 & 0 \setminus 0 \setminus 0 & 0 \setminus 0 \setminus 0 \\ 0.96 \setminus 1.16 \setminus 1.17 & -0.59 \setminus 0.01 \setminus 0.03 & 0.95 \setminus 1.06 \setminus 1.09 & -0.02 \setminus -0.03 \setminus -0.04 & 0.02 \setminus 0.02 \setminus 0 & 0 \setminus 0 \setminus 0 \\ -0.02 \setminus -0.02 \setminus -0.03 & 0.95 \setminus 1.06 \setminus 1.09 & 0.19 \setminus 0.67 \setminus 0.03 & 0.61 \setminus 0.64 \setminus 0.77 & -0.03 \setminus -0.03 \setminus -0.04 & -0.01 \setminus -0.02 \setminus 0 \\ 0 \setminus 0.01 \setminus 0.01 & -0.02 \setminus -0.03 \setminus -0.04 & 0.61 \setminus 0.64 \setminus 0.77 & -0.12 \setminus 0.24 \setminus 0.03 & 0.90 \setminus 1.07 \setminus 1.07 & -0.02 \setminus -0.02 \setminus -0.03 \\ 0 \setminus 0 \setminus 0 & 0.02 \setminus 0.02 \setminus 0 & -0.03 \setminus -0.03 \setminus -0.04 & 0.90 \setminus 1.07 \setminus 1.07 & -1.03 \setminus -0.44 \setminus -0.15 & 1.00 \setminus 1.15 \setminus 1.11 \\ 0 \setminus 0 \setminus 0 & 0 \setminus 0 \setminus 0 & -0.01 \setminus -0.02 \setminus 0.01 & -0.02 \setminus -0.02 \setminus -0.03 & 1.00 \setminus 1.16 \setminus 1.11 & 0 \setminus 0 \setminus 0 \end{bmatrix} \quad (\text{A.10})$$

Bridge filter

$$\begin{bmatrix} 0 \setminus 0 \setminus 0 & 0.73 \setminus 0.92 \setminus 1.13 & 0 \setminus 0 \setminus -0.03 & 0 \setminus 0 \setminus 0 & 0 \setminus 0 \setminus 0 & 0 \setminus 0 \setminus 0 \\ 0.73 \setminus 0.92 \setminus 1.13 & 1.65 \setminus 1.31 \setminus -0.06 & 0.67 \setminus 0.87 \setminus 0.99 & 0 \setminus 0 \setminus -0.05 & 0 \setminus 0 \setminus 0 & 0 \setminus 0 \setminus 0 \\ 0 \setminus 0 \setminus -0.03 & 0.67 \setminus 0.87 \setminus 0.99 & 0.94 \setminus 0.94 \setminus 0.02 & 0.49 \setminus 0.56 \setminus 0.73 & 0 \setminus 0 \setminus -0.05 & 0 \setminus -0.01 \setminus 0 \\ 0.01 \setminus 0.01 \setminus 0 & 0 \setminus 0 \setminus -0.05 & 0.49 \setminus 0.56 \setminus 0.73 & 0.64 \setminus -0.90 \setminus 0.04 & 0.54 \setminus 0.54 \setminus 1.11 & 0 \setminus 0 \setminus -0.03 \\ 0 \setminus 0 \setminus 0 & 0 \setminus 0 \setminus 0.01 & 0 \setminus 0 \setminus -0.05 & 0.54 \setminus 0.54 \setminus 1.11 & -0.81 \setminus -1.54 \setminus -0.12 & 0.82 \setminus 1.05 \setminus 1.16 \\ 0 \setminus 0 \setminus 0 & 0 \setminus 0 \setminus 0 & -0.01 \setminus -0.01 \setminus 0 & 0 \setminus 0 \setminus -0.03 & 0.82 \setminus 1.05 \setminus 1.16 & 0 \setminus 0 \setminus 0 \end{bmatrix} \quad (\text{A.11})$$

Box filter

$$\begin{bmatrix} 0 \setminus 0 \setminus 0 & 0.83 \setminus 1.26 \setminus 1.05 & 0 \setminus 0 \setminus -0.02 & 0 \setminus 0 \setminus 0 & 0 \setminus 0 \setminus 0 & 0 \setminus 0 \setminus 0 \\ 0.83 \setminus 1.27 \setminus 1.05 & 1.77 \setminus 1.58 \setminus -0.13 & 0.76 \setminus 0.95 \setminus 0.97 & -0.01 \setminus 0 \setminus -0.04 & -0.01 \setminus -0.01 \setminus 0 & 0 \setminus 0 \setminus 0 \\ 0 \setminus 0 \setminus -0.02 & 0.76 \setminus 0.95 \setminus 0.97 & 0.62 \setminus -0.09 \setminus 0 & 0.47 \setminus 0.48 \setminus 0.70 & -0.01 \setminus -0.01 \setminus -0.04 & 0 \setminus 0 \setminus -0.01 \\ 0 \setminus 0 \setminus 0 & -0.01 \setminus 0 \setminus -0.04 & 0.47 \setminus 0.48 \setminus 0.7 & 0.20 \setminus 0.19 \setminus -0.10 & 0.67 \setminus 0.69 \setminus 0.96 & 0 \setminus 0 \setminus -0.02 \\ 0 \setminus 0 \setminus 0 & -0.01 \setminus -0.01 \setminus 0.01 & -0.01 \setminus -0.01 \setminus -0.04 & 0.67 \setminus 0.69 \setminus 0.96 & 1.92 \setminus 1.76 \setminus -0.45 & 0.75 \setminus 1.24 \setminus 1.15 \\ 0 \setminus 0 \setminus 0 & 0 \setminus 0 \setminus 0 & 0 \setminus 0 \setminus -0.01 & 0 \setminus 0 \setminus -0.02 & 0.75 \setminus 1.24 \setminus 1.15 & 0 \setminus 0 \setminus 0 \end{bmatrix} \quad (\text{A.12})$$

U-shaped filter

$$\begin{bmatrix} 0 \setminus 0 \setminus 0 & 0.76 \setminus 1.20 \setminus 1.39 & -0.01 \setminus -0.01 \setminus -0.02 & 0 \setminus 0.01 \setminus 0 & -0.01 \setminus 0 \setminus 0 & 0 \setminus 0 \setminus 0 \\ 0.76 \setminus 1.20 \setminus 1.30 & -0.37 \setminus 0.51 \setminus -1.15 & 0.81 \setminus 0.81 \setminus 1.10 & -0.01 \setminus -0.01 \setminus -0.03 & -0.03 \setminus -0.01 \setminus 0 & 0.01 \setminus 0 \setminus 0 \\ -0.01 \setminus -0.01 \setminus -0.02 & 0.81 \setminus 0.81 \setminus 1.10 & -1.71 \setminus -0.59 \setminus -1.11 & 0.63 \setminus 0.75 \setminus 0.74 & -0.01 \setminus -0.01 \setminus -0.04 & 0.01 \setminus 0.01 \setminus 0 \\ 0 \setminus 0.01 \setminus 0 & -0.01 \setminus -0.02 \setminus -0.03 & 0.63 \setminus 0.75 \setminus 0.74 & -1.65 \setminus -0.92 \setminus -0.94 & 0.77 \setminus 0.70 \setminus 0.98 & -0.01 \setminus -0.01 \setminus -0.02 \\ -0.01 \setminus 0 \setminus 0 & -0.03 \setminus -0.01 \setminus 0 & -0.01 \setminus -0.01 \setminus -0.04 & 0.77 \setminus 0.70 \setminus 0.98 & 0.23 \setminus 0.70 \setminus -1.30 & 0.73 \setminus 1.23 \setminus 1.33 \\ 0 \setminus 0 \setminus 0 & 0.01 \setminus 0 \setminus 0 & 0.01 \setminus 0.01 \setminus 0 & -0.01 \setminus -0.01 \setminus -0.02 & 0.73 \setminus 1.23 \setminus 1.33 & 0 \setminus 0 \setminus 0 \end{bmatrix} \quad (\text{A.13})$$

A.2.2 Tuned devices

Extracted coupling matrices for the measured pre-tuned (blue), simulated target (black) and measured tuned (red) filters.

C-shaped filter

$$\begin{bmatrix} 0\backslash0\backslash0 & 1.11\backslash1.07\backslash1.08 & -0.01\backslash0\backslash-0.02 & 0.02\backslash0\backslash0.01 & -0.01\backslash0\backslash0 & 0\backslash0\backslash0 \\ 1.11\backslash1.07\backslash1.08 & -0.89\backslash0.16\backslash0.20 & 1.13\backslash0.98\backslash0.96 & -0.02\backslash0\backslash-0.02 & 0.02\backslash0\backslash0 & 0.01\backslash0\backslash0 \\ -0.01\backslash0\backslash-0.02 & 1.13\backslash0.98\backslash0.96 & 0.33\backslash0.23\backslash0.21 & 0.78\backslash0.76\backslash0.79 & -0.02\backslash0\backslash-0.02 & -0.02\backslash0\backslash0.01 \\ 0.02\backslash0\backslash0.01 & -0.02\backslash0\backslash-0.02 & 0.78\backslash0.76\backslash0.79 & -0.60\backslash0.21\backslash0.13 & 1.15\backslash0.95\backslash0.94 & -0.02\backslash0\backslash-0.02 \\ -0.01\backslash0\backslash0 & 0.02\backslash0\backslash0 & -0.02\backslash0\backslash-0.03 & 1.15\backslash0.95\backslash0.94 & -1.73\backslash-0.11\backslash0.27 & 1.01\backslash1.03\backslash1.04 \\ 0\backslash0\backslash0 & 0.01\backslash0\backslash0 & -0.02\backslash0\backslash0.01 & -0.02\backslash0\backslash-0.02 & 1.01\backslash1.03\backslash1.04 & 0\backslash0\backslash0 \end{bmatrix} \quad (\text{A.14})$$

Bridge filter

$$\begin{bmatrix} 0\backslash0\backslash0 & 1.03\backslash1.05\backslash1.01 & 0\backslash0.04\backslash0 & 0.01\backslash0\backslash0.02 & -0.01\backslash0\backslash0 & 0\backslash0\backslash0 \\ 1.03\backslash1.05\backslash1.01 & 2.30\backslash-0.13\backslash1.11 & 1.35\backslash0.88\backslash0.93 & -0.01\backslash0.07\backslash-0.01 & 0\backslash0\backslash0 & 0\backslash0\backslash0 \\ 0\backslash0.04\backslash0 & 1.35\backslash0.88\backslash0.93 & 0.88\backslash-0.04\backslash-0.33 & 0.98\backslash0.68\backslash0.80 & -0.01\backslash0.06\backslash-0.01 & -0.02\backslash0\backslash0 \\ 0.01\backslash0\backslash0.02 & -0.01\backslash0.07\backslash-0.01 & 0.98\backslash0.68\backslash0.80 & 0.27\backslash-0.03\backslash-0.25 & 1.08\backslash0.94\backslash0.92 & 0\backslash0.04\backslash0 \\ -0.01\backslash0\backslash0 & 0\backslash0\backslash0 & -0.01\backslash0.06\backslash-0.01 & 1.08\backslash0.94\backslash0.92 & -2.62\backslash-0.13\backslash-0.39 & 1.16\backslash1.13\backslash1.11 \\ 0\backslash0\backslash0 & 0\backslash0\backslash0 & -0.02\backslash0\backslash0 & -0.01\backslash0.04\backslash0 & 1.16\backslash1.13\backslash1.11 & 0\backslash0\backslash0 \end{bmatrix} \quad (\text{A.15})$$

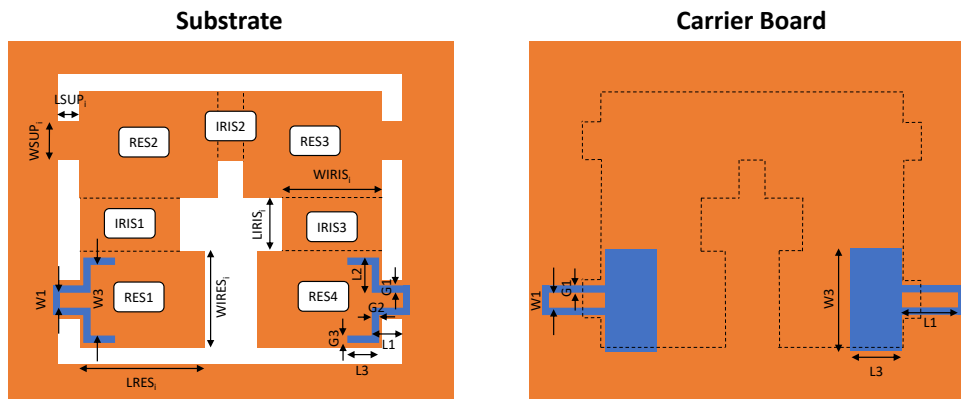
Box filter

$$\begin{bmatrix} 0\backslash0\backslash0 & 1.03\backslash0.99\backslash0.99 & -0.01\backslash0.01\backslash0 & 0.01\backslash-0.02\backslash0 & 0\backslash0\backslash0 & 0\backslash0\backslash0 \\ 1.03\backslash0.99\backslash0.99 & 1.19\backslash0.06\backslash-0.14 & 1.17\backslash0.88\backslash0.89 & -0.01\backslash0.02\backslash-0.01 & -0.02\backslash-0.02\backslash0 & 0\backslash0\backslash0 \\ -0.01\backslash0.01\backslash0 & 1.17\backslash0.88\backslash0.89 & -0.58\backslash0.07\backslash0.22 & 0.72\backslash0.65\backslash0.66 & -0.01\backslash0.02\backslash-0.01 & 0\backslash-0.02\backslash0 \\ 0.01\backslash-0.02\backslash0 & -0.01\backslash0.02\backslash-0.01 & 0.72\backslash0.65\backslash0.66 & -1.25\backslash0.07\backslash-0.04 & 1.03\backslash0.88\backslash0.92 & 0\backslash0.01\backslash0 \\ 0\backslash0\backslash0 & -0.02\backslash-0.02\backslash0 & -0.01\backslash0.02\backslash-0.01 & 1.03\backslash0.88\backslash0.92 & 1.42\backslash0.04\backslash-0.15 & 0.93\backslash0.99\backslash0.99 \\ 0\backslash0\backslash0 & 0\backslash0\backslash0 & 0\backslash-0.02\backslash0 & -0.01\backslash0.01\backslash0 & 0.93\backslash0.99\backslash0.99 & 0\backslash0\backslash0 \end{bmatrix} \quad (\text{A.16})$$

U-shaped filter

$$\begin{bmatrix} 0\backslash0\backslash0 & 0.94\backslash0.99\backslash0.99 & -0.02\backslash0.01\backslash0 & -0.01\backslash-0.02\backslash0 & -0.02\backslash0\backslash0 & 0\backslash0\backslash0 \\ 0.94\backslash0.99\backslash0.99 & 0.98\backslash0.06\backslash-0.14 & 1.24\backslash0.88\backslash0.89 & -0.02\backslash0.02\backslash-0.01 & -0.03\backslash-0.02\backslash0 & 0.01\backslash0\backslash0 \\ -0.02\backslash0.01\backslash0 & 1.24\backslash0.88\backslash0.89 & -1.10\backslash0.07\backslash0.22 & 0.97\backslash0.65\backslash0.66 & -0.02\backslash0.02\backslash-0.01 & 0.01\backslash-0.02\backslash0 \\ -0.01\backslash-0.02\backslash0 & -0.02\backslash0.02\backslash-0.01 & 0.97\backslash0.65\backslash0.66 & -1.00\backslash0.07\backslash-0.04 & 1.17\backslash0.88\backslash0.92 & -0.02\backslash0.01\backslash0 \\ -0.02\backslash0\backslash0 & -0.03\backslash-0.02\backslash0 & -0.02\backslash0.02\backslash-0.01 & 1.17\backslash0.88\backslash0.92 & 1.91\backslash0.04\backslash-0.15 & 0.91\backslash0.99\backslash0.99 \\ 0\backslash0\backslash0 & 0.01\backslash0\backslash0 & 0.01\backslash-0.02\backslash0 & -0.02\backslash0.01\backslash0 & 0.91\backslash0.99\backslash0.99 & 0\backslash0\backslash0 \end{bmatrix} \quad (\text{A.17})$$

A.3 LMST G4



Parameter	Design			
	Filter	Access (substrate)	Access (board)	Supports
WRES1, WRES4	1.44	-	-	0.54
LRES1, LRES4	1.44	-	-	0.3
WRES2, WRES3	1.37	-	-	0.54
LRES2, LRES3	1.37	-	-	0.3
WIRIS1, WIRIS3	1.06	-	-	-
LIRIS1, LIRIS3	0.14	-	-	-
WIRIS2	1.13	-	-	-
LIRIS2	0.34	-	-	-
W1	-	0.11	0.15	-
G1	-	0.05	0.02	-
L1	-	0.30	1.2	-
G2	-	0.05	-	-
W3	-	1.33	1.54	-
G3	-	0.05	-	-
L3	-	0.05	0.44	-

Table A.1: LMST G4 filter footprint dimensions (in millimeters).

B

Bibliography

Summary

Bibliography	225
------------------------	-----

Bibliography

- [1] J. S. Belrose, “Fessenden and Marconi: their differing technologies and transatlantic experiments during the first decade of this century,” *IEE Conference Publication*, no. 411, pp. 32–43, 1995.
- [2] T. S. Rappaport, *Wireless Communications: Principles and Practice*, 2nd ed. Englewood Cliffs, NJ, USA: Prentice-Hall, 2002.
- [3] A. Goldsmith, “Wireless Communications,” *Wireless Communications*, vol. 978-0-521-83716-3, pp. 1–644, Jan. 2005.
- [4] G. Liu and D. Jiang, “5G: Vision and Requirements for Mobile Communication System towards Year 2020,” *Chinese Journal of Engineering*, vol. 2016, J. Lee, Ed., p. 5 974 586, Apr. 2016.
- [5] TeraSense. “Radio frequency bands.” (2022), [Online]. Available: <https://terasense.com/terahertz-technology/radio-frequency-bands/> (visited on 03/01/2022).
- [6] ITU-R, “Nomenclature of the frequency and wavelength bands used in telecommunications,” ITU, Tech. Rep., 2015.
- [7] D. L. Woolard, J. O. Jensen, R. J. Hwu, and M. S. Shur, *Terahertz Science and Technology for Military and Security Applications*. WORLD SCIENTIFIC, 2007. eprint: <https://www.worldscientific.com/doi/pdf/10.1142/6608>.
- [8] “521-2019 - IEEE Standard Letter Designations for Radar-Frequency Bands,” 2020.
- [9] M. Adnan, S. M. S Hilles, and W. M. S Yafooz, “An Evolution to Next Generation Heterogeneous Cellular Networks,” *IJCSNS International Journal of Computer Science and Network Security*, vol. 17, no. 04, p. 251, 2017.
- [10] T. Farley, “Mobile telephone history,” *Teletronikk*, vol. 101, no. 3–4, pp. 22–34, 2005.

- [11] F. Hillebrand, "The creation of standards for global mobile communication: GSM and UMTS standardization from 1982 to 2000," *IEEE Wireless Communications*, vol. 20, no. 5, pp. 24–33, 2013.
- [12] H. Holma and A. Toskala, "WCDMA for UMTS : radio access for third generation mobile communications," p. 313, 2001.
- [13] J. A. Del Peral-Rosado, R. Raulefs, J. A. López-Salcedo, and G. Seco-Granados, "Survey of Cellular Mobile Radio Localization Methods: From 1G to 5G," *IEEE Communications Surveys and Tutorials*, vol. 20, no. 2, pp. 1124–1148, Apr. 2018.
- [14] L. Chettri and R. Bera, "A Comprehensive Survey on Internet of Things (IoT) Toward 5G Wireless Systems," *IEEE Internet of Things Journal*, vol. 7, no. 1, pp. 16–32, Jan. 2020.
- [15] M. S. Raza, T. Zongsheng, and M. M. Ali Muslam, "A review of human-to-machine and machine-to-machine approaches for internet of things," pp. 1–5, Apr. 2021.
- [16] Z. M. Temesvári, D. Maros, and P. Kádár, "Review of Mobile Communication and the 5G in Manufacturing," *Procedia Manufacturing*, vol. 32, pp. 600–612, Jan. 2019.
- [17] M. Agiwal, A. Roy, and N. Saxena, "Next generation 5g wireless networks: A comprehensive survey," *IEEE Communications Surveys Tutorials*, vol. 18, no. 3, pp. 1617–1655, thirdquarter 2016.
- [18] J. Cheng, W. Chen, F. Tao, and C. L. Lin, "Industrial IoT in 5G environment towards smart manufacturing," *Journal of Industrial Information Integration*, vol. 10, pp. 10–19, Jun. 2018.
- [19] E. Dahlman, G. Mildh, S. Parkvall, *et al.*, "5G wireless access: Requirements and realization," *IEEE Communications Magazine*, vol. 52, no. 12, pp. 42–47, Dec. 2014.
- [20] J. Yang, X. Ge, and Y. Zhong, "How much of wireless rates can smartphones support in 5g networks?" *IEEE Network*, vol. 33, no. 3, pp. 122–129, May 2019.
- [21] J. Navarro-Ortiz, P. Romero-Diaz, S. Sendra, P. Ameigeiras, J. J. Ramos-Munoz, and J. M. Lopez-Soler, "A Survey on 5G Usage Scenarios and Traffic Models," *IEEE Communications Surveys and Tutorials*, vol. 22, no. 2, pp. 905–929, Apr. 2020.
- [22] S. Gangakhedkar, H. Cao, A. R. Ali, K. Ganesan, M. Gharba, and J. Eichinger, "Use cases, requirements and challenges of 5G communication for industrial automation," *2018 IEEE International Conference on Communications Workshops, ICC Workshops 2018 - Proceedings*, pp. 1–6, Jul. 2018.

- [23] O. Alamu, B. Iyaomolere, and A. Abdulrahman, "An overview of massive MIMO localization techniques in wireless cellular networks: Recent advances and outlook," *Ad Hoc Networks*, vol. 111, p. 102 353, Feb. 2021.
- [24] A. Eid, X. He, R. Bahr, *et al.*, "Inkjet-/3D-/4D-Printed perpetual electronics and modules," *IEEE Microwave Magazine*, vol. 21, no. 12, pp. 87–103, Dec. 2020.
- [25] A. Tikhomirov, E. Omelyanchuk, and A. Semenova, "Recommended 5G frequency bands evaluation," *2018 Systems of Signals Generating and Processing in the Field of on Board Communications*, vol. 2018-Janua, pp. 1–4, Apr. 2018.
- [26] W. Hong, Z. H. Jiang, C. Yu, *et al.*, "The Role of Millimeter-Wave Technologies in 5G/6G Wireless Communications," *IEEE Journal of Microwaves*, vol. 1, no. 1, pp. 101–122, Jan. 2021.
- [27] ITU, "ITU8 - R R15 - WRC19PREPWORK contribution 12: WRC - 19 agenda item 1.13 – IMT-2020 between 24.25 and 86 GHz," 2019.
- [28] "Study on using satellite access in 5G," Tech. Rep. 22.822 V16.0.0, Jun. 2018.
- [29] M. Giordani and M. Zorzi, "Non-Terrestrial Networks in the 6G Era: Challenges and Opportunities," *IEEE Network*, vol. 35, no. 2, pp. 244–251, Mar. 2021. arXiv: [1912.10226](https://arxiv.org/abs/1912.10226).
- [30] M. Boschiero, M. Giordani, M. Polese, and M. Zorzi, "Coverage Analysis of UAVs in Millimeter Wave Networks: A Stochastic Geometry Approach," *2020 International Wireless Communications and Mobile Computing, IWCMC 2020*, pp. 351–357, Jun. 2020.
- [31] M. Giordani and M. Zorzi, "Satellite Communication at Millimeter Waves: A Key Enabler of the 6G Era," *2020 International Conference on Computing, Networking and Communications, ICNC 2020*, pp. 383–388, Feb. 2020.
- [32] F. Babich, M. Comisso, A. Cuttin, M. Marchese, and F. Patrone, "Nanosatellite-5G integration in the millimeter wave domain: A full top-down approach," *IEEE Transactions on Mobile Computing*, vol. 19, no. 2, pp. 390–404, Feb. 2020.
- [33] Y. Cho, H. K. Kim, M. Nekovee, and H. S. Jo, "Coexistence of 5G with satellite services in the millimeter-wave band," *IEEE Access*, vol. 8, pp. 163 618–163 636, 2020.
- [34] P. McNeil, "Non-Terrestrial 5G: The Growing Role of Satellites and the mmWave Infrastructure," *Microwaves & RF*, Tech. Rep., May 2020.
- [35] H. Tataria, M. Shafi, A. F. Molisch, M. Dohler, H. Sjoland, and F. Tufvesson, "6G Wireless Systems: Vision, Requirements, Challenges, Insights, and Opportunities," *Proceedings of the IEEE*, 2021.

- [36] W. Hong, Z. H. Jiang, C. Yu, *et al.*, “Multibeam Antenna Technologies for 5G Wireless Communications,” *IEEE Transactions on Antennas and Propagation*, vol. 65, no. 12, pp. 6231–6249, Dec. 2017.
- [37] F. Balteanu, H. Modi, Y. Choi, J. Lee, S. Drogi, and S. Khesbak, “5G RF Front End Module Architectures for Mobile Applications,” *2019 49th European Microwave Conference, EuMC 2019*, pp. 252–255, Oct. 2019.
- [38] C. E. Shannon, “A mathematical theory of communication,” *The Bell System Technical Journal*, vol. 27, no. 3, pp. 379–423, 1948.
- [39] F. Balteanu, S. Drogi, H. Modi, *et al.*, “New architecture elements for 5G RF front end modules,” *Asia-Pacific Microwave Conference Proceedings, APMC*, vol. 2019-Decem, pp. 321–323, Dec. 2019.
- [40] P. P. Shome, T. Khan, S. K. Koul, and Y. M. Antar, “Two Decades of UWB Filter Technology: Advances and Emerging Challenges in the Design of UWB Bandpass Filters,” *IEEE Microwave Magazine*, vol. 22, no. 8, pp. 32–51, Aug. 2021.
- [41] S. Rangan, T. S. Rappaport, and E. Erkip, “Millimeter-wave cellular wireless networks: Potentials and challenges,” *Proceedings of the IEEE*, vol. 102, no. 3, pp. 366–385, 2014.
- [42] M. Xiao, S. Mumtaz, Y. Huang, *et al.*, “Millimeter Wave Communications for Future Mobile Networks,” *IEEE Journal on Selected Areas in Communications*, vol. 35, no. 9, pp. 1909–1935, Sep. 2017.
- [43] X. Luo, J. Ouyang, Z. H. Chen, *et al.*, “A Scalable Ka-Band 1024-Element Transmit Dual-Circularly-Polarized Planar Phased Array for SATCOM Application,” *IEEE Access*, vol. 8, pp. 156 084–156 095, 2020.
- [44] B. Yang, Z. Yu, J. Lan, R. Zhang, J. Zhou, and W. Hong, “Digital Beamforming-Based Massive MIMO Transceiver for 5G Millimeter-Wave Communications,” *IEEE Transactions on Microwave Theory and Techniques*, vol. 66, no. 7, pp. 3403–3418, Jul. 2018.
- [45] A. Simsek, S. K. Kim, A. S. Ahmed, R. Maurer, M. Urteaga, and M. J. Rodwell, “A dual-conversion front-end with a w-band first intermediate frequency for 1-30 GHz reconfigurable transceivers,” *IEEE Radio and Wireless Symposium, RWS*, May 2019.
- [46] R. Gomez-Garcia, D. Psychogiou, J. M. Munoz-Ferreras, and L. Yang, “Avoiding RF Isolators: Reflectionless Microwave Bandpass Filtering Components for Advanced RF Front Ends,” *IEEE Microwave Magazine*, vol. 21, no. 12, pp. 68–86, Dec. 2020.

- [47] D. Zhao, J. Zhang, Y. Yi, P. Gu, and N. Jiang, "5G millimeter-wave phased-array transceiver: System considerations and circuit implementations," *Proceedings - IEEE International Symposium on Circuits and Systems*, vol. 2019-May, 2019.
- [48] L. Ma, Z. Chen, and J. Zhou, "Design of a Q-band superheterodyne transceiver," *9th International Conference on Microwave and Millimeter Wave Technology, ICMMT 2016 - Proceedings*, vol. 2, pp. 904–906, Nov. 2016.
- [49] J. Ma, "The Design-for-Cost of millimeter-wave Front-End for 5G and beyond," *2020 IEEE/CIC International Conference on Communications in China, ICCIC 2020*, pp. 395–400, Aug. 2020.
- [50] K. Onaka, H. Kojima, K. Matsutani, *et al.*, "28 GHz wideband filter using quartz crystal waveguide for massive MIMO antenna unit," *IEEE MTT-S International Microwave Symposium Digest*, pp. 1468–1471, Oct. 2017.
- [51] D. K. Misra, "Radio-Frequency and Microwave Communication Circuits: Analysis and Design: Second Edition," *Radio-Frequency and Microwave Communication Circuits: Analysis and Design: Second Edition*, pp. 1–614, Sep. 2004.
- [52] R. J. Cameron, C. M. Kudsia, and R. R. Mansour, "Microwave filters for communication systems: Fundamentals, design and applications," *Microwave Filters for Communication Systems: Fundamentals, Design and Applications*, pp. 1–804, Feb. 2018.
- [53] R. J. Cameron, "General coupling matrix synthesis methods for Chebyshev filtering functions," *IEEE Transactions on Microwave Theory and Techniques*, vol. 47, no. 4, pp. 433–442, 1999.
- [54] A. M. Soreng and A. Mishra, "Design Techniques of Microwave Cavity And Waveguide Filters: A Literature Review," *International Journal of Engineering and Technical Research*, vol. 8, no. 4, 2018.
- [55] X. P. Chen and K. Wu, "Substrate integrated waveguide filter: Basic design rules and fundamental structure features," *IEEE Microwave Magazine*, vol. 15, no. 5, pp. 108–116, 2014.
- [56] Y. Tang, K. Wu, and N. Khaddaj Mallat, "Development of substrate-integrated waveguide filters for low-cost high-density rf and microwave circuit integration: Direct-coupled cavity bandpass filters with chebyshev response," *Access, IEEE*, vol. 3, pp. 1313–1325, Jan. 2015.
- [57] R. R. Mansour, "High-Q Tunable Dielectric Resonator Filters," *IEEE Microwave Magazine*, vol. 10, no. 6, pp. 84–98, 2009.
- [58] S. W. Wong, J. Y. Lin, Y. Yang, Z. C. Guo, L. Zhu, and Q. X. Chu, "Waveguide Components Based on Multiple-Mode Resonators: Advances in Microwave

- Multiple-Mode Waveguide Components, including Multiplexers, Three-State Diplexers, Crossovers, and Balanced/Unbalanced Elements,” *IEEE Microwave Magazine*, vol. 22, no. 2, pp. 33–45, Feb. 2021.
- [59] S. J. Fiedziuszko and S. Holme, “Dielectric resonators raise your high-Q,” *IEEE Microwave Magazine*, vol. 2, no. 3, pp. 51–60, 2001.
- [60] Y. Chen, Y. Zhang, and K.-L. Wu, “A dual-mode monoblock dielectric bandpass filter using dissimilar fundamental modes,” *IEEE Transactions on Microwave Theory and Techniques*, vol. 69, no. 8, pp. 3811–3819, 2021.
- [61] M. Bertrand, Z. Liu, E. Pistono, D. Kaddour, and P. Ferrari, “A compact slow-wave substrate integrated waveguide cavity filter,” in *2015 IEEE MTT-S International Microwave Symposium*, 2015, pp. 1–3.
- [62] S. Bastioli and R. V. Snyder, “Nonresonating Modes Do It Better!: Exploiting Additional Modes in Conjunction with Operating Modes to Design Better Quality Filters,” *IEEE Microwave Magazine*, vol. 22, no. 1, pp. 20–45, Jan. 2021.
- [63] R. Van Kemenade, A. B. Smolders, and B. P. De Hon, “Micromachined microwave cavity resonator filters for 5G: A feasibility study,” *Proceedings of the 2015 IEEE-APS Topical Conference on Antennas and Propagation in Wireless Communications, IEEE APWC 2015*, pp. 1024–1027, Oct. 2015.
- [64] T. Advisors, P. de Paco Sánchez, and O. Menéndez Nadal, “Specialty : Telecommunications Engineering Analysis and Design of Bulk Acoustic Wave Filters Based on Acoustically Coupled Resonators Edén Corrales López,” Ph.D. dissertation, 2011.
- [65] Wohlers Associates, *Wohlers Annual Report: Additive Manufacturing and 3D Printing State of the Industry*. 2021.
- [66] F. Gianesello, A. Bisognin, D. Titz, *et al.*, “3D printing technology: Enabling innovative & cost effective industrial antenna solution,” *2016 International Workshop on Antenna Technology, iWAT 2016*, pp. 55–56, Mar. 2016.
- [67] S. A. Nauroze, J. G. Hester, B. K. Tehrani, *et al.*, “Additively manufactured RF components and modules: Toward empowering the birth of cost-efficient dense and ubiquitous IoT implementations,” *Proceedings of the IEEE*, vol. 105, no. 4, pp. 702–722, Apr. 2017.
- [68] A. Delage, N. Delhote, S. Verdeyme, *et al.*, “Aerosol jet printing of millimeter wave transmission lines on 3D ceramic substrates made by additive manufacturing,” in *IEEE MTT-S International Microwave Symposium Digest*, vol. 2018-June, Institute of Electrical and Electronics Engineers Inc., Aug. 2018, pp. 1557–1560.

- [69] R. Sorrentino, P. Martin-Iglesias, O. A. Peverini, and T. M. Weller, "Additive Manufacturing of Radio-Frequency Components [Scanning the Issue]," *Proceedings of the IEEE*, vol. 105, no. 4, pp. 589–592, Mar. 2017.
- [70] C. Menudier, M. Thevenot, L. Huitema, *et al.*, "Innovative materials and fabrication process to develop new RF components and concepts," *2017 11th European Conference on Antennas and Propagation, EUCAP 2017*, pp. 594–597, May 2017.
- [71] C. Tomassoni, L. Silvestri, N. Delmonte, *et al.*, "A New Class of Doublet Based on Slotted Slant Ridge in Additive Manufacturing Technology," *IMWS-AMP 2019 - 2019 IEEE MTT-S International Microwave Workshop Series on Advanced Materials and Processes for RF and THz Applications*, pp. 10–12, Jul. 2019.
- [72] C. Tomassoni, G. Venanzoni, M. Dionigi, and R. Sorrentino, "Compact quasi-elliptic filters with mushroom-shaped resonators manufactured with 3-d Printer," *IEEE Transactions on Microwave Theory and Techniques*, vol. 66, no. 8, pp. 3579–3588, Aug. 2018.
- [73] G. Venanzoni, M. Dionigi, C. Tomassoni, and R. Sorrentino, "3-D-Printed Quasi-Elliptical Evanescent Mode Filter Using Mixed Electromagnetic Coupling," *IEEE Microwave and Wireless Components Letters*, vol. 28, no. 6, pp. 497–499, Jun. 2018.
- [74] G. Venanzoni, M. Dionigi, C. Tomassoni, and R. Sorrentino, "Design of a compact 3d printed coaxial filter," in *2018 48th European Microwave Conference (EuMC)*, 2018, pp. 280–283.
- [75] G. Venanzoni, C. Tomassoni, M. Dionigi, M. Mongiardo, and R. Sorrentino, "Design and Fabrication of 3-D Printed Inline Coaxial Filters with Improved Stopband," *IEEE Transactions on Microwave Theory and Techniques*, vol. 68, no. 7, pp. 2633–2643, Jul. 2020.
- [76] R. Sorrentino and O. A. Peverini, "Additive manufacturing: A key enabling technology for next-generation microwave and millimeter-wave systems [point of view]," *Proceedings of the IEEE*, vol. 104, no. 7, pp. 1362–1366, Jul. 2016.
- [77] J. M. Flynn, A. Shokrani, S. T. Newman, and V. Dhokia, "Hybrid additive and subtractive machine tools - Research and industrial developments," *International Journal of Machine Tools and Manufacture*, vol. 101, pp. 79–101, Feb. 2016.
- [78] ASTM F2792-12a, "Standard Terminology for Additive Manufacturing Technologies, (Withdrawn 2015)," ASTM International, West Conshohocken, PA, Tech. Rep., 2012.

- [79] R. Bahr, B. Tehrani, and M. M. Tentzeris, "Exploring 3-D printing for new applications," *IEEE Microwave Magazine*, vol. 19, no. 1, pp. 57–66, Jan. 2018.
- [80] F. Cai, W. T. Khan, and J. Papapolymerou, "A low loss X-band filter using 3-D Polyjet technology," *2015 IEEE MTT-S International Microwave Symposium, IMS 2015*, Jul. 2015.
- [81] B. K. Tehrani, B. S. Cook, and M. M. Tentzeris, "Inkjet printing of multilayer millimeter-wave yagi-uda antennas on flexible substrates," *IEEE Antennas and Wireless Propagation Letters*, vol. 15, pp. 143–146, 2016.
- [82] J. Kimionis, A. Georgiadis, M. Isakov, H. J. Qi, and M. M. Tentzeris, "3D/inkjet-printed origami antennas for multi-direction RF harvesting," *2015 IEEE MTT-S International Microwave Symposium, IMS 2015*, Jul. 2015.
- [83] D. M. Martínez, S. Bila, F. Seyfert, M. Olivi, O. Tantot, and L. Carpentier, "Synthesis method for manifold-coupled multiplexers," in *2019 49th European Microwave Conference (EuMC)*, 2019, pp. 308–311.
- [84] E. Laplanche, O. Tantot, N. Delhote, *et al.*, "A ku-band diplexer based on 3dB directional couplers made by plastic additive manufacturing," *European Microwave Week 2017: "A Prime Year for a Prime Event", EuMW 2017 - Conference Proceedings; 47th European Microwave Conference, EuMC 2017*, vol. 2017-January, pp. 428–431, Dec. 2017.
- [85] S.-Y. Wu, C. Yang, W. Hsu, and L. Lin, "3D-printed microelectronics for integrated circuitry and passive wireless sensors," *Microsystems & Nanoengineering 2015 1:1*, vol. 1, no. 1, pp. 1–9, Jul. 2015.
- [86] O. A. Peverini, G. Addamo, M. Lumia, *et al.*, "Additive manufacturing of Ku/K-band waveguide filters: A comparative analysis among selective-laser melting and stereolithography," *IET Microwaves, Antennas and Propagation*, vol. 11, no. 14, pp. 1936–1942, Nov. 2017.
- [87] N. T. Nguyen, N. Delhote, M. Ettorre, D. Baillargeat, L. Le Coq, and R. Sauleau, "Design and characterization of 60-GHz integrated lens antennas fabricated through ceramic stereolithography," *IEEE Transactions on Antennas and Propagation*, vol. 58, no. 8, pp. 2757–2762, Aug. 2010.
- [88] V. Tornielli Di Crestvolant, P. Martin Iglesias, and M. J. Lancaster, "Advanced Butler Matrices with Integrated Bandpass Filter Functions," *IEEE Transactions on Microwave Theory and Techniques*, vol. 63, no. 10, pp. 3433–3444, Oct. 2015.
- [89] F. Zhang, C. Guo, Y. Zhang, *et al.*, "A 3-D Printed Bandpass Filter Using TM-Mode Slotted Spherical Resonators with Enhanced Spurious Suppression," *IEEE Access*, vol. 8, pp. 213 215–213 223, 2020.

- [90] G. Addamo, O. A. Peverini, D. Manfredi, *et al.*, “Additive manufacturing of ka-band dual-polarization waveguide components,” *IEEE Transactions on Microwave Theory and Techniques*, vol. 66, no. 8, pp. 3589–3596, Aug. 2018.
- [91] G. Addamo, O. A. Peverini, F. Calignano, *et al.*, “3-d printing of high-performance feed horns from Ku-to V-bands,” *IEEE Antennas and Wireless Propagation Letters*, vol. 17, no. 11, pp. 2036–2040, Nov. 2018.
- [92] G. Addamo, O. A. Peverini, D. Manfredi, *et al.*, “Electromagnetic and mechanical analyses of a 3D-printed ka-band integrated twist and orthomode transducer,” *IMWS-AMP 2019 - 2019 IEEE MTT-S International Microwave Workshop Series on Advanced Materials and Processes for RF and THz Applications*, pp. 31–33, Jul. 2019.
- [93] N. Delhote, D. Baillargeat, S. Verdeyme, C. Delage, and C. Chaput, “Ceramic layer-by-layer stereolithography for the manufacturing of 3-D millimeter-wave filters,” *IEEE Transactions on Microwave Theory and Techniques*, vol. 55, no. 3, pp. 548–554, Mar. 2007.
- [94] H. Khalil, N. Delhote, D. Baillargeat, *et al.*, “Advanced design and manufacturing of microwave components based on shape optimization and ceramic stereolithography process,” *2008 IEEE MTT-S International Microwave Workshop Series IMWS on Art of Miniaturizing RF and Microwave Passive Components - Proceeding*, pp. 15–18, 2008.
- [95] B. Liu, X. Gong, and W. J. Chappell, “Applications of layer-by-layer polymer stereolithography for three-dimensional high-frequency components,” *IEEE Transactions on Microwave Theory and Techniques*, vol. 52, no. 11, pp. 2567–2575, Nov. 2004.
- [96] N. Delhote, D. Baillargeat, S. Verdeyme, C. Delage, and C. Chaput, “Narrow Ka bandpass filters made of high permittivity ceramic by layer-by-layer polymer stereolithography,” *Proceedings of the 36th European Microwave Conference, EuMC 2006*, pp. 510–513, 2006.
- [97] N. Delhote, “Composants céramiques 3D par procédé de stéréolithographie : solutions de filtrage hyperfréquence innovantes,” <http://www.theses.fr>, Jan. 2007.
- [98] A. Perigaud, O. Tantot, N. Delhote, S. Verdeyme, S. Bila, and D. Baillargeat, “Bandpass Filter Based on Skeleton-like Monobloc Dielectric Pucks Made by Additive Manufacturing,” *2018 48th European Microwave Conference, EuMC 2018*, pp. 296–299, Nov. 2018.
- [99] N. Delhote, M. Chatras, D. Baillargeat, and S. Verdeyme, “Ku band filter based on low loss alumina octagonal dielectric resonators made by 3d ceramic stere-

- olithography,” in *2009 European Microwave Conference (EuMC)*, 2009, pp. 1397–1400.
- [100] Y. Marchives, N. Delhote, S. Verdeyme, and P. M. Iglesias, “Wide-band dielectric filter at C-band manufactured by stereolithography,” *European Microwave Week 2014: Connecting the Future, EuMW 2014 - Conference Proceedings; EuMC 2014: 44th European Microwave Conference*, pp. 187–190, Dec. 2014.
- [101] X. Shang, J. Li, C. Guo, M. J. Lancaster, and J. Xu, “3-D printed filter based on helical resonators with variable width,” *IEEE MTT-S International Microwave Symposium Digest*, pp. 1587–1590, Oct. 2017.
- [102] A. Périgaud, N. Delhote, R. Segalen, Y. Mancuso, and P. Garrec, “Compact reconfigurable ceramic filter based on combline type 3-D resonators,” *2014 International Radar Conference, Radar 2014*, Mar. 2014.
- [103] A. Perigaud, O. Tantot, N. Delhote, *et al.*, “Continuously Tuned Ku-Band Cavity Filter Based on Dielectric Perturbers Made by Ceramic Additive Manufacturing for Space Applications,” *Proceedings of the IEEE*, vol. 105, no. 4, pp. 677–687, Feb. 2017.
- [104] F. Le Borgne, E. Rius, K. Donnart, *et al.*, “Principle demonstration of a mechanically tunable uhf bandpass filter based on sir coaxial resonators,” in *2019 IEEE Asia-Pacific Microwave Conference (APMC)*, 2019, pp. 351–353.
- [105] A. H. Khalil, N. Delhote, S. Pacchini, *et al.*, “3-D pyramidal and collective Ku band pass filters made in Alumina by ceramic stereolithography,” *IEEE MTT-S International Microwave Symposium Digest*, 2011.
- [106] Y. Dia, L. Huitema, S. Bila, M. Thevenot, N. Delhote, and C. Delaveaud, “3D Compact High-Q Filter Made of High-Permittivity Ceramic,” *2019 49th European Microwave Conference, EuMC 2019*, pp. 304–307, Oct. 2019.
- [107] Y. Marchives, N. Delhote, S. Verdeyme, and P. M. Iglesias, “Wide-band dielectric filter at C-band manufactured by stereolithography,” *European Microwave Week 2014: Connecting the Future, EuMW 2014 - Conference Proceedings; EuMC 2014: 44th European Microwave Conference*, pp. 187–190, Dec. 2014.
- [108] A. Khalil, “Technologies LTCC et stéréolithographie céramique 3D appliquées à la conception de dispositifs millimétriques et sub-millimétriques,” Ph.D. dissertation, Jan. 2010.
- [109] M. K. Drissi, “Composants céramiques 3D innovants pour des applications spatiales de télécommunications millimétriques en bandes Q et V,” Theses, Université de Limoges, Dec. 2016.

- [110] S. W. Sattler, F. Gentili, R. Teschl, C. Carceller, and W. Bösch, "Emerging technologies and concepts for 5G applications-A. making additive manufactured ceramic microwave filters ready for 5G," *2018 International Symposium on VLSI Design, Automation and Test, VLSI-DAT 2018*, pp. 1–6, Jun. 2018.
- [111] J. Li, G. Huang, T. Yuan, J. Xu, and H. Li, "A Ku-Band Wideband 3-D Printed Interdigital Bandpass Filter Free of Post Fabrication Tuning," *2018 IEEE Antennas and Propagation Society International Symposium and USNC/URSI National Radio Science Meeting, APSURSI 2018 - Proceedings*, pp. 1439–1440, 2018.
- [112] C. Guo, X. Shang, M. J. Lancaster, and J. Xu, "A 3-D Printed Lightweight X-Band Waveguide Filter Based on Spherical Resonators," *IEEE Microwave and Wireless Components Letters*, vol. 25, no. 7, pp. 442–444, Jul. 2015.
- [113] X. Shang, P. Penchev, C. Guo, *et al.*, "W-Band Waveguide Filters Fabricated by Laser Micromachining and 3-D Printing," *IEEE Transactions on Microwave Theory and Techniques*, vol. 64, no. 8, pp. 2572–2580, Aug. 2016.
- [114] M. Dionigi, C. Tomassoni, G. Venanzoni, and R. Sorrentino, "Simple High-Performance Metal-Plating Procedure for Stereolithographically 3-D-Printed Waveguide Components," *IEEE Microwave and Wireless Components Letters*, vol. 27, no. 11, pp. 953–955, Nov. 2017.
- [115] C. Guo, Y. Gao, Y. Wang, *et al.*, "A 3-D Printed E-Plane Waveguide Magic-T Using Air-Filled Coax-to-Waveguide Transitions," *IEEE Transactions on Microwave Theory and Techniques*, vol. 67, no. 12, pp. 4984–4994, Dec. 2019.
- [116] N. T. Nguyen, N. Delhote, M. Ettorre, D. Baillargeat, L. Le Coq, and R. Sauleau, "Design and characterization of 60-GHz integrated lens antennas fabricated through ceramic stereolithography," *IEEE Transactions on Antennas and Propagation*, vol. 58, no. 8, pp. 2757–2762, Aug. 2010.
- [117] P. T. Timbie, J. Grade, D. Van Der Weide, B. Maffei, and G. Pisano, "Stereolithographed MM-wave corrugated horn antennas," *IRMMW-THz 2011 - 36th International Conference on Infrared, Millimeter, and Terahertz Waves*, 2011.
- [118] F. Kouki, M. Thevenot, S. Bila, *et al.*, "Miniature ceramic filter-antenna for wireless communications systems at 60GHz," *European Microwave Week 2014: "Connecting the Future", EuMW 2014 - Conference Proceedings; EuMIC 2014: 9th European Microwave Integrated Circuits Conference*, pp. 644–647, Dec. 2014.
- [119] Y. H. Lou, Y. X. Zhu, G. F. Fan, W. Lei, W. Z. Lu, and X. C. Wang, "Design of Ku-Band Flat Luneburg Lens Using Ceramic 3-D Printing," *IEEE Antennas and Wireless Propagation Letters*, vol. 20, no. 2, pp. 234–238, Feb. 2021.

- [120] Y. J. Zhu, J. Li, X. Zhang, *et al.*, “A 3-D Printed Spherical Antenna with Bandwidth Enhancement under Operation of Dual Resonance,” *IEEE Access*, vol. 8, pp. 19 345–19 352, 2020.
- [121] Q. Lamotte, G. Mazingue, J. Bhatker, *et al.*, “Multi-permittivity 3d-printed ceramic dual-band circularly polarized dielectric resonator antenna for space applications,” in *2021 15th European Conference on Antennas and Propagation (EuCAP)*, 2021, pp. 1–5.
- [122] Z. A. Khan, “A Novel Transmission Line Structure for High-Speed High-Density Copper Interconnects,” *IEEE Transactions on Components, Packaging and Manufacturing Technology*, vol. 6, no. 7, pp. 1077–1086, Jul. 2016.
- [123] Swissto12. “Antenna components.” (2022), [Online]. Available: <https://swissto12.com/products/antenna-components/> (visited on 03/01/2022).
- [124] H. Tataria, M. Shafi, A. F. Molisch, M. Dohler, H. Sjoland, and F. Tufvesson, “6G Wireless Systems: Vision, Requirements, Challenges, Insights, and Opportunities,” *Proceedings of the IEEE*, 2021.
- [125] H. Leblond, J. Villemazet, J. Cazaux, *et al.*, “When new needs for satellite payloads meet with new filters architecture and technologies,” in *2009 European Microwave Integrated Circuits Conference (EuMIC)*, 2009, pp. 359–362.
- [126] S. Shinjo, K. Nakatani, K. Tsutsumi, and H. Nakamizo, “Integrating the front end,” *IEEE Microwave Magazine*, vol. 18, pp. 31–40, 5 2017.
- [127] R. Aigner, “Tunable filters? reality check,” *IEEE Microwave Magazine*, vol. 16, pp. 82–88, 7 Aug. 2015.
- [128] R. Zhang and R. R. Mansour, “Low-cost dielectric-resonator filters with improved spurious performance,” *IEEE Transactions on Microwave Theory and Techniques*, vol. 55, no. 10, pp. 2168–2175, 2007.
- [129] D. Tiradossi, A. Cazzorla, L. Pelliccia, M. Bartocci, P. Bia, and A. Manna, “Planar and low-consumption switchable filter banks with tunable passband and stop-band responses,” in *2021 IEEE MTT-S International Microwave Filter Workshop (IMFW)*, 2021, pp. 224–226.
- [130] I. Reines, C. Goldsmith, C. Nordquist, *et al.*, “A low loss rf mems ku-band integrated switched filter bank,” *IEEE Microwave and Wireless Components Letters*, vol. 15, no. 2, pp. 74–76, 2005.
- [131] X. Yang, M. Xing, E. Wang, L. Zhang, N. Li, and Z. Qian, “A design of s-band monolithic integrated switched filter bank,” in *2017 18th International Conference on Electronic Packaging Technology (ICEPT)*, 2017, pp. 177–181.

- [132] T. Kawamura, M. Fuse, and S. Mattori, "Evaluation of 140-ghz band filter bank prototype," in *2018 Asia-Pacific Microwave Conference (APMC)*, 2018, pp. 13–15.
- [133] E. Laplanche, N. Delhote, A. Périgaud, *et al.*, "Tunable filtering devices in satellite payloads: A review of recent advanced fabrication technologies and designs of tunable cavity filters and multiplexers using mechanical actuation," *IEEE Microwave Magazine*, vol. 21, pp. 69–83, 3 Mar. 2020.
- [134] A. Périgaud, O. Tantot, N. Delhote, *et al.*, "Continuously tuned ku-band cavity filter based on dielectric perturbors made by ceramic additive manufacturing for space applications," *Proceedings of the IEEE*, vol. 105, no. 4, pp. 677–687, 2017.
- [135] P. Aurelien, V. Serge, D. Nicolas, B. Stephane, T. Olivier, and L. Carpentier, "Continuously tunable x-band filter using a 3d spiral ribbon," *2018 IEEE MTT-S International Conference on Numerical Electromagnetic and Multiphysics Modeling and Optimization, NEMO 2018*, Oct. 2018.
- [136] S.-J. Park, I. Reines, C. Patel, and G. M. Rebeiz, "High- Q rf-mems 4–6-ghz tunable evanescent-mode cavity filter," *IEEE Transactions on Microwave Theory and Techniques*, vol. 58, no. 2, pp. 381–389, 2010.
- [137] J. S. Hong, "Reconfigurable planar filters," *IEEE Microwave Magazine*, vol. 10, pp. 73–83, 6 2009.
- [138] R. Gomez-Garcia, D. Psychogiou, J. M. Munoz-Ferreras, and L. Yang, "Avoiding rf isolators: Reflectionless microwave bandpass filtering components for advanced rf front ends," *IEEE Microwave Magazine*, vol. 21, pp. 68–86, 12 Dec. 2020.
- [139] D. Psychogiou and R. Gomez-Garcia, "Tunable reflectionless microstrip bandpass filters," *IEEE Radio and Wireless Symposium, RWS*, vol. 2018-January, pp. 49–51, Feb. 2018.
- [140] D. Psychogiou and R. Gómez-García, "Reflectionless adaptive rf filters: Bandpass, bandstop, and cascade designs," *IEEE Transactions on Microwave Theory and Techniques*, vol. 65, no. 11, pp. 4593–4605, 2017.
- [141] L.-H. Hsieh and K. Chang, "Tunable microstrip bandpass filters with two transmission zeros," *IEEE Transactions on Microwave Theory and Techniques*, vol. 51, no. 2, pp. 520–525, 2003.
- [142] W.-H. Tu and K. Chang, "Piezoelectric transducer-controlled dual-mode switchable bandpass filter," *IEEE Microwave and Wireless Components Letters*, vol. 17, no. 3, pp. 199–201, 2007.

- [143] N. Sekiya, Y. Nakagawa, A. Saito, and S. Ohshima, "Novel trimming technique for tunable hts microstrip filters," *Physica C: Superconductivity*, vol. 468, pp. 1958–1961, Sep. 2008.
- [144] P. P. Shome, T. Khan, S. K. Koul, and Y. M. Antar, "Two decades of uwb filter technology: Advances and emerging challenges in the design of uwb bandpass filters," *IEEE Microwave Magazine*, vol. 22, pp. 32–51, 8 Aug. 2021.
- [145] R. Gómez-García, J. M. Muñoz-Ferreras, and D. Psychogiou, "Dual-behavior resonator-based fully reconfigurable input reflectionless bandpass filters," *IEEE Microwave and Wireless Components Letters*, vol. 29, pp. 35–37, 1 Jan. 2019.
- [146] R. Gómez-García, J.-M. Muñoz-Ferreras, and D. Psychogiou, "Fully-reconfigurable bandpass filter with static couplings and intrinsic-switching capabilities," in *2017 IEEE MTT-S International Microwave Symposium (IMS)*, 2017, pp. 914–917.
- [147] R. Gomez-Garcia, D. Psychogiou, and D. Peroulis, "Single/multi-band multi-functional passive components with reconfiguration capabilities," *IEEE Radio and Wireless Symposium, RWS*, pp. 9–12, Mar. 2017.
- [148] D. J. Simpson and D. Psychogiou, "Coupling matrix-based design of fully reconfigurable differential/balanced rf filters," *IEEE Microwave and Wireless Components Letters*, vol. 28, no. 10, pp. 888–890, 2018.
- [149] H. Wu, X. Cai, Y. Wu, Z. Lai, Q. Yang, and W. Wang, "An investigation on extraction of material parameters in longitudinal mode of fbar," *IEEE Transactions on Circuits and Systems II: Express Briefs*, vol. 67, no. 6, pp. 1024–1028, 2020.
- [150] M. Zolfagharloo Koochi, S. Lee, and A. Mortazawi, "Compact intrinsically switchable fbar filters utilizing ferroelectric bst," *IEEE Transactions on Ultrasonics, Ferroelectrics, and Frequency Control*, vol. 65, no. 8, pp. 1468–1474, 2018.
- [151] M. Z. Koochi, S. Nam, and A. Mortazawi, "Intrinsically switchable and bandwidth reconfigurable ferroelectric bulk acoustic wave filters," *IEEE Transactions on Ultrasonics, Ferroelectrics, and Frequency Control*, vol. 67, no. 5, pp. 1025–1032, 2020.
- [152] K. Zhao and D. Psychogiou, "Single-to-multi-band reconfigurable acoustic-wave-lumped-resonator bandpass filters," *IEEE Transactions on Circuits and Systems II: Express Briefs*, 2021.
- [153] D. Psychogiou, "Reconfigurable all-pass-to-bandstop acoustic-wave-lumped-element resonator filters," *IEEE Microwave and Wireless Components Letters*, vol. 30, no. 8, pp. 745–748, 2020.
- [154] D. Psychogiou, R. Gomez-Garcia, and D. Peroulis, "Single and multiband acoustic-wave-lumped-element-resonator (awlr) bandpass filters with reconfigurable trans-

- fer function,” *IEEE Transactions on Microwave Theory and Techniques*, vol. 64, pp. 4394–4404, 12 Dec. 2016.
- [155] D. Psychogiou, R. Gómez-García, and D. Peroulis, “Tunable acoustic-wave-lumped-element resonator (awlr)-based bandpass filters,” in *2016 IEEE MTT-S International Microwave Symposium (IMS)*, 2016, pp. 1–4.
- [156] D. Psychogiou, R. Gómez-García, R. Loeches-Sánchez, and D. Peroulis, “Hybrid acoustic-wave-lumped-element resonators (awlrs) for high- Q bandpass filters with quasi-elliptic frequency response,” *IEEE Transactions on Microwave Theory and Techniques*, vol. 63, no. 7, pp. 2233–2244, 2015.
- [157] K. Entesari, A. P. Saghati, V. Sekar, and M. Armendariz, “Tunable siw structures: Antennas, vcos, and filters,” *IEEE Microwave Magazine*, vol. 16, pp. 34–54, 5 Jun. 2015.
- [158] F. Giuppi, A. Georgiadis, A. Collado, M. Bozzi, and L. Perregrini, “Tunable siw cavity backed active antenna oscillator,” *Electronics Letters*, vol. 46, pp. 1053–1055, 15 Jul. 2010.
- [159] V. Sekar, M. Armendariz, and K. Entesari, “A 1.2–1.6-ghz substrate-integrated-waveguide rf mems tunable filter,” *IEEE Transactions on Microwave Theory and Techniques*, vol. 59, no. 4, pp. 866–876, 2011.
- [160] A. El Mostrah, A. Muller, J.-F. Favennec, *et al.*, “An rf-mems-based digitally tunable siw filter in x-band for communication satellite applications,” *Applied Sciences*, vol. 9, May 2019.
- [161] B. Potelon, “Etude des techniques et technologies de conception et de réalisation de filtres hyperfréquences basés sur des guides d’onde intégrés au substrat: Performances, compacité, accordabilité,” Sep. 2016.
- [162] J. C. Bohórquez, B. Potelon, C. Person, *et al.*, “Reconfigurable planar siw cavity resonator and filter,” *IEEE MTT-S International Microwave Symposium Digest*, pp. 947–950, 2006.
- [163] M. Armendariz, V. Sekar, and K. Entesari, “Tunable siw bandpass filters with pin diodes,” in *The 40th European Microwave Conference*, 2010, pp. 830–833.
- [164] W. Gautier, A. Stehle, B. Schoenlinner, V. Ziegler, U. Prechtel, and W. Menzel, “Rf-mems tunable filters on low-loss ltcc substrate for uav data-link,” in *2009 European Microwave Integrated Circuits Conference (EuMIC)*, 2009, pp. 347–350.
- [165] S. Sirci, J. D. Martínez, M. Taroncher, and V. E. Boria, “Varactor-loaded continuously tunable siw resonator for reconfigurable filter design,” in *2011 41st European Microwave Conference*, 2011, pp. 436–439.

- [166] S. Sirci, J. D. Martínez, M. Taroncher, and V. Boria, "Analog tuning of compact varactor-loaded combline filters in substrate integrated waveguide," in *2012 42nd European Microwave Conference*, 2012, pp. 257–260.
- [167] S. Sirci, J. D. Martínez, and V. E. Boria, "Low-loss 3-bit tunable siw filter with pin diodes and integrated bias network," in *2013 European Microwave Conference*, 2013, pp. 1211–1214.
- [168] S. Sirci, J. D. Martinez, R. Stefanini, P. Blondy, and V. E. Boria, "Compact smd packaged tunable filter based on substrate integrated coaxial resonators," *IEEE MTT-S International Microwave Symposium Digest*, 2014.
- [169] S. Sirci, J. D. Martínez, M. Taroncher, and V. E. Boria, "Varactor-loaded continuously tunable siw resonator for reconfigurable filter design," in *2011 41st European Microwave Conference*, 2011, pp. 436–439.
- [170] L.-R. Tan, R.-X. Wu, C.-Y. Wang, and Y. Poo, "Ferrite-loaded siw bowtie slot antenna with broadband frequency tunability," *IEEE Antennas and Wireless Propagation Letters*, vol. 13, pp. 325–328, 2014.
- [171] F. Mira, J. Mateu, and C. Collado, "Mechanical tuning of substrate integrated waveguide resonators," *IEEE Microwave and Wireless Components Letters*, vol. 22, no. 9, pp. 447–449, 2012.
- [172] A. Anand, J. Small, D. Peroulis, and X. Liu, "Theory and design of octave tunable filters with lumped tuning elements," *IEEE Transactions on Microwave Theory and Techniques*, vol. 61, no. 12, pp. 4353–4364, 2013.
- [173] C. Wang and K. A. Zaki, "Dielectric resonators and filters," *IEEE Microwave Magazine*, vol. 8, no. 5, pp. 115–127, 2007.
- [174] R. A. Meyers, *Encyclopedia of Physical Science and Technology*, Third Edition. Academic Press, 2001.
- [175] F. Huang and R. R. Mansour, "Tunable compact dielectric resonator filters," in *2009 European Microwave Conference (EuMC)*, 2009, pp. 559–562.
- [176] F. Huang, S. Fouladi, and R. Mansour, "A novel mems-based tunable dielectric resonator filter," *IEEE MTT-S International Microwave Symposium Digest*, 2011.
- [177] A. Périgaud, N. Delhote, R. Segalen, Y. Mancuso, and P. Garrec, "Compact reconfigurable ceramic filter based on combline type 3-d resonators," in *2014 International Radar Conference*, 2014, pp. 1–4.
- [178] C. Montgomery, *Technique des mesures en micro-ondes*, P. Chiron, Ed. 1953, vol. 1.

- [179] S. Sirci, M. A. Sánchez-Soriano, J. D. Martínez, and V. E. Boria, “Electronically reconfigurable doublet in dual-mode coaxial siw,” in *2019 IEEE MTT-S International Microwave Symposium (IMS)*, 2019, pp. 17–20.
- [180] J. C. Bohórquez, B. Potelon, C. Person, *et al.*, “Reconfigurable planar siw cavity resonator and filter,” *IEEE MTT-S International Microwave Symposium Digest*, pp. 947–950, 2006.
- [181] H. Alaaeddine, O. Tantot, M. Aubourg, and S. Verdeyme, “Characterization of high permittivity substrates by a thickness resonance method,” in *2011 41st European Microwave Conference*, 2011, pp. 206–209.
- [182] W. Chew, M.-S. Tong, and B. hu. 2008.
- [183] “Mode-matching method,” in *Analysis Methods for RF, Microwave, and Millimeter-Wave Planar Transmission Line Structures*. John Wiley & Sons, Ltd, ch. 8, pp. 191–235.
- [184] S. Bila, D. Baillargeat, M. Aubourg, *et al.*, “Finite-element modeling for the design optimization of microwave filters,” *IEEE Transactions on Magnetics*, vol. 40, no. 2, pp. 1472–1475, 2004.
- [185] X.-P. Chen, K. Wu, and D. Drolet, “Substrate integrated waveguide filter with improved stopband performance for satellite ground terminal,” *IEEE Transactions on Microwave Theory and Techniques*, vol. 57, no. 3, pp. 674–683, 2009.
- [186] S. Amari and U. Rosenberg, “Characteristics of cross (bypass) coupling through higher/lower order modes and their applications in elliptic filter design,” *IEEE Transactions on Microwave Theory and Techniques*, vol. 53, no. 10, pp. 3135–3141, 2005.
- [187] *Design with pin diodes*, AG312, V3, MACOM.
- [188] T. H. Lin, S. N. Daskalakis, A. Georgiadis, and M. M. Tentzeris, “Achieving Fully Autonomous System-on-Package Designs: An Embedded-on-Package 5G Energy Harvester within 3D Printed Multilayer Flexible Packaging Structures,” *IEEE MTT-S International Microwave Symposium Digest*, vol. 2019-June, pp. 1375–1378, Jun. 2019.
- [189] A. Delage, N. Delhote, S. Verdeyme, *et al.*, “Aerosol jet printing of millimeter wave transmission lines on 3d ceramic substrates made by additive manufacturing,” vol. 2018-June, Institute of Electrical and Electronics Engineers Inc., Aug. 2018, pp. 1557–1560.
- [190] B. K. Tehrani and M. M. Tentzeris, “Fully Inkjet-Printed Ramp Interconnects for Wireless Ka-Band MMIC Devices and Multi-Chip Module Packaging,” in *2018*

- 48th European Microwave Conference, EuMC 2018*, Institute of Electrical and Electronics Engineers Inc., Nov. 2018, pp. 1037–1040.
- [191] B. K. Tehrani, R. A. Bahr, W. Su, B. S. Cook, and M. M. Tentzeris, “E-band characterization of 3d-printed dielectrics for fully-printed millimeter-wave wireless system packaging,” Institute of Electrical and Electronics Engineers Inc., Oct. 2017, pp. 1756–1759.
- [192] S. Sirci, J. D. Martinez, R. Stefanini, P. Blondy, and V. E. Boria, “Compact smd packaged tunable filter based on substrate integrated coaxial resonators,” *IEEE MTT-S International Microwave Symposium Digest*, 2014.
- [193] A. Delage, “Technologie aérosol appliquée à l’intégration 3D et aux composants hyperfréquences,” Theses, Université de Limoges, Dec. 2019.
- [194] W. Feuray, A. Delage, A. Abdelghani, *et al.*, “Evaluation of metal coating techniques up to 66 ghz and their application to additively manufactured bandpass filters,” *European Microwave Week 2017: "A Prime Year for a Prime Event", EuMW 2017 - Conference Proceedings; 47th European Microwave Conference, EuMC 2017*, vol. 2017-January, pp. 512–515, Dec. 2017.
- [195] L. Carpentier, “Filtres céramiques microondes par stéréolithographie 3D,” Theses, Université de Limoges, Dec. 2012.
- [196] G. Wen, X. Guo, and C. Davies, “Electroless plating for the enhancement of material performance,” *Materials Technology*, vol. 14, no. 4, pp. 210–217, 1999.
- [197] J. White and P. Bindra, *Electroless plating : fundamentals and applications*. William Andrew Publishing, 1990, pp. 289–329.
- [198] J. Metal™. “Spray metallization.” (2021), [Online]. Available: <https://www.jetmetal-tech.com/entreprise> (visited on 12/11/2021).
- [199] E. Doumanis, G. Goussetis, and S. Kosmopoulos, “Filter design for satellite communications : Helical resonator technology.,” p. 207, 2015.
- [200] M. R. F. for, M. A. J.-S. Hong, and M. J. Lancaster, “Microstrip filters for rf/microwave applications,” *Microstrip Filters for RF/Microwave Applications*, Dec. 2001.
- [201] A. Périgaud, D. Baillargeat, S. Bila, and U. de Limoges. Faculté des sciences et techniques, *Conception de banques de filtres micro-ondes passifs compacts dans la bande 2-20 GHz à l'aide des technologies multicouches*, ser. Lille thèses. 2009.
- [202] P. Martin-Iglesias, M. Van Der Vorst, J. Gumpinger, and T. Ghidini, “ESA’s recent developments in the field of 3D-printed RF/microwave hardware,” *2017 11th European Conference on Antennas and Propagation, EUCAP 2017*, pp. 553–557, May 2017.

- [203] A. Kanso, E. Arnaud, T. Monédière, *et al.*, “Inkjet printing of coplanar wire-patch antenna on a flexible substrate,” *2012 15th International Symposium on Antenna Technology and Applied Electromagnetics, ANTEM 2012*, 2012.
- [204] R. Bahr, B. Teharani, M. M. Tentzeris, and K. Byers, “A novel integration of stereolithography and inkjet printing for multichip modules with high frequency packaging applications,” *Proceedings - Electronic Components and Technology Conference*, vol. 2018-May, pp. 2498–2504, Aug. 2018.
- [205] X. Wang, K. L. Wu, and W. Y. Yin, “A novel surface-mounted monoblock dielectric filter,” *IEEE Transactions on Components, Packaging and Manufacturing Technology*, vol. 4, no. 11, pp. 1822–1827, Nov. 2014.
- [206] J. Hesselbarth, “Surface-mount cavity filter technology,” *Proceedings of the 37th European Microwave Conference, EUMC*, pp. 442–445, 2007.
- [207] D. Lohinetong, P. Minard, C. Nicolas, *et al.*, “Surface mounted millimeter waveguide devices based on metallized dielectric foam or plastic materials,” *IEEE MTT-S International Microwave Symposium Digest*, vol. 2005, pp. 1409–1412, 2005.
- [208] X. Wang, K. L. Wu, and W. Y. Yin, “A novel surface-mounted monoblock dielectric filter,” *IEEE Transactions on Components, Packaging and Manufacturing Technology*, vol. 4, pp. 1822–1827, 11 Nov. 2014.
- [209] H. Kojima, M. Nakahori, K. Matsutani, *et al.*, “A compact 28ghz bandpass filter using quartz folded waveguide,” *IEEE MTT-S International Microwave Symposium Digest*, vol. 2018-June, pp. 1110–1113, Aug. 2018.
- [210] J. Hesselbarth and R. Vahldieck, “Dual-mode surface-mount cavity resonator and filter,” *IEEE MTT-S International Microwave Symposium Digest*, pp. 1241–1244, 2009.
- [211] J. Schorer, J. Bornemann, and U. Rosenberg, “Design of a surface mounted waveguide filter in substrate integrated waveguide technology,” *European Microwave Week 2015: "Freedom Through Microwaves", EuMW 2015 - Conference Proceedings; 2015 45th European Microwave Conference Proceedings, EuMC*, pp. 757–760, Dec. 2015.
- [212] A. Basti, S. Bila, S. Verdeyme, A. Perigaud, L. Estagerie, and H. Leblond, “Design of a compact hybrid filter using microstrip resonators and surface mounted cavities,” *IEEE MTT-S International Microwave Symposium Digest*, 2014.
- [213] C. Lu, X. Yin, L. Xie, Q. Chen, and H. Zhao, “A miniaturized surface mount bandpass filter implemented with substrate integrated coaxial line,” in *Proceed-*

- ings of 2014 3rd Asia-Pacific Conference on Antennas and Propagation*, 2014, pp. 1198–1200.
- [214] T. Charlet, “Filtres hyperfréquences reportés en surface, à fort facteur de qualité et compensés en température,” Theses, Université de Limoges, Jan. 2021.
- [215] E. Laplanche, O. Tantot, N. Delhote, *et al.*, “A ku-band diplexer based on 3db directional couplers made by plastic additive manufacturing,” in *2017 47th European Microwave Conference (EuMC)*, 2017, pp. 428–431.
- [216] E. Laplanche, N. Delhote, A. Périgaud, *et al.*, “Tunable filtering devices in satellite payloads: A review of recent advanced fabrication technologies and designs of tunable cavity filters and multiplexers using mechanical actuation,” *IEEE Microwave Magazine*, vol. 21, no. 3, pp. 69–83, 2020.
- [217] P. Harscher, R. Vahldieck, and S. Amari, “A novel technique for automated post production filter tuning,” in *APMC 2001. 2001 Asia-Pacific Microwave Conference (Cat. No.01TH8577)*, vol. 2, 2001, 751–754 vol.2.
- [218] Y. Zhang, H. Meng, and K.-L. Wu, “A hybrid genetic algorithm for robot automatic tuning of microwave filters,” in *2020 IEEE MTT-S International Wireless Symposium (IWS)*, 2020, pp. 1–3.
- [219] A. Dia, C. Dourousseau, C. Menudier, L. Carpentier, O. Ruatta, and S. Bila, “Gradient descent shape optimization of microwave circuits using bézier curves parametrization,” in *2018 48th European Microwave Conference (EuMC)*, 2018, pp. 158–161.
- [220] S. Courrèges, J. Fan, A. Crunteanu, V. Madrangeas, M. Maignan, and L. Rigaudeau, “Study of tuning innovative solution for the realization of high temperature superconducting IMUX filters,” in *International Workshop on Microwave Filters, IWMF 2009*, Toulouse, France, Nov. 2009, inconnu.
- [221] S. Courreges, C. Thibon, F. A. Houndonougbo, A. Crunteanu, V. Madrangeas, and M. Maignan, “Tuning of superconducting filters with laser ablation technique,” *IEEE Transactions on Applied Superconductivity*, vol. 19, no. 5, pp. 3715–3721, 2009.
- [222] K. Hiroshi, K. Hiroyuki, M. Meiji, and S. Kazuhisa, *Dielectric waveguide filter and mounting structure thereof*, 2004.
- [223] S. Wu, A. Zhao, and Z. Ren, “Design of dual-band millimeter-wave antenna array for 5g communication system,” 2018, pp. 1–2.
- [224] P. Aurélien *et al.*, “Continuously tunable x-band filter using a 3d spiral ribbon,” in *2018 IEEE MTT-S International Conference on Numerical Electromagnetic and Multiphysics Modeling and Optimization (NEMO)*, 2018, pp. 1–4.

- [225] L. Huitema, Y. Dia, M. Thevenot, S. Bila, A. Perigaud, and C. Delaveaud, “Miniaturization of a filter-antenna device by co-design,” *IEEE Open Journal of Antennas and Propagation*, vol. 2, pp. 498–505, 2021.
- [226] B.-L. Zheng, S.-W. Wong, L. Zhu, and Y. He, “Broadband duplex–filtenna based on low-profile metallic cavity packaging,” *IEEE Transactions on Components, Packaging and Manufacturing Technology*, vol. 8, no. 8, pp. 1451–1457, 2018.
- [227] E. Meyer, T. A. H. Bressner, A. B. Bart Smolders, and U. Johannsen, “Miniaturized conical waveguide filtenna for 5g millimeter wave base stations,” in *2021 15th European Conference on Antennas and Propagation (EuCAP)*, 2021, pp. 1–5.
- [228] R. A. Alhalabi and G. M. Rebeiz, “High-gain yagi-uda antennas for millimeter-wave switched-beam systems,” *IEEE Transactions on Antennas and Propagation*, vol. 57, no. 11, pp. 3672–3676, 2009.
- [229] W. Gautier, B. Schoenlinner, V. Ziegler, U. Prechtel, and W. Menzel, “High q micro-machined cavity resonator filter in low-cost silicon technology,” in *2008 38th European Microwave Conference*, Oct. 2008, pp. 1193–1196.
- [230] L. Rigaudeau, P. Ferrand, D. Baillargeat, *et al.*, “Ltc 3d resonator applied to the design of a very compact bandpass filter for q band applications,” in *2005 European Microwave Conference*, vol. 1, 2005, 4 pp.-.
- [231] Y. H. Cho, D. Y. Jung, Y. C. Lee, *et al.*, “A fully embedded ltcc multilayer bpf for 3-d integration of 40-ghz radio,” *IEEE Transactions on Advanced Packaging*, vol. 30, no. 3, pp. 521–525, 2007.
- [232] P. Ferrand, D. Baillargeat, S. Verdeyme, J. Puech, M. Lahti, and T. Jaakola, “Ltc reduced-size bandpass filters based on capacitively loaded cavities for q band application,” in *IEEE MTT-S International Microwave Symposium Digest, 2005.*, 2005, pp. 2083–2086.
- [233] Y. Wang, M. Ke, and M. J. Lancaster, “Micromachined 38 GHz cavity resonator and filter with rectangular-coaxial feed-lines,” *IET Microwaves, Antennas Propagation*, vol. 3, no. 1, pp. 125–129, Feb. 2009.
- [234] P. Farinelli, L. Pelliccia, B. Margesin, and R. Sorrentino, “Ka-band surface-mountable pseudo-elliptic filter in multilayer micromachined technology for on-board communication systems,” in *2016 IEEE MTT-S International Microwave Symposium (IMS)*, 2016, pp. 1–4.
- [235] K. J. Vanhille *et al.*, “Ka-band miniaturized quasi-planar high-Q resonators,” *IEEE Transactions on Microwave Theory and Techniques*, vol. 55, no. 6, pp. 1272–1279, Jun. 2007.

- [236] A. Perigaud et al., “Low loss substrate integrated filters made by laser micro-machining of alumina substrates,” in *2017 IEEE MTT-S International Microwave Workshop Series on Advanced Materials and Processes for RF and THz Applications (IMWS-AMP)*, Sep. 2017, pp. 1–3.
- [237] T. Martin, A. Ghiotto, T.-P. Vuong, F. Lotz, L. Carpentier, and P. Martín-Iglesias, “Self-temperature-compensated air-filled substrate integrated waveguide (afsiw) quasi-elliptic filters,” *IEEE Transactions on Microwave Theory and Techniques*, vol. 69, no. 10, pp. 4510–4520, 2021.
- [238] T. Martin, A. Ghiotto, T.-P. Vuong, and F. Lotz, “Self-temperature-compensated air-filled substrate-integrated waveguide cavities and filters,” *IEEE Transactions on Microwave Theory and Techniques*, vol. 66, no. 8, pp. 3611–3621, 2018.
- [239] V. Nova, C. B. Martin, J. A. Martínez, et al., “Thermal stability analysis of filters in substrate integrated technologies under atmospheric pressure and vacuum conditions,” *IEEE Access*, vol. 8, pp. 118 072–118 082, 2020.
- [240] A. Belenguer, H. Esteban, A. L. Borja, and V. E. Boria, “Empty siw technologies: A major step toward realizing low-cost and low-loss microwave circuits,” *IEEE Microwave Magazine*, vol. 20, no. 3, pp. 24–45, 2019.
- [241] A. Périgaud, K. Drissi, and N. Delhote, “Ceramic q-band bandpass filters by laser micro-machining of alumina substrates,” in *2017 IEEE MTT-S International Microwave Symposium (IMS)*, Jun. 2017, pp. 1456–1459.
- [242] A. Fontana et al., “Laser-machined substrate technology (lmst) for q-band applications,” in *2020 XXXIIIrd General Assembly and Scientific Symposium of the International Union of Radio Science*, 2020, pp. 1–4.
- [243] D. D. Marco, K. Drissi, N. Delhote, et al., “Dielectric properties of pure alumina from 8ghz to 73ghz,” *Journal of the European Ceramic Society*, vol. 36, no. 14, pp. 3355–3361, 2016.
- [244] Y. Kalkal and V. Kumar, “Understanding energy propagation during reflection of an evanescent electromagnetic wave,” *American Journal of Physics*, vol. 89, pp. 877–884, 9 Sep. 2021.
- [245] K. H. Yeap, K. H. Teh, K. C. Yeong, K. C. Lai, and M. C. Loh, “Propagation in dielectric rectangular waveguides,” *Optica Applicata*, vol. 46, pp. 317–330, 2 2016.
- [246] D. Pozar, *Microwave Engineering*, ser. Addison-Wesley series in electrical and computer engineering. Wiley, 2012.
- [247] M. Milosevic, “On the nature of the evanescent wave.,” *Applied spectroscopy*, vol. 67, pp. 126–31, 2 Feb. 2013.

- [248] R. Jamal, T. Olivier, P. Damien, D. Nicolas, and V. Serge, "Monitoring of electromagnetic characteristics of split cylinder resonator and dielectric material for temperature caraterization," in *2014 44th European Microwave Conference*, 2014, pp. 120–123.
- [249] D. Deslandes and Ke Wu, "Integrated transition of coplanar to rectangular waveguides," in *2001 IEEE MTT-S International Microwave Symposium Digest (Cat. No.01CH37157)*, vol. 2, May 2001, 619–622 vol.2.
- [250] A. Patrovsky, M. Daigle, and Ke Wu, "Millimeter-wave wideband transition from cpw to substrate integrated waveguide on electrically thick high-permittivity substrates," in *2007 European Microwave Conference*, Oct. 2007, pp. 138–141.
- [251] A. Fontana *et al.*, "Laser-machined ceramic band-pass filters development for mm-wave applications," in *International Microwave Filters Workshop (IMWF 2021)*, 2021, pp. 1–4.
- [252] G. Brown, P. Zeitzoff, G. Bersuker, and H. Huff, "Scaling CMOS," *Materials Today*, vol. 7, no. 1, pp. 20–25, Jan. 2004.
- [253] A. Fontana *et al.*, "Collective fabrication of lmst thermally-stable smd ceramic devices for millimeter-wave bands," in *51st European Microwave Conference (EuMC)*, Apr. 2022, pp. 1–4.
- [254] K. Ito and K. Sano, "60-GHz band dielectric waveguide filters made of crystalline quartz," in *IEEE MTT-S International Microwave Symposium Digest*, vol. 2005, 2005, pp. 2087–2090.
- [255] S. Bila, D. Baillargeat, M. Aubourg, *et al.*, "Finite-element modeling for the design optimization of microwave filters," *IEEE Transactions on Magnetics*, vol. 40, no. 2, pp. 1472–1475, 2004.
- [256] F. Seyfert, L. Baratchart, J.-P. Marmorat, S. Bila, and J. Sombrin, "Extraction of coupling parameters for microwave filters: Determination of a stable rational model from scattering data," in *IEEE MTT-S International Microwave Symposium Digest, 2003*, vol. 1, 2003, 25–28 vol.1.
- [257] Y. H. Cho *et al.*, "A fully embedded LTCC multilayer bpf for 3-d integration of 40-GHz radio," *IEEE Transactions on Advanced Packaging*, vol. 30, no. 3, pp. 521–525, Aug. 2007.
- [258] D. Scarbrough and C. Goldsmith, "Lightweight filter technology for UAV and satellite applications," *Proc. Government Microcircuit Appl. Crit. Technol. Conf. Dig.*, pp. 599–602, Mar. 2013.
- [259] *26 ghz surface mount bandpass filter*, B259MC1S, Dielectric Laboratories, 2018.

- [260] *38.5 ghz surface mount bandpass filter*, B385MD0S, Dielectric Laboratories, 2018.
- [261] T. Martin, A. Ghiotto, F. Lotz, and T. Vuong, "Air-filled siw filters for k- to e-band substrate integrated systems," in *2018 IEEE MTT-S International Conference on Numerical Electromagnetic and Multiphysics Modeling and Optimization (NEMO)*, Aug. 2018, pp. 1–3.
- [262] K. Ito and K. Sano, "60-GHz band dielectric waveguide filters made of crystalline quartz," in *IEEE MTT-S International Microwave Symposium Digest, 2005.*, Jun. 2005, 4 pp.-.
- [263] N. Wainstein, G. Adam, E. Yalon, and S. Kvatinsky, "Radiofrequency switches based on emerging resistive memory technologies - a survey," *Proceedings of the IEEE*, vol. 109, no. 1, pp. 77–95, 2021.
- [264] W. Tian, H. Cui, and W. Yu, "Analysis and experimental test of electrical characteristics on bonding wire," *Electronics*, vol. 8, p. 365, 3 Mar. 2019.
- [265] A. Chandrasekhar, S. Stoukatch, S. Brebels, *et al.*, "Characterisation, modelling and design of bond-wire interconnects for chip-package co-design," *Conference Proceedings - 33rd European Microwave Conference, EuMC 2003*, vol. 1, pp. 301–305, 2003.
- [266] *The mosis service*, <https://www.themosisservice.com/>, Aug. 2022.

Mise en œuvre de technologies de fabrication par impression 3-D et usinage laser pour la conception de dispositifs céramiques à haute fréquence et leur intégration dans les systèmes de communication modernes

Résumé :

L'utilisation de matériaux céramiques est étudiée pour réaliser l'intégration de technologies micro-ondes axées sur les systèmes de communication sans fil. La conception, la modélisation et la caractérisation des dispositifs passifs à micro-ondes et à ondes millimétriques sont abordées avec l'utilisation des technologies de fabrication additive et soustractive. Le travail est principalement axé sur la conception de filtres passe-bande développés dans des matériaux céramiques de pointe afin de fournir des composants légers et compacts offrant de bonnes performances. Les dispositifs étudiés sont conçus pour répondre aux spécifications des frontaux MIMO massifs, normalisés ces dernières années pour la 5G et au-delà. Les techniques de stéréolithographie céramique et d'usinage laser sont également mises en œuvre pour le développement de composants 2,5-D et 3-D montés en surface et basés sur des dispositifs à cavité remplie de céramique pour des applications terrestres, aériennes et spatiales.

Mots clés : Impression 3D, céramiques, filtres passe-bande, ondes millimétriques, 5G, communications, stéréolithographie, ablation laser, satellite, MIMO front-end, montage en surface .

Implementation of 3-D printing and laser machining manufacturing technologies for the conception of high-frequency ceramic devices and their integration in modern communication systems

Abstract:

The utilization of ceramic materials is studied to perform the integration of microwave technologies focused on wireless communication systems. The design, modelling and characterization of microwave and millimeter-wave passive devices is addressed with the use of additive and subtractive manufacturing technologies. The work is mainly focused on the conception of band-pass filters developed in state-of-the-art ceramic materials to provide light-weight and compact components with good performances. The devices investigated are designed to fulfill the specifications of massive MIMO front-ends, standardized during the recent years for 5G and beyond. Ceramic stereolithography and laser machining techniques are equally implemented for the development of surface-mounted 2.5-D and 3-D components based on ceramic-filled cavity devices for terrestrial, aerial and space applications.

Keywords: 3-D printing, ceramics, band-pass filters, millimeter-wave, 5G, communications, stereolithography, laser ablation, satellite, MIMO front-end, surface-mount .